

INVESTIGATIONS INTO THE IMPROVEMENT OF A SINGLE PHASE PERMANENT MAGNET BRUSHLESS DC MOTOR

Thesis submitted for the degree of

Doctor of Philosophy

at the University of Leicester

by

Saeed Ahmed

Department of Engineering

University of Leicester

2011

INVESTIGATIONS INTO THE IMPROVEMENT OF A SINGLE PHASE PERMANENT MAGNET BRUSHLESS DC MOTOR

by

Saeed Ahmed

Abstract

The work presented in this thesis is aimed at improving single phase permanent magnet brushless DC motors; including their operation, design, efficiency and smoothness. Three main areas were identified and researched for further improvement. As a precursor to this work, a detailed literature study related to each area is also presented.

The first of these areas concentrates on the improvement of the open circuit torque for a single phase BLDC motor. The open circuit torque is not only due to the slot openings, but is also contributed by the uneven airgap which is conventionally used to solve starting problem. The aim is to enhance the starting torque at alignment positions and attenuate the torque ripple between null points where the back EMF is non-zero. The improvement of the open circuit torque was investigated in two stages. In the first stage the open circuit torque due to the slot openings was reduced, and in the second stage the focus was on enhancing the open circuit torque contributed from the uneven air gap topology with minimum ripple.

The second area of investigation was to devise a new encoderless control method for a single phase BLDC motor. A detailed analysis on the derivation of the method is presented. The method has been validated both analytically and numerically.

The third area of investigation was the creation of a new non-complex phase advance control method. The details of the analytical simulation and practical implementation are presented. The method has been validated experimentally and it was shown that the experimental results agree well with the analytical predictions.

Acknowledgements

First and foremost, I would like to express sincere gratitude and appreciation to my supervisor, Dr Paul W Lefley, for his guidance and enthusiasm during this work. He has inspired me to never accept facts without questioning and to challenge my own thinking.

Similar recognition is due to Luigi Alessandro, Alan Rice and Alan Wale for all their help providing the tools and equipment needed for the experiments.

I would like to thank my colleagues in the Power Research group for our many useful discussions that have enabled me to get to where I am now. Thanks are also due to my managers at Cummins for their understanding during the writing-up of this thesis.

It would never have been possible to get this far without the unwavering support of my parents whose positive outlook inspired me, taught me the value of knowledge and encouraged me to seek it all the time. Thank you Dad for the confidence you have in me and Mum for your never-ending emotional support and prayers.

Writing up this thesis has been a challenging and time consuming process and one which would not have been possible without my mother in law Ala who, on many occasions, has dropped everything at a moments notice to come and help my family when we have needed it.

Most importantly my love and gratitude goes to my wife Anna for her encouragement, patience and understanding, especially during the final phase of my research. And to my beautiful daughter Samaya; thank you for brightening every day and sorry for not being able to play and read for you as much as I would have liked.

Contents

1. INTRODUCTION.....	1
1.1 INTRODUCTION	1
1.1.1 <i>Zero current or open circuit torque improvement</i>	1
1.1.2 <i>Efficiency improvement</i>	2
1.1.3 <i>Reliability improvement</i>	2
1.2 PERMANENT MAGNET BRUSHLESS MOTORS	2
1.3 PERMANENT-MAGNET MACHINE CONFIGURATIONS	5
1.4 POSITION SENSING REQUIREMENT	7
1.4.1 <i>Optical encoder</i>	8
1.4.2 <i>Hall Effect sensors</i>	8
1.4.3 <i>Resolver</i>	8
1.4.4 <i>Other sensor possibilities</i>	9
1.5 THE DRIVE FOR A SINGLE PHASE BLDC MOTOR	9
1.5.1 <i>One phase one pulse (unidirectional current) motors</i>	9
1.5.2 <i>One phase two pulse motors</i>	10
1.5.3 <i>Bifilar wound two pulse motor</i>	11
1.6 LAYOUT OF THE THESIS	11
2. COGGING TORQUE REDUCTION METHODS FOR PERMANENT MAGNET BRUSHLESS DC MOTOR	13
2.1 INTRODUCTION	13
2.2 MAGNETIC TORQUE CALCULATION	14
2.2.1 <i>Maxwell stress tensor</i>	14
2.2.2 <i>Co-energy method</i>	15
2.2.3 <i>Coulomb’s virtual work</i>	16
2.3 METHODS IN COGGING TORQUE REDUCTION.....	16
2.3.1 <i>Slotless stator topology</i>	17
2.3.2 <i>Skewing</i>	18
2.3.3 <i>Non-integer slot pole ratio</i>	19
2.3.4 <i>Positional rotation of the permanent magnet poles relative to each other</i>	19
2.3.5 <i>Optimize rotor pole-arc length</i>	21
2.3.6 <i>Auxiliary slots or notches</i>	21
2.3.7 <i>Magnet pole shape optimization</i>	22
2.4 THE NATURE OF COGGING TORQUE FOR SINGLE PHASE PM BLDC MOTOR.....	23
3. NEW APPROACH FOR OPEN CIRCUIT TORQUE IMPROVEMENT FOR SINGLE PHASE PM BLDC MOTOR.....	24
3.1 INTRODUCTION	24
3.2 THE EFFECT OF ASYMMETRICAL STATOR POLES ON COGGING TORQUE	27
3.3 THE SHAPE OF THE BACK EMF PROFILE.....	29
3.3.1 <i>The effect of asymmetrical stator topology on K_e</i>	30
3.4 OBTAINING THE OPTIMUM COMBINATION OF STATOR POLE ARC RATIO AND MAGNET ARC WIDTH	31
3.5 SUPERPOSITION PROPERTY OF K_e PROFILE	32
3.6 THE K_e EXPRESSION	42
3.7 DISCUSSION	44
3.8 IRON REDUCTION	46
3.9 DESIGN PROCEDURE OF A 1 kW SINGLE PHASE BLDC MOTOR BASED ON THE NEW TOPOLOGY	49
3.9.1 <i>Requirements</i>	49

3.9.2	<i>Equivalent magnetic circuit</i>	50
3.9.3	<i>Calculating the dimensions</i>	51
3.9.4	<i>FEM Results</i>	55
3.10	CONCLUSIONS	56
4.	TAILORING THE OPEN CIRCUIT TORQUE PROFILE FOR THE NEW SINGLE PHASE PM BLDC MOTOR	57
4.1	INTRODUCTION	57
4.2	STARTING TORQUE IN SINGLE PHASE BLDC MOTOR	57
4.3	CONVENTIONAL SOLUTION FOR THE STARTING PROBLEM IN SINGLE PHASE PM BLDC MOTOR	59
4.4	THE PROPERTY OF SUPERPOSITION FOR TWO INDEPENDENT AIRGAP SHAPES	61
4.5	UNIFORM AIRGAP RELUCTANCE TORQUE PROFILE (COGGING TORQUE).....	64
4.6	SMALL UNIT CHANGE IN THE AIRGAP SHAPE	67
4.7	PROPERTIES OF AUXILIARY SLOTS (OR NOTCHES)	68
4.7.1	<i>Varying the angular position of the auxiliary slot</i>	68
4.7.2	<i>Varying the radial depth of the auxiliary slot</i>	69
4.7.3	<i>Varying the width of the auxiliary slot</i>	72
4.8	OPEN CIRCUIT TORQUE IMPROVEMENT FOR THE NEW SINGLE PHASE BLDC MOTOR	74
4.9	NOTCH PROPERTIES FOR TAPERED PERMANENT MAGNET MOTOR DESIGN.	77
4.9.1	<i>The effect of tapering the magnet on the torque due to slot openings</i>	78
4.9.2	<i>The effect of tapering the magnet on the notches reluctance torque profile</i>	79
4.9.3	<i>Varying the arc width of the permanent magnet</i>	86
4.10	SYNTHESIZING THE OPEN CIRCUIT TORQUE PROFILE FOR A MOTOR WITH TAPERED MAGNETS	87
4.10.1	<i>Experimental results</i>	92
4.11	CONCLUSIONS	95
5.	REVIEW ON ENCODERLESS POSITION SENSING METHODS FOR PM BLDC MOTOR	96
5.1	INTRODUCTION	96
5.2	BACK EMF BASED TECHNIQUES	98
5.2.1	<i>Zero crossing points</i>	98
5.2.2	<i>Sensing from the third harmonic</i>	100
5.2.3	<i>Freewheeling diode conduction method</i>	103
5.2.4	<i>Observer based methods</i>	104
5.3	INDUCTANCE VARIATION ENCODERLESS METHODS	106
5.3.1	<i>Current waveform detection techniques</i>	107
5.3.2	<i>Voltage Pulse Techniques</i>	109
5.3.3	<i>Modulation Based Techniques</i>	111
5.3.4	<i>Switching Frequency Based Estimation</i>	111
5.4	SUMMARY OF METHODS	112
6.	NEW ENCODERLESS CONTROL METHOD FOR SINGLE PHASE BLDC MOTOR	113
6.1	INTRODUCTION	113
6.2	COMMUTATION OF A SINGLE PHASE BLDC MOTOR	114
6.3	SENSING THE MAGNETIC FLUX IN IRON	115
6.4	SENSING THE TANGENTIAL COMPONENT OF THE ROTOR PM FLUX.....	120
6.5	SEARCH COIL PARAMETERS	122
6.6	ANALYTICAL SIMULATION RESULTS	125
6.7	FEM VALIDATION	131
6.8	DISCUSSIONS AND CONCLUSIONS.....	133

7.	NEW PHASE ADVANCE CONTROL FOR SINGLE PHASE PM BRUSHLESS DC MOTORS	135
7.1	INTRODUCTION	135
7.2	ADVANCING THE COMMUTATION SIGNAL	136
7.3	PHASE ANGLE BETWEEN BACK EMF AND CURRENT	136
7.3.1	<i>No phase advance mode</i>	<i>137</i>
7.3.2	<i>Phase advance to match current polarity with back EMF</i>	<i>138</i>
7.3.3	<i>Phase advance with current leading back EMF waveform</i>	<i>139</i>
7.4	PHASE ADVANCE FOR MULTI-PHASE AND SINGLE-PHASE BLDC MOTORS	141
7.5	PREVIOUS WORK ON PHASE ADVANCE CONTROL FOR SINGLE PHASE BLDC MOTORS	141
7.6	A REVIEW ON PHASE ADVANCE CONTROL TECHNIQUES FOR MULTI PHASE BLDC MOTORS	144
7.7	THE NEW PHASE ADVANCE CONTROL METHOD.....	146
7.8	PHASE ERROR CALCULATION ALGORITHM	147
7.8.1	<i>PI controller</i>	<i>148</i>
7.8.2	<i>Advanced commutation signal production.....</i>	<i>149</i>
7.9	SIMULINK MODEL OF A SINGLE PHASE BLDC MOTOR.....	149
7.10	SIMULINK MODEL OF THE NEW PHASE ADVANCE CONTROL	156
7.10.1	<i>Phase mismatch by standard Simulink blocks.....</i>	<i>157</i>
7.10.2	<i>Phase mismatch by Simulink embedded function</i>	<i>159</i>
7.10.3	<i>Advanced commutation signal production</i>	<i>161</i>
7.11	SIMULINK RESULTS OF THE PROPOSED PHASE ADVANCE CONTROL	162
7.12	PRACTICAL IMPLEMENTATION.....	165
7.13	DISCUSSIONS AND CONCLUSIONS.....	169
8.	CONCLUSIONS.....	171
8.1	OPEN CIRCUIT TORQUE IMPROVEMENT.....	171
8.2	ENCODERLESS CONTROL METHOD	172
8.3	PHASE ADVANCE CONTROL	172
8.4	KEY CONTRIBUTIONS.....	173
8.5	LIST OF PUBLICATIONS	174
9.	APPENDIX	175
9.1	MEPS.....	175
9.2	MINIMUM SURFACE AREA OF A CYLINDER.....	178
9.3	THE MATLAB CODE FOR THE SIZING OF 1 kW SINGLE PHASE BLDC MOTOR.	179
9.4	ENCODERLESS METHOD FOR A NOVEL BRUSHLESS SR MOTOR.....	183
9.4.1	<i>Search coils wiring configurations</i>	<i>184</i>
9.4.2	<i>Running the motor without position Encoder.....</i>	<i>187</i>
9.4.3	<i>The signal processing</i>	<i>188</i>
9.4.4	<i>Signal processing circuit tests.....</i>	<i>190</i>
9.4.5	<i>Effect of Loading.....</i>	<i>191</i>
9.5	MATLAB CODE OF PHASE MISMATCH MAGNITUDE CALCULATOR	193
9.6	MATLAB CODE OF PHASE MISMATCH ERROR POLARITY DETERMINATION CODE.....	194
9.7	EXPERIMENTAL SET UP PHOTOS FOR PHASE ADVANCE CONTROL TESTING	195
9.8	TORQUE TRANSDUCER DATASHEET	197
10.	REFERENCES.....	199

1. Introduction

1.1 Introduction

The primary aim of this thesis is to investigate into the development of a single phase permanent magnet brushless DC (PM BLDC) motors. Three research areas have been investigated for improvements. These areas are the open circuit torque, the efficiency and the reliability. The motor is mainly used for low starting torque applications i.e. fans and pumps. This thesis presents a range of work performed on the motor which has led to new solutions that improve certain aspects of this type of motor. This has been addressed by the following:-

1.1.1 Zero current or open circuit torque improvement

Open circuit torque is the rotor torque that exists when the current in the winding is zero. For three phase motors this torque is due to the slot openings and it is commonly referred to as cogging torque. However in single phase BLDC motor the open circuit torque is due to the slot opening (cogging torque) and auxiliary reluctance torque that designed to solve the common problem of null points in the electromagnetic torque. All the methods used to overcome the null point problem in single phase BLDC motors are based on creating an asymmetrical (non constant) air gap that enhances the excitation torque at the alignment positions. In this thesis the open circuit torque was improved in two stages. In the first stage the open circuit torque due to the slot opening only was reduced and in the second stage the open circuit torque due to the air gap topology was enhanced. A new topology has been investigated with a goal of finding a topology that preserves the trapezoidal back EMF with reduced open circuit torque ripple and efficient starting torque.

1.1.2 Efficiency improvement

In this age of climate change and energy efficiency the EU have imposed strict new legislation governing the manufacture of industrial electric motors which will see an increase in the minimum permitted motor efficiency, see appendix 9.1. Therefore the second aim of this thesis is to improve the efficiency of an existing prototype single phase BLDC motor by employing a phase advance control method to increase the torque per amp which results in a reduced current for the same torque demand and hence reduced copper losses.

1.1.3 Reliability improvement

The work related to reliability improvement of the single phase BLDC motor is concerned with the elimination of rotor position encoder. Position encoders are a source for reliability issue when the motor is to be operated in a harsh environment. Another disadvantage of position encoders is the intricacy of the assembly process which requires great care to achieve the required commutation timings. An attempt to eliminate this position encoder and find a new novel way to detect rotor position information that is independent from rotor saliency and loading condition is presented in chapter 6.

All the solutions proposed in this chapter can be combined in one single phase BLDC motor or depending on the design requirement a machine can employ only one or two of the solutions.

1.2 Permanent magnet brushless motors

In brushed DC machines the commutation function is performed by the commutator and brushes. The mechanical commutator has some disadvantages which are speed limitation, noise and wear, overcoming those disadvantages has been a major reason behind the development of PM brushless motors. As the name implies, PM brushless

motors do not use brushes for commutation; instead, they are electronically commutated. The advantages of BLDC motor over the brushed DC machine are

- Better speed torque characteristics
- High dynamic response
- High efficiency
- Long operating life
- Low noise operation
- Higher speed range

Fig. 1.1 shows a classification of electrical machines. PM motors are classified into two subcategories. The first is called the brushless DC (BLDC) motor which has a trapezoidal back EMF shape and driven by a square phase voltages. The second is called Permanent Magnet Synchronous Motor (PMSM) which has sinusoidal back EMF and it is driven by a sinusoidal phase voltages. A BLDC motor drive is less expensive than a PMSM drive because BLDC drive needs a discrete rotor position feedback. Where as the PMSM drive requires continuous rotor position feedback to control the sinusoidal voltages and currents in the motor [1]. Therefore, BLDC motors are mainly used for low cost low power applications and PMSM are used for high power applications. The two factors that determine the shape of the back EMF are the rotor magnet flux distribution in the air gap, and the stator winding configuration [2, 3].

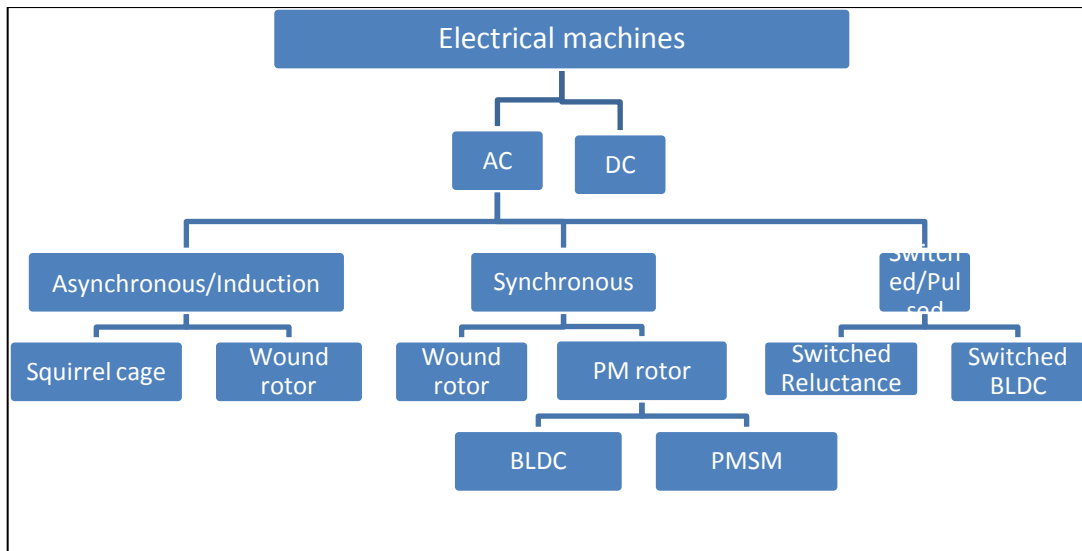


Fig. 1.1 Classification of electrical machines

Both the trapezoidal and sinusoidal machines can be represented by the same equivalent circuit for each phase winding as shown in Fig. 1.2, in which the source voltage V supplies current i to the phase circuit consisting of a series-connected resistance R , inductance L , and motional EMF. The back EMF (or motional EMF) is caused by the movement of the permanent magnet rotor and is therefore dependent on rotor position, as well as being proportional to rotor rotational velocity.

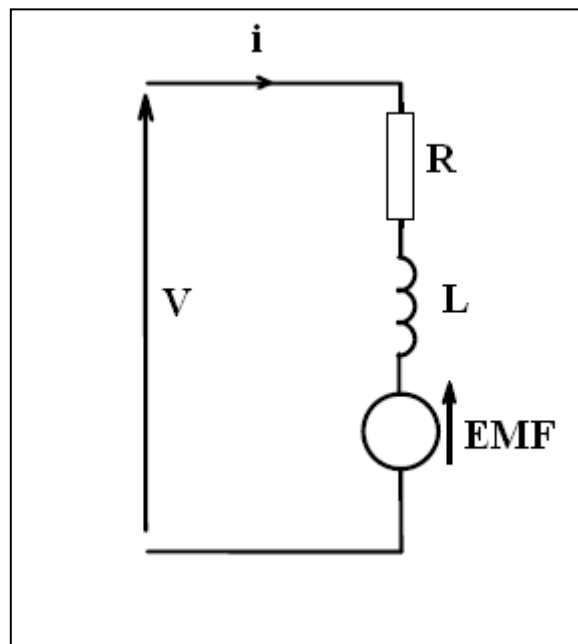


Fig. 1.2 Equivalent electrical circuit for one phase of PM brushless motor

Based on the number of phases, a BLDC machine can be further classified into two subcategories single phase BLDC and multi phase BLDC motors. Single phase PM BLDC motors are being used increasingly for low cost low power applications [4-7] due to their relatively simple control combined with cost effectiveness. The lower cost of this machine is due to the simpler winding and the electronic commutation scheme.

1.3 Permanent-magnet machine configurations

Position variation of inductance and back EMF in the permanent magnet motor depends on the magnetic structure. Permanent magnet motors are characterized by having a field produced by the permanent magnet on the rotor and the armature winding on the stator. The motor may be of the inner or outer rotor type, see Fig. 1.3, according to the application. The inner rotor configuration is more suitable for high speed operation and has smaller rotor inertia. However, the outer rotor configuration may be useful in applications requiring constant speed operation, because the larger rotor inertia can reduce speed fluctuations arising from torque ripple.

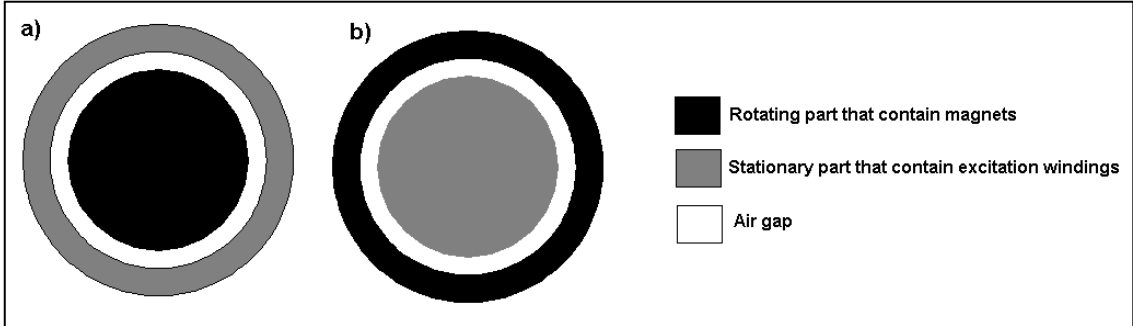


Fig. 1.3 a) Inner rotor b) Outer rotor

For the inner rotor, radial-field machine, there are three common rotor structures, as shown in Fig. 1.4. The surface-mounted magnet arrangement is easily manufactured,

but the magnets must be glued to the rotor body, and so the configuration is less suitable for high speed applications unless carbon fiber sleeves are used. The relative magnetic permeability μ_r of modern rare-earth magnet materials is close to unity, so the effective airgap of this configuration is equal to the sum of the physical airgap between rotor and stator plus the magnet depth. Consequently, the large equivalent airgap in the armature conductors produces only a small magnetic flux component and therefore the inductance of the phase winding is small.

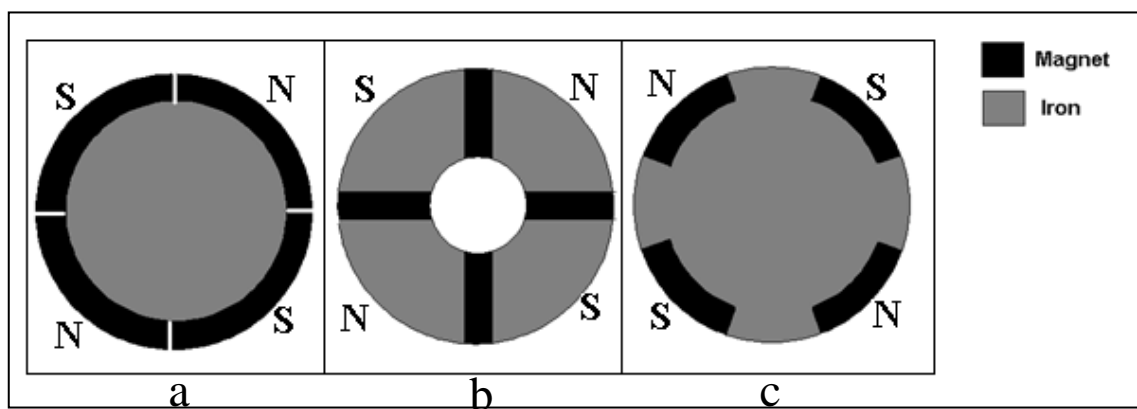


Fig. 1.4 Configurations of inner rotor permanent magnet motor

Furthermore, if the entire rotor surface is covered by permanent magnets, the variation of winding inductance with rotor position will be negligible. The second type is the interior or buried-magnet, or flux-concentrating rotor configuration, Fig. 1.4, this configuration has a more complex mechanical and magnetic design. The magnets are located with their magnetic axes in the circumferential direction, so that the flux over a rotor pole arc is contributed by two separate magnets. This configuration exhibits significant saliency effects, and there may be a substantial variation of winding inductance with rotor position. Finally the inset magnet configuration, Fig. 1.4c, has the advantage that the magnet is buried into the rotor, and therefore, is mechanically secured. The configuration is often preferred for trapezoidal machines, where the magnet pole-arc can be adjusted to assist in shaping the motional EMF waveform. The presence of soft-

magnetic material at the physical airgap in the regions between the magnet poles causes a significant variation in winding inductance, with maximum inductance appearing at rotor positions where the magnet pole arcs are misaligned from the winding axis. Variation in the inductance, as in the inset magnet configuration, is referred to as 'saliency'.

1.4 Position sensing requirement

In commutation control, the brushless DC motor must include some means of detecting the position of the rotor poles so the stator currents are commutated to produce an MMF that is synchronized with the rotor MMF. The power electronic inverter supplies the windings with voltages and currents at a frequency which is matched to the speed of rotation. As the drive starts from rest, the supply frequency increases with increasing rotor speed, and the machine accelerates up to the speed defined by the speed demand.

For a trapezoidal back EMF BLDC motor the position feedback is not continuous, but is obtained at fixed rotor positions, usually every 60° (electrical) in the three phase machine and 180° (electrical) in single phase machine. Therefore a low resolution sensor is sufficient to produce the commutation signal.

The sinusoidal PMSM motor is commutated by a sinusoidal current, consequently, position feedback must be continuous. Poor resolution of the position information available to the controller causes the current waveform to change in discrete steps, and that will cause a high frequency component of torque ripple in the machine output.

The position information is obtained by an encoder which is usually installed in the motor and the output signal is fed back to the drive circuit. However, there are various types of position sensors available for position detection. The following summarises the different position encoder used to detect rotor position:

1.4.1 Optical encoder

The rotor is fitted with a slotted metal disc. This passes through a housing (mounted on the stator core or case) which contains a light emitting diode (LED) and a phototransistor. The phototransistor is turned on when the slotted disc permits light from the LED to pass through. The performance of most optical encoder is limited by temperature. This limitation demands careful location of the sensor. Advantages of the optical sensor are that the output signal rises and falls quite sharply which leads to well defined switching points.

1.4.2 Hall Effect sensors

Hall Effect devices give an output in response to a magnetic field. They are usually mounted around the permanent magnet rotor to detect either the main magnetic flux or end leakage flux. One device per phase is required for commutation. As mentioned above, Hall Effect sensors must also be mounted in precisely defined positions for accurate commutation. Recent developments have enabled Schmitt Triggers to be built into the devices, thus resulting in a fast rise and fall times permitting low switching points error.

1.4.3 Resolver

Resolvers are ac devices giving sinusoidal outputs as a function of rotor position which can be decoded for speed information. The outputs can be used in analogue form or converted to digital signals using commercially available resolver to digital converter integrated circuits. The sinusoidal output signals make the device most suited to speed feedback control applications with a sinusoidal back EMF permanent magnet motor. This type of rotor position sensor is typically expensive and therefore not appropriate for low cost PM BLDC design.

1.4.4 Other sensor possibilities

Precision encoders suitable for servo use are more sophisticated versions of the optical encoder devices which are explained in section 1.4.1. The Output comes with particular coded patterns (e. g. binary coded decimal or Gray code), thus giving an absolute indication of position at any point with reduced signal processing needs. These types of encoders are known as 'absolute' encoders. Incremental encoders simply give out a number of pulses per revolution which are counted and averaged for speed measurement or for positional information.

1.5 The drive for a single phase BLDC motor

The commutation signal for a single phase BLDC motor is generated from one position encoder mounted on the shaft of the rotor. Single phase PM BLDC motors come in three forms [8]:

1.5.1 One phase one pulse (unidirectional current) motors

This have a stator with a single phase winding, as illustrated in Fig. 1.5, which is energised via a transistor once per electrical cycle. The main advantage of this type of motor is that only one power switch is required. However, a significant drawback is the relatively low utilisation of the copper winding, which results in a low output power (50% maximum) compared to a fully utilized winding of the same number of turns. The rotation in the unexcited region (i. e. the remaining 180° elec.) is achieved by the inertia of the rotor or by means of auxiliary reluctance torques.

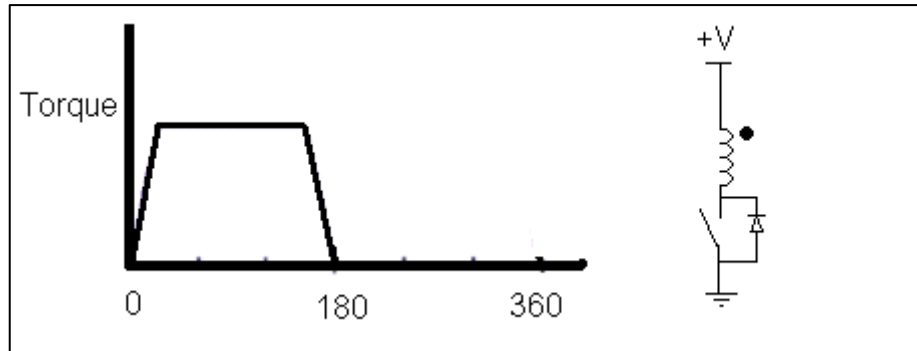


Fig. 1.5 Single phase one pulse BLDC motor.

1.5.2 One phase two pulse motors

Two pulses per revolution are sent to the stator coil. The drive can be either be a half bridge or a full bridge inverter as shown in Fig. 1.6. The resulting torque is, therefore, more favourable than the one pulse motor. However, the output electromagnetic torque is not smooth. As will be evident, there are instants of zero torque, which have to be eliminated with additional or auxiliary torque. This is explained in more detail in chapter 3 and 4. However, the advantage of this motor topology is its simple design, the high (100%) utilisation of the winding, simple winding construction, and less components for the power converter.

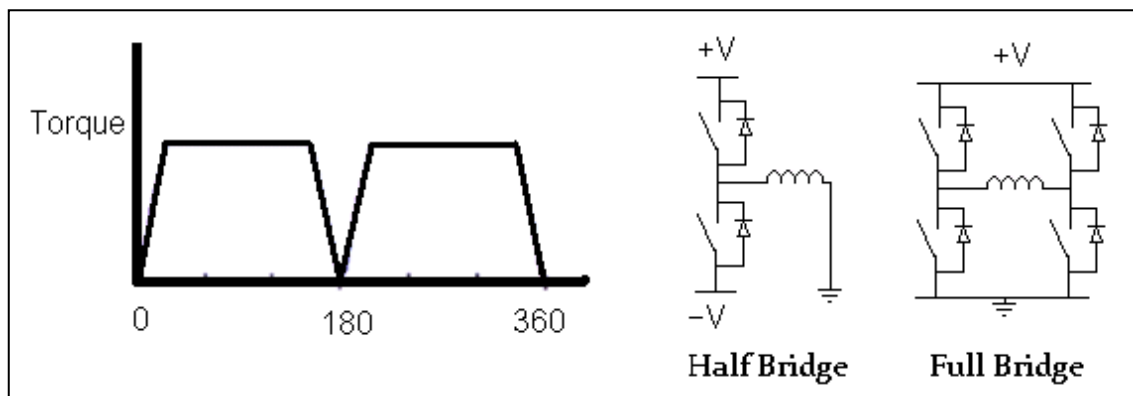


Fig. 1.6 One phase two pulse single phase BLDC motor

1.5.3 Bifilar wound two pulse motor

Also referred as a "two-phase motor", whose stator has two opposite wound coils which are alternatively energised by two current pulses. Therefore, the torque generated is basically the same as with a one-phase, two-pulse motor, as shown in Fig. 1.7. Nonetheless, the winding utilization will be only 50 % only. The advantage of this motor is that it requires only half the number of power switches. This winding arrangement is favoured, compared with full bridge, by a low power application where the cost of the drive circuit represents most of the overall cost. Again the null points in the electromagnetic torque will have to be eliminated by means of suitable auxiliary torque.

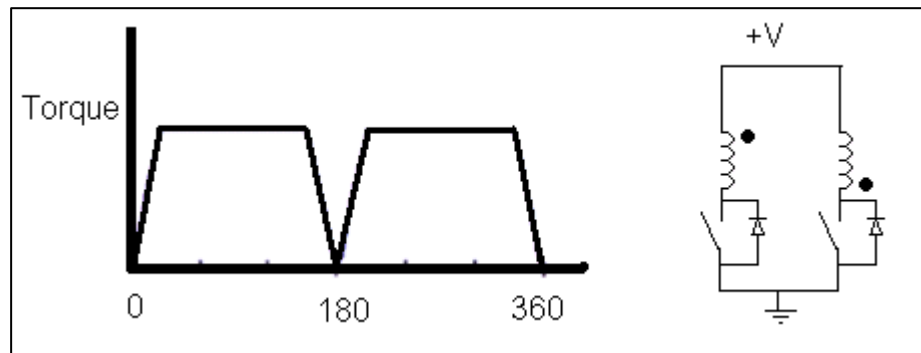


Fig. 1.7 Bifilar wound two pulse single phase BLDC motor

1.6 Layout of the thesis

In chapter two a literature review on cogging torque reduction techniques for PM brushless motors is presented.

In chapter three, the first stage of the open circuit torque improvement is implemented. An analytical approach is followed to find the only combination of magnet width and stator arc ratio that achieves the best reduction in slot openings torque with maintaining the trapezoidal shape of the back EMF.

In chapter 4, the second stage of enhancing the open circuit torque is implemented. It presents a method that enables the improvement of the open circuit torque for the single phase BLDC motor by using asymmetrically distributed notches with different depths and widths that are placed in certain locations in the stator.

In chapter 5 a literature review on encoderless control methods is presented with an overview on the advantages and disadvantages of each method.

In chapter 6 a new encoderless position sensing method is presented. A search coil is used to sense the tangential flux density component from the permanent magnet. Analytical development of the method together with Simulink and FEM validation is presented.

Chapter 7 presents a new phase control strategy for a single phase BLDC motor which is based on a non-complex automatic phase advance control to minimize the copper loss.

Chapter 8 contains the conclusions derived from this work together with a summary of key contributions to the field of research.

2. Cogging Torque Reduction Methods for Permanent Magnet Brushless DC Motor

2.1 Introduction

Rare earth magnets are becoming more attractive for electrical machines applications, because of their high energy density. One of the drawbacks of brushless permanent magnet machines is the cogging torque. Cogging torque is also called detent torque [9] and it is the open circuit torque caused by the physical and magnetic structure of the motor. This causes a variation of the air-gap permeance which exert a position dependent torque on the rotor caused by the tendency of the rotor poles to align with the stator poles at a number of stable positions with minimum reluctance (or maximum permeance). This torque component is typically independent of stator current excitation unless saturation is present [2, 10-16]. For a precise computation of cogging torque, taking account of magnetic saturation in the stator teeth and rotor flux barrier, it is necessary to use numerical methods such as finite Element Method FEM, and the boundary element method [13].

This torque is undesirable because of the following disadvantages:

1. It causes vibration and acoustic noise. This may be amplified in variable frequency drives when the torque frequency coincides with a mechanical resonant frequency of the vibration due to cogging torque.
2. Reduces the life of the bearings [13, 15, 17].
3. It can affect the performance of position control systems such as robots and speed control systems particularly at low speed [18].

For these reasons there has been much research work on finding methods to reduce cogging torque in these permanent magnet machines.

2.2 Magnetic torque calculation

The torque of permanent magnet motors can be determined analytically or numerically. The accuracy of the analytical methods depends on the assumptions made. Some analytical models of torque calculation ignore the core saturation, while in fact saturation widely exists in PM motors. Analytical torque calculation is only fit for machines with simple geometries [9]. Numerical calculation methods of torque can be used for complex geometries and it takes into account saturation. The Finite Element Method (FEM) is a powerful and effective tool to numerically determine the torque for permanent magnet motors. The three most common numerical methods for torque calculation are Maxwell stress tensor method, co-energy method, and Coulomb virtual work method [19-23].

2.2.1 Maxwell stress tensor

Maxwell Stress Tensor method is one of the well known methods in calculating the torque for permanent magnet motors. In this method the torque can be determined by a surface integration around a closed surface S located in the airgap [19]

$$\vec{T} = \frac{1}{\mu_0} \iint_S [(\vec{r} \times \vec{B}) \cdot (\vec{B} \cdot \vec{n}) - \frac{1}{2} B^2 (\vec{n} \times \vec{r})] dS \quad 2.1$$

\vec{r} : is the radial vector from a point to the axis of rotation.

\vec{B} : is the flux density vector

\vec{n} : is the normal vector to \vec{B}

Since radial flux permanent magnet motors can be modelled in 2D, equation 2.1 can be simplified to line integration along a closed contour Γ in the airgap. This has the benefit of quick calculations.

$$T = \frac{l}{\mu_0} \oint_{\Gamma} r B_t B_n d\Gamma \quad 2.2$$

B_t : is the tangential component of the flux density in the airgap.

B_n : is the normal flux density component in the airgap.

l : is the motor core length.

r : is the air gap radius.

The torque derived from this method depends on the accuracy of the flux densities and the selection of the integration contour [19, 20, 24].

2.2.2 Co-energy method

The Co-energy method also referred to as virtual work method and it is the second most commonly used method for cogging torque calculation after Maxwell stress method. The torque is expressed as the derivative of co-energy with respect to a small change in rotor position [19]:

$$T = \frac{dW_{co-energy}}{d\theta} \quad 2.3$$

Two main disadvantages of this method 1) increased calculation time due to the need of two finite element solutions for two angular positions to calculate the torque. 2) Trial and error procedure is required to choose suitable angular position increment $d\theta$, if the position increment is too large the accuracy will be affected and if it is too small the

change in co-energy will be insufficient. Therefore, modelling tests have to be carried out to determine an appropriate value of rotor position increment.

2.2.3 Coulomb's virtual work

This is an improvement to the co-energy method, because the co-energy derivative of this method can be obtained directly from one finite element solution [19]. Since the stator and the rotor are mechanically stiff, the field distribution in these structures will be unaffected by a very small rotational displacement. Therefore, the co-energy in the stator and the rotor can be assumed to be constant under a very small change in rotor position. This reasonable assumption makes it possible to consider the co-energy change in the airgap only, instead of in the entire machine. The co-energy in the airgap is calculated as [25]:

$$W = \frac{1}{2\mu_0} \iiint B^2 dv \quad 2.4$$

where B is the airgap flux density, v is the volume of the airgap. The torque is then calculated from:

$$T = - \frac{dW}{d\theta} \quad 2.5$$

2.3 Methods in cogging torque reduction

The conventional cogging torque reduction methods include modification in the parts of the motor that are in contact with the airgap either the stator or rotor surfaces.

The simplest way of reducing cogging torque is by increasing the airgap but it causes a decrease in the output power for the same machine size [26]. Generally, the smaller the stator slot opening, the lower is the cogging torque. However, since the slot opening

width should be larger than the conductor diameter, cogging torque reduction through the adjustment of slot opening width is limited. In this section an overview of the most common methods in cogging torque reduction for permanent magnet motors are presented.

2.3.1 Slotless stator topology

One of the methods that reduces the cogging torque significantly is a slotless stator topology [27]. However slotless stator winding adds difficulty to the winding process. Fig 2.1 shows an example of a slotless stator topology. The complexity of the winding process can be reduced by closing the slot after the winding process with a soft magnetic material. These are called wedges and they have to be laminated, otherwise eddy current losses will be significant. One concern is the thickness of the wedge. The wedges has to be designed to avoid saturation, because saturated wedges become effectively like air ($\mu_{wedge} \rightarrow \mu_0$) and that will defeat the object of having a slotless design [28].

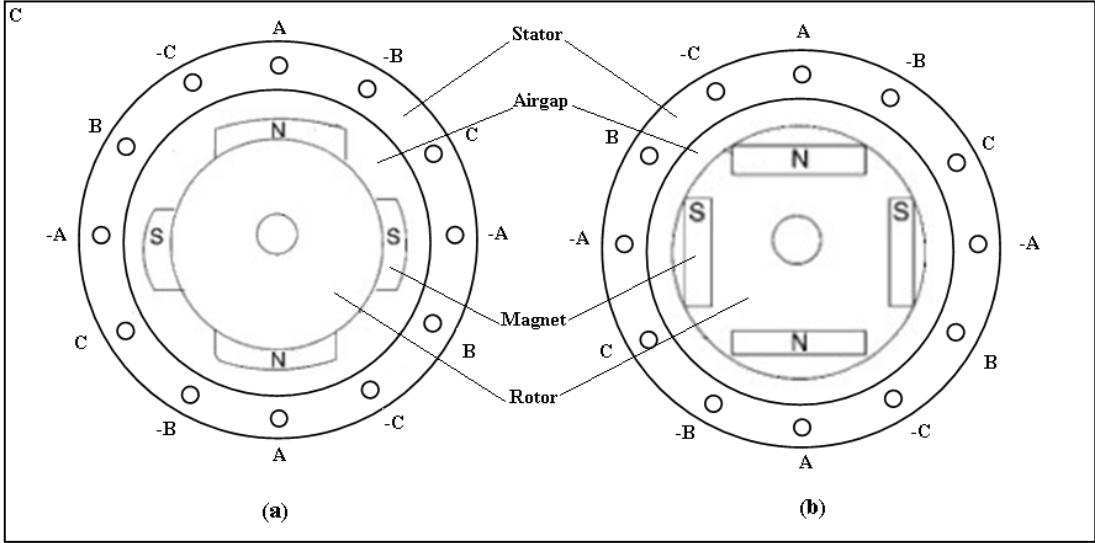


Fig 2.1 Slotless Stator topology (a) Surface mounted PM rotor, (b) Interior mounted PM rotor

2.3.2 Skewing

Cogging torque in permanent magnet machines can be reduced by skewing either the stator or rotor lamination stack. It is well recognised technique for cogging torque reduction. To eliminate the fundamental cogging torque as well as other high order components, the skew angle of the stator or rotor should be equal to the wavelength of the fundamental component of cogging torque [29-31].

$$\theta_{sk} = \frac{2\pi}{N_L} \quad 2.6$$

Where N_L is the least common multiple of stator slot and rotor pole number. Theoretically, skewing the angle in equation 2.6 should eliminate the cogging torque. However, because cogging torque is sensitive to θ_{sk} , and practically it is impossible to precisely skew the specific angle due to manufacturing tolerances, thus cogging torque can't be completely eliminated [32].

A surface mounted permanent magnet motor can have either the stator or rotor continuously skewed. However, the rotor of an interior PM machine can only be step skewed [33], because the magnets are inserted to the rotor body, and there may exist a squirrel cage or damping winding beyond the magnets.

Skewing adds complexity to the manufacturing process and increases the industrial cost of the machine and sometimes it may make the automatic slot filling process almost impossible [9, 34]. Another drawback of skewing is the reduction of the available torque [33] or the shape and value of back EMF due to the skewing factor [27, 31]. The analysis of the effects of this method on the level of cogging torque cannot be carried out using a simple 2D plane-parallel FE approach on the machine. A simplified way for the analysis of skewed configurations consists in solving several 2D problems for different portions of the stator lamination in the axial direction and finally averaging the

field solutions. A more detailed analysis of a skewed configurations requires a 3D finite element model, which is more time consuming and much more demanding in terms of computer hardware resources [27].

2.3.3 Non-integer slot pole ratio

Cogging torque can be reduced by employing a fractional slot/pole design. This is favoured in machines with a large number of rotor and stator poles to save cost. This is because employing other cogging torque reduction methods such as skewing is costly. For a machine that requires a large skew angle, employing the fractional slot/pole design will have the advantage of reducing the required skew angle which will make the winding process less difficult [9].

2.3.4 Positional rotation of the permanent magnet poles relative to each other

There are two ways of shifting the angular position of the rotor poles to reduce the cogging torque. The first method was proposed by Touzuh [18] where the shift in rotor poles is achieved by rotating pole pairs as shown in Fig. 2.2. This method can eliminate or reduce all harmonic components. Shifting the PM position will reduce the EMF [31]. This rotor pole configuration will make the rotor symmetrical for 180° mechanical, see Fig. 2.2.

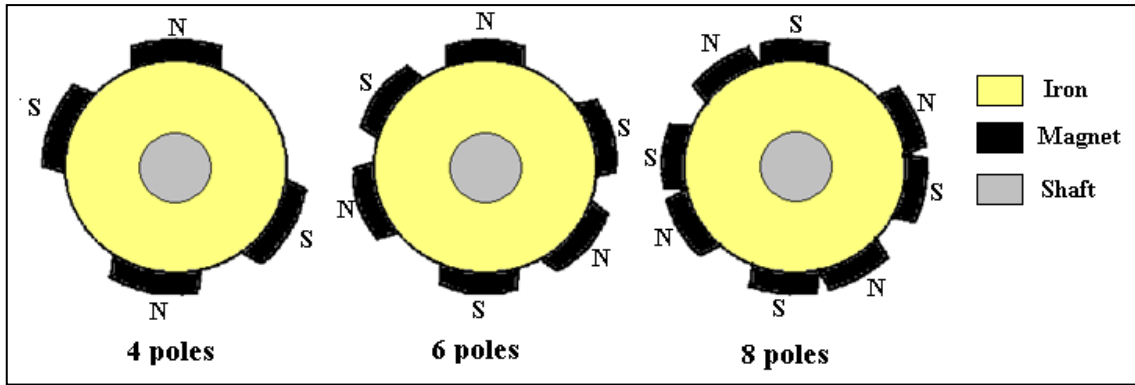


Fig. 2.2 Shifting pairs of rotor poles

The second method is to shift each rotor pole individually [27]. The cogging torque can be reduced by finding the best inter-magnet angle α that leads to minimum cogging torque peak value, see Fig. 2.3, Some authors [18, 35] have proposed that the cogging torque can be reduced by shifting one pole pair by half a slot pitch (for a two pole pair machine) with a harmonic content below the 24th order being negligible.

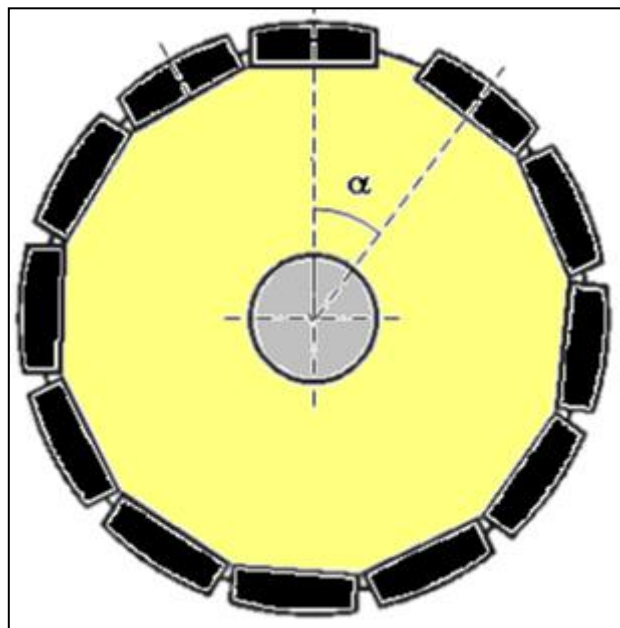


Fig. 2.3 Shifting the rotor poles

In this method the cogging torque is reduced because the effects of the interaction of the PM edge and slot opening during a rotation of a slot pitch are distributed along the slot pitch itself. This can be considered as being “circumferential” skewing with an effect similar to that of the stepped axial skewing [34].

2.3.5 Optimize rotor pole-arc length

Changing the rotor pole arc length can also help reduce or eliminate some harmonic components of cogging torque in permanent magnet motors [31], see Fig. 2.4. Because each stator tooth and slot are at a different position with respect to the magnetic field produced by the PMs on the rotor, so that the total cogging torque can be reduced [35]. The disadvantage of this solution is that the change in the magnet pole arc length is limited and it can negatively affect the back EMF characteristics of the motor [9].

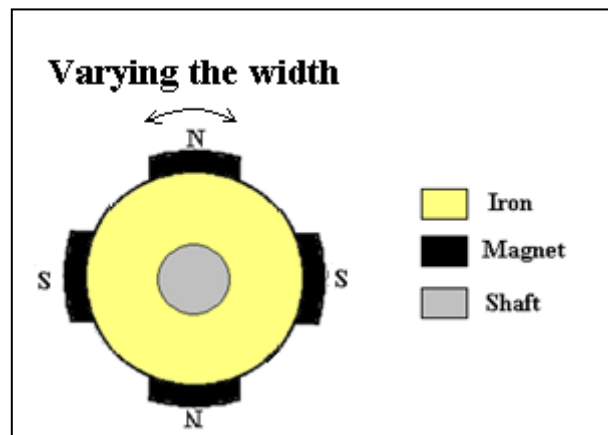


Fig. 2.4 Varying the width of rotor magnets

2.3.6 Auxiliary slots or notches

Auxiliary slots can be added to the surface of the rotor or to the stator as shown in Fig. 2.5. This causes an increase in the number of interactions between stator slots and rotor magnets that reduces the variation of airgap permeance [13]. The auxiliary slots do not have copper windings and are introduced in the stator only for additional cogging torque removal [14, 36]. The introduction of a number of notches in each stator tooth

creates a number of equally spaced dummy slots [33]. Some auxiliary grooves are placed on the surface of the PM poles to remove these harmonics [37]. In the case of an interior permanent magnet motor, the shape optimization of the rotor pole face has a significant effect in a reducing cogging torque [13]. It is known that the fundamental harmonic of the cogging is the minimum common multiple of the number of rotor poles with the number of slots. With the introduction of auxiliary slots, the amplitude of the torque oscillation is decreased. The width of notches should generally be equal to the slot width between two adjacent convex poles [14, 31].

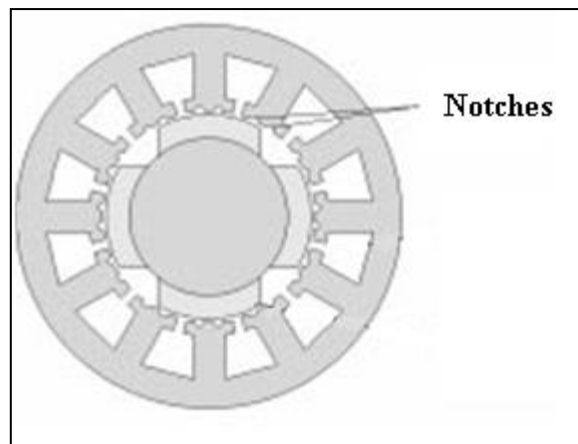


Fig. 2.5 Auxiliary slots in the stator

2.3.7 Magnet pole shape optimization

This method is implemented in surface mounted permanent magnet motors where the magnet geometry can be modified to reduce the cogging torque [38]. Chamfered edged magnet profile and tapered magnet profile can result in a reduction of cogging torque [39]. Another way of modifying the magnet geometry is to add grooves on the surface of the magnet which has been shown to be effective in reducing the cogging torque [37]. The drawback of this method is the added cost incurred for machining the magnets [22, 23, 40, 41].

2.4 The nature of cogging torque for single phase PM BLDC motor

A single phase BLDC motor has a starting problem which is usually solved by a compensating reluctance torque component created from having a non-uniform airgap topology. Special attention should be given when analysing the open circuit torque of a single phase BLDC motor. This is because the open circuit torque in a single phase BLDC motor is due to the stator slot openings and the uneven airgap topology. Some authors have referred to this open circuit torque as cogging torque which is only true for even airgap machines (multi phase machines) and that creates some confusion when optimizing the open circuit torque for a single phase BLDC motor. This is because when the cogging torque for multi-phase machine is to be optimized, the optimization function is to minimize the cogging torque level without significant reduction of machine constant. Where in a single phase BLDC motor the optimization function is more complex i.e. to reduce the slot cogging torque and maximize the reluctance starting torque.

Cogging torque in PM machines is influenced by many factors, for example air gap length, slot opening, and magnet shape and size [9]. The cogging torque calculation methods and reduction techniques will be discussed in following two chapters.

3. New Approach for Open Circuit Torque Improvement for Single Phase PM BLDC Motor

3.1 Introduction

One of the intensively researched issues for single phase PM BLDC motors is the reduction of the oscillations in the torque waveform which are known as torque ripples. These ripples are due to both phase current oscillations and motor topology [2, 42]. The ripple due to the motor topology is referred to as open circuit torque. Fig. 3.1 illustrates how torque ripple in a single phase PM BLDC motor can be classified.

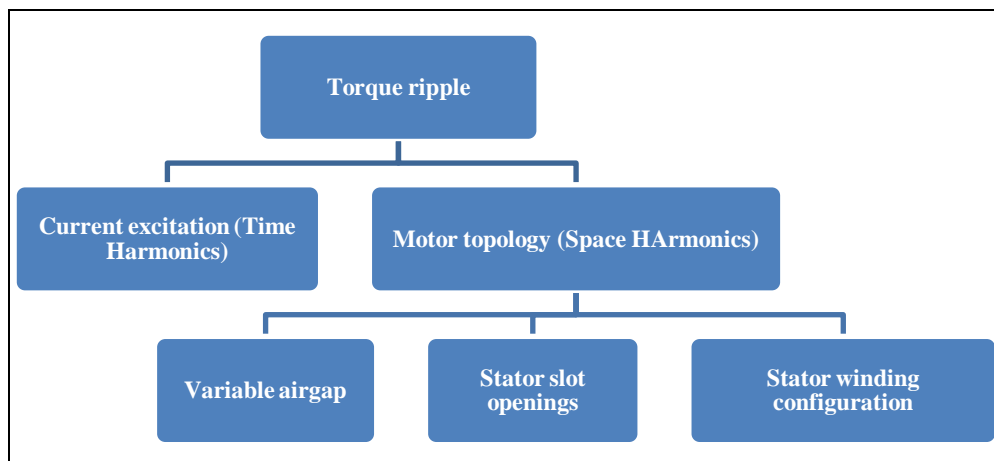


Fig. 3.1 Torque ripple classification in a single phase BLDC motor.

Open circuit torque in a single phase PM BLDC motor is due to the variations in the reluctance of the magnetic circuit during rotation. This variation is caused by two factors, stator slot openings, and other reluctance features such as employing a variable air gap to solve the starting problem.

One of the ways to reduce the slot cogging torque in PM BLDC motors, see chapter 2, is skewing the stator teeth or rotor magnet, but this is only at the expense of added complexity and cost in the stator construction and some loss of output torque [18]. Another way is to have a fractional slot motor [43] (non integer stator to rotor poles ratio).

However, this technique is only applicable to multi phase BLDC motors. Single phase BLDC motors can only have integer stator/rotor pole ratios which causes the cogging torque created by the edges of all of the rotor magnets to add in phase alignment with the edges of all of the slots. Whereas they are out of phase with each other in fractional slot motors. Therefore, the problem is worse in single phase BLDC motors [44, 45].

From the literature review conducted on cogging torque reduction methods (see chapter 2) it can be concluded that most of the work in reducing the cogging torque are suitable for multiphase BLDC motors. The research related to cogging torque reduction for single phase BLDC motors did not distinguish between the two elements of cogging torques [46-49]. Furthermore none of them considered the back EMF in the process of cogging torque reduction. Since the open circuit torque for single phase BLDC motors is due to the stator slot openings and airgap shape the open circuit torque improvement will be performed in two stages:

1. In the first stage the cogging torque due to the stator slot opening is reduced, but with maintaining the trapezoidal shape of the back EMF.
2. In the second stage the focus will be on optimizing the airgap profile to achieve an optimum starting torque characteristic with minimum torque ripple.

This chapter will deal with first stage of the open circuit torque improvement. The following chapter will deal with second stage.

Fig. 3.2 shows a generic 4 pole single phase BLDC motor with a surface mounted PM rotor. The motor has a rotor diameter of 22.5 mm and stack length of 35mm, and with NdFeB magnets and 240 Amp.turns of excitation, the rated torque for this motor is 5Nm.

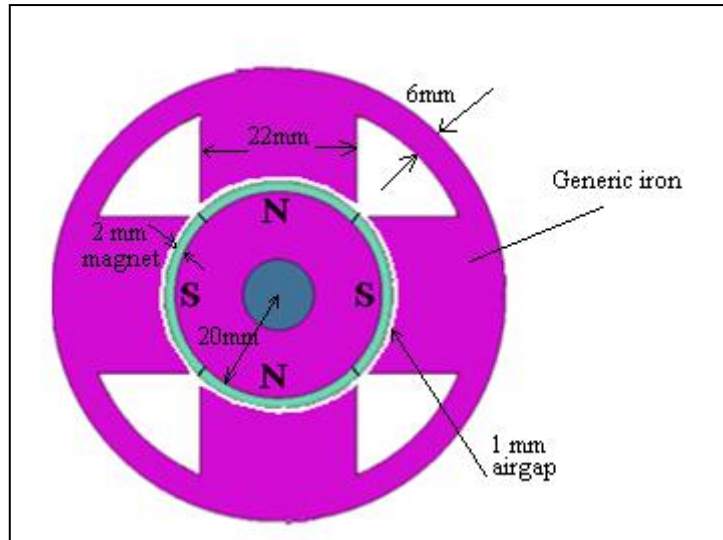


Fig. 3.2 The 4 pole single-phase PM BLDC motor

With the aid of FEM software the open circuit torque profile of the model shown in Fig. 3.2 was obtained. A linear static solver was set to provide values for the open circuit torque (calculated using Maxwell stress method) at every 2° (mechanical) of rotor position. The open circuit torque of the model in Fig. 3.2 is shown in Fig. 3.3. It can be noticed that there is a high level of torque ripple due to the stator openings. The peak to peak value of the torque ripple is 2 Nm, this is considered to be high in relation to the rated torque of the motor.

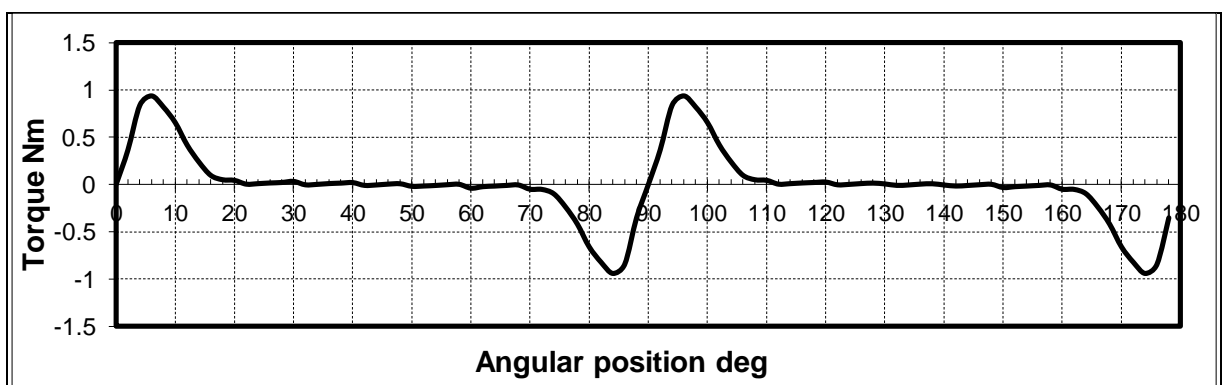


Fig. 3.3 Open circuit torque of a 4 pole single phase BLDC motor

3.2 The effect of asymmetrical stator poles on cogging torque

Asymmetrical stator topology for single phase interior PM BLDC motors has been investigated at the University of Leicester by Paul Lefley [50], Fig. 3.4 shows the topology of the existing motor. The research was based on an interior PM motor with no analytical justification to the asymmetrical topology. Therefore the need to investigate and analyse the effect of asymmetrical topology on the open circuit torque for surface mounted PM BLDC motor was apparent.

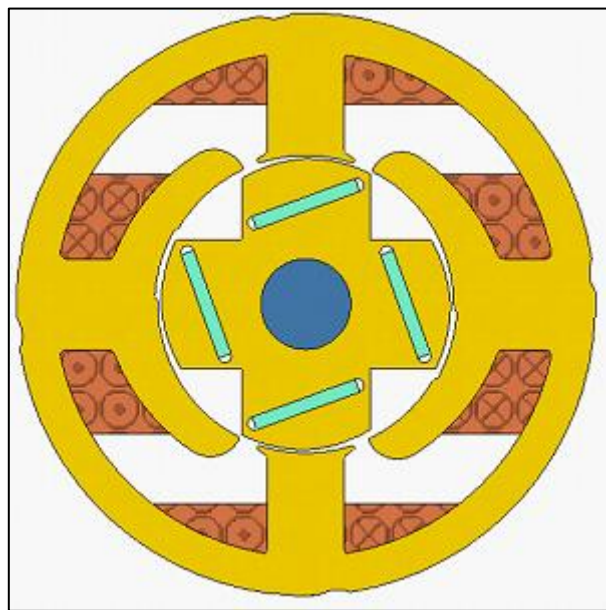


Fig. 3.4 Prototype of single phase BLDC motor with asymmetrical stator topology

An asymmetrical stator topology has a similar effect as having a fractional slot stator, because the magnet edges are not crossing the stator slot openings at the same time as in the symmetrical stator topology. Consequently the slot cogging torque level is reduced. This section will show that employing an asymmetrical stator pole for the design shown in Fig. 3.2 will result in a reduction in the cogging torque. However, this will disturb the change in flux linkage with respect to rotor position, which in turn will cause the back EMF to divert from the ideal trapezoidal shape.

Three Different asymmetrical stator topologies were investigated. The variation in the stator is achieved by reducing the arc length of poles A and increasing the arc length of poles B, see Fig. 3.5. The selection was based on a small sample of integer ratios between poles A and poles B. In Fig. 3.5 (b) the ratio between the arc lengths of poles A to poles B is 1:2. In Fig. 3.5 (c) poles A is one third of poles B, the final topology considered in 3.4(d) in which the ratio between A to B is 1:4. Depending on the results further ratios would have been considered.

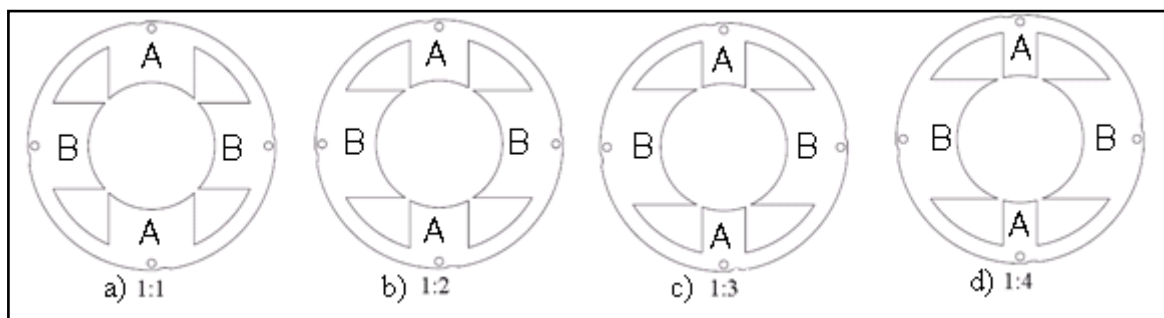


Fig. 3.5 The four stator shapes under study

Fig. 3.6 shows how the open circuit torque varies as the stator pole ratio changes from 1:1 to 1:4. It is obvious that the torque is a maximum with the 1:1 stator ratio model, because the edges of all four magnets cross the four stator slots at the same time. With the other ratios the torque level is reduced significantly. They all have about the same level of torque ripple but the peaks occur at different rotor angular positions. Therefore, in terms of cogging torque reduction any of the ratios 1:2, 1:3 or 1:4 can be chosen, seemingly without any difference. So analysis of the back EMF shape is required.

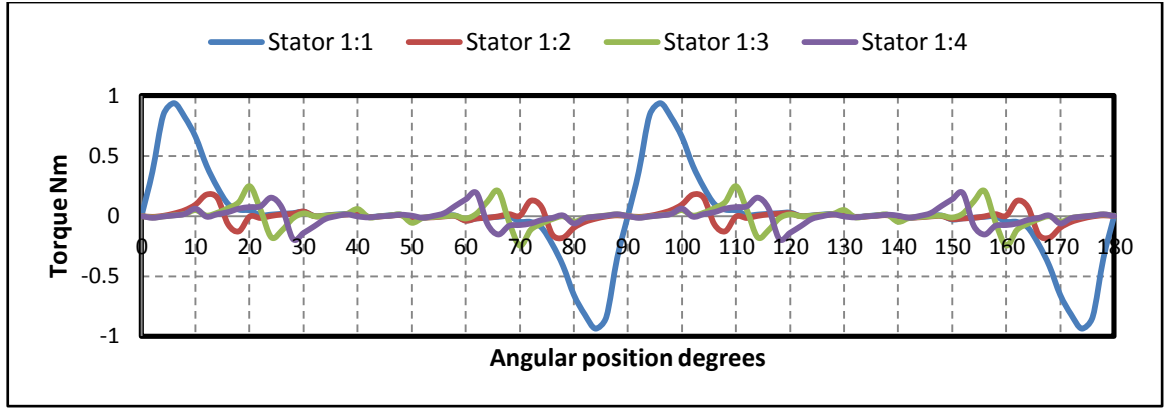


Fig. 3.6 Cogging torque profiles for different ratios of stator poles

3.3 The shape of the back EMF profile

The back EMF shape is determined from the instantaneous value of the motor constant K_e . The back EMF and torque constants are used in the control-system design for the BLDC motor. Their values determine the output ratings of the motor because they represent an essential gain of the motor in converting voltage into speed or current into torque. Viewed from the DC source the ideal single phase BLDC motor is electrically identical to the brushed DC motor. Hence they share the same basic equations which are:

$$e = K_e \omega_m \quad (3.1)$$

$$T = K_T I \quad (3.2)$$

$$V_s = e + RI \quad (3.3)$$

Where e is the back EMF, ω_m is the mechanical angular speed in rad/s, T is the electromagnetic torque, I is the average DC current, K_T is the torque constant, V_s is the supplied voltage to the motor and R is the winding resistance. For the ideal DC machine $K_e = K_T$ [2] provided that the units are consistent i.e. Vs/rad and Nm/A.

3.3.1 The effect of asymmetrical stator topology on K_e

Changing the stator arc ratio from 1:1 has resulted in a lower cogging torque. However, this change will also affect the flux distribution in the motor. Hence the shape of the back EMF waveform will be affected. The back EMF in a single phase PM BLDC can be found from the following expression:

$$e = \frac{d\Psi}{dt} = \frac{d\theta_m}{dt} \frac{d\Psi}{d\theta_m} \quad (3.4)$$

Where Ψ is the is the open circuit flux linkage in weber-turns, θ is the angular rotor position in radians.

$$\frac{d\theta_m}{dt} = \omega_m \quad (3.5)$$

$$e = \omega_m \frac{d\Psi}{d\theta_m} \quad (3.6)$$

From (3.1) and (3.6) K_e is equal to $\frac{d\Psi}{d\theta}$. With the aid of FEM software $\frac{d\Psi}{d\theta}$ can be calculated and plotted with respect to rotor angular position. The back EMF constant profiles for each of the four stator configurations are shown in Fig. 3.7

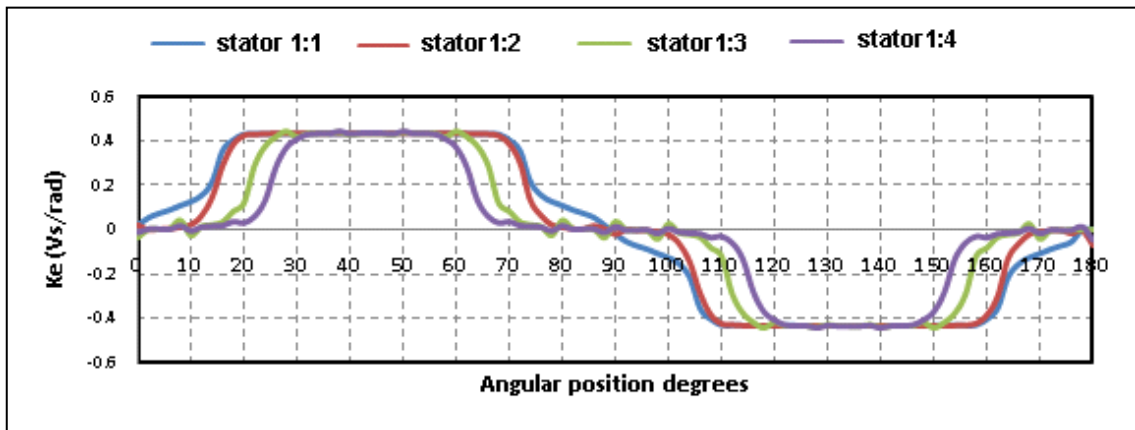


Fig. 3.7 K_e profiles for different ratios of stator poles

It is obvious from the figure that the asymmetrical stator ratio configuration has deteriorated the back EMF shape of the machine. The asymmetrical stator poles have introduced a region in the back EMF where the magnitude of the back EMF is close to zero. Such regions in the back EMF is not desirable for a single phase BLDC motor where the conduction period is 100%, because this will create high levels of current during the period when $e \approx 0$. This will affect the efficiency of the machine and creates a need to increase the required current ratings of the drive components.

3.4 Obtaining the optimum combination of stator pole arc ratio and magnet arc width

The previous section showed that an asymmetrical stator topology will reduce the level of cogging torque, but will also influence on the back EMF shape. In fact any asymmetrical stator topology can reduce the cogging torque level but not all produce a trapezoidal back EMF shape. This section aims to investigate the asymmetry in the topology which is achieved by varying the ratio between the small stator pole arc S_1 and the large stator pole arc S_2 (measured at the centre of the slot) with variation in rotor magnet arc width m_1 and m_2 as shown in Fig. 3.8. Since any asymmetrical stator pole ratio will reduce the cogging torque, the criteria for determining the optimum combination will be based on the back EMF shape.

There are an infinite number of asymmetrical stator pole arc ratio topologies and magnet width combinations. One way of investigating the different combinations is by varying the stator pole arc ratio and rotor magnets discretely and the resulting back EMF shape for each combination is obtained by FEM modelling. However, this will require large number of FEM simulations which is time consuming, plus this method is

not exhaustive and can not guarantee that the optimum solution can be found without considering an infinite number of combinations.

In this section an analytical method to obtain the optimum combination is presented. The method is based on a mathematical model that approximates the back EMF constant K_e for any combination of S_1 , S_2 , m_1 and m_2 within the range shown in Fig. 3.8.

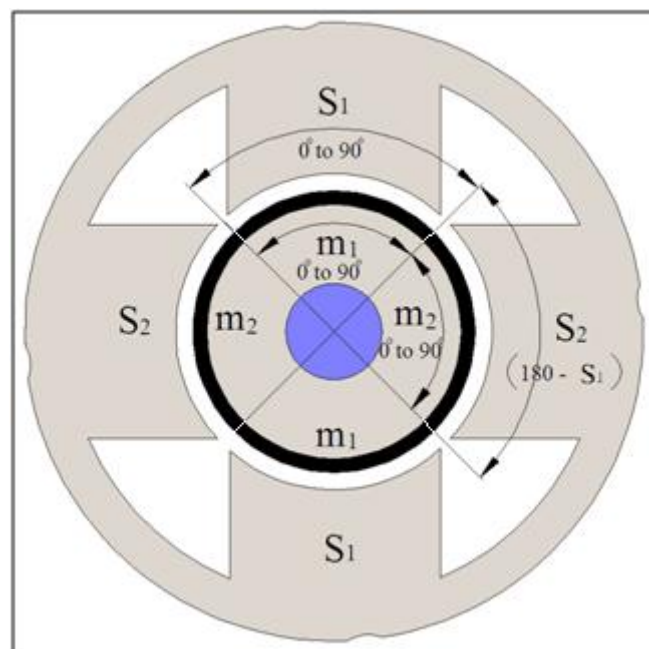


Fig. 3.8 The variation in the topology asymmetry

3.5 Superposition property of K_e profile

Fig. 3.9 shows an example of an asymmetrical topology with $S_1 = 60^\circ$, $m_1=40^\circ$ and $m_2=40^\circ$. This section will show that the vertical pair of magnet poles m_1 has an independent contribution to the K_e profile from the horizontal pair of magnet pole m_2 .

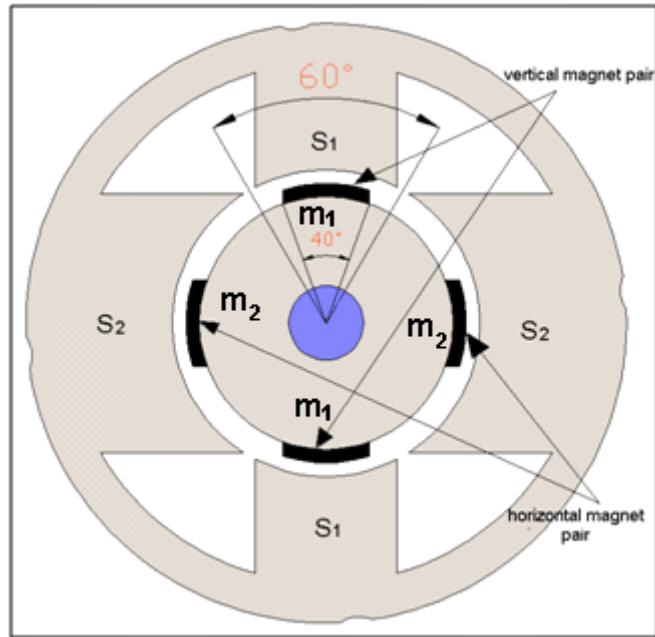


Fig. 3.9 Asymmetrical topology with $S1=60^\circ$ and magnet width = 40°

Fig. 3.10 shows the back EMF shape profile for half electrical cycle produced by FEM software with only the vertical pair of magnets m_1 are enabled (90° mechanical anti-clockwise rotation). The back EMF shape for when only the horizontal pair of magnets m_2 are enabled is shown in Fig. 3.11. The resulting K_e profile for when all four magnets are enabled is shown in Fig. 3.12. It can be seen that the resultant K_e can simply be formed by adding the individual back EMF profiles K_{e1} and K_{e2} . The figure shows that there is a good agreement between the synthesised and the FEM produced K_e .

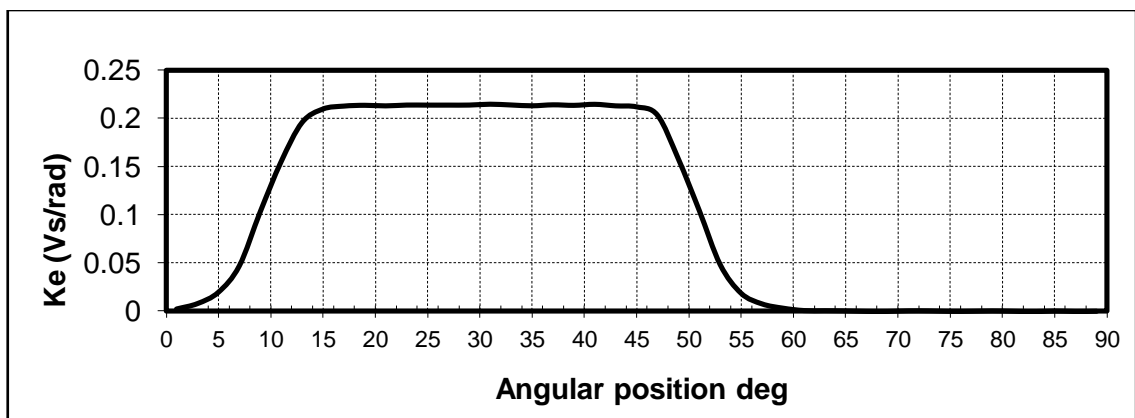


Fig. 3.10 K_{e1} profile from the vertical pair of magnet

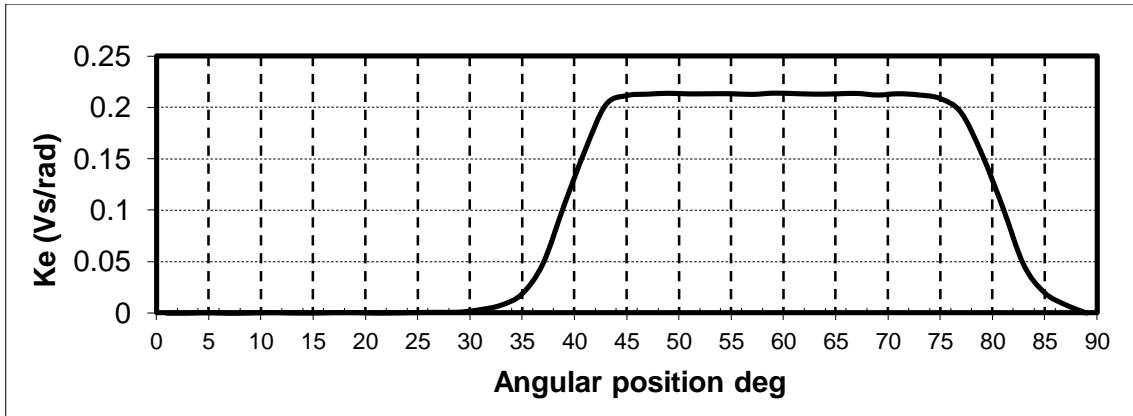


Fig. 3.11 K_{e2} profile from the horizontal pair of magnet

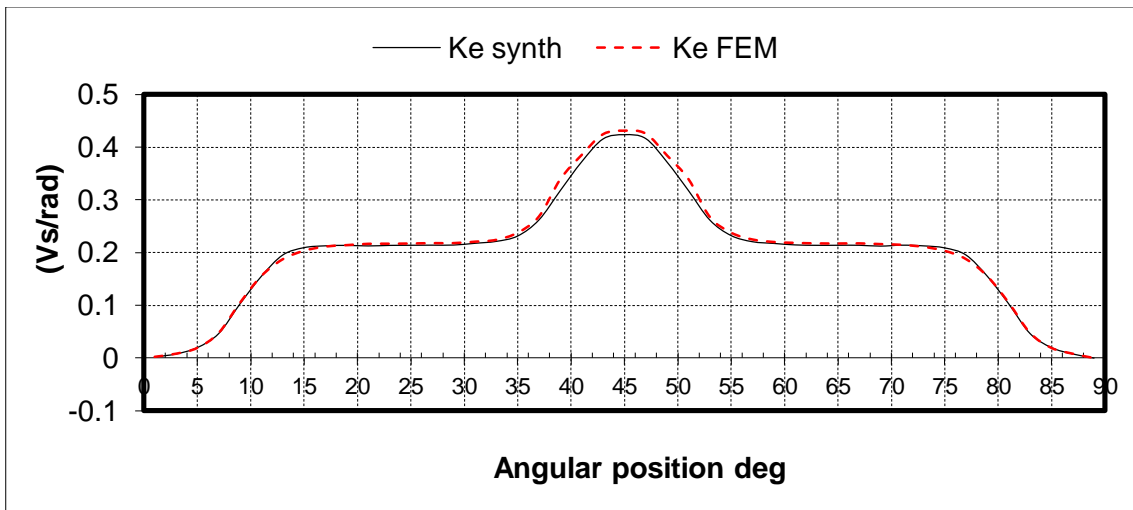


Fig. 3.12 Synthesised and the FEM produced K_e

3.5.1.1 Prediction of K_{e1} and K_{e2}

K_{e1} and K_{e2} can be represented as a piecewise function based on in Fig. 3.13

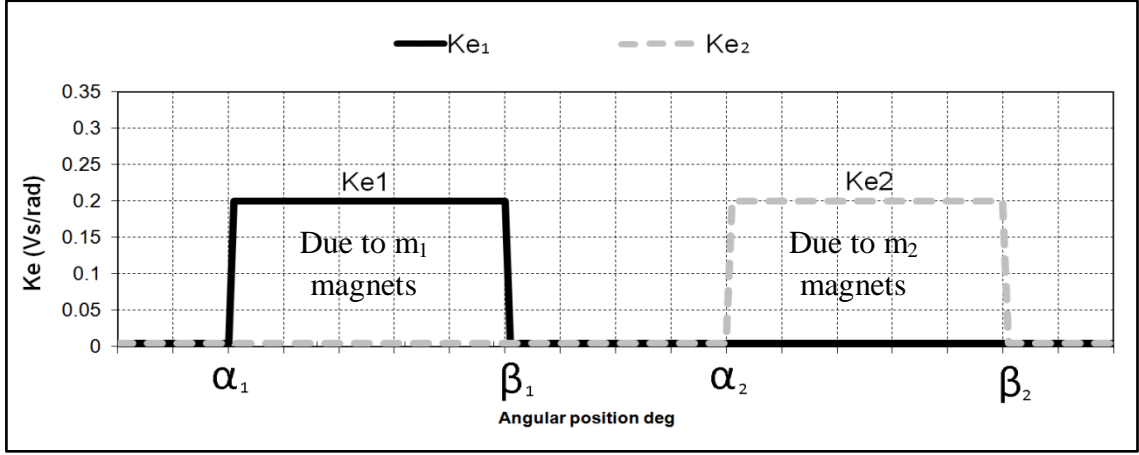


Fig. 3.13 back EMF shapes due to m_1 and m_2 magnets

$$K_{e1}(\theta) = \begin{cases} 0, & 0 \leq \theta < \alpha_1 \\ K1, & \alpha_1 \leq \theta < \beta_1 \\ 0, & \beta_1 \leq \theta < 90^\circ \text{ (mech)} \end{cases} \quad (3.7)$$

$$K_{e2}(\theta) = \begin{cases} 0, & 0 \leq \theta < \alpha_2 \\ K2, & \alpha_2 \leq \theta < \beta_2 \\ 0, & \beta_2 \leq \theta < 90^\circ \text{ (mech)} \end{cases} \quad (3.8)$$

$\alpha_1, \alpha_2, \beta_1$ and β_2 are the angles that characterize K_{e1} and K_{e2} . These angles are functions of the topology asymmetry variables S_1, S_2, m_1 and m_2 . In order to determine the relationship between them three different topologies are considered which have the following asymmetry:

- 1) S_1 is larger than the magnet width, see Fig. 3.14 .
- 2) S_1 is equal to magnet width, see Fig. 3.15.
- 3) S_1 is smaller than magnet width, see Fig. 3.16.

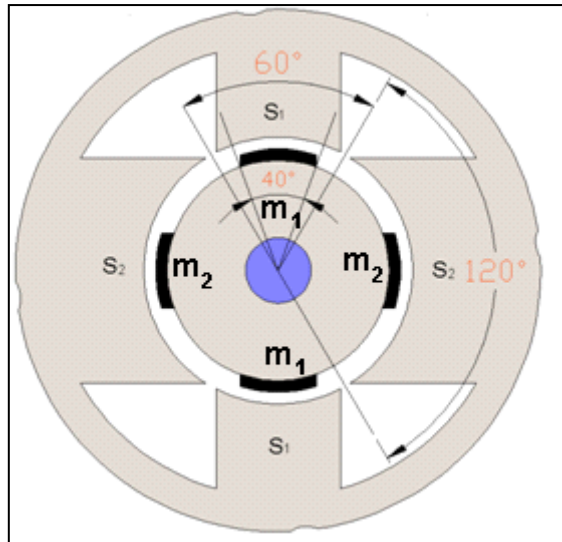


Fig. 3.14 Topology A, $S_1 >$ magnet width

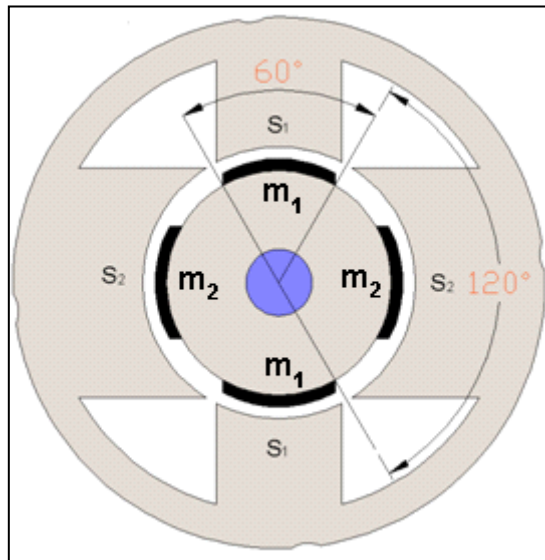


Fig. 3.15 Topology B, $S_1 =$ magnet width

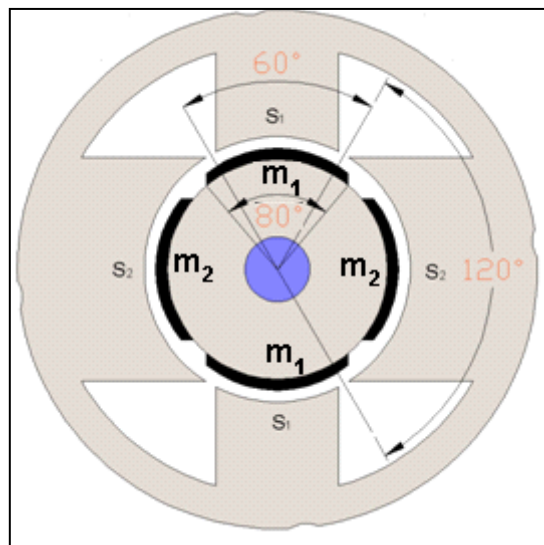


Fig. 3.16 Topology C, $S_1 <$ magnet width

When the rotor in topology A, Fig. 3.14, starts to rotate anticlockwise from 0° to 90° the flux linking the winding starts changing as soon as the leading edge of the vertical pair of magnets m_1 meet the trailing edge of S_1 . Therefore

$$\alpha_1 = \frac{S_1 - m_1}{2} \quad (\text{for topology A}) \quad (3.9)$$

The change in the flux linkage will stop when the trailing edge of the vertical pair of magnets m_1 meets the trailing edge of S_1 . Therefore the width of the K_{e1} will be equal to the width of the magnet and β_1 for topology A will be

$$\beta_1 = \alpha_1 + m_1 \quad (\text{for topology A}) \quad (3.10)$$

In topology B m_1 has the same angular width of S_1 which means that the change in the flux linkage occurs at 0° and it will keep changing until the trailing edge of m_1 meets the trailing edge of S_1 . Therefore, the start and end angles of K_{e1} for topology B will be:

$$\alpha_1 = 0 \quad (\text{for topology B}) \quad (3.11)$$

$$\beta_1 = m_1 = S_1 \quad (\text{for topology B}) \quad (3.12)$$

The magnet width in topology C is larger than the width of S_1 . Therefore, the winding will not exhibit a change in the flux linkage until the trailing edge of the magnet meets the leading edge of S_1 . The variation in the flux linkage will continue until the trailing edge of m_1 reaches the trailing edge of S_1 . Therefore, the width of K_{e1} for topology C is determined by S_1 unlike topology A, where the width of K_{e1} is determined by the width of m_1 . Therefore, the start and end angles of K_{e1} for topology C will be.

$$\alpha_1 = \frac{m_1 - S_1}{2} \quad (\text{for topology C}) \quad (3.13)$$

$$\beta_1 = \alpha_1 + S_1 \quad (\text{for topology C}) \quad (3.14)$$

The characterizing angles $\alpha_{2(A,B,C)}$ and $\beta_{2(A,B,C)}$ of K_{e2} profile can be produced for the three topologies in the same way but with the horizontal pair of magnets m_2 . So for topology A:

$$\alpha_2 = \frac{S_2 - m_2}{2} \quad (3.15)$$

$$\beta_2 = \alpha_2 + m_2 \quad (3.16)$$

For topology B:

$$\alpha_2 = \frac{S_2 - m_2}{2} \quad (3.17)$$

$$\beta_2 = \alpha_2 + S_1 = \alpha_2 + m_2 \quad (3.18)$$

For topology C:

$$\alpha_2 = \frac{m_2 - S_2}{2} \quad (3.19)$$

$$\beta_2 = \alpha_2 + S_2 \quad (3.20)$$

From equations 3.9 to 3.20 the following can be noticed:

- The starting angle α_1 for K_{e1} is always equal to half the absolute difference between m_1 and S_1 for all the three topologies. Therefore α_1 can take the general form of

$$\alpha_1 = \frac{|S_1 - m_1|}{2} \quad (3.21)$$

- The starting angle for K_{e2} α_2 is always equal to half the difference between the magnet and S_2 for all the three topologies. So α_2 can be

$$\alpha_2 = \frac{|S_2 - m_2|}{2} \quad (3.22)$$

The end angle β is always equal to α plus the minimum among S_1 , m_1 and m_2 . So β_1 and β_2 for K_{e1} and K_{e2} can take the general equation

$$\beta_1 = \alpha_1 + \min(S_1, m_1) \quad (3.23)$$

$$\beta_2 = \alpha_2 + \min(S_2, m_2) \quad (3.24)$$

Fig. 3.17 shows how a trapezoidal resultant K_e can be formed from K_{e1} and K_{e2} . It is clear that k_{e1} should not overlap with K_{e2} , $\alpha_1 = 0$, $\alpha_2 = \beta_1$ and $\beta_2 = 90^\circ$.

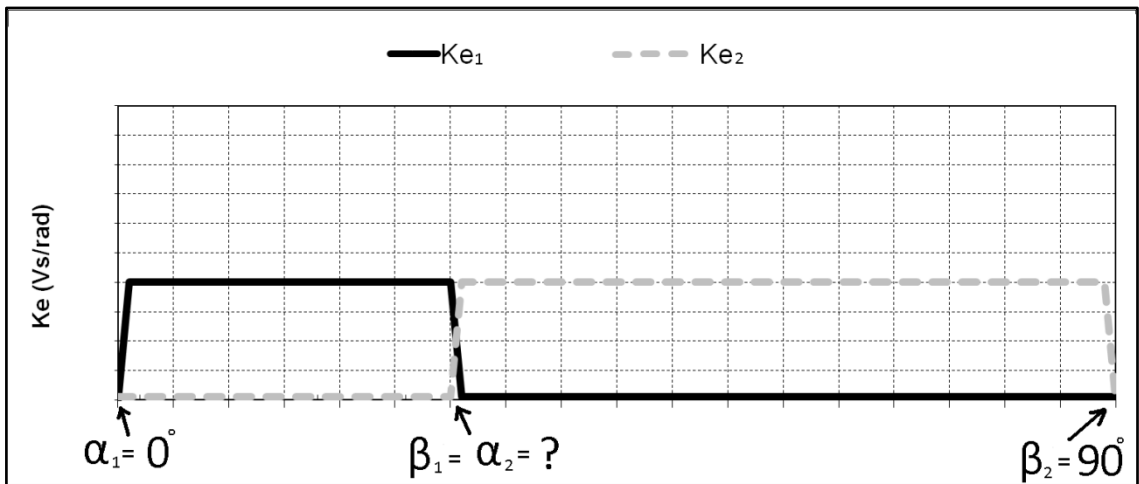


Fig. 3.17 K_{e1} and K_{e2} for trapezoidal resultant K_e

In order to obtain K_{e1} profile as in the Fig. 3.17 α_1 has to be equal to zero therefore from 3.21

$$0 = \frac{|S_1 - m_1|}{2} \quad (3.25)$$

$$\therefore S_1 = m_1 \quad (3.26)$$

And from 3.23

$$\beta_1 = 0 + \min(S_1, m_1) \quad (3.27)$$

$$\therefore \beta_1 = S_1 = m_1 \quad (3.28)$$

In order to obtain Ke_2 as shown in Fig. 3.17

$$\beta_2 = 90^\circ \quad (3.29)$$

And

$$\alpha_2 = \beta_1 \quad (3.30)$$

Then from 3.28

$$\alpha_2 = m_1 \quad (3.31)$$

$$S_2 = 180^\circ - S_1 = 180^\circ - m_1 \quad (3.32)$$

Substitute 3.31 and 3.32 into 3.22

$$m_1 = \frac{(180^\circ - m_1) - m_2}{2} \quad (3.33)$$

$$m_1 = \frac{180^\circ - m_2}{3} \quad (3.34)$$

Substituting 3.29, 3.31 and 3.32 in 3.24 will give

$$90^\circ = m_1 + \min(m_1, 180^\circ - m_1) \quad (3.35)$$

If $m_1 > 180 - m_1$ then 3.35 will be

$$90^\circ = m_1 + 180^\circ - m_1 \quad (3.36)$$

Equation 3.36 can not be solved.

If $m_1 < 180 - m_1$ then 3.35 will be

$$90^\circ = m_1 + m_1 \quad (3.37)$$

Therefore

$$m_1 = 45^\circ \quad (3.38)$$

Substitute 3.38 in 3.33 to find m_2

$$45^\circ = \frac{180^\circ - m_2}{3} \quad (3.39)$$

Therefore

$$m_2 = 45^\circ \quad (3.40)$$

Therefore from 3.26 and 3.32

$$S_1 = 45^\circ \quad (3.41)$$

$$S_2 = 180^\circ - 45^\circ = 135^\circ. \quad (3.42)$$

Therefore the asymmetrical topology for the single phase BLDC motor that will guarantee a trapezoidal back EMF shape should have $S_1=45^\circ$, $S_2=135^\circ$ and $m_1=m_2=45^\circ$ as shown in Fig. 3.18.

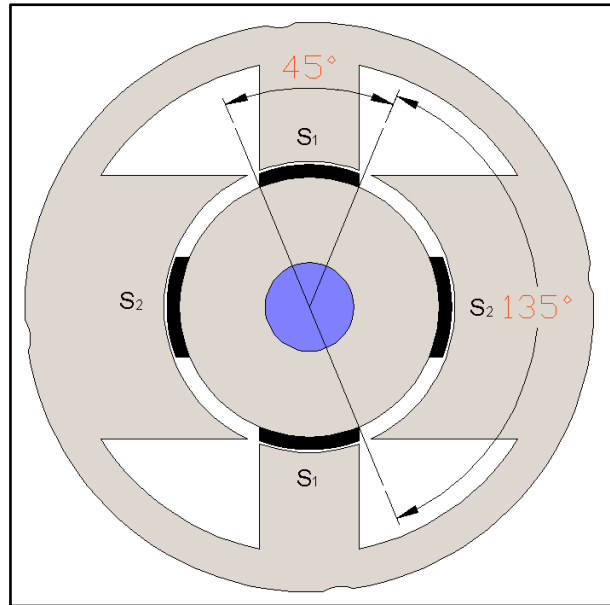


Fig. 3.18 Asymmetrical topology that produce trapezoidal back EMF

3.6 The K_e expression

Section 3.3.1 has shown that

$$K_e = \frac{d\lambda}{d\theta_m} \quad (3.43)$$

Where λ is the total flux linkage from the magnets and θ_m in radians and it is the mechanical angle range in which the flux linkage changes. Referring to Fig. 3.19 $\frac{d\lambda}{d\theta_m}$ can be calculated from 0 to π

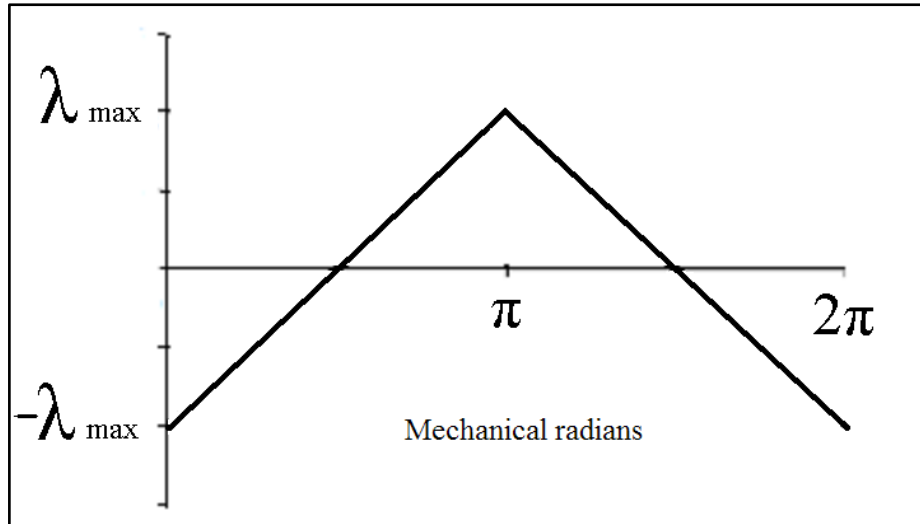


Fig. 3.19 ideal flux linkage waveform for a square (constant amplitude) back EMF

$$\frac{d\lambda}{d\theta_m} = \frac{2 \lambda_{max}}{\pi} = \frac{2N \phi_{max}}{\pi} = \frac{2N B_{max} A}{\pi} \quad (3.44)$$

Where N is the number of turns, ϕ_{max} is the maximum flux in webers, B_{max} is the peak airgap flux density in Tesla and A is the magnet surface area in m^2 .

$$A = 2 \pi r_r l_r \frac{\theta_m}{2\pi} \quad (3.45)$$

r_r is the radius of the rotor in metre and l_r is the depth of rotor in metre. Substituting 3.45 in 3.44 will give

$$\frac{d\lambda}{d\theta_m} = 4N B_{max} r_r l_r \frac{\theta_m}{\pi/4} \quad (3.46)$$

From 3.43 the instantaneous back EMF constant is equal to

$$K_e(\theta_m) = N B_{max} r_r l_r \frac{\theta_m}{\pi/4} \quad (3.47)$$

When $N=320$ turns, $B_{max} = 0.8$ T (airgap flux density obtained from FEM model), $r_r=22.5 \times 10^{-3}$ m, $l_r= 35 \times 10^{-6}$ m and $\theta_m=45^\circ$ the magnitude of K_{e1} and K_{e2} will be equal to 0.2Vs/rad. The resultant K_e will be

$$K_e(\theta) = K_{e1} + K_{e2} \quad (3.48)$$

$$K_{e1}(\theta) = \begin{cases} 0.2, & 0 \leq \theta < \pi/4 \\ 0, & \pi/4 \leq \theta < \pi/2 \end{cases} \quad (3.49)$$

$$K_{e2}(\theta) = \begin{cases} 0, & 0 \leq \theta < \pi/4 \\ 0.2, & \pi/4 \leq \theta < \pi/2 \end{cases} \quad (3.50)$$

Fig. 3.20 shows the predicted back EMF constant shape results which are produced by using equation 3.48 compared with FEM produced result.

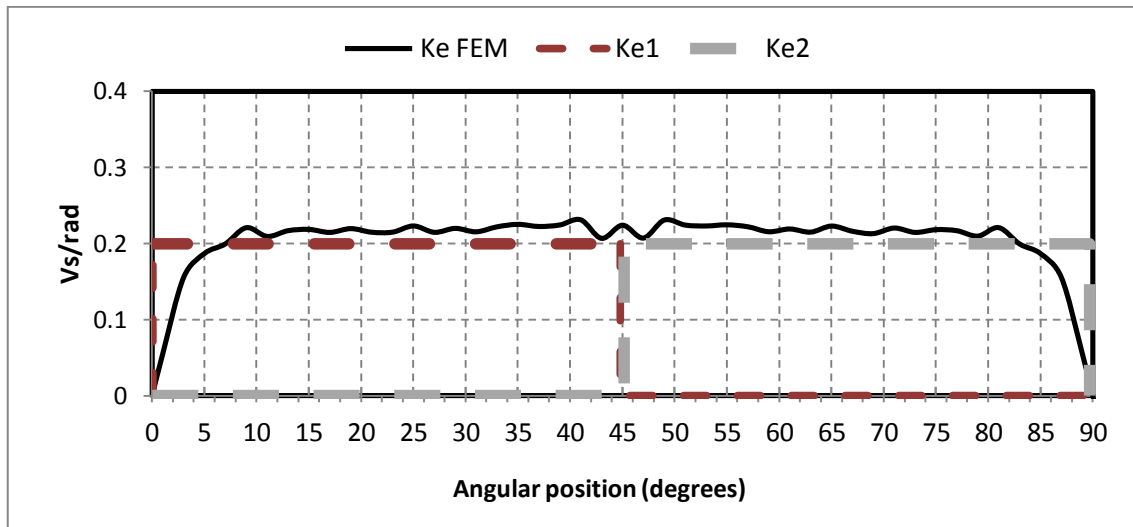


Fig. 3.20 FEM and calculated K_e for the new motor topology

3.7 Discussion

By obtaining a mathematical equation that relate the back EMF shape $K_e(\theta)$, the stator arc widths S_1, S_2 , and the magnets arc widths m_1 and m_2 , it was possible to find the only asymmetrical topology that produces a trapezoidal back EMF with reduced cogging

torque as shown in Fig. 3.21 and Fig. 3.22. The graphs compare the open circuit torque and back EMF shape of the original symmetrical model with the new asymmetrical model. It can be seen that the proposed topology has resulted in a reduction of 88% in the torque ripple while maintaining the ideal square shape of the back EMF unaffected.

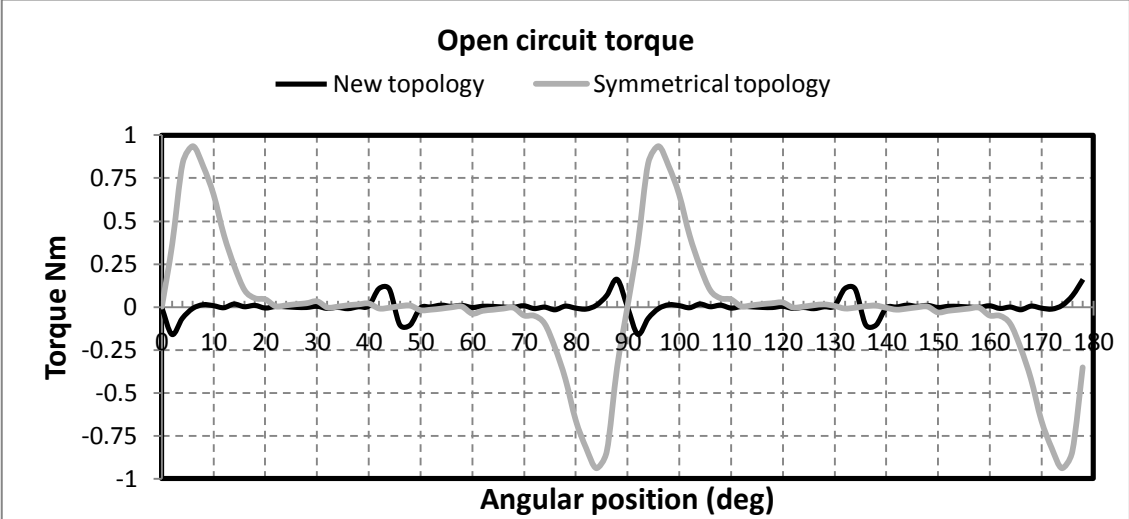


Fig. 3.21 Open circuit torque of new topology and the symmetrical topology

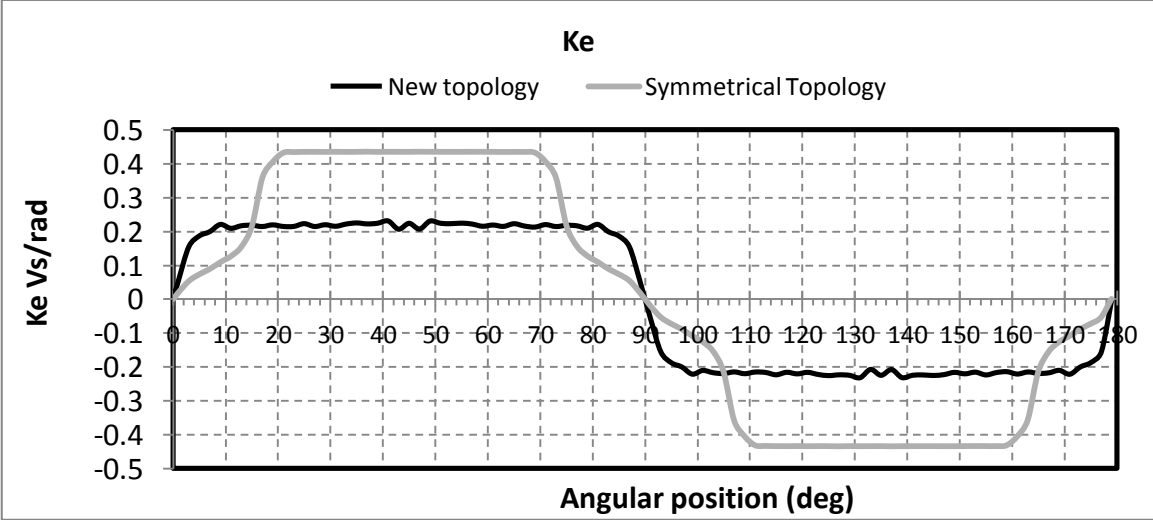


Fig. 3.22 back EMF shape of the new topology and the symmetrical topology

According to Fig. 3.22, the average back EMF constant of the new topology is 0.2 Vs/rad and for the symmetrical topology is 0.3 Vs/rad measured from 0° to 90° me-

chanical. So the new topology is 30% less in average K_e . This decrease is not a major drawback because of the following four reasons:

1. K_e in BLDC motors can be compensated by other motor parameters i.e. number of total turns and the remanance flux density of the magnets (i.e. use stronger magnets).
2. The reduction in the average back EMF constant results in a lower torque density motor. Since single phase BLDC motors are used in low cost low power applications the proposed topology does not have a significant effect on their required performance and it is still considered to be attractive from a cost and performance point of view.
3. The 30% reduction in the average back EMF constant is low compared to the significant reduction in the open circuit torque ripple which is around 88%.

3.8 Iron reduction

The aim of this section is to transform the asymmetrical topology into a practical model for the single phase PM BLDC motor. The efficient utilization of the iron in the proposed asymmetrical model is investigated to reduce cost and to create more winding space. The aim is to reduce the maximum amount of iron without distorting the back EMF and cogging torque profiles.

Efficient utilization of iron is necessary to avoid wasting this material and to create more winding space. Otherwise, the magnetic flux density in the large stator poles will be low and the electrical current density will be too high. In order to create more wind-

ing space some of the metal from the large stator poles has to be removed to create a pole shoe design as shown in Fig. 3.23.

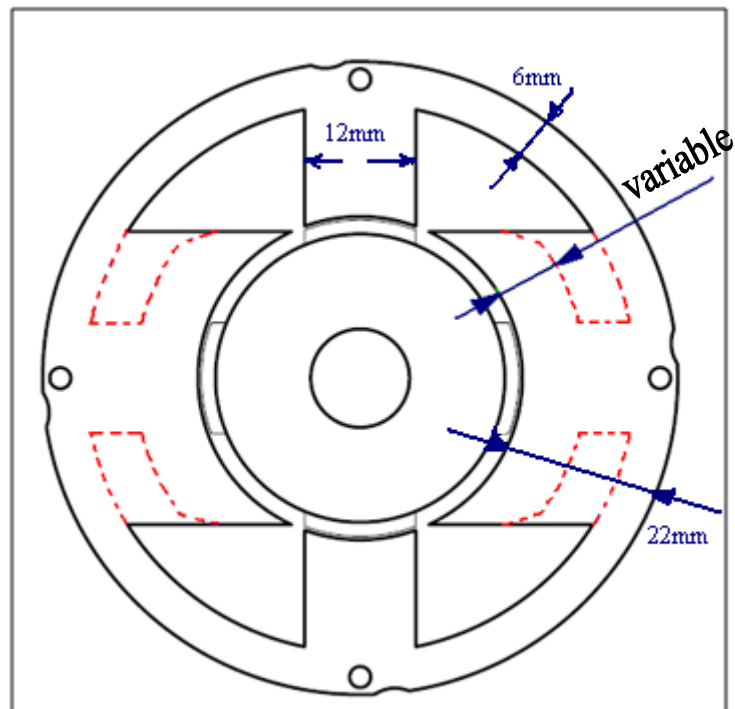
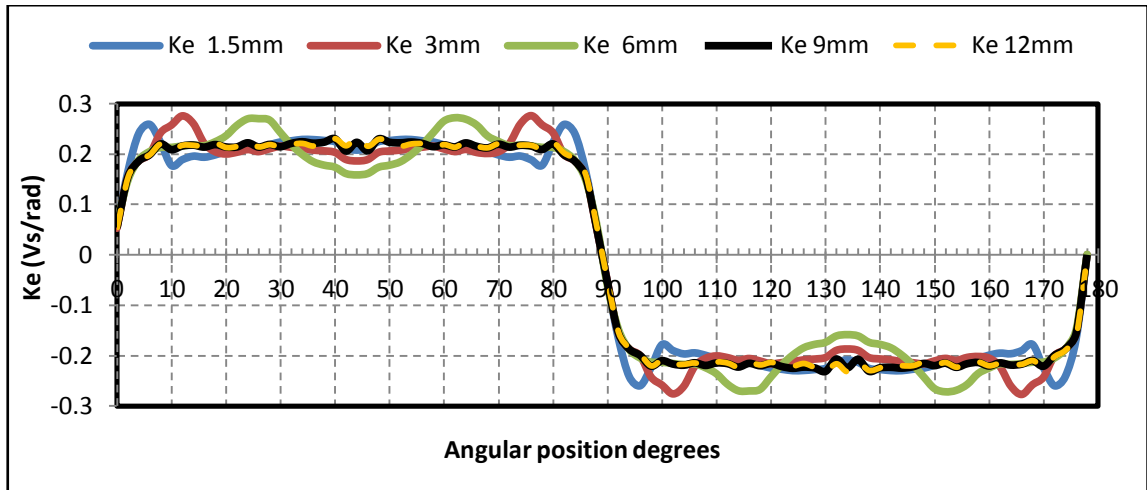


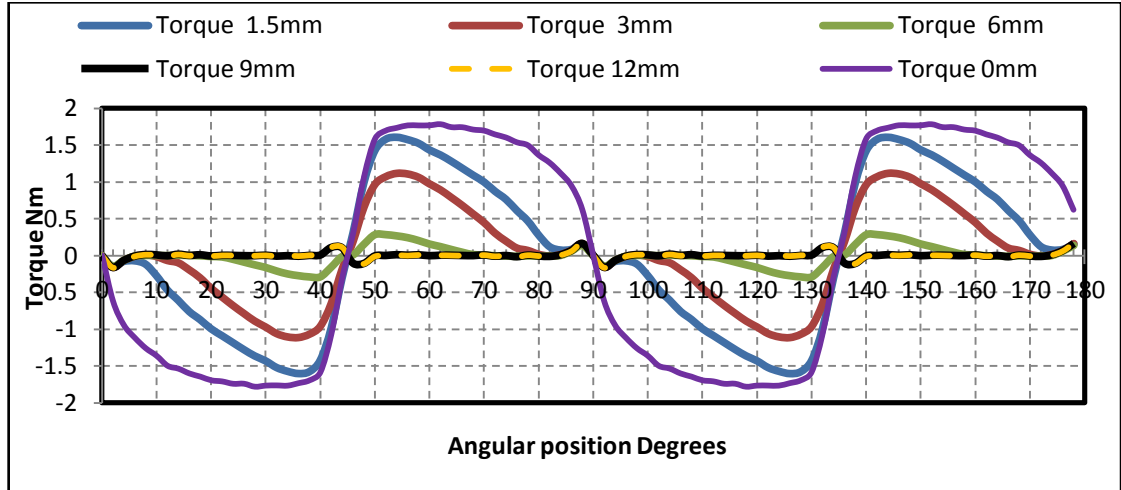
Fig. 3.23 Implementing a pole shoe design in the large stator poles in the proposed model.

This modification in the stator iron has two effects: 1) the level and distribution of the flux linkage in the stator and hence the Back EMF shape, 2) the open circuit torque. In order to determine the effect of this design change, different pole shoe radial widths were investigated in the FEM model, ranging from a radial thickness of 0mm to 12mm as shown in Fig. 3.23. Six different models were simulated for pole shoe thickness of 0mm, 1.5mm, 3mm, 6mm, 9mm, and 12mm. Fig. 3.24a shows the back EMF and cogging torque results. From the results it is obvious that the back EMF plots resulting from the models with shoe thickness less than 9mm deviate from the ideal trapezoidal shape. While the models with shoe thickness 9mm and above have preserved the trapezoidal back EMF shape. Comparing the cogging torque graphs in Fig. 3.24b, it is clear that the models shoe thickness widths of 9mm and above have the same reluctance

torque profile before removing the iron. However, it can be seen that for shoe thickness less than 9mm there is an increase in the cogging torque level. This is due to the narrower arcs becoming saturated by the shorted flux from two adjacent rotor pole magnets. This saturation will decrease the permeability of the iron which is apparent in the higher level of cogging torque.



(a)



(b)

Fig. 3.24 , (a) The back EMF profile, and (b) the reluctance torque, as functions of rotor angular position.

Based on the FEM results of the back EMF and cogging torque, the model with the shoe thickness of 9mm has shown to be the best design, because there is a good balance

between stator iron optimisation, a well preserved back EMF shape, and with a low cogging torque.

3.9 Design procedure of a 1 kW single phase BLDC motor based on the new topology

In this section the design of 1 kW single phase BLDC motor prototype is presented, based on the topology proposed earlier. A Matlab program was used to aid in the selection of the optimum motor dimensions for the required ratings and then the design is validated by the FEM software.

3.9.1 Requirements

The motor is required to have the following ratings 300v DC, 3.3A DC and 1500 rpm. The first step in the design is to calculate of an estimate of the motor constant that will produce the motor with required ratings. At no load the supply voltage can be approximated to be equal to the back EMF

$$V_{rated} = e = K_e \omega_{rated} \quad (3.51)$$

$$\therefore K_e = \frac{V_{rated}}{\omega_{rated}} = \frac{300}{1500 \times \frac{2\pi}{60}} = 1.91 \text{ Vs/rad} \quad (3.52)$$

Since K_e is equal to K_T the rated torque can be calculated

$$T_{rated} = K_T I_{rated} = 1.91 \times 3.3 = 6.3 \text{ Nm} \quad (3.53)$$

In the next section the overall dimension of the motor based on the back EMF constant equation derived in section 3.45 is calculated.

3.9.2 Equivalent magnetic circuit

Fig. 3.25 shows the equivalent magnetic circuit of a four pole single phase BLDC motor when the rotor is aligned with the stator poles. The total flux in the iron is the sum of the fluxes from the magnet and the current in winding

$$\phi = \phi_i + \phi_m \quad (3.54)$$

where ϕ_i is the flux due to the phase current I and ϕ_m is the flux due to the rotor magnets.

$$\phi_i = \frac{N I}{R_T} \quad (3.55)$$

$$\phi_m = \frac{2 R_m}{R_T} \phi_r \quad (3.56)$$

where R_T is the total reluctance of the circuit, R_m is the reluctance of the magnets, N is the total number of turns and ϕ_r is the remanence flux of the magnet.

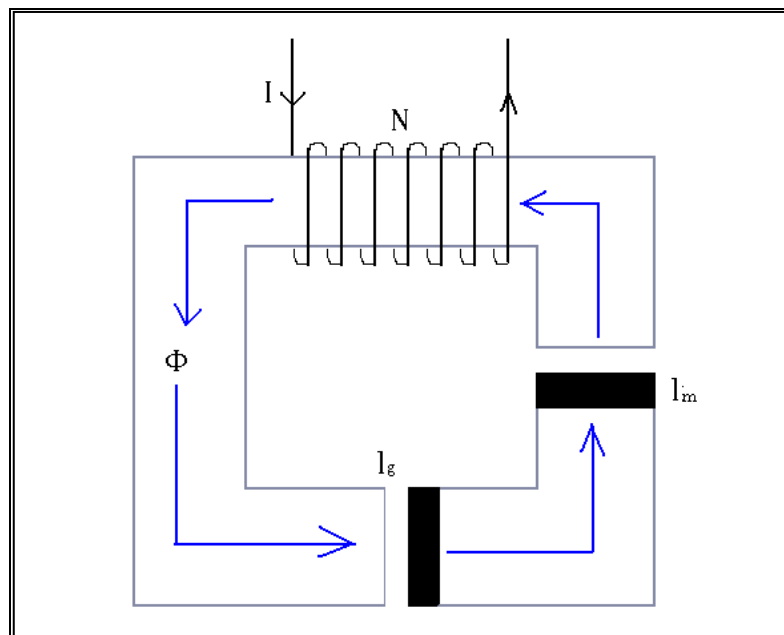


Fig. 3.25 The equivalent magnetic circuit

The total reluctance of the circuit can be represented as

$$R_T = 2R_m + 2R_g + R_{iron} \quad (3.57)$$

Using equations 3.54 – 3.57 the total flux will be

$$\phi = \frac{N I + 2R_m \phi_r}{2R_m + 2R_g + R_{iron}} \quad (3.58)$$

The reluctance of the magnets, air and the iron can be calculated using

$$R = \frac{l}{\mu_o \mu_r A} \quad (3.59)$$

Where l is the length of the magnetic path, μ_o is the permeability of free space, μ_r is the relative permeability of the material and A is the cross sectional area of the core.

Substituting 3.59 in 3.58 will give

$$\phi = \frac{N I A \mu_o + 2l_m \phi_r}{2l_m + 2l_g + l_{iron}/\mu_r} \quad (3.60)$$

Dividing by the cross sectional area will give us the flux density in the iron

$$B = \frac{N I \mu_o + 2l_m B_r}{2l_m + 2l_g + l_{iron}/\mu_r} \quad (3.61)$$

3.9.3 Calculating the dimensions

The dimensions for the prototype motor, see Fig. 3.26, can be determined from

$$K_e = N B_{max} r_2 l_r \quad (3.62)$$

By choosing the rotor radius r_2 , rotor length l_r and the number of turns N a motor with the required K_e of 1.91 Vs/rad can be obtained. B_{max} is the peak airgap flux density from the magnets. Fig. 3.26 shows the parameters of the motor that need to be determined.

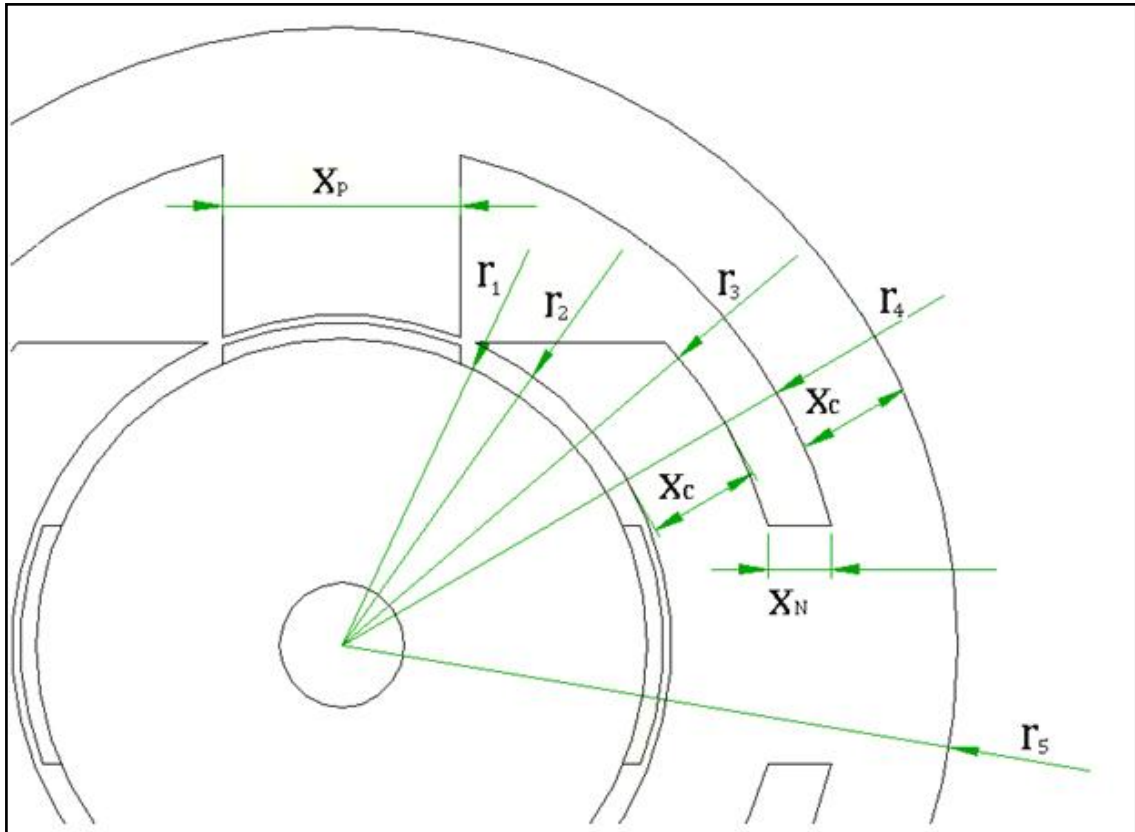


Fig. 3.26 1kW motor dimensions

A Matlab program was used to calculate the dimensions of a 1kW motor. The calculation was based on finding r_2 and l_r that will result in a motor with flux level below saturation at rated current and with minimum surface area. The minimum surface area for any shape is obtained when the length is twice the radius, see appendix 9.2 for more details. Fig. 3.27 shows the flowchart of the Matlab program used for calculating and selecting the motor dimensions.

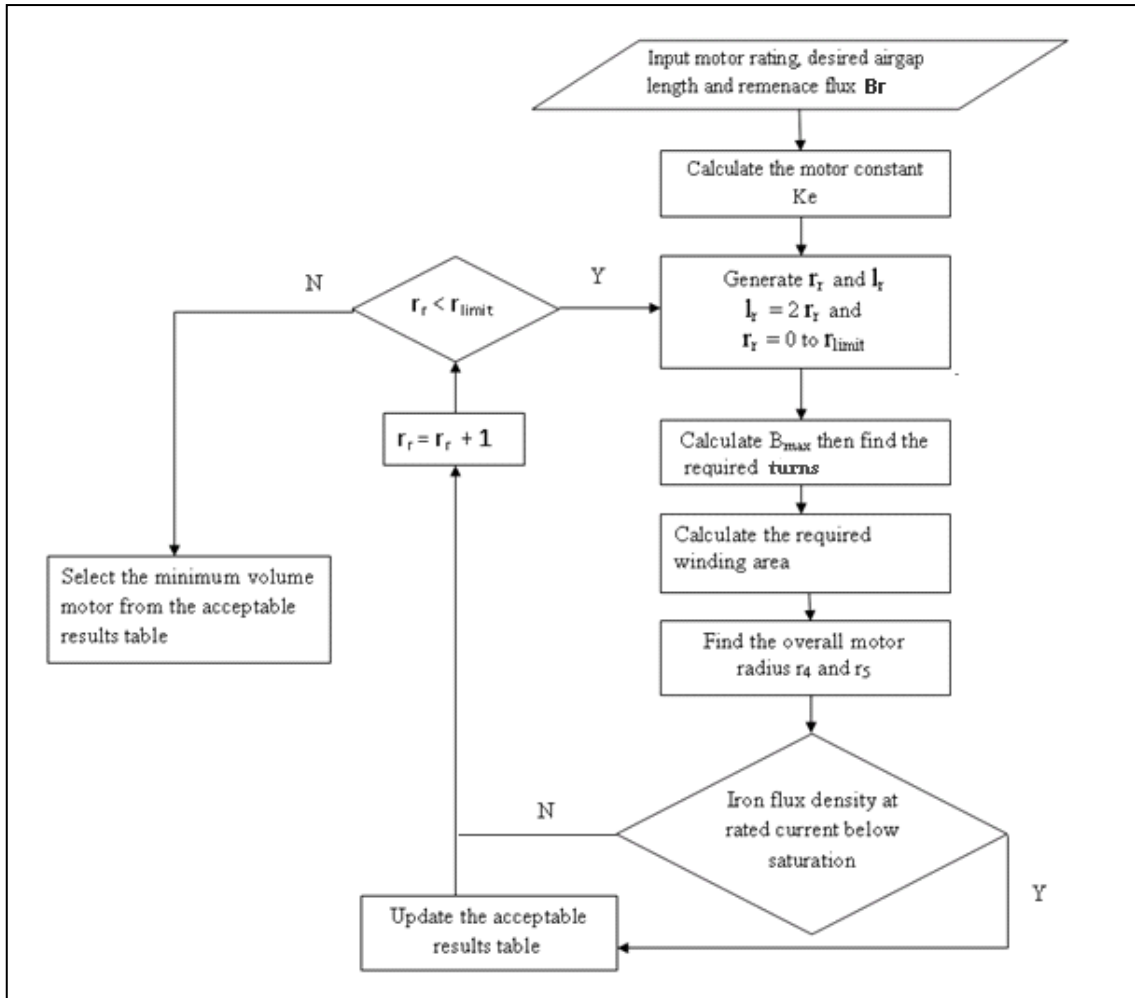


Fig. 3.27 flowchart for calculating motor dimensions

The programme generates a range of rotor radii r_2 and lengths l_r , and for every combination the required number of turns to achieve $k_e = 1.91$ is calculated using equation 3.63.

$$N = \frac{K_e}{B_{max} r_2 l_r} \quad (3.63)$$

B_{max} is the peak airgap flux density from the magnets which can be calculated using equation 3.59 with current I equal to zero.

$$B_{max} = \frac{2l_m B_r}{2l_m + 2l_g + l_{iron}/\mu_r} \quad (3.64)$$

l_m is the magnet radial thickness and l_g is the airgap length, both of them are provided as inputs to the program, l_{iron} is the length of the iron flux path which can be calculated as

$$l_{iron} = 2 \left(r_1 + \left(r_3 + \frac{x_c}{2} - r_2 \right) \right) + \frac{2\pi \left(r_4 + \frac{x_c}{2} \right)}{4} \quad (3.65)$$

At this stage the number of turns is not calculated and X_N and r_4 are unknowns therefore l_{iron} is calculated with r_4 approximated to r_3 which is found as in the following

$$r_1 = r_2 - l_g - l_m \quad (3.66)$$

$$x_p = \sqrt{2 r_2^2 (1 - \cos 40^\circ)} \quad (3.67)$$

$$x_c = \frac{x_p}{2} \quad (3.68)$$

$$r_3 = r_2 + x_c \quad (3.69)$$

Once l_{iron} is found B_{max} can be calculated using 3.64.

B_{max} is used in 3.63 to calculate the required number of turns. When the number of turns is found the following step is to find r_4 .

$$A_{slot} = A_{wire} \times 2N \times \text{winding factor} \quad (3.70)$$

Where A_{slot} is the total copper area, A_{wire} is the wire cross sectional area. A_{slot} should be equal to the total available winding area

$$A_{slot} = \pi r_4^2 - \pi r_3^2 - 4x_p x_N \quad (3.71)$$

This expression would give a suggested maximum available area for the copper. Solving 3.70 and 3.71 to find r_4 will result in the following quadratic equation

$$(\pi)r_4^2 - (4x_p)r_4 + (4x_p r_3 - \pi r_3^2 - 2N\pi r_{wire}) = 0 \quad (3.72)$$

Once r_4 is determined r_5 is calculated as

$$r_5 = r_4 + x_c \quad (3.73)$$

3.9.4 FEM Results

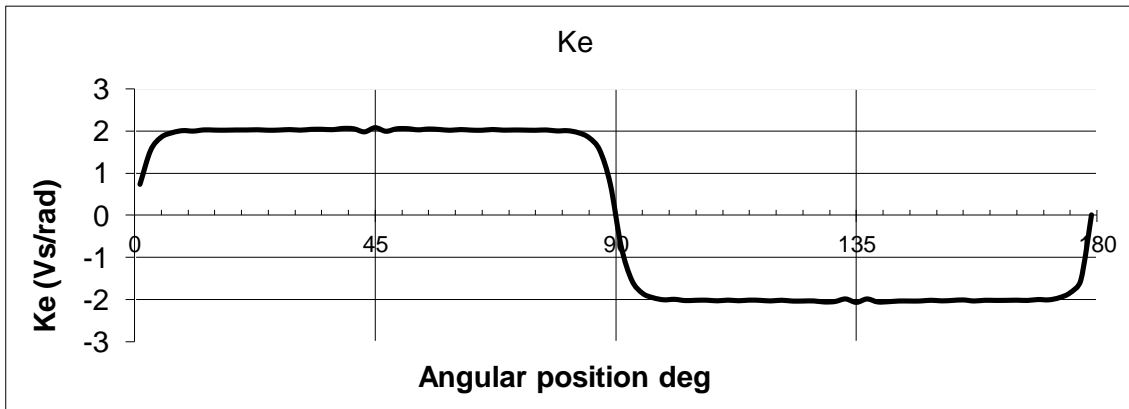
The following motor dimensions were calculated by the Matlab program:

$r_1 = 38\text{mm}$, $r_2 = 41\text{mm}$, $r_3 = 55\text{mm}$, $r_4 = 62.6\text{mm}$, $r_5 = 76.6\text{mm}$, $N = 648$ turns,

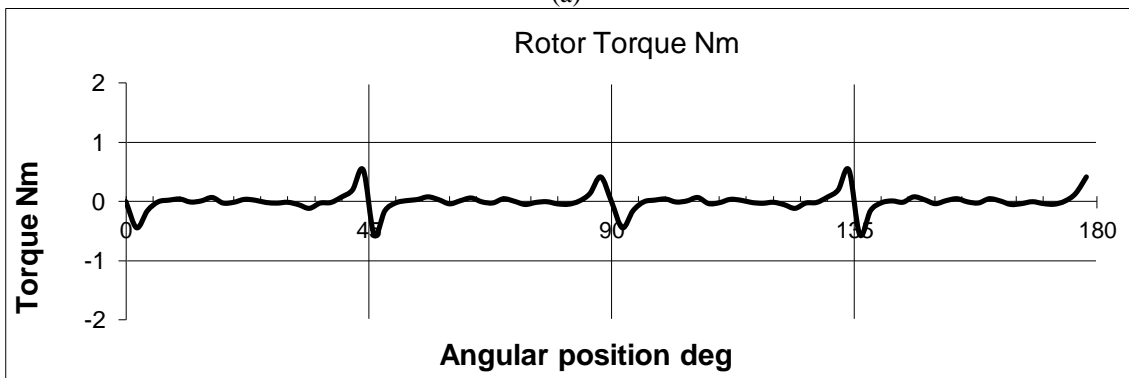
$l_r = 108\text{mm}$.

A model with these dimensions was created using FEM software with rare earth neodymium magnets of 1T remanence flux density and generic iron for the stator and rotor. Fig. 3.28 shows the back EMF constant K_e profile and the cogging torque. It can be noticed that the model has produced the required value of average back EMF constant

which is 1.91 Vs/rad.



(a)



(b)

Fig. 3.28 FEM results of the prototype single phase BLDC motor, (a) back EMF profile, (b) Cogging torque.

3.10 Conclusions

An investigative study on reducing the cogging torque for a new single phase PM brushless DC motor with maintaining the trapezoidal shape of back EMF was conducted. It was found that the cogging torque in the integral slot single phase BLDC motor can be reduced by employing an asymmetrical stator arc topology, but generally with a poor back EMF shape. This chapter presented an analytical method to obtain an asymmetrical motor topology that produces lower slot cogging torque while maintaining the ideal back EMF shape. Having a trapezoidal back EMF is an important feature for PM BLDC which is excited by a trapezoidal current in order to have minimum electromagnetic torque ripple.

The iron content in the new topology was minimized, and the limit for the maximum amount of iron that can be removed without distorting the trapezoidal back EMF shape and cogging torque was investigated. From the investigation it was found that employing pole shoe design in the large stator poles with a thickness of half the stator tooth the stator iron can be reduced without influencing the performance of the new asymmetrical surface mounted single phase motor.

Finally this chapter has demonstrated a method on automated sizing for a 1 kW design based on the new single phase BLDC motor topology.

4. Tailoring The Open Circuit Torque Profile for the New Single Phase PM BLDC Motor

4.1 Introduction

This chapter describes the modification of the air gap profile for the new single phase PM BLDC motor, presented in the previous chapter, to produce positive reluctance torque at the alignment positions. The motor has an asymmetrical stator pole topology that has the advantage of reducing the cogging torque level without affecting the trapezoidal shape of the back EMF. The developed motor topology does not produce reluctance starting torque at the aligning positions (0° , 90° ...) where the electromagnetic torque is zero and hence it needs further improvement. Since starting torque is a major issue for single phase BLDC motor this chapter is aiming to create a method that enable us to design a compensating reluctance torque component that solves the starting problem with low resultant torque ripple in the unaligned region.

4.2 Starting torque in single phase BLDC motor

One common issue between single phase BLDC motors is the starting problem. Single phase BLDC motors, unlike three phase BLDC motors, exhibit zero torque points at certain rotor positions or 'null points'. This is because the stator flux in single phase BLDC motors is produced by a single winding which does not present a rotating magnetic field to the rotor. Therefore, when the rotor poles or magnets are aligned with stator poles at 0° , 180° and 360° electrical degrees, the angle between the rotor and stator fluxes is zero and there will be no electromagnetic torque exerted on the rotor Fig. 4.1

shows a typical excitation torque of a four pole single phase BLDC motor with an ideal square back EMF.

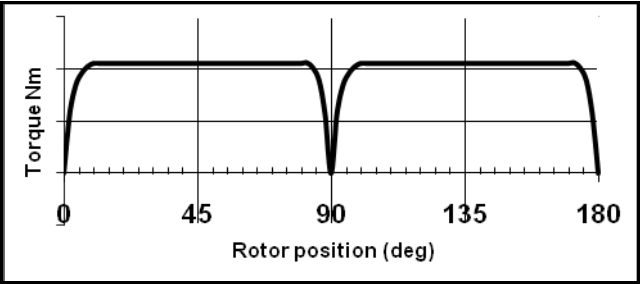


Fig. 4.1 Excitation torque of a 4 pole single phase BLDC motor with trapezoidal back EMF

All the previous methods used to overcome the ‘null point’ problem are based on providing reluctance torque by creating an asymmetrical (non constant) air gap. The asymmetry in the air gap creates a reluctance torque component with positive torque at the aligning positions which compensates the excitation torque to remove the null points. This way of introducing a reluctance starting torque is only suitable for unidirectional motors. Fig. 4.2 demonstrates ideally how the reluctance torque due to the air gap asymmetry and in conjunction with the excitation torque produces a constant net torque.

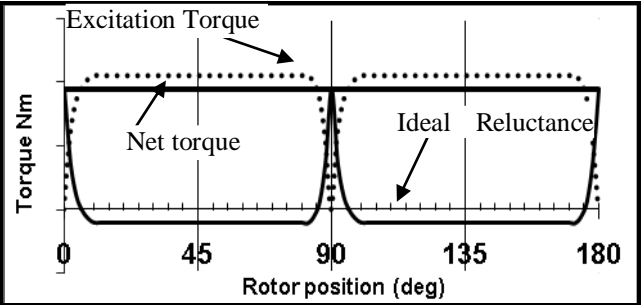


Fig. 4.2 Ideal reluctance torque waveform to eliminate ‘null points’ in the torque produced by a single phase BLDC motor.

The area under the positive part of the reluctance torque graph should always be equal to the area under the negative part. Therefore, the ideal reluctance torque profile re-

quires a peak at the alignment positions, and a low negative torque spread evenly elsewhere.

The null points in the torque profile are only a problem at start up. If the machine is running, the inertia of the rotor can be sufficient to allow the rotor to pass through the null points, assuming an idealised situation where excitation torque is the only component of torque acting on the rotor.

4.3 Conventional solution for the starting problem in single phase PM BLDC motor

All the research that is concerned with optimizing the air gap topology to solve the null point problem is based on investigating the effect of a set of parameters of a particular air gap topology [42, 45, 46, 48, 51-53]. In [46] a set of air gap profiles were investigated and the conclusion was that the air gap profile which is created by tapering the stator iron has produced the best result because it has resulted in a smooth reluctance torque.

Fig. 4.3 shows the resulting reluctance torque waveform when a 0.5mm tapered air gap, as shown in Fig. 4.4, is applied to the new asymmetrical stator pole single phase BLDC motor presented in chapter 3.

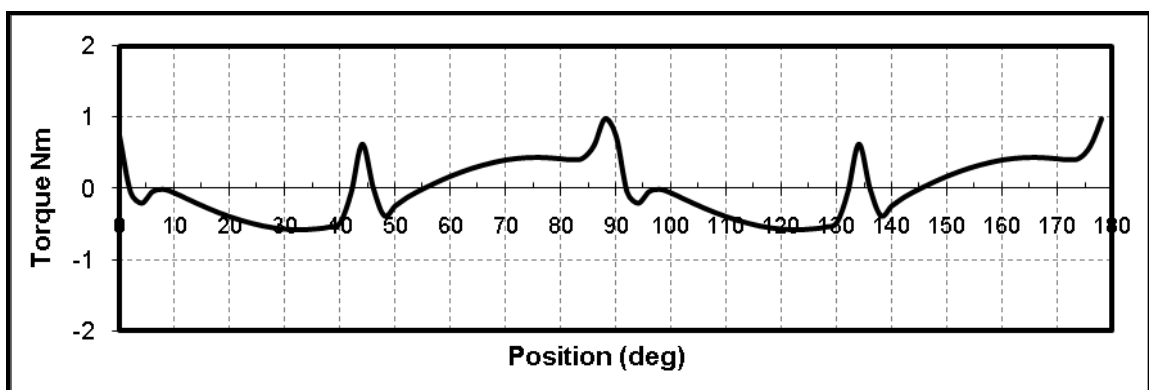


Fig. 4.3 Reluctance torque caused by a tapered air gap design 0.5mm air gap variation.

It can be seen that implementing the tapered air gap design on the new topology has produced a positive starting torque at the aligning positions, but with high 1Nm peak to peak ripple at the unaligned positions at 45° and 135° which will affect the smoothness of the resultant torque.

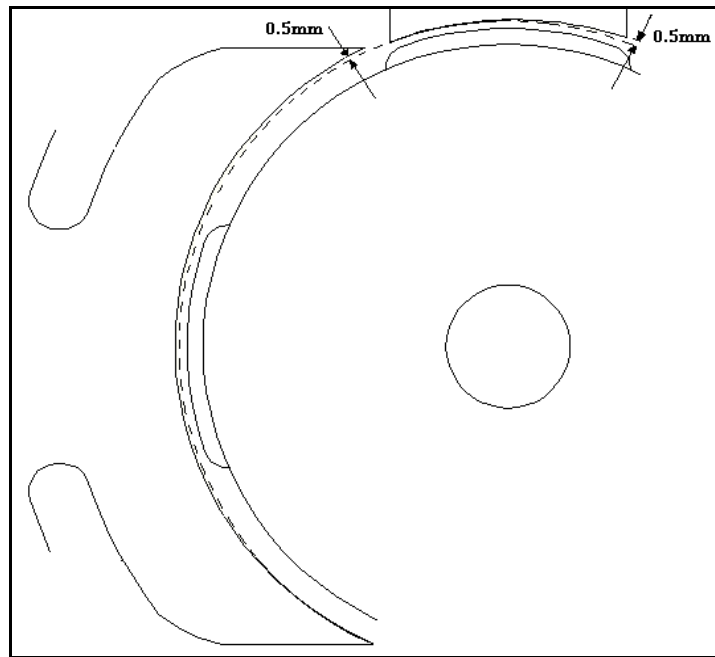


Fig. 4.4 tapered airgap design 0.5mm air gap variation.

Therefore employing the airgap design proposed in [46] on the new single phase BLDC motor will not produce the desired reluctance torque profile. There is no research that presents a method to design an airgap profile which results in a desired shape of the compensating reluctance torque for an asymmetrical single phase PM BLDC motor.

This chapter will present a new method in constructing an air gap topology for an asymmetrical single phase BLDC motor that will produce a resultant reluctance torque profile which has characteristics close to the ideal. The method will determine which part of the stator steel that needs to be shaped, removed or notched in order to create the desired asymmetrical air gap profile.

4.4 The property of superposition for two independent airgap shapes

The proposed method of synthesizing the reluctance torque waveform relies on the fact that the property of superposition is maintained when the asymmetry in the air gap is achieved by two or more independent modifications in the stator iron area that is adjacent to the air gap area. The modification area in the stator is represented by the grey area shown in Fig. 4.5.

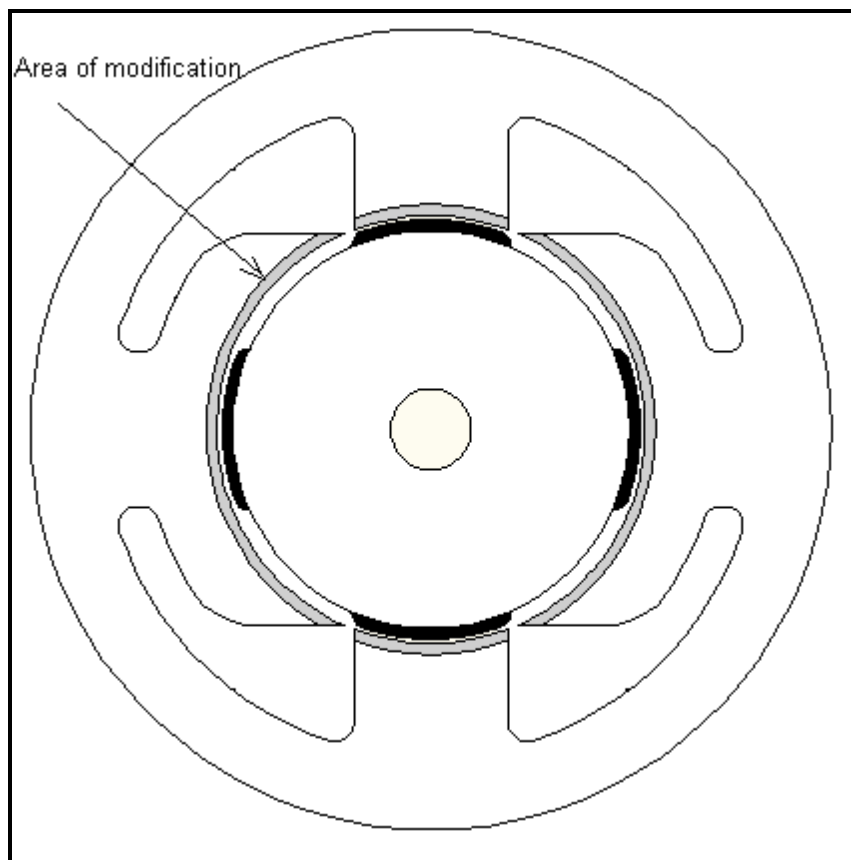


Fig. 4.5 The modified part of the stator iron to create asymmetrical airgap profile

Two different airgap profiles are modelled using FEM software in order to verify the property of superposition in the reluctance torque profile. The first FEM model has an airgap which is created by tapering the small stator poles to form a variable air gap that varies from 1mm to 1.5mm, as shown in Fig. 4.6a. the airgap of the second FEM model

is created by tapering the large stator pole arc to form a variable air gap that varies from 1mm to 1.5mm, see Fig. 4.6.

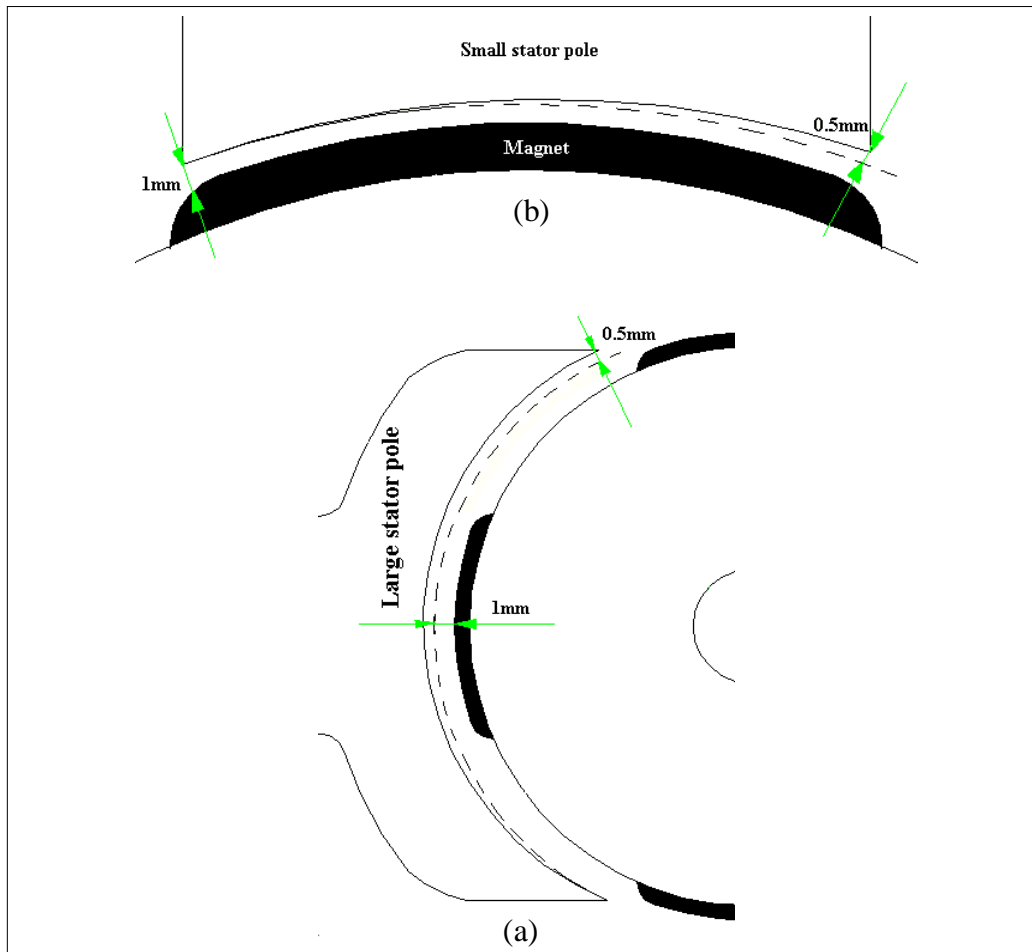


Fig. 4.6 (a) tapered small stator pole (b) tapered large stator pole

The resulted reluctance torque from the two models is shown in Fig. 4.7. It can be seen that each air gap design has produced a different reluctance torque profile. The results include the effects of the main stator slots (cogging torque). In order to confirm the superposition property the cogging torque element has to be subtracted from these reluctance torque profiles. Otherwise summing the independent reluctance torque profiles without removing the cogging torque component will produce a torque profile with double the level of cogging torque.

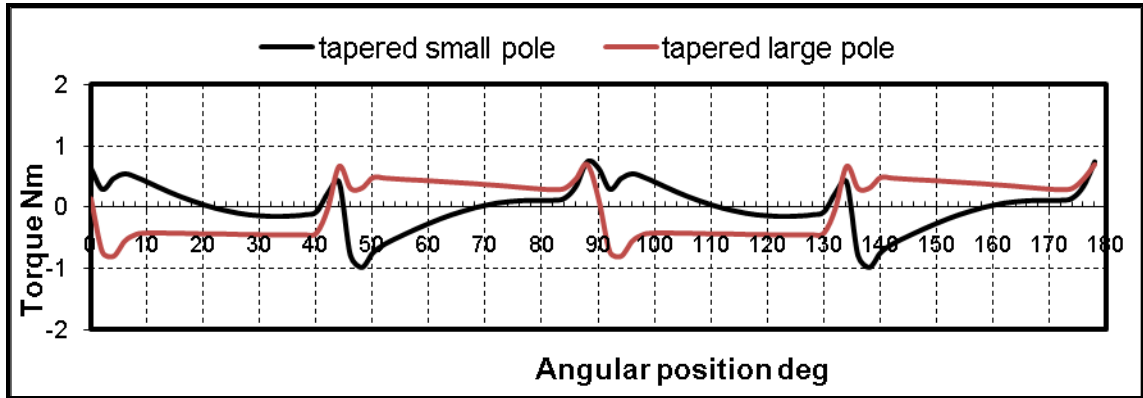


Fig. 4.7 Reluctance torque profiles of the tapered small stator poles and tapered large stator poles

Fig. 4.8 shows the reluctance torque profiles with the cogging torque component removed. The resulting reluctance torque profile from summing the two independent reluctance torque profiles of the two airgap designs is shown in Fig. 4.9 together with the FEM calculated reluctance torque profile for a model that combines the two airgap designs. It can be seen that the synthesized reluctance torque profile matches very well with the reluctance torque of the combined air gap design which was numerically calculated using the FEM software.

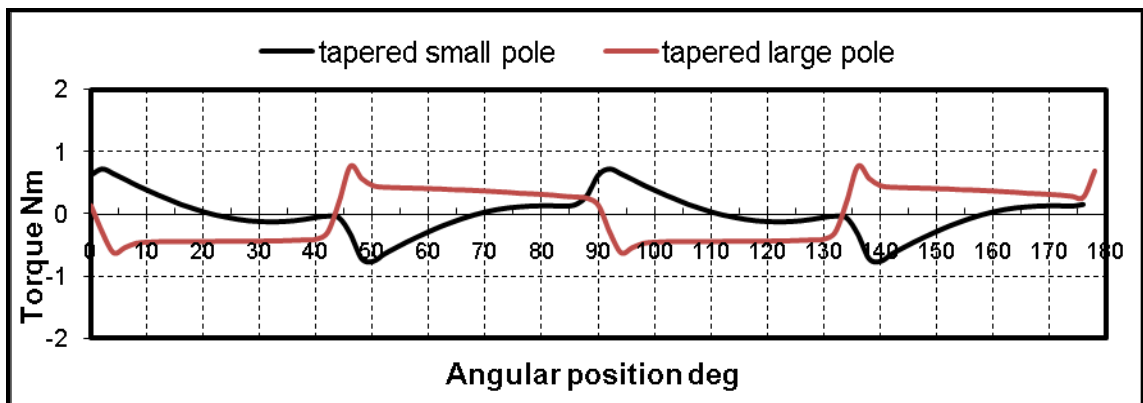


Fig. 4.8 Reluctance torque profiles of the tapered small stator poles and tapered large stator poles

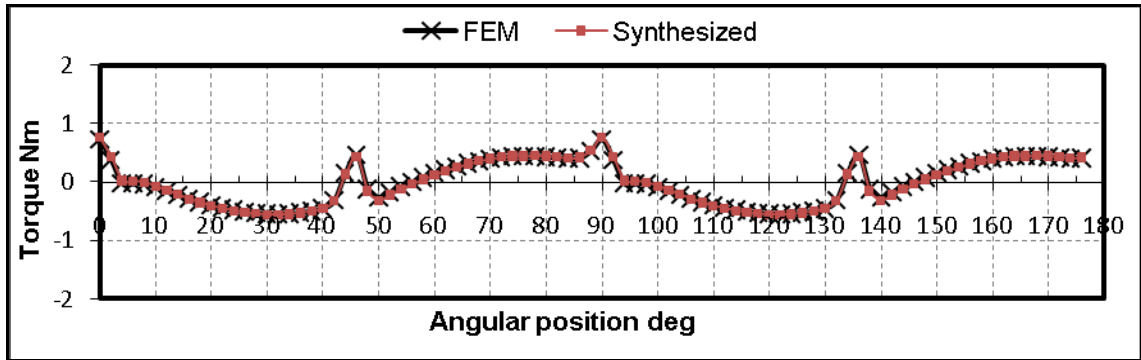


Fig. 4.9 Synthesized reluctance torque effect of the combined air gap design.

4.5 Uniform airgap reluctance torque profile (cogging torque)

In the literature the reluctance torque due to the main stator slots is referred to as cogging torque. The cogging torque profile for the new single phase BLDC motor (with a uniform air gap) is shown in Fig. 4.10. Assuming anticlockwise rotation, the negative peaks occur when the leading edge of the permanent magnet crosses under the stator slot, and the positive peak occurs when the trailing edge crosses under the stator slot.

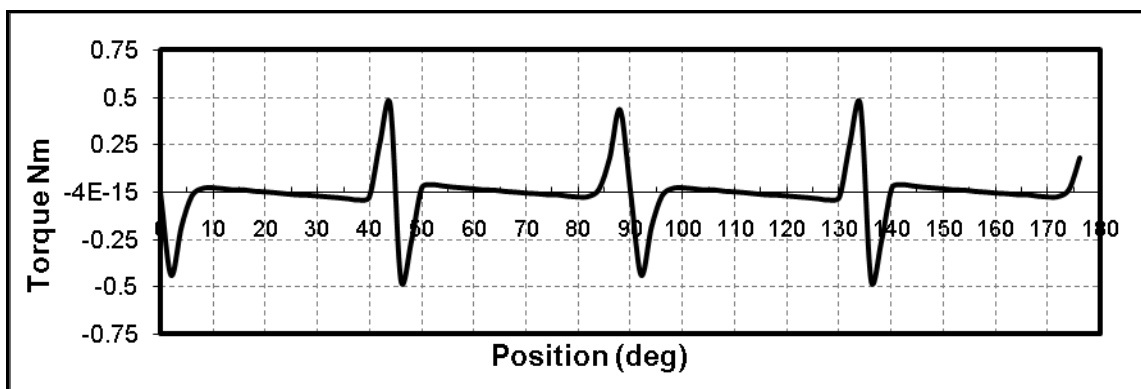


Fig. 4.10 Reluctance torque waveform for a uniform air gap design (cogging torque)

In order to demonstrate the formation of the negative and positive peaks in the torque profile a motor model with a magnet of arc length 24° mechanical is chosen as an example. See Fig. 4.11. The configuration is not the optimum magnet arc length, but it is used here to simplify understanding of the formation of the peaks in the cogging torque

waveform, since there is no overlap or coincidence between peaks as in the case when the magnet arc length is the same as the small stator pole arcs.

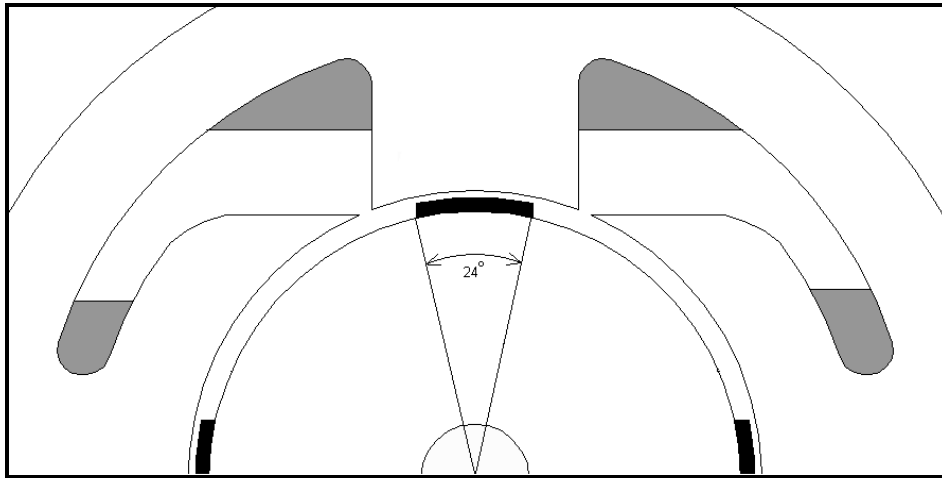


Fig. 4.11 a model with magnet width 24°

Fig. 4.12 shows the flux plots at one of the stator slots while the leading edge of the permanent magnet is passing the slot i.e. the formation of a negative peak. At that position the magnetic flux from the permanent magnet prefers to follow the path of minimum reluctance which is back to the small stator pole (see rotor position at 10°). This is represented in the reluctance torque waveform as a negative peak exerted on the rotor trying to resist the misalignment with the small stator pole. Once the leading edge of the magnet has passed the stator slot the reluctance torque exerted on the rotor will become zero.

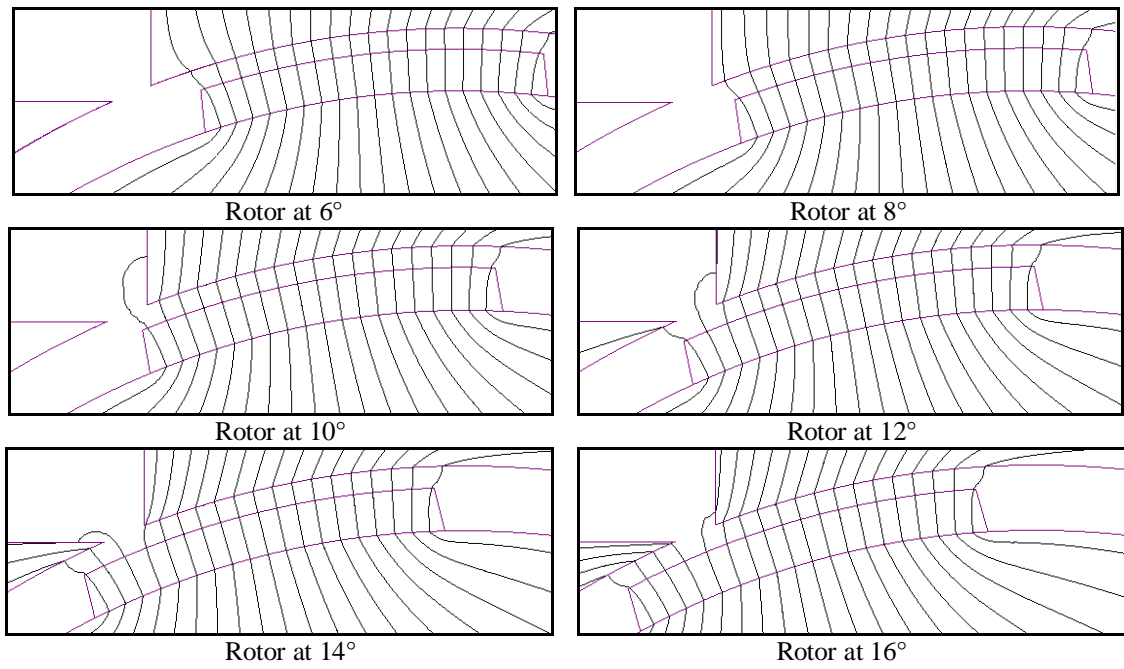


Fig. 4.12 Flux plots while the leading edge of the permanent magnet crossing the stator slot.

When the trailing edge of the permanent magnet passes across the stator slot, as shown in Fig. 4.13 the flux from the rotor magnet tries to align the magnet with the large stator pole (i.e. follow lower reluctance path) which causes the positive peak in the cogging torque profile.

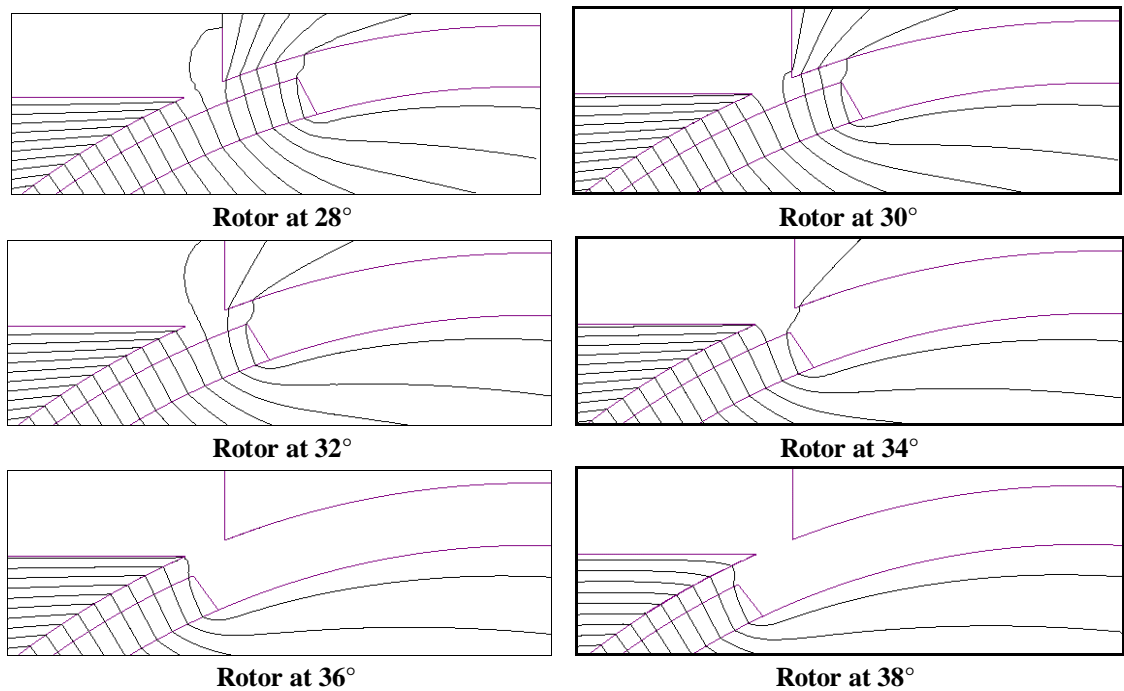


Fig. 4.13 Flux plots while the lagging edge of the permanent magnet crossing the stator slot.

4.6 Small unit change in the airgap shape

Taking the advantage of the property of superposition in the reluctance torque profile, the airgap can be considered to be composed of several small modifications which are represented as notches or auxiliary slots in the stator iron. In another way we can say that an airgap shape can be constructed using the slots as being the building blocks of the air gap. For example, the air gap design which is created by tapering the small stator poles pretended in section 4.4 can be approximated by using a few auxiliary slots as shown in Fig 4.14.

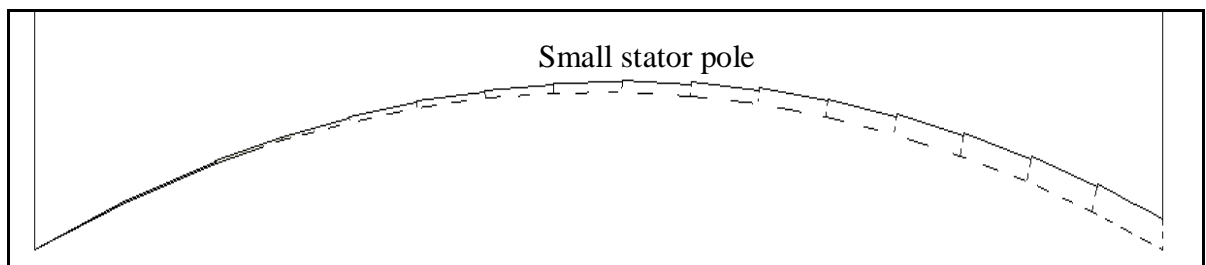


Fig. 4.14 Constructing a 0.5mm tapered air gap using dummy slots

In this chapter the smallest change in the air gap profile is represented by a pair of auxiliary slots in the stator iron placed 180° from each other and have a depth of 0.25mm, angular arc length of 2.5° . See Fig. 4.15 . The corresponding reluctance torque profile without the slotting effect is shown in Fig. 4.16.

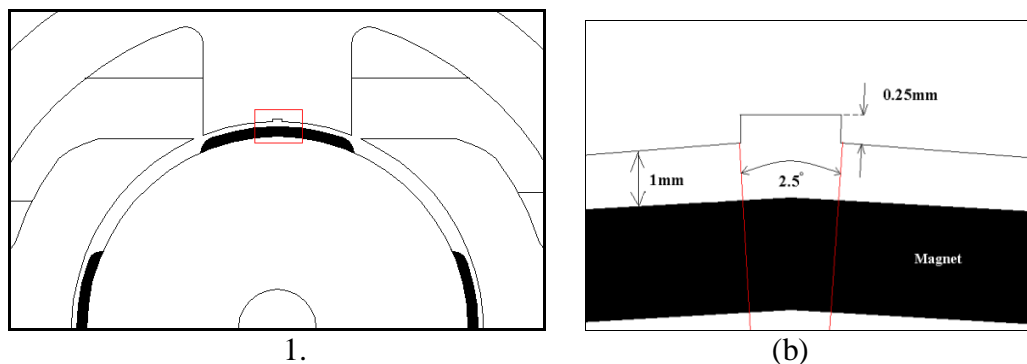


Fig. 4.15 Auxiliary slot of 2.5° width and 0.25mm depth (a) global view, (b) zoomed view.

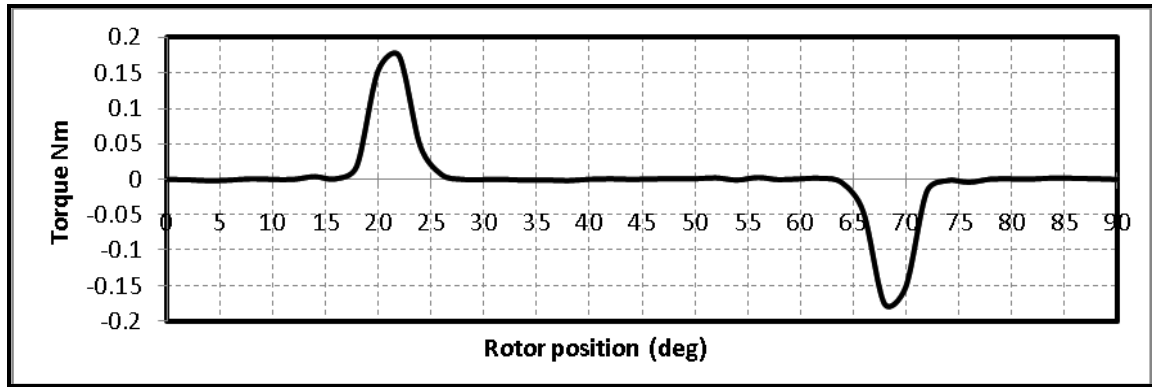


Fig. 4.16 The reluctance torque effect waveform of the slot in Fig. 4.15

4.7 Properties of auxiliary slots (or notches)

The reluctance torque profile produced by placing an auxiliary slot in the stator iron is composed of a cycle of a negative peak followed by a positive peak. The formation of these peaks is similar to the way in which the peaks due to the stator slot openings are formed. This is explained in section 4.5. Since the positive and negative peaks are due to the interaction of the magnet edges with the notches, the angular distance between the two peaks is determined by the angular width of the magnet. S. Ahmed [54] has concluded that the permanent magnet arc length must coincide with the arc length of the small stator poles in order to obtain a trapezoidal back EMF shape. Therefore, the arc length of the magnet (or the distance between the negative and positive peaks) can only be altered slightly in order not to distort the shape of the back EMF.

Before using the auxiliary slots to synthesize the air gap shape of the new single phase BLDC motor, an understanding of the characteristics of the slots is a prerequisite. The following section will investigate the factors that affect the phase, shape and magnitude of the reluctance torque profile for an auxiliary slot.

4.7.1 Varying the angular position of the auxiliary slot

Fig. 4.17 shows two reluctance torque profiles. Profile A is a result of placing a pair of auxiliary slots at 0° with an angular width of 2.5° and radial depth of 0.5mm. Profile B

is the reluctance torque after shifting the pair of auxiliary slots by 50° anticlockwise. From the figure it can be seen that shifting the slots by a certain angle has caused the effective reluctance torque waveform (or the peaks) to be shifted by the same angle.

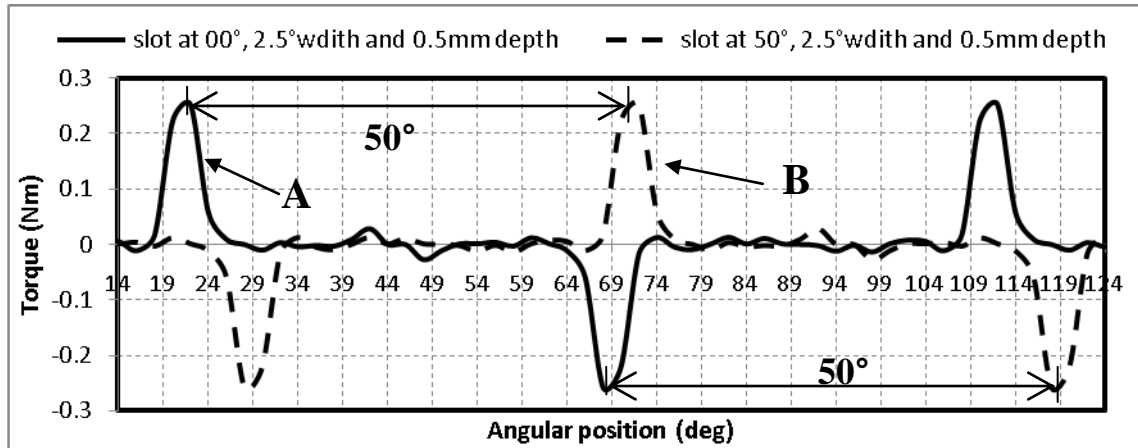


Fig. 4.17 The effect of shifting the position of the dummy slots on the reluctance torque waveform

4.7.2 Varying the radial depth of the auxiliary slot

In order to study the effect of the depth of the auxiliary slots on the magnitude of the peaks in the reluctance torque profile three different slot widths were considered 10° , 20° and 30° with seven depths for each one of them. The position and range of variation of the auxiliary slot is shown in Fig. 4.18. The slots were positioned at a fixed position of 90° . Fig. 4.19 shows the results of varying the depth for the three slots. Only the positive peaks are shown and that is because the negative peak varies in the same way as the positive peak but with opposite polarity.

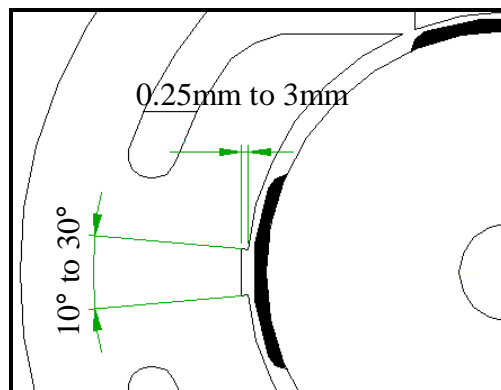
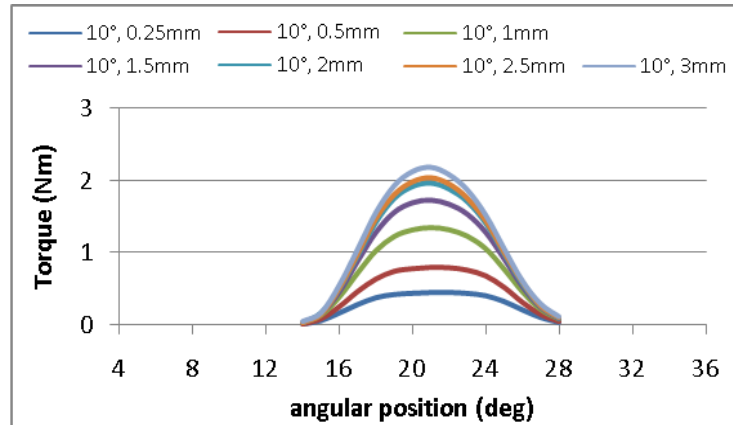
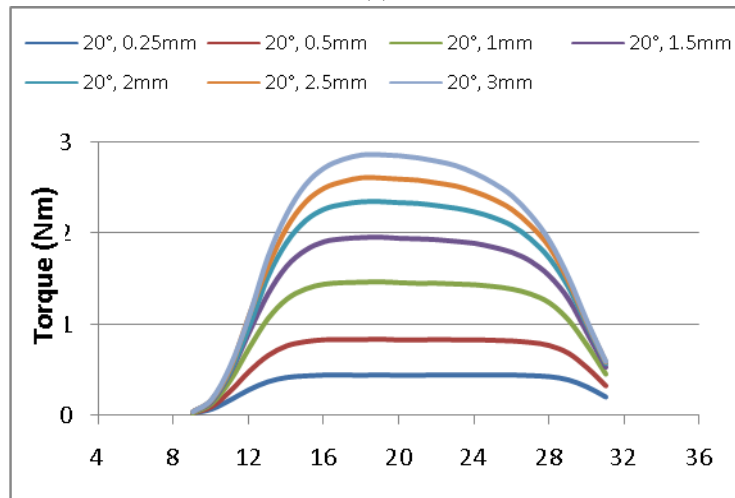


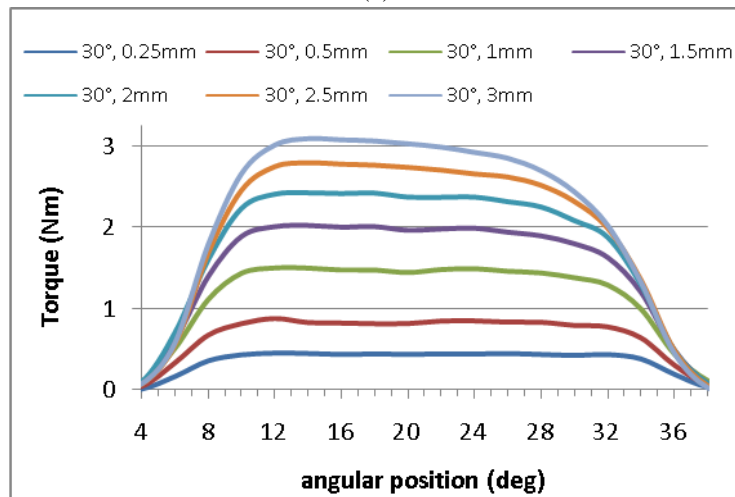
Fig. 4.18 Varying the slot width and depths



(a)



(b)



(c)

Fig. 4.19 The effect of slot radial depth on the reluctance torque peak. (a) 10° slot width, (b) 20° slot width, (c) 30° slot width.

It can be noticed that all the peaks have the same centre of 21° since they are all positioned at the same position on the stator pole at 90° . The results show that the magnitude of the peaks increases with depth of auxiliary slot while the shape of the peak is

unaffected for each slot width. The increase in the magnitude is not linearly proportional with the increase in the depth for a fixed width of slot. The relationship can be found by plotting the graph of peak torque against slot depth for each slot width as shown in Fig. 4.20.

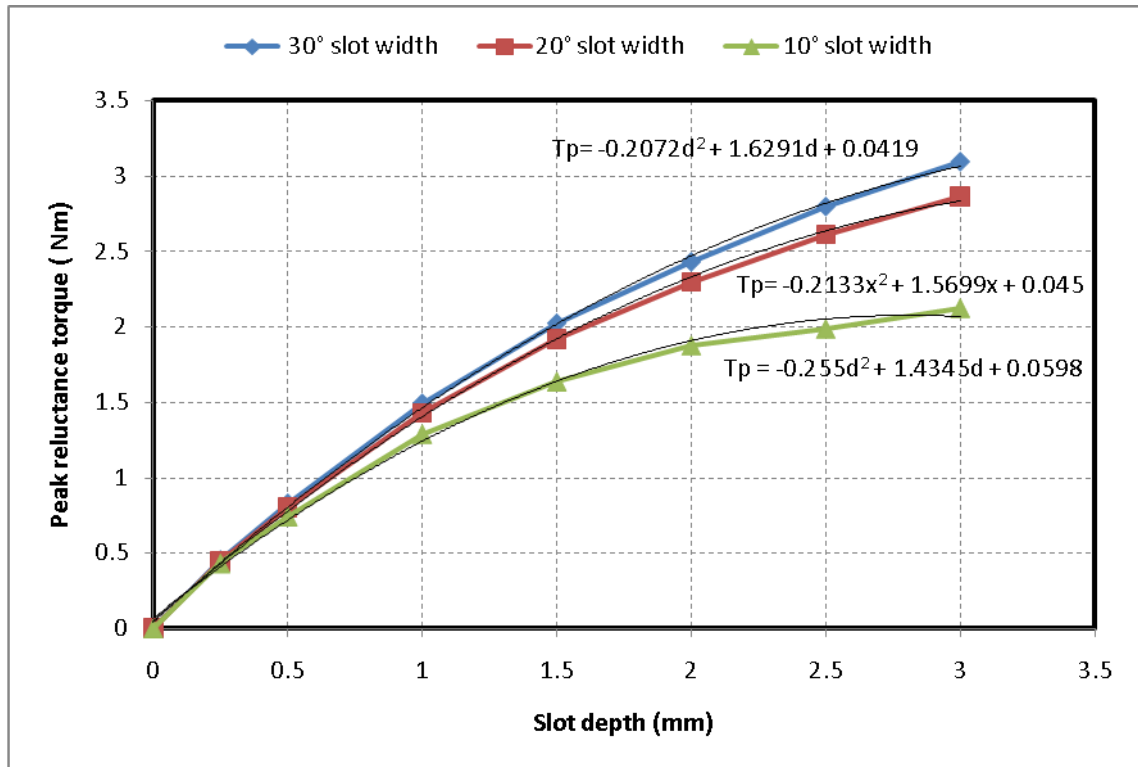


Fig. 4.20 The relationship between the depth increase of the auxiliary slot and the increase in the peak magnitude for slot widths 10°, 20° and 30°

The best line fit for the above data can be represented by a second order polynomial that relates the peak magnitude T_p with the slot depth d as follows:

$$\text{For slot width } 10^\circ \quad T_p = -0.21d^2 + 1.61d + 0.04 \quad (4.1)$$

$$\text{For slot width } 20^\circ \quad T_p = -0.21d^2 + 1.57d + 0.05 \quad (4.2)$$

$$\text{For slot width } 30^\circ \quad T_p = -0.26d^2 + 1.43d + 0.06 \quad (4.3)$$

Using this relation the magnitude of the peak for slots of higher depths can be extrapolated.

4.7.3 Varying the width of the auxiliary slot

In this section the effect of increasing the width of the auxiliary slot while the depth is fixed is presented. The variation of the width with six fixed slot depths of 0.5mm, 1mm, 1.5mm, 2mm, 2.5mm and 3mm was undertaken. For each slot depth the width was varied in four steps 5°, 10°, 20° and 30°. From Fig. 4.21 it can be seen that increasing the width of the slot has two effects on the reluctance torque peaks 1) change in the shape, 2) change in the magnitude. The increase in the slot width has caused the width of the peak to increase. Therefore, it can be concluded that the width of the peak is proportional to the width of the slot. The magnitude of the peak increases with slot width, but only up to a width of about 10°, and increasing the width beyond that negligible effect on the magnitude.

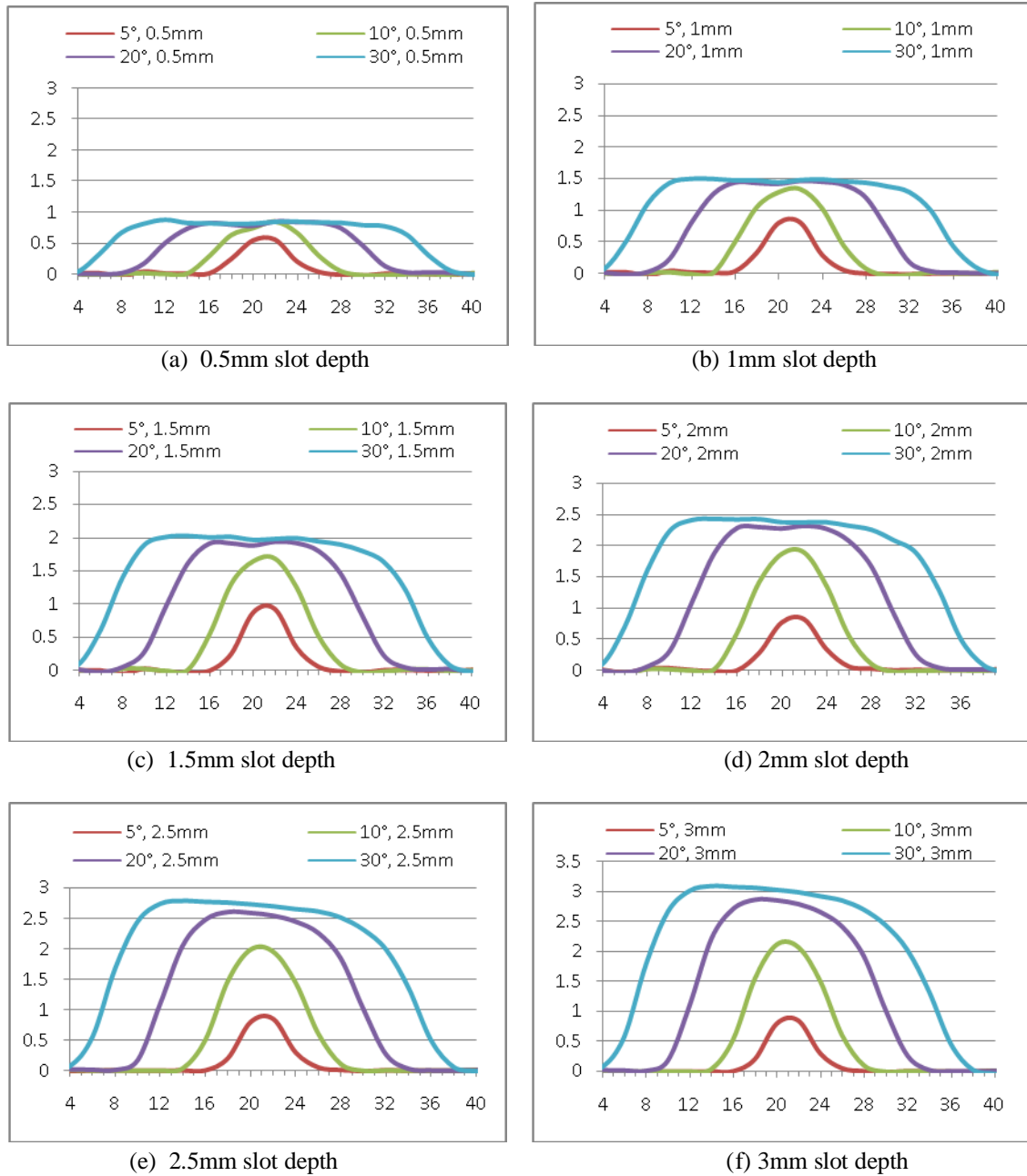


Fig. 4.21 The effect of increasing the width of the slot on the magnitude of the reluctance torque peak.

4.8 Open circuit torque improvement for the new single phase BLDC motor

The use of a combination of auxiliary slots with the right width, depth and position can be used to enhance the open circuit torque of the single phase BLDC motor. The open circuit torque is composed of two reluctance torque components 1) due to the slot openings 2) due to the air gap topology. The improvement of the open circuit torque is aimed at achieving an efficient starting torque at the null points with minimum ripple between cogging torque ripple.

This section shows how the auxiliary slots are added to enhance the open circuit torque profile. The motor has an airgap shape which is created by tapering the small stator poles to form 0.5mm airgap variation as shown in Fig. 4.6a. The resulting reluctance torque profile and back EMF waveforms for the design are shown in Fig. 4.22. From the results it can be observed that the reluctance torque profile exhibits a large ripple in the range 20° to 70° of rotor position where a minimum ripple is desired in this region.

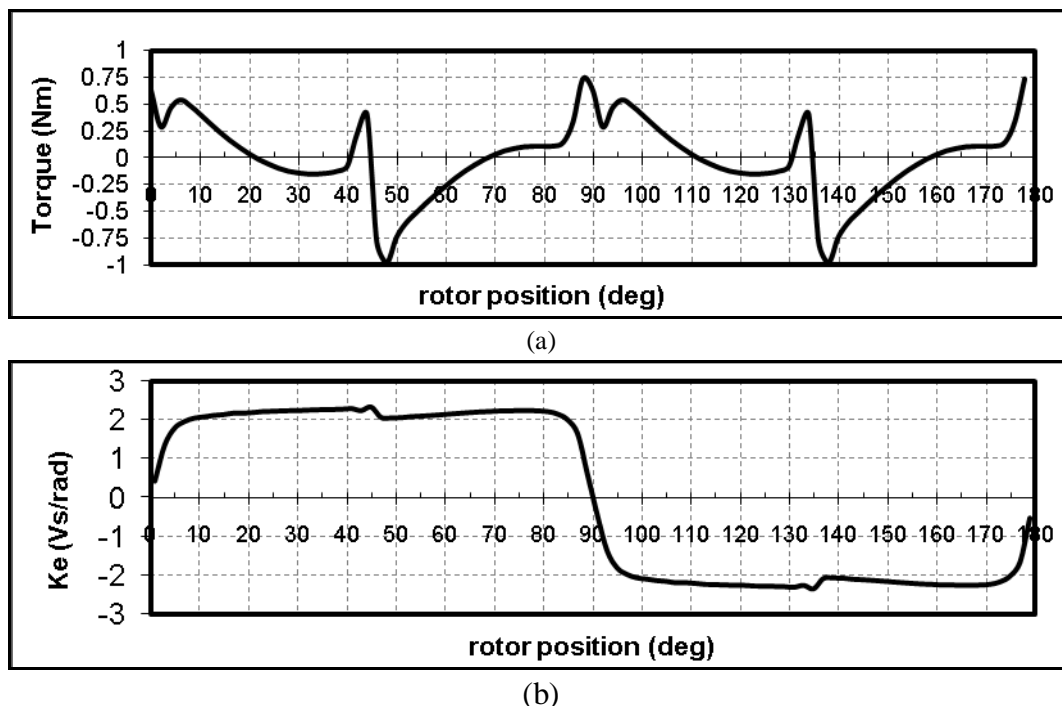


Fig. 4.22 Results of 0.5mm tapered small stator poles. (a) Reluctance torque profile (b) Back EMF

It is also desirable to attain an efficient reluctance torque at the alignment positions compared with the magnitude of the negative peaks. Ideally the negative part of the open circuit torque must be evenly spread with low magnitude across the region where positive starting torque is not required i.e. 20° to 70° . Ideally the added notches must produce a compensating reluctance torque profile that will reduce the ripple between 20° to 70° and enhance the starting torque.

By experimenting different combinations of notches it was found that the following combination can enhance the reluctance torque profile of the motor (asymmetrical topology with tapered small stator pole):

- Notch 1: single slot at 70° of width 10° and depth 1.5mm.
- Notch 2: double slots at 116° of width 5° and depth 1mm.
- Notch 3: single slot at -116° of width 5° and depth 0.5mm.
- Notch 4: single slot at 122° of width 10° and depth 0.5mm.
- Notch 5: single slot at -104° of width 5° and depth 2mm.

The contribution from each slot to the overall reluctance torque profile is shown in Fig. 4.23. Notch 1 is responsible for increasing the starting torque. The magnitude of the starting torque can be modified by increasing the depth and/or the width of this notch (see section 4.7). Notches 2 to 5 are responsible for reducing the ripple between 20° to 70° . Where two or more slots overlap the depth of the combined slot at that point is equal to the sum of individual notch depths.

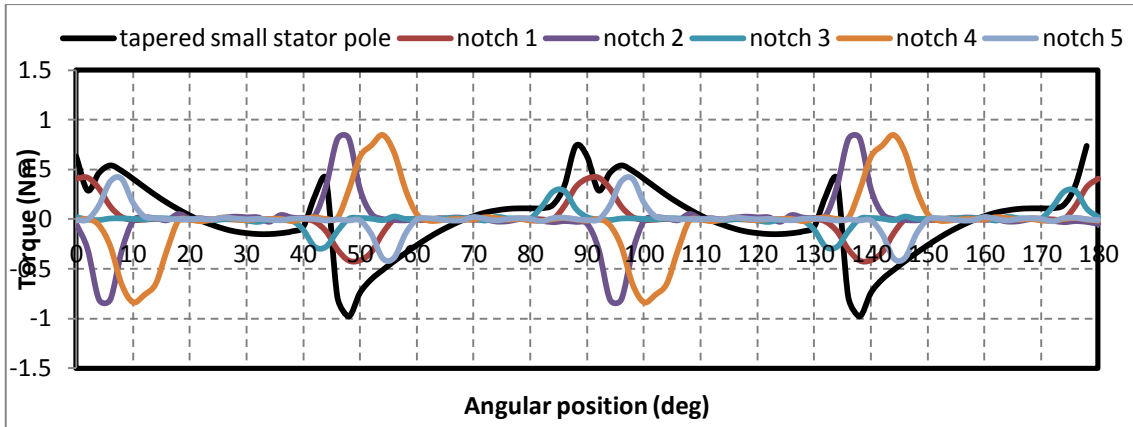


Fig. 4.23 The individual reluctance torque effect of each slot.

Fig. 4.24 shows the positions and sizes of the auxiliary slots on the stator of the new single phase BLDC motor which results in the reluctance torque profiles shown in Fig. 4.23 . Using the FEM software the resulting reluctance torque profile is plotted and compared with the reluctance torque before the addition of the slots. It can be seen that there is an increase in the starting torque value by 50% and a reduction in the ripple between 20° to 70° by 32%.

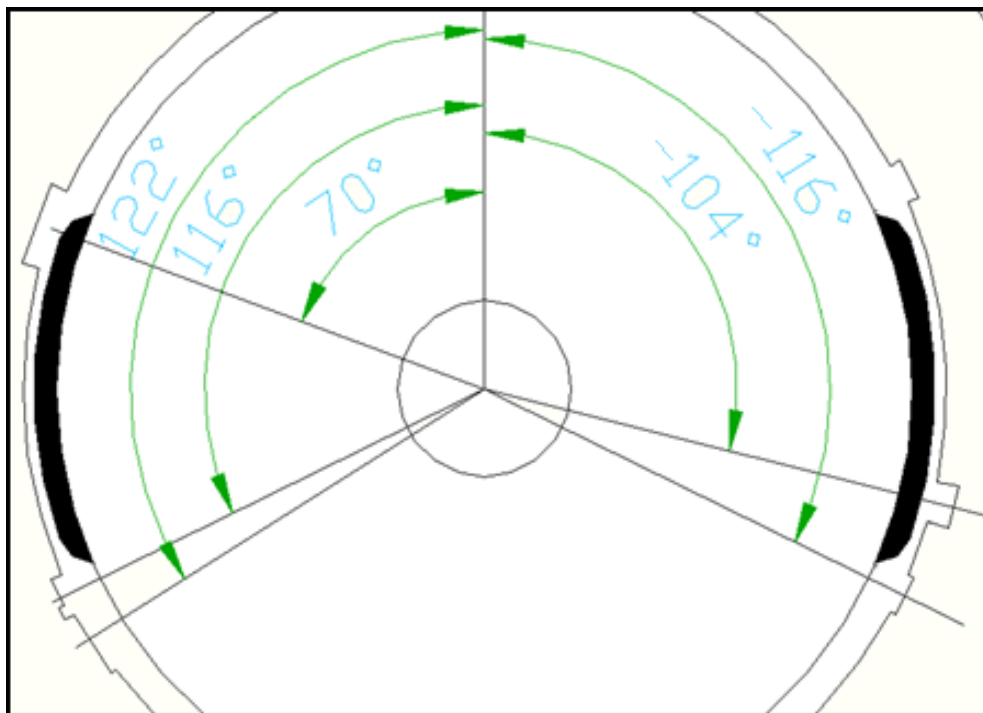


Fig. 4.24 The five slots in the stator iron to enhance the reluctance torque profile

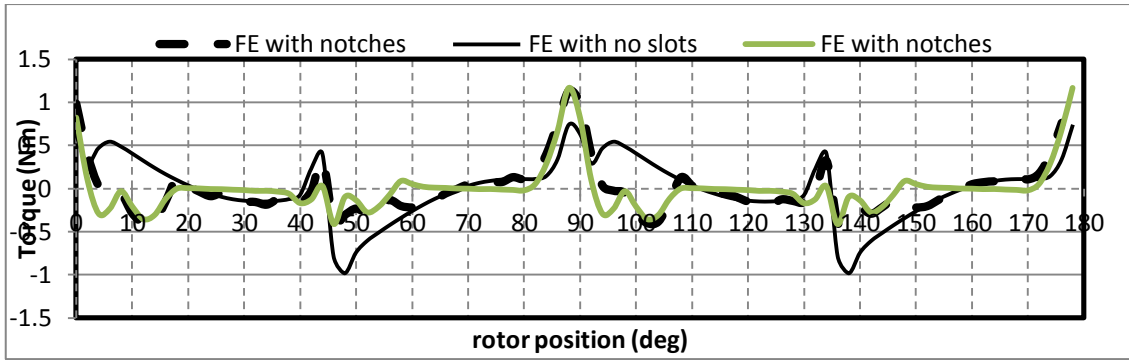


Fig. 4.25 Comparison between the reluctance torque profile before and after the addition of the auxiliary slots

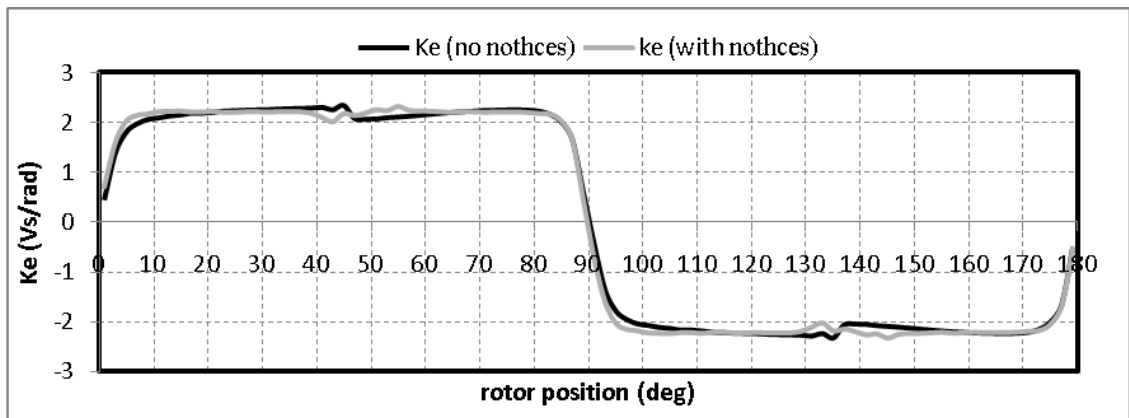


Fig. 4.26 Comparison between the back EMF shape before and after the addition of the slots

The back EMF shape before and after adding the slots is shown in Fig. 4.26. It can be seen that adding the slots did not affect the shape of the back EMF significantly and the trapezoidal shape of the back EMF is preserved.

4.9 Notch properties for tapered permanent magnet motor design.

In the previous sections it was shown that a variable air gap profile can be designed by modification in the stator iron (notches and taper) to synthesize the desired open circuit torque profile. Another way of achieving a variation in the air gap topology is by modifications in the rotor permanent magnet shape. In this section an air gap profile that is formed by tapering the permanent magnet in combination with notches in the stator iron

is presented. Fig. 4.27 shows how the surface of the permanent magnet is tapered in order to create a variation of 0.5mm in the air gap.

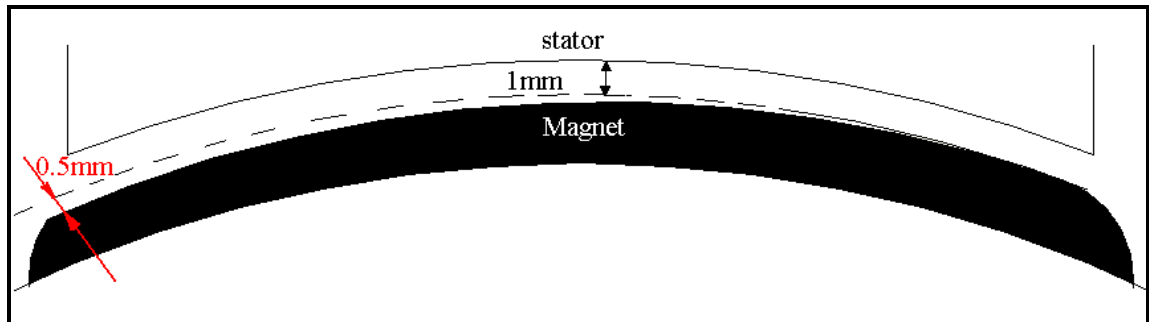


Fig. 4.27 tapered permanent magnet by 0.5mm

Since the peaks in the open circuit torque waveform are due to the interaction of the permanent magnet edges with the notches or main stator slots. Tapering the magnet will increase the radial distance between the leading edge of the magnet and the slot. As a result the negative peak will have lower magnitude with a wider base and the magnitude of the positive peak will remain unaffected. In the next section the factors that affect the open circuit torque profile for a tapered magnet motor design will be presented.

4.9.1 The effect of tapering the magnet on the torque due to slot openings

Fig. 4.28 compares the reluctance torque profiles due to the main stator slots before and after tapering the permanent magnets (with no stator tapering or notches). It can be seen that tapering the permanent magnet has caused the negative peaks of the waveform to have a lower magnitude and spread over wider range.

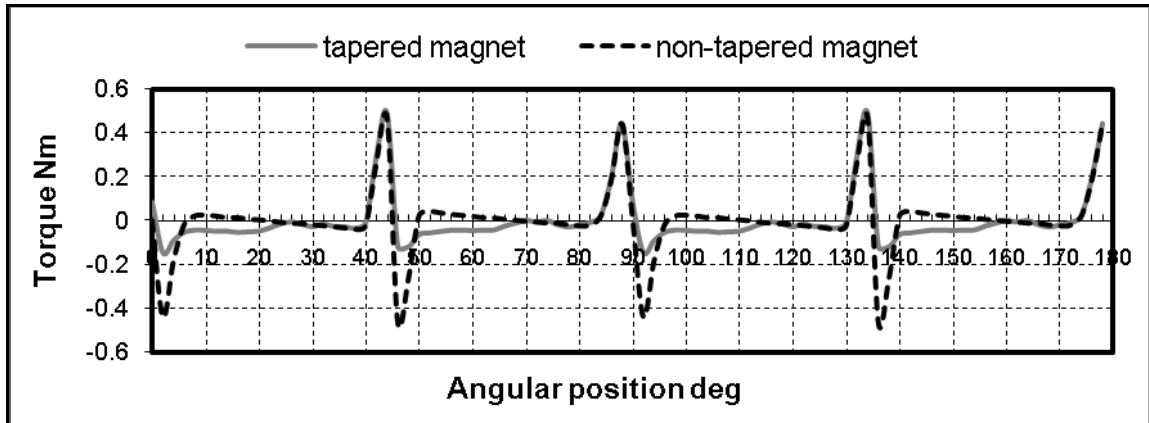


Fig. 4.28 The effect of tapering the magnet by 0.5mm on the cogging torque due to the main slots

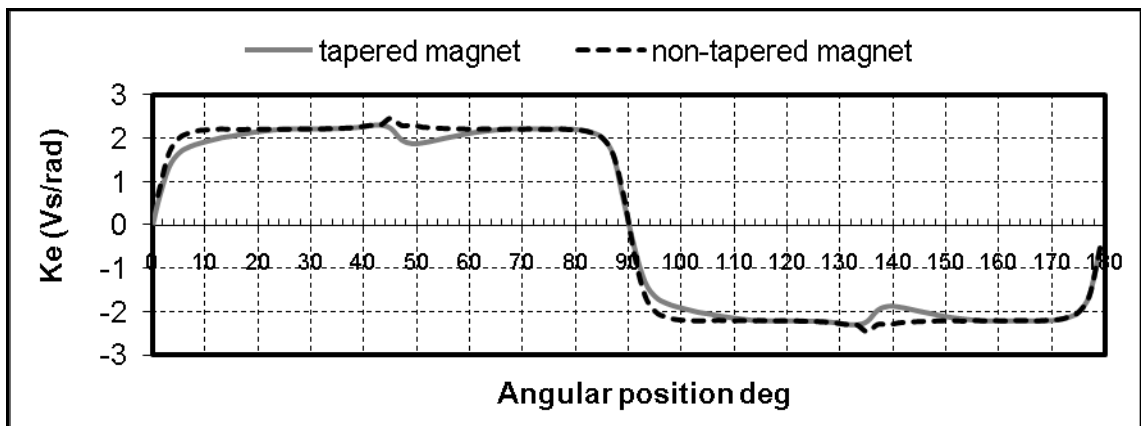


Fig. 4.29 the effect of tapering the magnet by 0.5mm on the back EMF shape

4.9.2 The effect of tapering the magnet on the notches reluctance torque profile

The effect of tapering the magnets on the notches torque profile is similar to the effect that tapering the magnet has on the main stator slots. And that is reducing the magnitude of the negative peak and extending its range while the positive peak stays unaffected. Fig. 4.30 shows how tapering the magnets affects the reluctance torque peaks of an auxiliary slot positioned at 90° with 1mm depth and 10° width.

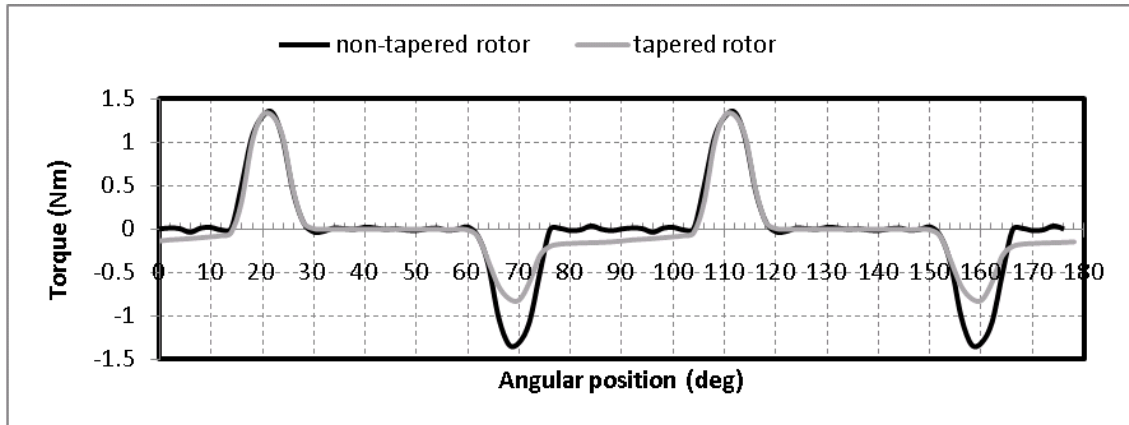


Fig. 4.30 the effect of tapering the magnet by 0.5mm on the reluctance torque of the auxiliary slot of 1mm depth and 10° width

In order to study the factors that affect the shape of the reluctance torque waveform from a slot in the stator with a tapered rotor configuration a set of reluctance torque profiles for different slot depths and widths were investigated.

4.9.2.1 Varying the radial depth of the notch

Three auxiliary slots of different widths were used for this investigation; 10°, 20° and 30°. The slots were placed at a fixed position of 90°, and the depth of each slot was varied with following depths 0.25mm, 0.5mm, 1mm, 1.5mm, 2mm, 2.5mm and 3mm. The reluctance torque profile for all three slots is presented in Fig. 4.31 Fig. 4.34. From these figures it can be seen that the magnitude of the negative peaks are smaller than the magnitude of the positive peaks for all widths and depths. The relationship between the increase in depth and the increase in peak magnitude is also plotted for both the positive and negative peaks. It can also be seen that the relative increase between the positive peaks as a function of slot depth is the same as the relative increase between the negative peaks.

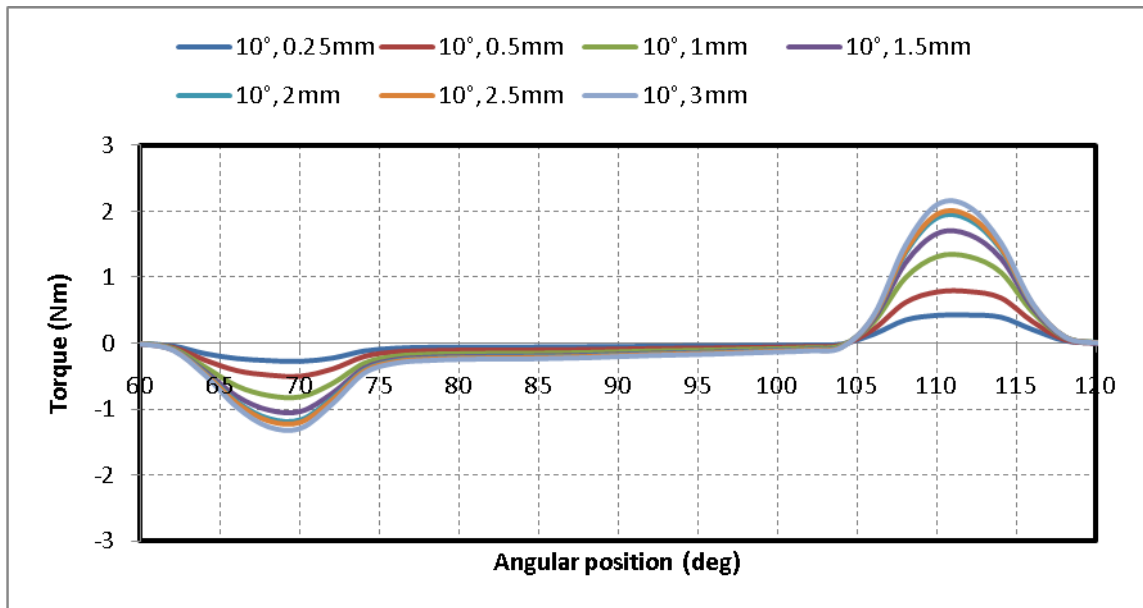
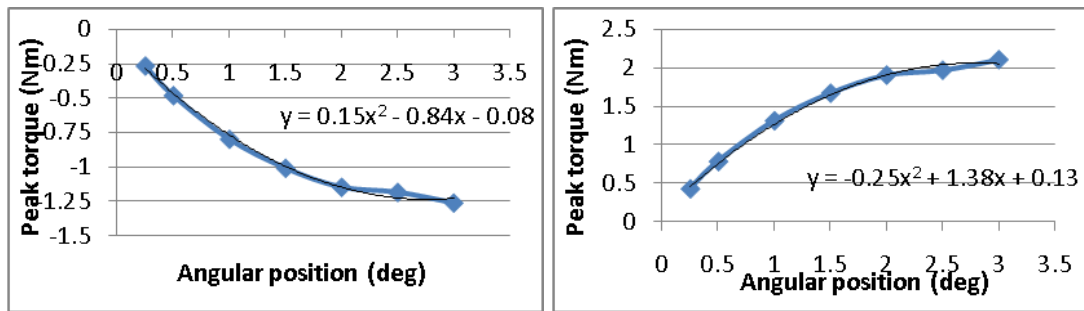


Fig. 4.31 Reluctance torque profile for an auxiliary slot of width 10° and varying depth



(a) Negative peak

(b) Positive peak

Fig. 4.32 The relation between the increase of depth and increase in peak torque for an auxiliary slot of width 10°

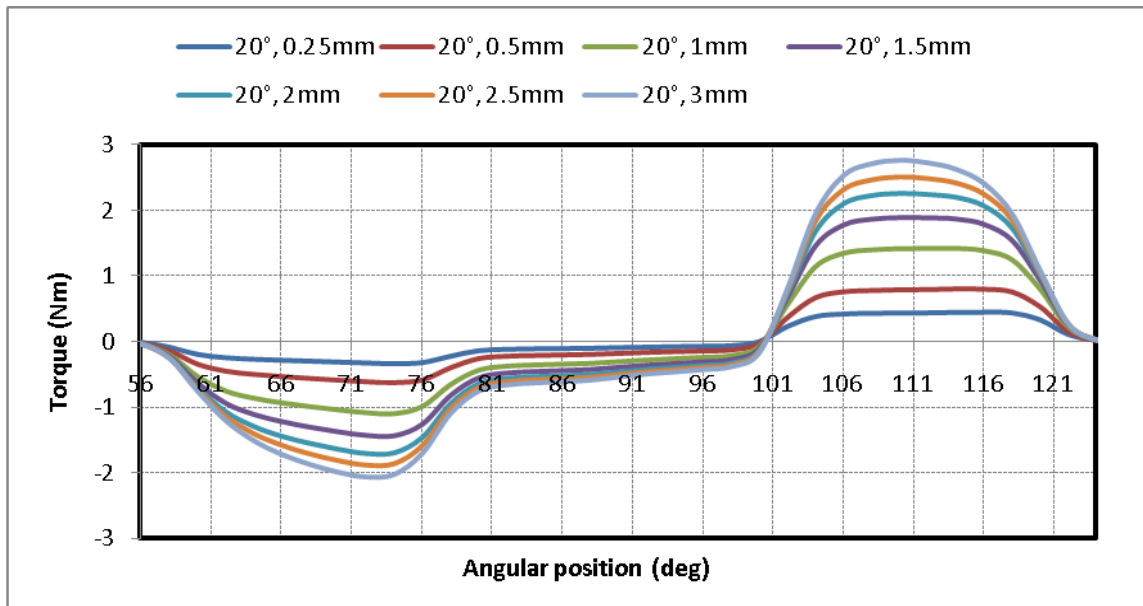


Fig. 4.33 Reluctance torque profile for an auxiliary slot of width 20°

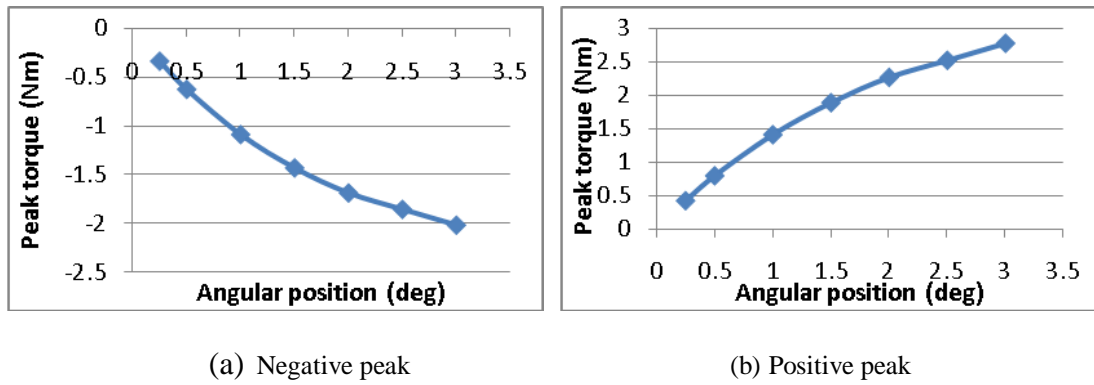


Fig. 4.34 The relation between the increase of depth and increase in peak torque for an auxiliary slot of width 20°

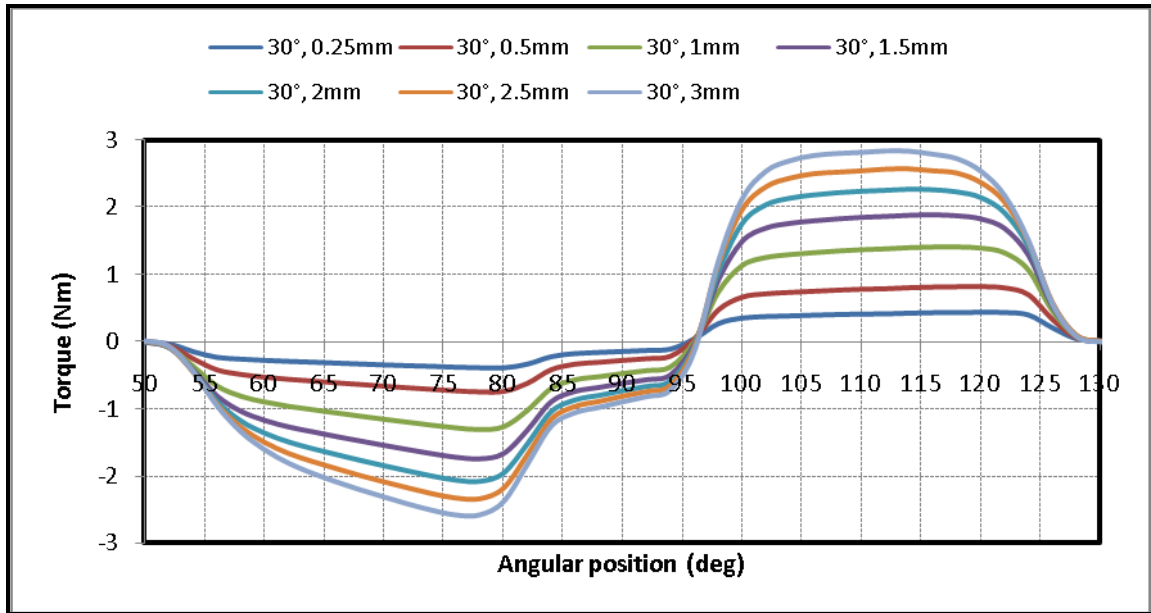
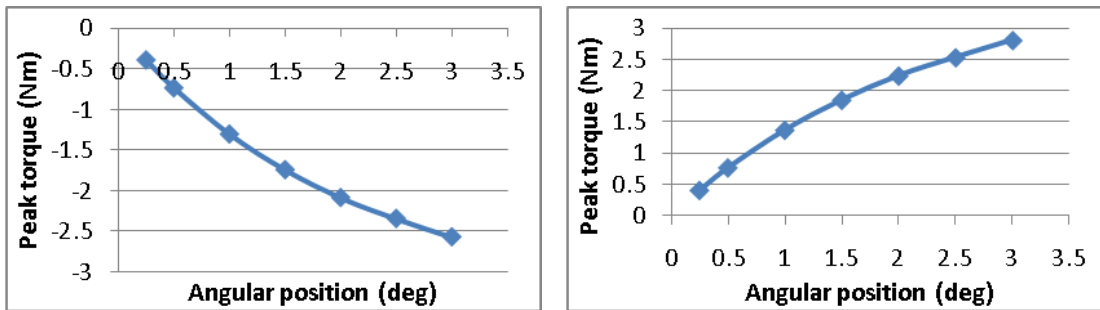


Fig. 4.35 Reluctance torque profile for an auxiliary slot of width 30°



(a) Negative peak

(b) Positive peak

Fig. 4.36 The relation between the increase of depth and increase in peak torque for an auxiliary slot of width 30°

4.9.2.2 Varying the arc width of the notches for a tapered magnet design

Fig. 4.35 to Fig. 4.42 show how the peaks in the reluctance torque profiles for a tapered magnet rotor design are affected with varying the arc width of the notch. The effect is similar to that when the magnet is not tapered (see section 4.7.3). An increase in the width of the slot has two effects on the reluctance torque peaks 1) increase in the width of the peak base 2) increase in the magnitude of the peak which is proportional with slot width but up to a certain width which is 10° . Beyond 10° the magnitude of the peak stays at a constant value that is dependent on the depth of the slot.

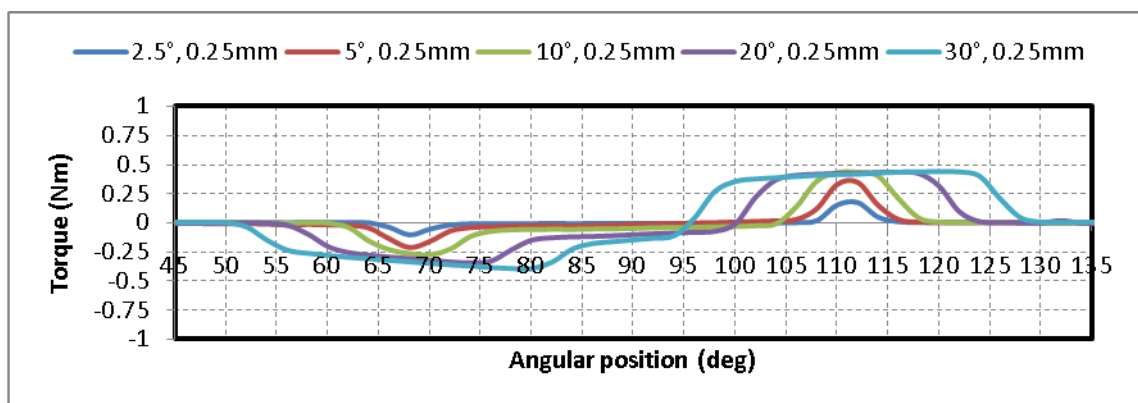


Fig. 4.37 The effect of slot width on the reluctance torque profile for a fixed depth slot of 0.25mm

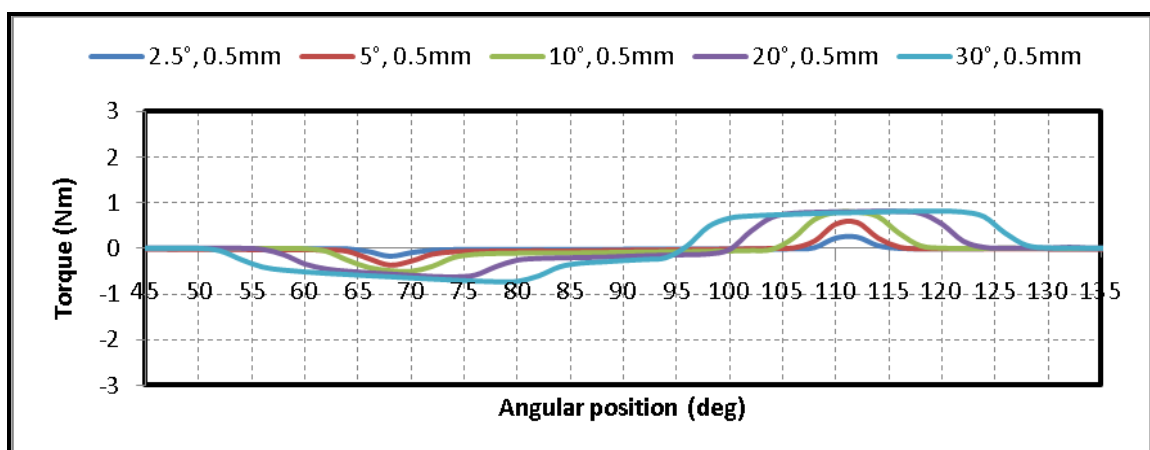


Fig. 4.38 The effect of slot width on the reluctance torque profile for a fixed depth slot of 0.5mm

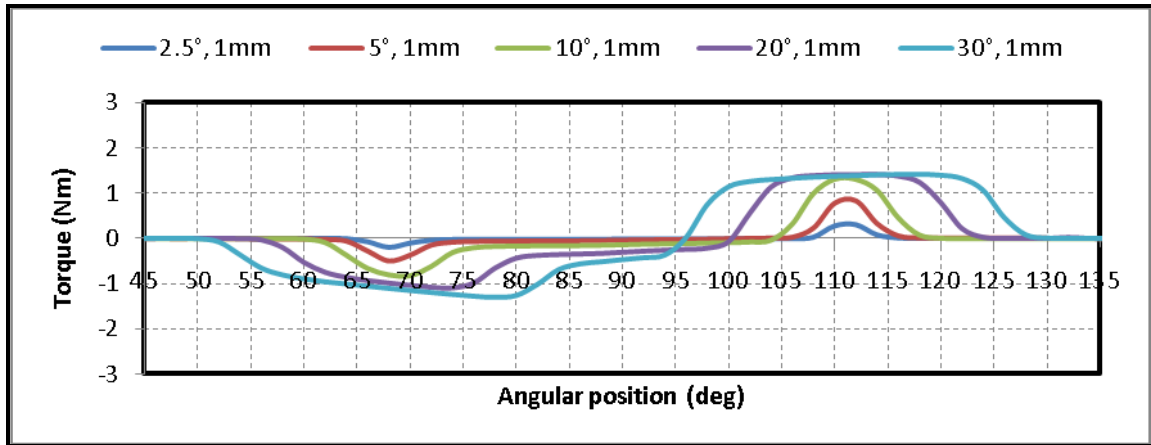


Fig. 4.39 The effect of slot width on the reluctance torque profile for a fixed depth slot of 1mm

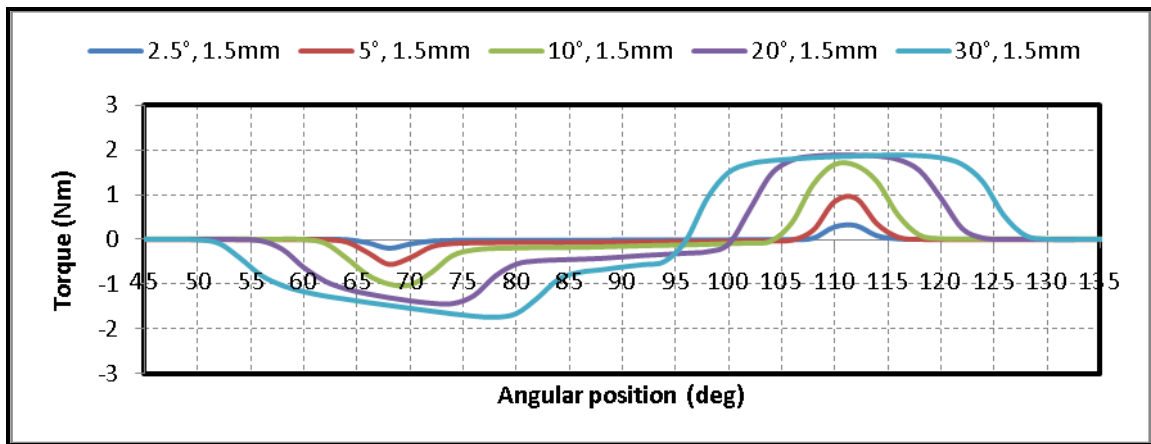


Fig. 4.40 The effect of slot width on the reluctance torque profile for a fixed depth slot of 1.5mm

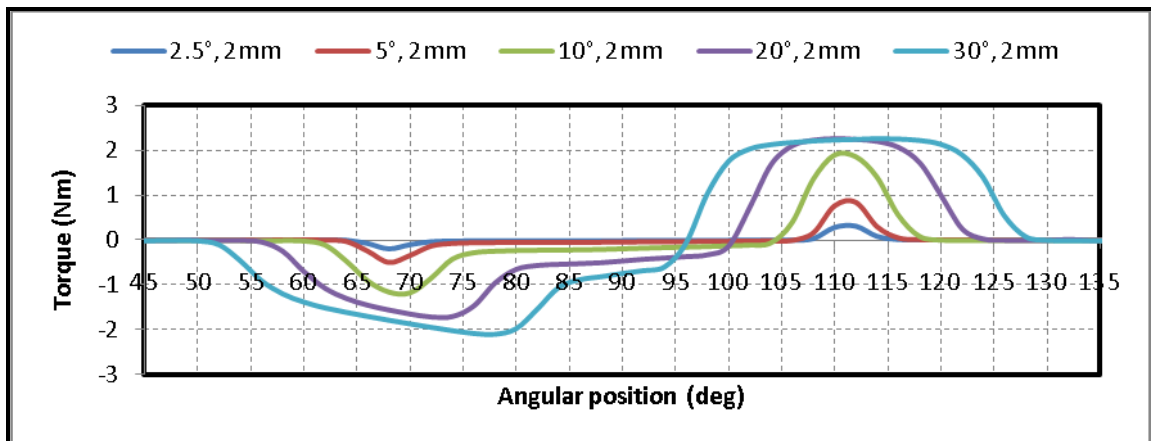


Fig. 4.41 The effect of slot width on the reluctance torque profile for a fixed depth slot of 2mm

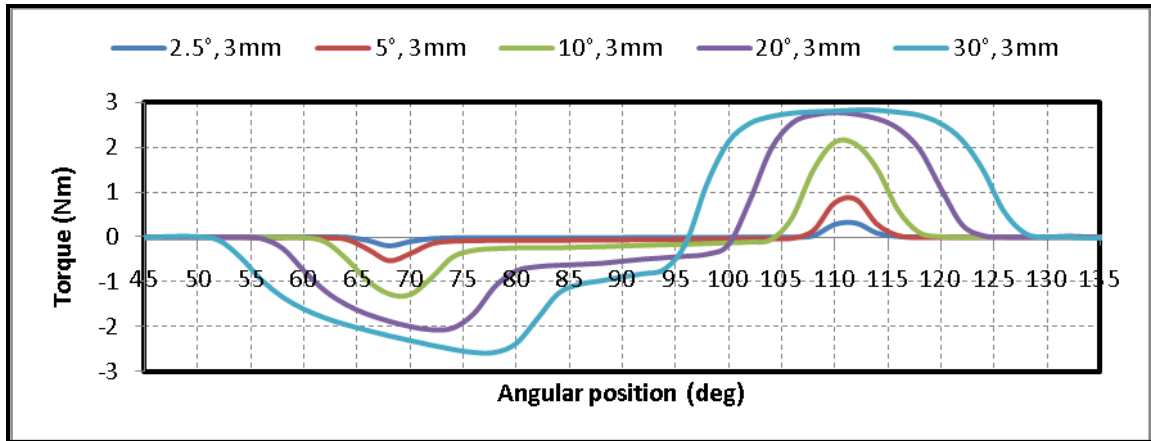


Fig. 4.42 The effect of slot width on the reluctance torque profile for a fixed depth slot of 3mm

4.9.3 Varying the arc width of the permanent magnet

The range in which the arc width of the permanent magnet can be varied is limited by the maximum allowed ripple in the back EMF shape. See chapter 3. Fig. 4.43 shows the range in which the width of permanent magnet is varied. All widths have a tapered rotor magnet with 0.5mm variation in the airgap. The resulting back EMF shape for each width is shown in Fig. 4.44.

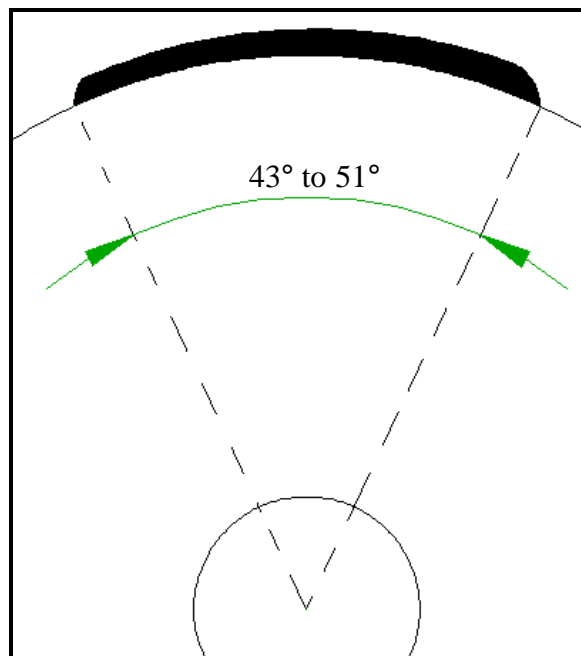


Fig. 4.43 varying the width of the permanent magnet

It can be seen from the results that the lowest ripple in the back EMF occurs when the magnet arc width is between 45° and 47°.

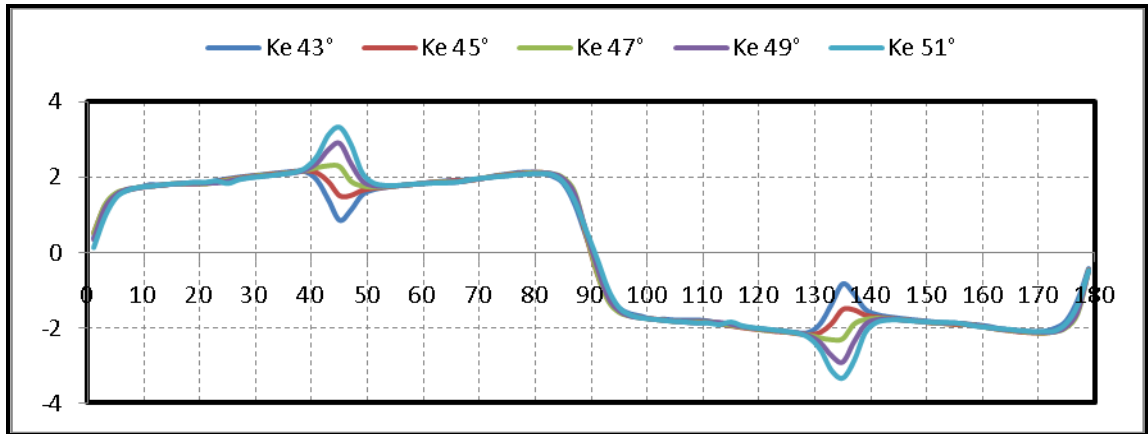


Fig. 4.44 the effect of varying the width of the permanent magnet on the shape of the back EMF

The variation of the magnet width also effect the angular distant between the positive and negative peaks in the manner shown in Fig. 4.45. The width of the permanent magnet determines the angular distance between the positive and negative peaks.

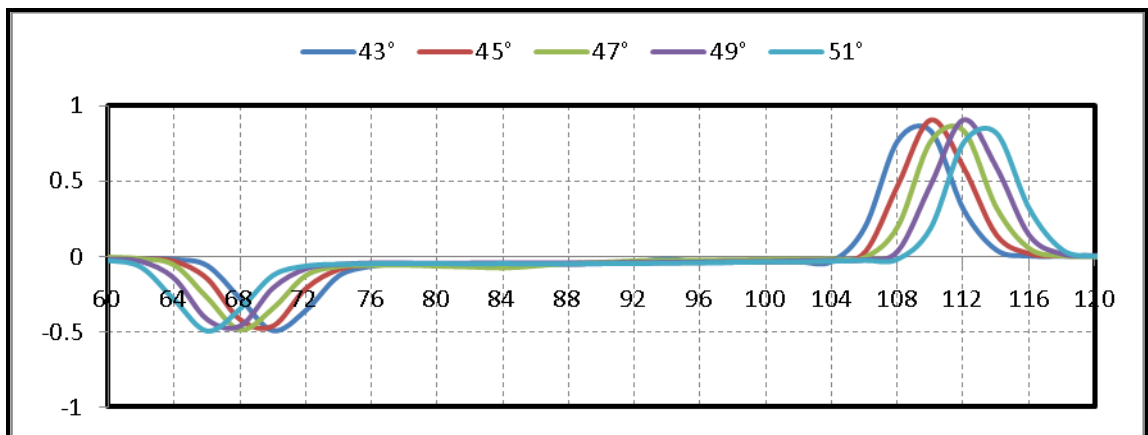


Fig. 4.45 The effect of varying the width of the permanent magnet on the angular distance of the reluctance torque peak.

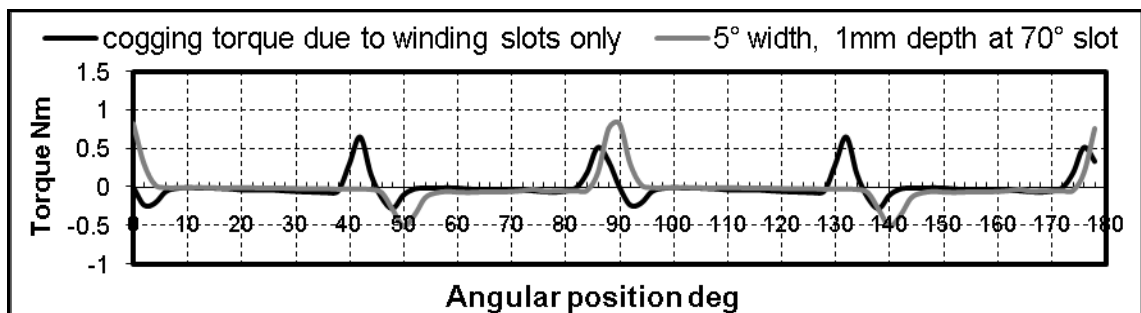
4.10 Synthesizing the open circuit torque profile for a motor with tapered magnets

It was shown in section 4.9.2.2 that tapering the magnet causes the negative peak of the notch torque profile to be lower than the positive peak. Therefore the tapered magnet design has the potential to employ one pair of notches to remove the null point and with

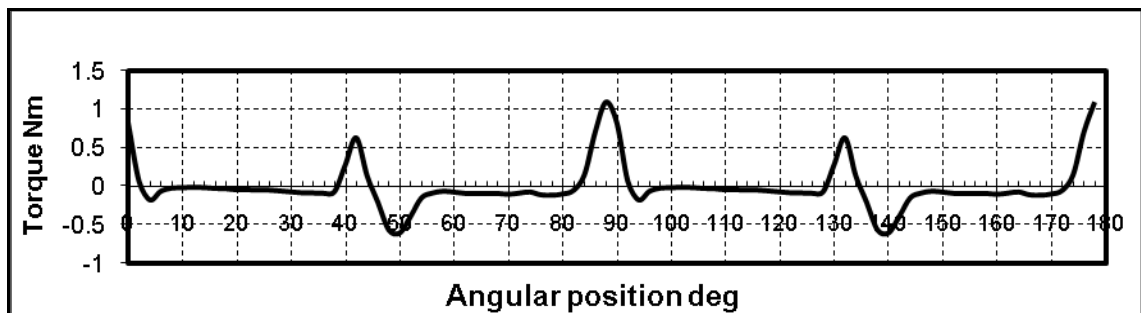
no introduction of significant ripple. This can be achieved with an appropriate combination of notch position and permanent magnet width.

In the following a notch of width 5° and depth 1mm is used as an example. Other notch size could be used depending on the desired level of starting torque. The widths of magnets are limited by the maximum allowable ripple in the back EMF shape. So based on Fig. 4.44 the range was chosen to be 43° to 51° in steps of 2° .

The example shows how a notch of 5° width and 1mm depth can be positioned appropriately to remove the null points in the open circuit torque profile. This is done for several magnet width designs.

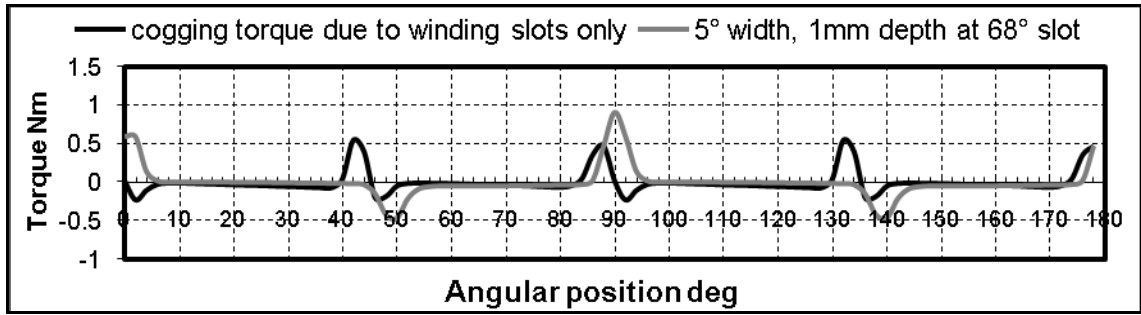


(a)

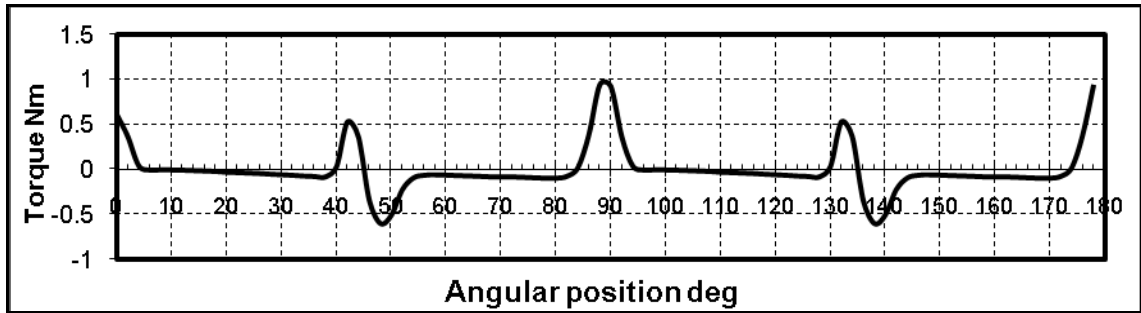


(b)

Fig. 4.46 Reluctance torque profile for 43° permanent magnet, a) Cogging torque and slot reluctance torque due to 5° width 1mm slot, b) Resultant reluctance torque profile.

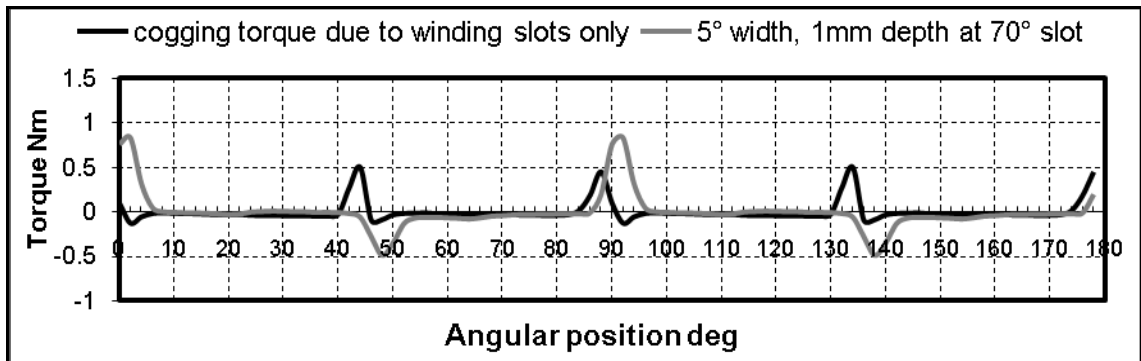


(a)

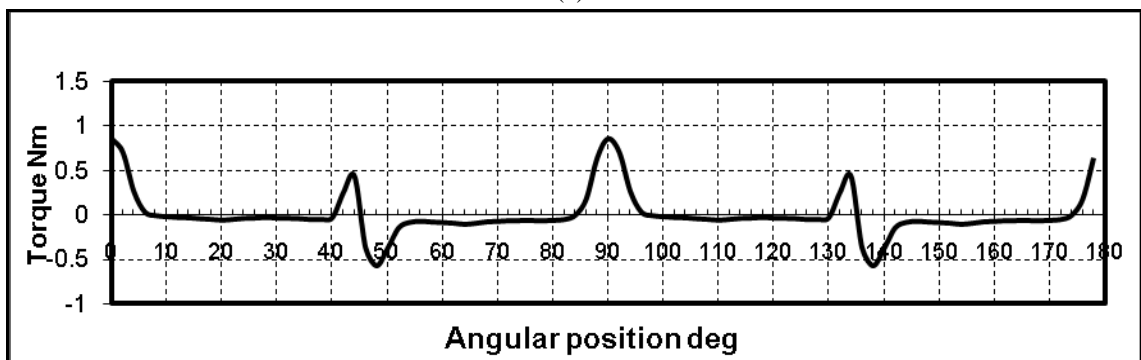


(b)

Fig. 4.47 Reluctance torque profile for 45° permanent magnet, a) Cogging torque and slot reluctance torque due to 5° width 1mm slot, b) Resultant reluctance torque profile.

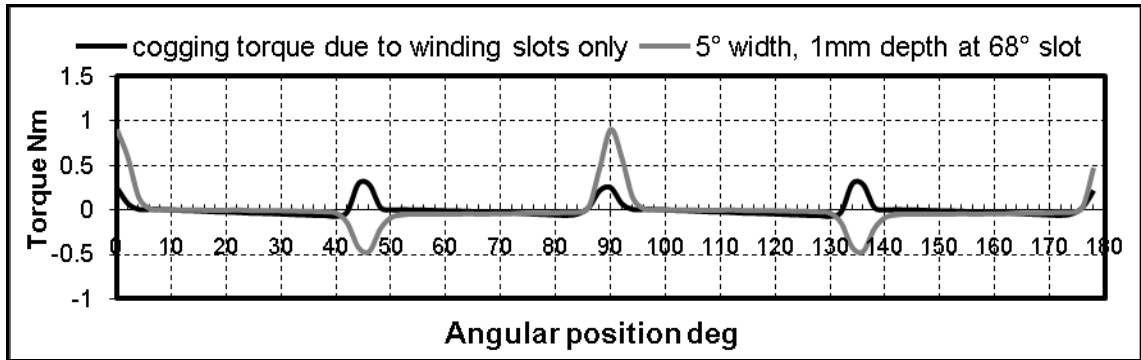


(a)

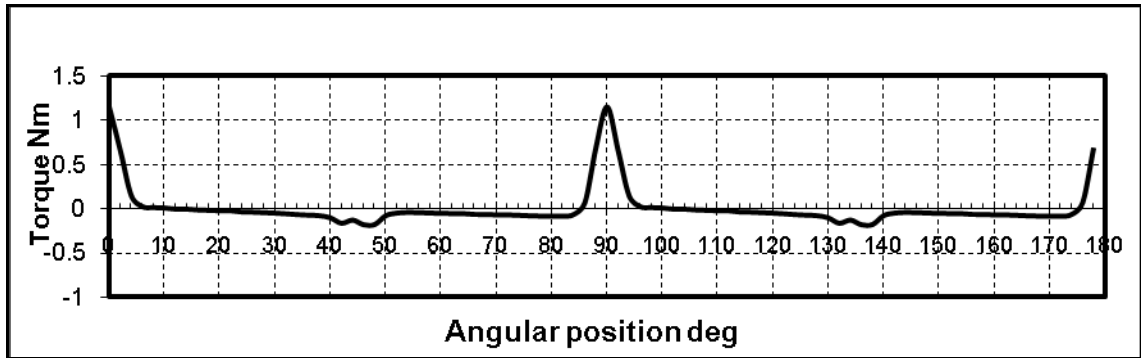


(b)

Fig. 4.48 Reluctance torque profile for 47° permanent magnet, a) Cogging torque and slot reluctance torque due to 5° width 1mm slot, b) Resultant reluctance torque profile.

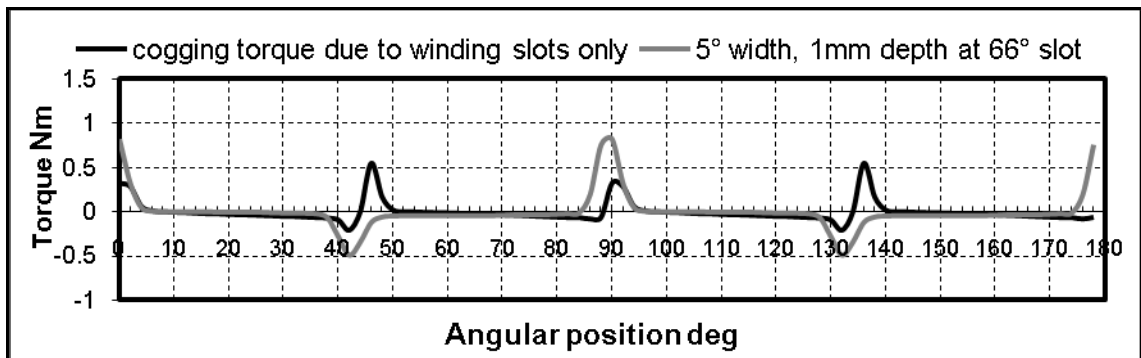


(a)

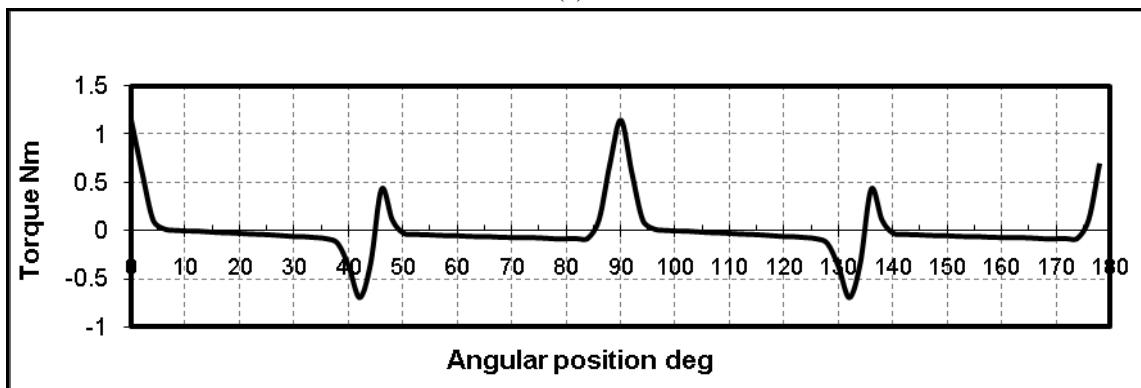


(b)

Fig. 4.49 Reluctance torque profile for 49° permanent magnet, a) Cogging torque and slot reluctance torque due to 5° width 1mm slot, b) Resultant reluctance torque profile.



(a)



(b)

Fig. 4.50 Reluctance torque profile for 51° permanent magnet, a) Cogging torque and slot reluctance torque due to 5° width 1mm slot, b) Resultant reluctance torque profile.

From the results it can be seen that placing the notch at a certain position in the stator has eliminated the null point in the open circuit torque profile for all designs. But it has resulted in a ripple around 45° except for one design, see Fig. 4.49. That is because 49° magnet width produces a reluctance torque profile with the negative peak placed at a position to cancel the ripple at 45° rotor position. Fig. 4.51 shows the corresponding motor topology.

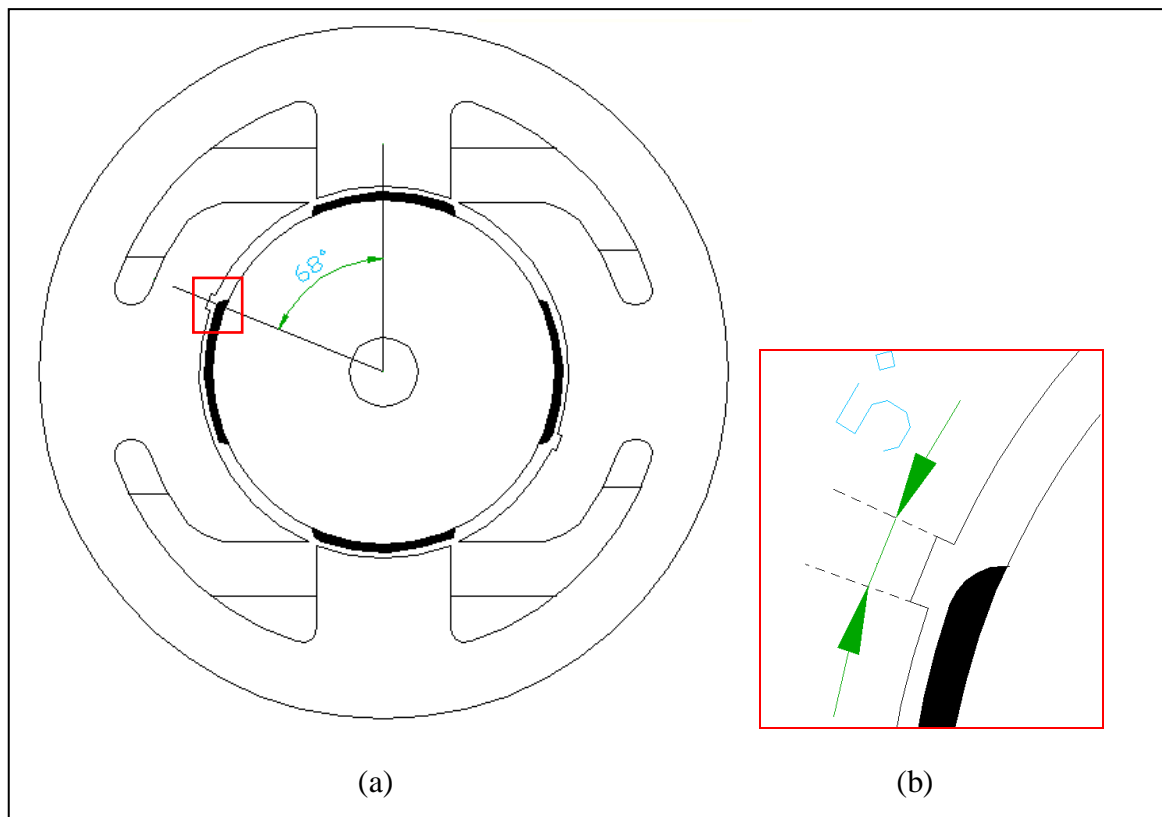


Fig. 4.51 tapered magnet of width 49° combined with a pair of slots at 68° with 5° width and 1mm depth to achieve optimum reluctance torque profile

4.10.1 Experimental results

Two methods of tailoring the reluctance torque profile for the single phase PM BLDC motor were presented. Both methods have produced the desired reluctance torque profiles, see Fig. 4.25 and Fig. 4.49 , however the first method relies on using notches in the stator iron and therefore it is simpler to prototype than the second method. Because in the second method the magnet need to be tapered by 0.5mm and that is more expensive. Therefore only the first method is experimentally validated in this section.

In order to verify the results presented in section 4.8 and Fig. 4.25 a scaled down motor has been built with the magnet width and notches proposed in Fig. 4.24. See Fig. 4.52 and Fig. 4.53

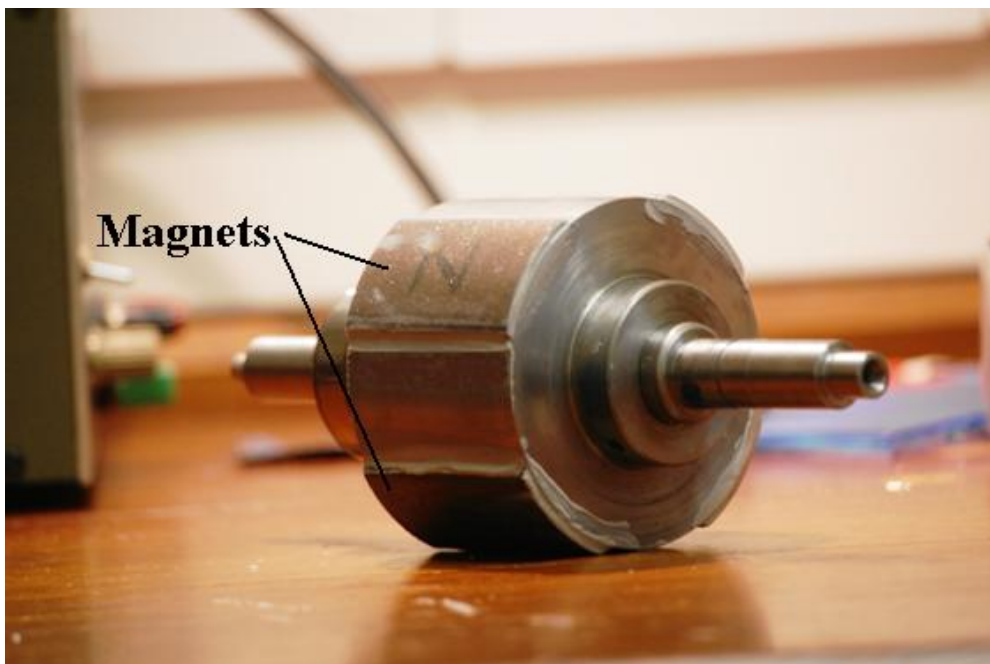


Fig. 4.52 Rotor with surface mounted magnets

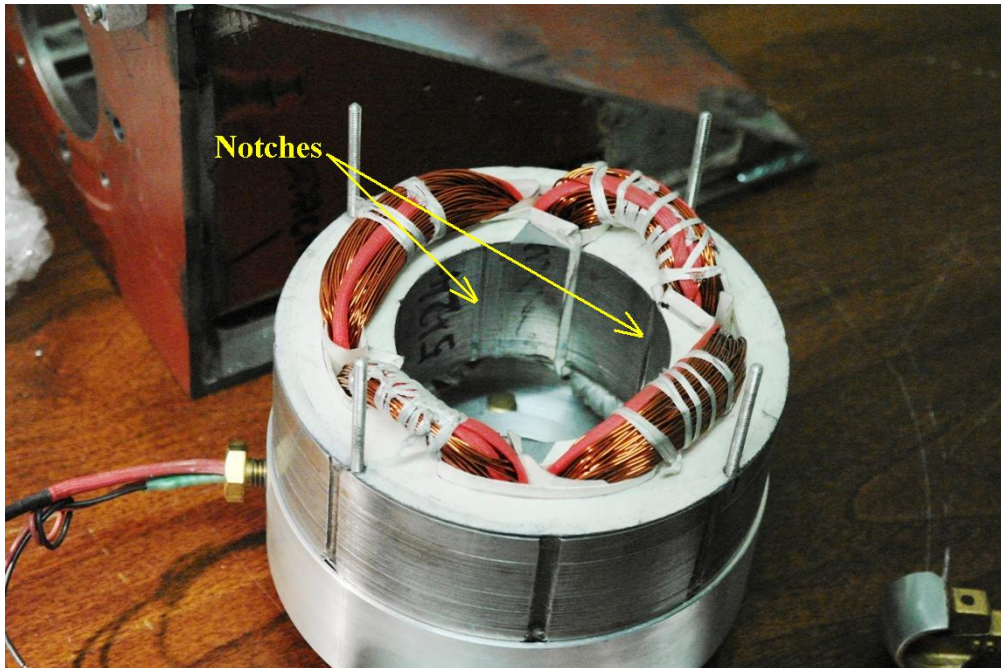


Fig. 4.53 Stator with the proposed notches

To cut the cost of the experimental set up, the motor was manufactured with half the core length, and to eliminate the risk fracturing the magnets while machining the 3mm chamfers on the edges of the magnets, a bonded magnet were chosen. As result of this modifications the measured open circuit torque will be multiplied by a scaling up factor. It is known that the torque is directly proportional with core length and the square of the air gap flux density. Since the core length is halved and a bonded magnet with remenace flux density of 0.7T was used (instead of 1.2T simulated in the FEM), the measured torque will be multiplied with a scaling factor which is calculated as below:

$$\text{Scaling factor} = 2 \times \left(\frac{1.2}{0.7}\right)^2 = 1.7$$

The open circuit torque was measured with a torque transducer positioned between the dividing head and the motor as shown in Fig. 4.54.

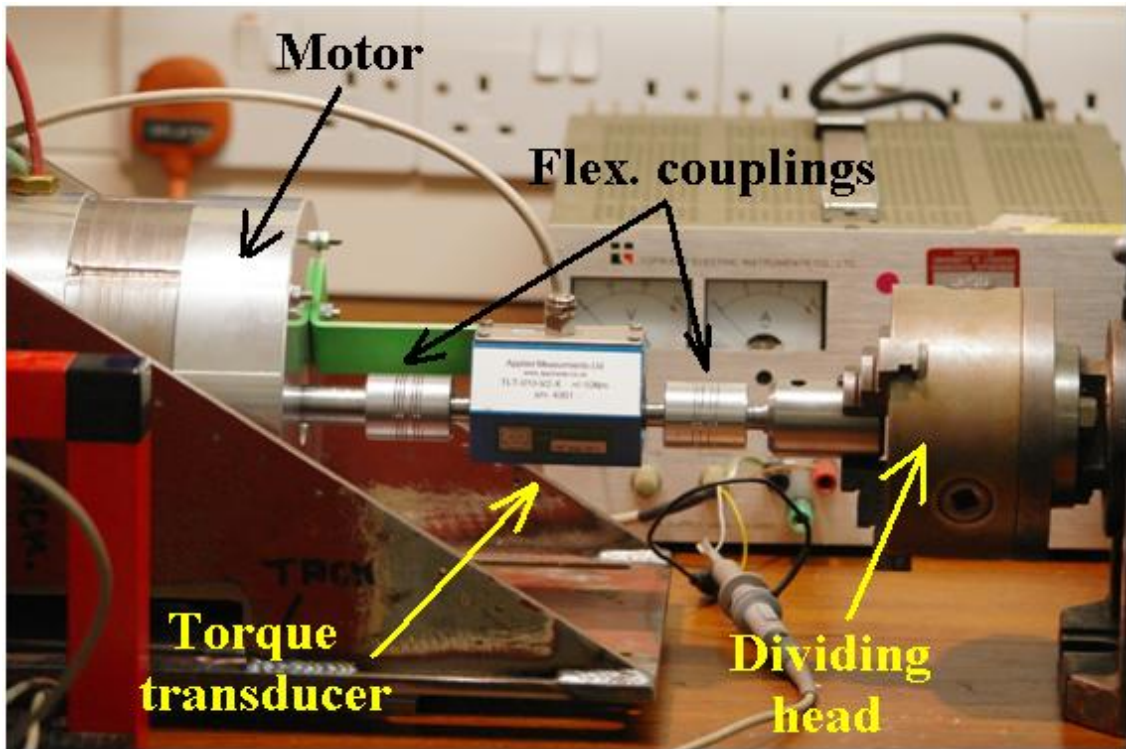


Fig. 4.54 Experimental set up for measuring the open circuit torque

The reading from the torque transducer was taken at every 5° mechanical for one complete electrical cycle. See appendix 9.8. After multiplying the measured torque with the scaling factor the results were compared with the FEM predicted results as shown in Fig. 4.55.

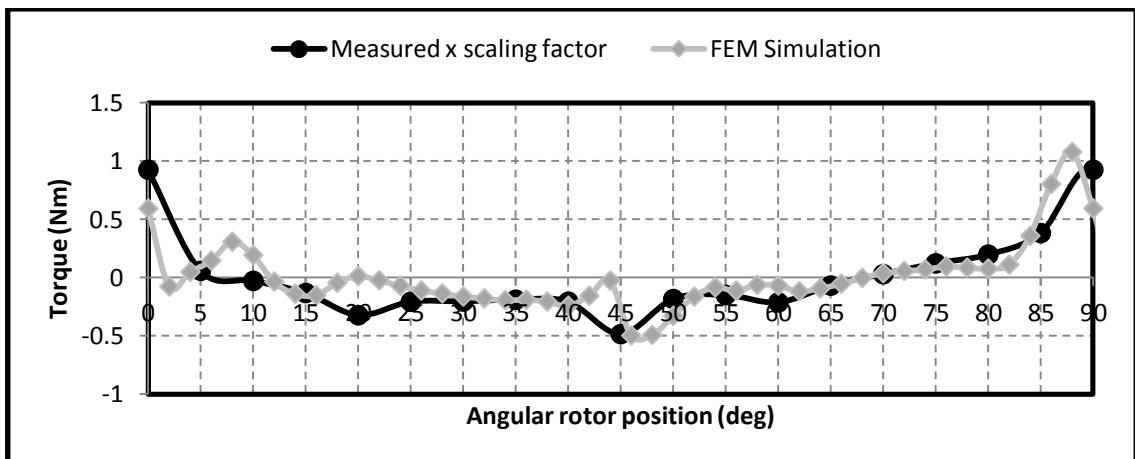


Fig. 4.55 Comparison between the predicted and measured open circuit torque profiles

It can be seen that the measured open circuit torque matches very well with predicted FEM results. The small discrepancy between the two results could be due to human reading error and/or the accuracy of the torque transducer.

4.11 Conclusions

This chapter has demonstrated that the property of superposition in the reluctance torque profile does exist for independent modifications in the stator iron (i.e. notches or taper). Using this property, it was shown that employing asymmetrically distributed notches with different depths and widths can enhance the open circuit torque of a single phase BLDC motor. Using the notches has allowed us to synthesize the compensating reluctance torque that has enhanced the starting torque capability and reduced the slot cogging torque between the null points in the open circuit torque profile. Experimental results were obtained to validate the predicted FEM results. It was shown that there is a good match between the measured results and the predicted FEM results with small discrepancy. The properties of the notches for tapered and non-tapered rotor designs were investigated and the relationship between the notch dimension and magnitude of peak torque was established. For a tapered rotor magnet configuration it was found that by using one pair of notches that are positioned at an appropriate position will result in a reluctance torque profile without null point and low torque ripple.

5. Review on Encoderless Position Sensing Methods for PM BLDC Motor

5.1 Introduction

In conventional DC machines the commutation function is performed by the commutator and brushes. These act as both position sensors and switches. The mechanical commutator has some disadvantages which are speed limitation, noise and wear. Overcoming those disadvantages has been a major reason behind the development of brushless DC (BLDC) motors. BLDC motors and their drives are penetrating the market of home appliances, and automotive applications in recent years because of their high efficiency, low noise, compact form, reliability, and low maintenance.

The commutation in BLDC motors is performed by power electronic devices forming an inverter bridge. Position sensing is an essential requirement since switching of the power electronic devices has to be synchronised with the rotor position. Unlike the induction motor which can be easily operated without rotary sensors. However the use of speed control or Field oriented and direct torque control algorithms requires the need for sensors to be reintroduced. The wound field synchronous machine can also be operated without rotary sensors, although this results in a limited dynamic performance. Traditionally BLDC motors are commutated with an inverter controlled by position sensors. These position sensors are mounted on the shaft to produce the required current commutation signal. However there are some concerns about using this type of position sensor due to its added cost and reliability issues and as a result several researches have been carried out to eliminate this type of sensors and find methods to detect rotor position without an encoder that limits the operating range of the motor.

Frus [55] was the first to research into eliminating the rotor position sensor for brushless DC motors using a technique called “waveform detection”. The technique was based on analysing the current waveform to predict the rotor position. Since that time, several research works in this area has been conducted. Some authors use the title “indirect position sensing” which was justified by the observation that position information was not directly extracted from the rotor shaft. Other authors have used the term “direct position sensing” because position information was obtained directly from the machine not from a separate external encoder [1]. Recently most of the authors refer to this technology as a “Sensorless control method”. But the term “Sensorless control” can be misleading because some sort of sensing is required (i.e current or voltage) for determining rotor position. In this chapter the term “Encoderless control” will be used instead as it gives a more accurate representation of the technique. In any Encoderless method, sensing is required but not from a conventional shaft attached encoder. This chapter presents a review on the previous methods used to eliminate the rotor position sensor.

Encoderless control involves the application of signal processing techniques to extract the necessary information from voltage/currents in the machine. These can be measured using simple rugged transducers which maybe already present in the drive system for current control strategies and fault detecting [56].

Encoderless methods can be broadly categorised into two categories 1) methods based on the back EMF of the brushless DC motor, 2) methods based on motor saliency characteristics. In the following a review on the main methods that fall under these two categories are presented.

5.2 Back EMF based techniques

The rotation of the permanent magnet rotor will cause a change in the magnetic field applied to the stator winding of the BLDC motor. From Faraday's law of induction this will cause a voltage to be induced across the stator winding which is called the back EMF or motional EMF. This waveform is related to the rotor position and hence rotor position information can be obtained.

There are two main problems for encoderless methods based on the back EMF [57], 1) it is difficult to measure the back EMF because of the rapidly changing current. 2) The back EMF is proportional to speed and hence at zero and low speed the magnitude of the back EMF is not sufficient to extract rotor position information. One solution to the starting up problem is the open loop acceleration of the motor from stand still to a speed where the back EMF is sufficient and above the noise floor. The ramping parameters, voltage and frequency, should be carefully selected to match the starting torque of the motor. One main problem is that the open loop acceleration may cause the motor to start rotating in the reverse direction. Below are some of the main encoderless methods that depend on the back EMF waveform.

5.2.1 Zero crossing points

This is the most common back EMF based encoderless method. In a typical three-phase wye connected BLDC motor utilizing six-step commutation, current flows in only two phases at any one time. This leaves the third phase available for commutation timing by sensing back EMF. Commutation timing is determined when the unused phase back EMF reaches its zero potential point. This is referred to as “zero crossing”.

This method was first reported by Iizuka [58]. The simplest form of this method can be explained referring to Fig. 5.1. The zero crossings of the back EMF are an attractive feature that can be used as a reference for current commutation.

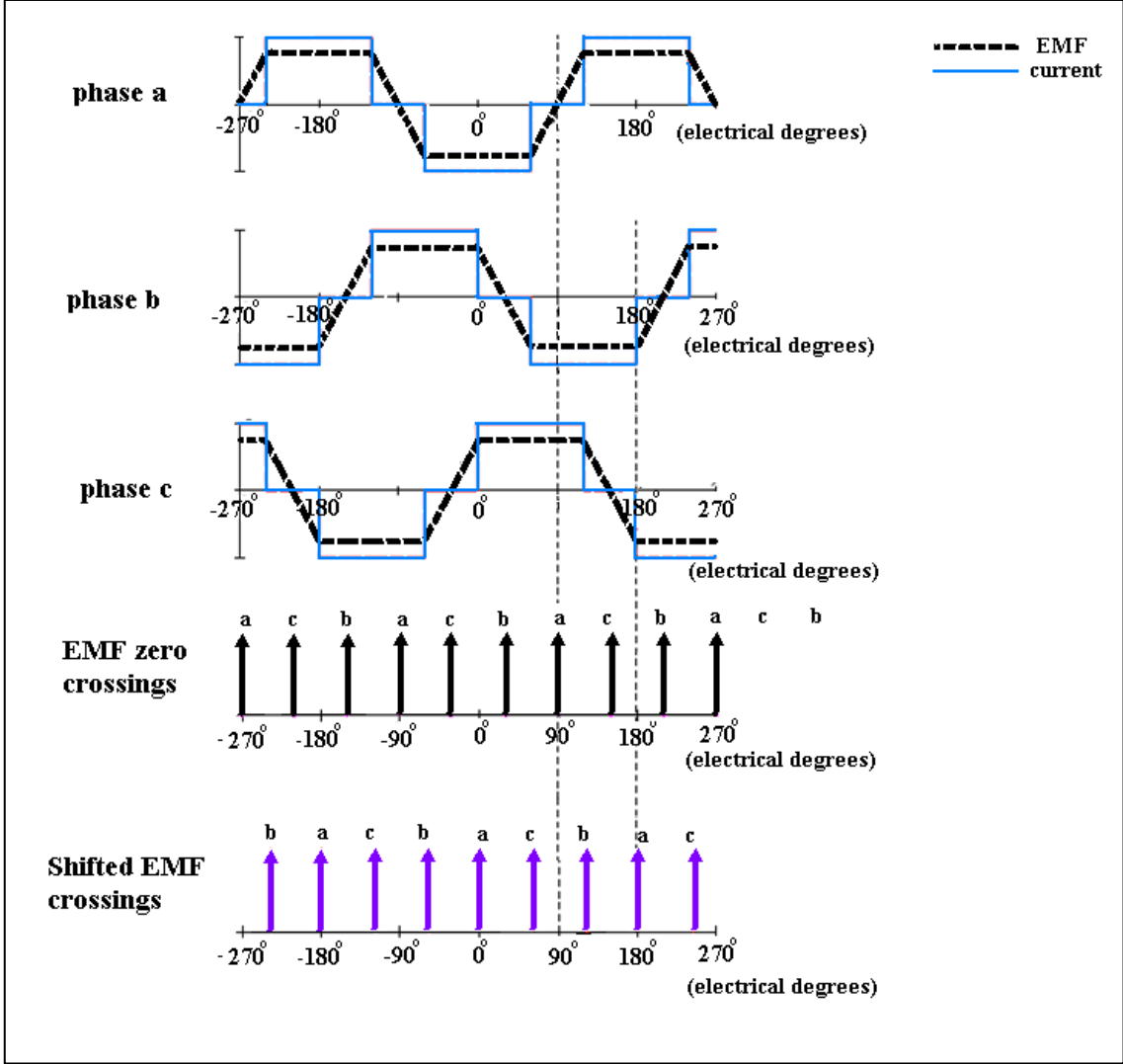


Fig. 5.1 Using the zero crossings of back EMF waveform for sensorless or encoderless control

For example from Fig. 5.1 the zero crossing of the back EMF of phase *a* at 90° can be used to switch the current in phases *b* and *c*. In addition to low speed limitation the zero crossing method has a number of other limitations:

- 1) The requirement to phase shift the zero crossing points by 90° (for a three phase BLDC motor only) In the original work, the phase shifting was achieved by us-

ing three separate R–C networks that produce the necessary phase shift only when the working frequency is sufficiently high. The dynamic performance of the control is limited because of the heavy filtering inherent in the signal processing.

- 2) It is assumed that there is a very rapid decay of current when a phase is switched off, so the voltage appearing across the terminals of the unexcited phase is equal to the back EMF. This assumption may not be true at high speeds. Therefore, there is an upper limit on the useful speed range obtainable with this form of back EMF sensing [59].

5.2.2 Sensing from the third harmonic

An improvement to the back EMF zero crossing method mentioned above was introduced by Moriera [60]. His method has the advantage of reducing the filtering requirement because of the utilization of the third-harmonic component in the back EMF waveform. Fig. 5.2 shows the three windings of a star-connected machine with accessible star point s . An additional star connection of three identical resistors is connected between the phase ends a , b , c , and a separate star point n . Assuming that the resistances and inductances of the three machine windings are identical and that the phase back EMFs are as shown in Fig. 5.3, it can be seen that the voltage between the two star points n and s is equal to the mean of the three phase EMFs.

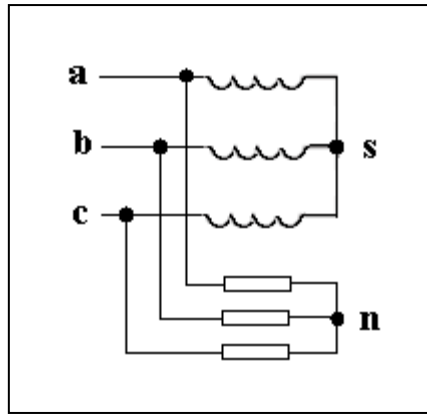


Fig. 5.2 Star-connected machine with resistor network

Fig. 5.3 shows the voltage v_{ns} and its relationship to the rotor positions for switching between phases. The v_{ns} waveform has a frequency three times that of the fundamental component of any of the phase back EMFs, and therefore, it is referred to as the “third harmonic” of back EMF.

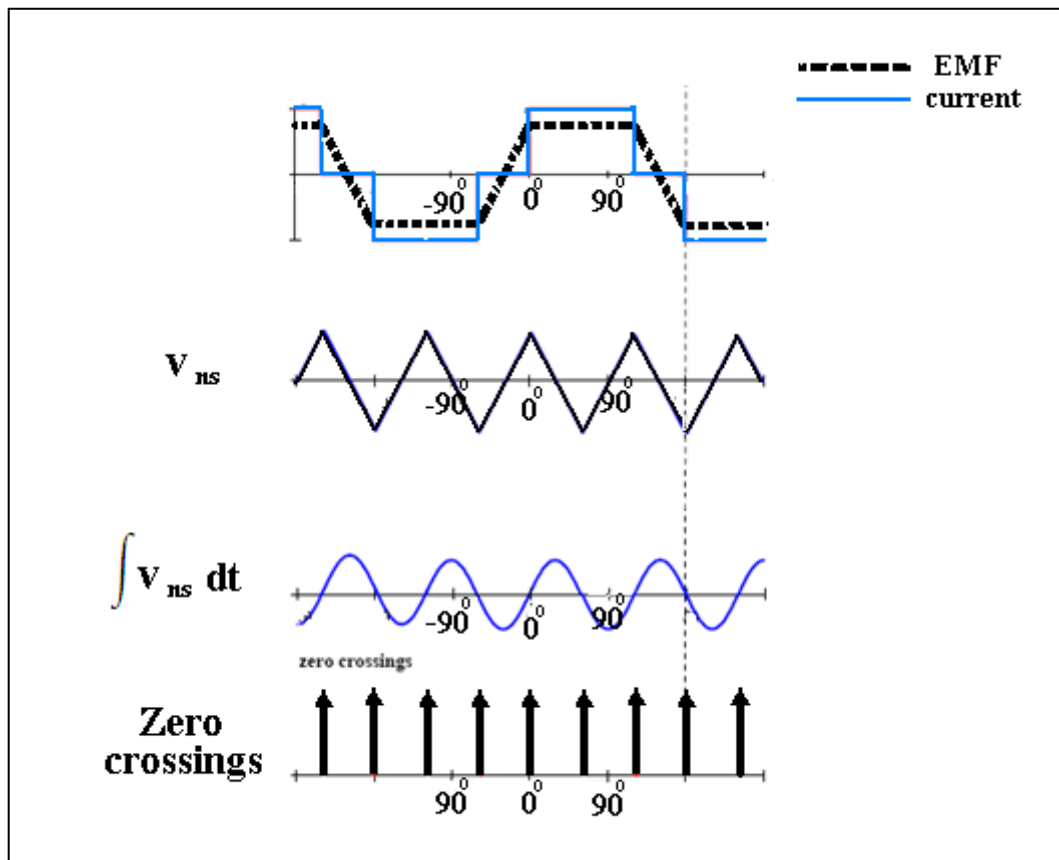


Fig. 5.3 Commutation signal from the 3rd harmonic of back EMF

The waveform is shifted through a rotor position of 30° electrical by integration. The zero crossings of the integrated waveform correspond to the rotor positions at which excitation must be switched between the phases, and therefore, the zero crossings are suitable excitation switching signals. During each cycle of excitation, the v_{ns} waveform passes through three cycles. Therefore, the excitation trigger signals must be synchronized with the appropriate phase excitation change, depending on the required directions of torque and speed. The trigger signals are synchronized once per excitation cycle by identifying a suitable reference position, such as the positive-going zero crossing of back EMF in phase *a*. In comparison to the basic method of position sensing using back EMF (see section 5.2.1), The third-harmonic method has the following advantages.

- 1) There is a reduced filtering requirement, because the integration (low-pass filtering) function is performed on a signal, which has a frequency three times that of the fundamental signal. The lighter filtering improves the dynamic performance.
- 2) Operation at higher speeds is possible in principle, because the voltage v_{ns} can be recovered even if current continues to flow in the third (unexcited) phase.

An important limitation on the third-harmonic approach is the initial assumption in the analysis that the inductance is equal in all three phases. This assumption is usually valid for surface-mounted magnet machines, but is not correct for salient permanent magnet motor. This can cause errors in position information due to rapidly changing phase currents and extra low-pass filtering may be needed. The main disadvantage is the relatively low value of the third harmonic voltage at low speed [61].

Back EMF integration method

In this technique the rotor position information is obtained by integrating the back EMF of the unexcited phase [62, 63]. The integration is based on the absolute value of the open phase's back EMF. The period of the integration starts when the back EMF crosses the zero level and stops at a set threshold before the start of the commutation. As the back EMF is assumed to vary linearly from positive to negative (trapezoidal back EMF assumed), and this linear slope is assumed to be speed insensitive, the threshold voltage is kept constant throughout the speed range. Once the integrated value reaches the threshold voltage, a reset signal forces the integrator output to zero. The reset signal is kept on long enough to ensure the integrator does not start until the residual current in the open phase has passed a zero crossing. The integration approach is less sensitive to switching noise, automatically adjusts to speed changes, but the low speed operation is poor [64].

5.2.3 Freewheeling diode conduction method

This method can be categorized under the methods that uses back EMF for rotor position detection. It uses indirect sensing of the zero crossings of the phase back EMF to obtain the switching instants of the BLDC motor [65]. The method is applicable to a 120° conducting wye-connected three phase BLDC motor. The indirect sensing of the back EMF is achieved by monitoring the zero crossings of the current in the freewheeling diodes. The zero crossings of the current coincides with the zero crossings of the back EMF. The biggest disadvantage of this method is the requirement of six additional current sensors and possibly six isolated power supplies for the comparator circuitry for each free wheeling diode.

This system only produces discrete position information and therefore would only be suitable for use with trapezoidal permanent magnet BLDC motors. However, it does have the advantage over the back EMF techniques that it will work at lower speeds since there is no requirement for direct voltage measurements. The sensing circuit is relatively complicated [61].

5.2.4 Observer based methods

An observer based state estimator provides another method of encoderless control for BLDC motors. In this method, the dynamics of the motor are modelled in state space and the mathematical model is run in parallel with the real machine. A block diagram of the observer is shown in Fig. 5.4 [66], the motor model has the same inputs as the real machine and the difference between its outputs and the measured outputs are used to force the state estimation to converge. Errors can occur because of measurement imperfections or because of inaccuracies in the model. The phase voltage is the input and the current the output, besides the current output all the variables in the state observer are accessible including those which are difficult or expensive to measure (e.g. rotor position, θ , or phase flux linkage, λ). The estimated current output of the machine model is compared with the actual phase current and the error is used to adjust the estimator feedback gain in order to correct the algorithm of the observer.

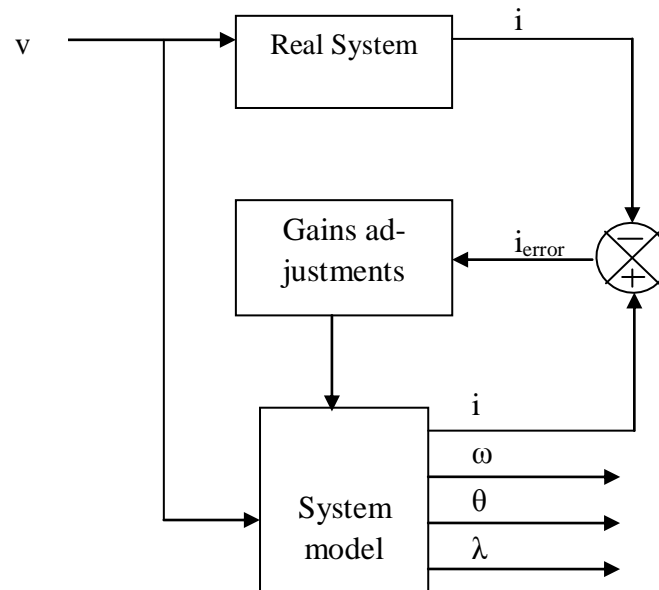


Fig. 5.4 Observer based position estimator model

One commonly used observer for encoderless control is the extended Kalman Filter (EKF), it estimates the internal states of a dynamic non-linear systems with inherent robustness against parameter variation [67]. The theory of EKF technique have been deeply studied in the literature [68]. Basically EKF has two main stages [69], the first is the estimation stage which utilises the system mathematical model. The next stage is the correction stage which corrects the estimates using the weighted (by the ‘Kalman Gain’) difference between the predicted and actual output vectors.

There exist many other observers, as well as the EKF. These are all based on essentially the same principle, but differ slightly in their operation. They include Luenberger based observer [70] and sliding mode observers [71-73].

The advantages of observer based methods are that it does not require additional diagnostic pulse (i.e. injecting a high frequency signal) and does not have any inherent speed limitations. However, the scheme requires a substantial real-time computing with a fast and powerful processor. The method needs knowledge of load parameters and an

accurate machine model. Also, the estimator takes time to converge and the performance may be unreliable during the convergence interval.

5.3 Inductance variation encoderless methods

An alternative method of position sensing depends on monitoring a position dependent inductance (variation of inductance due to saliency) of the main winding or search coils. The inductance is measured by observing the rate of change of a high frequency injected current in the main winding/search coils. Since the rate of current change depends on the inductance of the winding, and this inductance is a function of rotor position (due to rotor saliency) and winding current, then rotor position can be deduced from the change in amplitude of the high frequency current. Such a scheme has the important advantage of zero speed operation where there is no back EMF. Sensing of rotor position by inductance variation in the brushless PM machine is complicated [57] because of the following two reasons:

- 1) There is no inherent saliency in a machine with surface-mounted magnets, so any variation in the inductance will be only due to magnetic saturation.
- 2) The rate of change of current in the PM machine can be affected by the back EMF.

Despite these obvious difficulties, there have been numerous attempts to use inductance variation to detect rotor position in PM machines.

The first application of inductance methods addresses the problem of starting, including identification of the rotor position at zero speed. Initial identification of rotor position is particularly important in applications where reverse starting rotation is unacceptable. Exploratory voltage signals have been applied to the phase windings of a salient PM machine that was stationary [74-78]. The resulting current amplitudes depended on the incremental inductance, and therefore the rotor position can be deduced.

5.3.1 Current waveform detection techniques

The fundamental idea behind this technique is that the rate of change of current depends on the incremental inductance of the phase circuit, and the incremental inductance is in turn a function of rotor position and phase current. Acarnley [79] was first to apply this method to detect rotor position in variable reluctance stepping and switched reluctance motors, since the variation of incremental inductance is largest in these types, and he applied this technique successfully to the variable reluctance stepping motor. This technique is applicable to any motor (including the hybrid stepping motor), in which the winding inductances vary with rotor position. The important advantage of this method is the zero speed starting ability.

For a doubly salient stepping motor (with windings concentrated on the stator teeth or poles) the mutual coupling between phases is negligible, so the voltage equation for one phase can be written in terms of the current i and flux linkage ψ for that phase as in equation 5.1

$$v = iR + \frac{d\Psi}{dt} \quad 5.1$$

where R is the resistance of the phase winding, and, since the flux linkage is a function of phase current and rotor position θ equation 5.1 can be represented as

$$v = iR + \frac{d\Psi}{di} \cdot \frac{di}{dt} + \frac{d\Psi}{d\theta} \cdot \frac{d\theta}{dt} \quad 5.2$$

$$v = iR + L \frac{di}{dt} + \frac{d\Psi}{d\theta} \cdot \frac{d\theta}{dt} \quad 5.3$$

where $L = \frac{d\Psi}{di}$. Rearranging 5.3 to give an expression for the rate of change of phase current with time will give

$$\frac{di}{dt} = \frac{v - iR - \frac{d\Psi}{d\theta} \cdot \frac{d\theta}{dt}}{L} \quad 5.4$$

The incremental inductance L appearing as the denominator of equation 5.4 is rotor-position dependent, so the rate of change of current is also related to rotor position. However, this relationship is complicated by the dependence of incremental inductance on current and by the appearance of back EMF term $\frac{d\Psi}{d\theta} \cdot \frac{d\theta}{dt}$. Errors can arise from these effects when the current gradient is used for rotor position detection, but by careful matching of the detection technique to the drive circuit and operating mode [80] the errors can be minimized or eliminated.

Aarnley suggested that if the back EMF and iR drop can be neglected, then L can be obtained from equation 5.4, and consequently the rotor position from L . Aarnley proposed three methods of position sensing, two of which are based on current waveform monitoring in the active phase. The methods on active phase current monitoring specifically applies to the current controlled mode of operation of a stepping motor when the current is increasing and decreasing at a high frequency due to chopping or PWM. The current rise and fall times can be derived from equation 5.4 as follows

$$t_{rise} = \frac{Ldi}{v - iR - \frac{d\Psi}{d\theta} \cdot \frac{d\theta}{dt}} \quad 5.5$$

$$t_{fall} = \frac{Ldi}{iR - \frac{d\Psi}{d\theta} \cdot \frac{d\theta}{dt}} \quad 5.6$$

The major problem of waveform detection techniques is the restriction to low speed applications, since otherwise the back EMF errors affect the accuracy severely, see Fig. 5.5. The control flexibility is also limited due to the requirement for a fixed average current during chopping. Aarnley suggested monitoring t_{rise} for maximum immunity from back EMF effects.

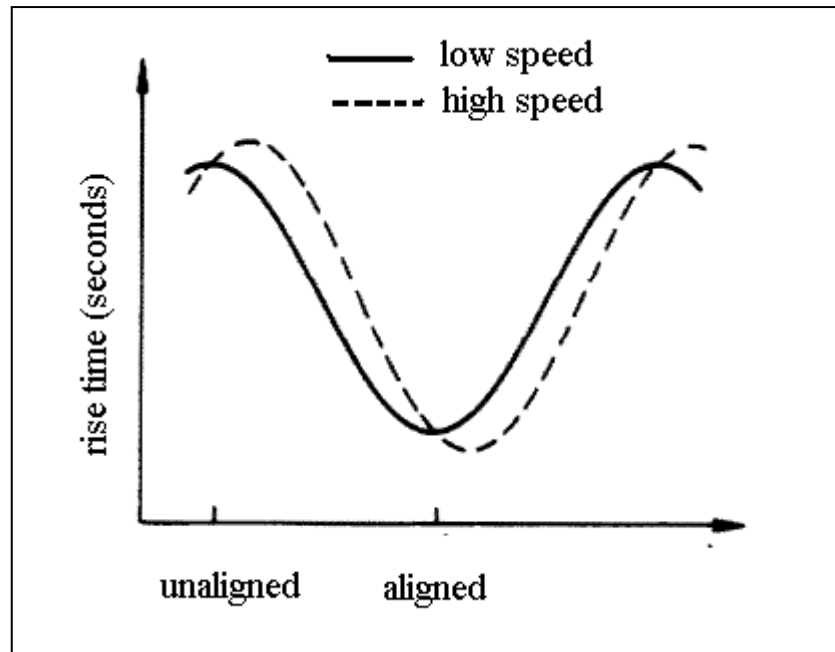


Fig. 5.5 the effect of speed on the current rise time

Panda [81] in later research demonstrated the detrimental effects of neglecting back EMF even at low speeds of several hundred rpm during the chopping mode. In order to compensate for the effects of back EMF, Panda modified the approach of Acarnley by adaptively changing the Δt_{ref} and the dwell angle based on operating speed. Panda also applied the method for position estimation in the single pulse mode at higher speeds, where the initial rate of rise of current was used to find the rotor position at the beginning of each phase current pulse.

5.3.2 Voltage Pulse Techniques

These techniques are based on the idea that if a voltage pulse is applied to a non-conducting phase for a short duration of time Δt , the phase inductance remains unsaturated, and the current amplitude remains small; hence, back EMF effect and phase winding resistance can be neglected. The method is essentially based on the third method proposed by Acarnley [79]. Several researchers subsequently implemented the

scheme with modifications and improvements. For low current levels, the motor phase voltage equation can be written as in equation 5.7

$$v = iR + L(\theta) \frac{di}{dt} + \omega L(\theta) + \frac{dL(\theta)}{d\theta} \omega \theta \quad 5.7$$

Where ω is the angular speed in rad/second. If the voltage is applied for a short period of time, the equation can be approximated as in equation 5.8.

$$v = L(\theta) \frac{\Delta i}{\Delta t} \quad 5.8$$

Therefore the position dependant inductance can be found as in equation 5.9.

$$L(\theta) = v \frac{\Delta t}{\Delta i} \quad 5.9$$

The unsaturated phase inductance value can be determined by keeping either Δi or Δt constant while measuring the other. The main limitation of the voltage pulse technique is the inter-phase coupling effect which is particularly severe when the active phase is undergoing high frequency chopping for current regulation. Eddy currents also affect the accuracy of position sensing. Another drawback of this technique is associated with injecting a diagnostic pulse from the main converter is that their magnitude could be significant, and hence can generate negative torque. Also, since the pulses are large there will be a long waiting period for the sensing pulse to decay to negligible levels before the next pulse can be applied. The rotor might move a considerable distance during that period; therefore, the resolution of sensing will decrease. All these factors limit the maximum attainable operating speed with this method of position sensing. Mvungi [82] used a look-up table to compensate for the mutual coupling effects. His method generated a continuously sampled rotor position rather than detecting a threshold level for phase commutation.

5.3.3 Modulation Based Techniques

Several alternatives of sensorless techniques based on modulation techniques have been developed in order to eliminate some of the drawbacks mentioned previously with voltage pulse techniques [83, 84]. The modulation encoding techniques of rotor position detection are based on extracting the periodically varying base inductance in an encoded form by applying a high frequency carrier signal. The signal containing the phase inductance information is assumed to have a much lower frequency of variation compared to the carrier frequency. The encoded inductance information is decoded using a suitable demodulation technique. Sometimes an external resistance is added in series with the phase inductance in these methods, to make the signal measurements easier, but the associated penalty is the need for additional switches to isolate the sensing circuit from the power circuit.

5.3.4 Switching Frequency Based Estimation

This technique is based on the same principles as signal injection estimation except that, rather than injecting a fixed frequency signal for the specific purpose of detecting position, it uses the effect of the PWM switching as the injected signal. This would suggest similar capabilities in terms of position sensing, as the system is essentially the same apart from operating at a higher frequency. However, at standstill, the inverter would not necessarily be switching and hence there would be no signal to use for a sensorless start. In addition, the frequency spectrum of the PWM "injection" is extremely complex, with a large number of harmonics and sub-harmonics [85]. Therefore, it is difficult to isolate the required components from the other harmonics, which are essentially noise.

5.4 Summary of Methods

The techniques presented in this literature review fall into two main classifications. The first of these contains the 'at speed' back EMF techniques and the second contains the saliency based techniques. Back EMF techniques operate effectively when the shaft is rotating at a sufficient speed to overcome measurement noise, but are unable to work when the machine is stationary. However, they are considerably simpler in terms of implementation and computational requirements than the saliency techniques. The back EMF models are the simplest of the 'at speed' techniques, but are more sensitive to parameter variations than the observer techniques. The latter, however, require significantly greater computational capacity and a longer design cycle prior to implementation.

The saliency based techniques have the considerable advantage that they operate at zero speed. Some of these techniques are capable of operating over the full speed range. However, this is unlikely to be desirable in many applications due to the increased computational demand (compared to back EMF or observer techniques), the possibility of torque ripple and the reduction of available DC link voltage, both as a result of the need for a superimposed injection signal.

In the next chapter a novel encoderless control method is presented. The method is based on injecting a high frequency current into a search coil that is positioned in a particular location in the stator iron. The method has the following advantages:

- 1) Can sense the zero speed rotor position for any type of BLDC motor including surface mounted PM rotor.
- 2) The varying main flux has no influence on the sensed rotor position signal.

6. New Encoderless Control Method for Single Phase BLDC Motor

6.1 Introduction

The reliability of the position encoder is a major concern when brushless permanent magnet motors are used in a harsh environment. The position encoder has sensors which have electrical, mechanical and thermal constraints that limit their operation. Many investigations to eliminate this type of encoder have been conducted (see chapter 5). However, as an alternative, the use of search coils to detect rotor position has been employed already. For Switched Reluctance Motors SRM the search coils are used to detect the rotor position due to the high rotor saliency. This method can detect the rotor position at zero speed irrespective of the excitation polarity, because either polarity of excitation for any phase will allow the correct rotation provided it is in the right phase sequence. The disadvantage of this method is that it can only be used for high saliency ratio motors. It has limited operation when the motor is loaded, because when the iron starts to saturate the ability of the search coil in detecting rotor saliency will be affected.

For the PM BLDC motor, search coils can not be used for rotor saliency detection even for a highly salient motor because of the difficulty of determining the initial excitation polarity. Instead search coils are used to produce rotor position information by sensing the open circuit back EMF. But this method is useless for low and zero speeds. Rotor position information can only be obtained when the rotor speed is high enough to produce sufficient detectable back EMF.

There is no method presented in the literature that proposes the use of search coils to detect the rotor position for PM motors at any speed (including zero speed) and with no influence from the main winding flux on the search coil signal. In this chapter a new and novel encoderless control method is presented. The method relies on using a single search coil positioned in the stator iron to detect the rotor position independent of rotor saliency, speed and load. To simplify the analysis the effect of cross saturation is assumed to be negligible.

6.2 Commutation of a single phase BLDC motor

A single phase BLDC motor is commutated by a two step sequence. The excitation polarity is positive for half an electrical cycle and negative for the other half. Since single phase PM BLDC motors are usually required to have only a unidirectional rotation, the start up commutation sequence is critical for the motor to start rotating in the correct direction. Using a rotor saliency detection method to determine the start up commutation sequence is not possible for two reasons:

- 1) For an unsaturated surface mount magnet motor the saliency ratio is negligible.
- 2) For a salient interior permanent magnet rotor the inductance variation cycle has twice the frequency of the excitation frequency, which means for each inductance value either excitation polarities is possible as shown in Fig. 6.1.

Therefore another method for detecting rotor position that is independent from rotor saliency need to be developed.

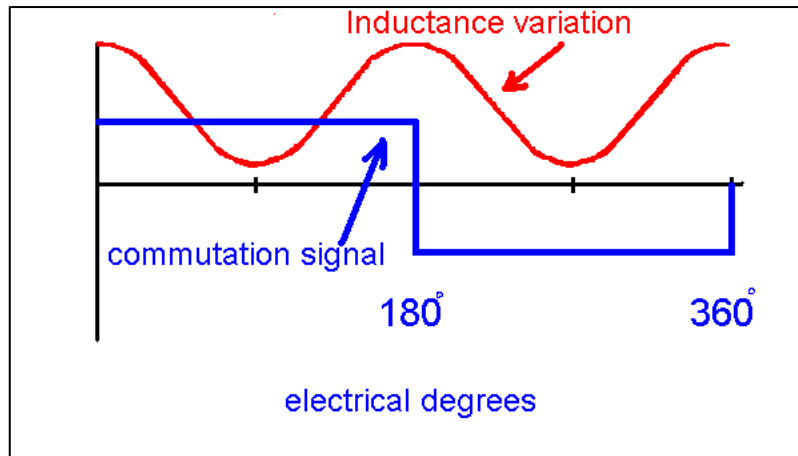
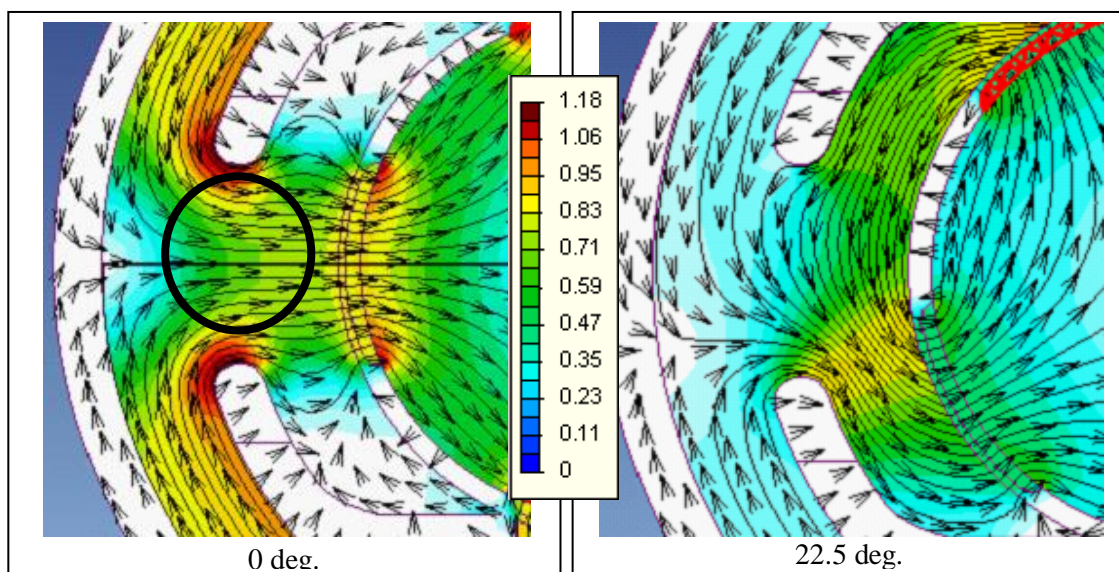


Fig. 6.1 Inductance variation of a salient motor

6.3 Sensing the Magnetic Flux in Iron

Fig. 6.2 shows the open circuit flux plots of the new single phase BLDC motor at different rotor positions from 0° to 180° mechanical degrees (i.e. one full electrical cycle). The area of interest is shown below by a circle. It can be seen that the flux in this area rotates about the centre of the circle with rotor position. Therefore, the flux density vector in this area can be represented by a rotating space vector in the stator reference frame as shown in Fig. 6.3



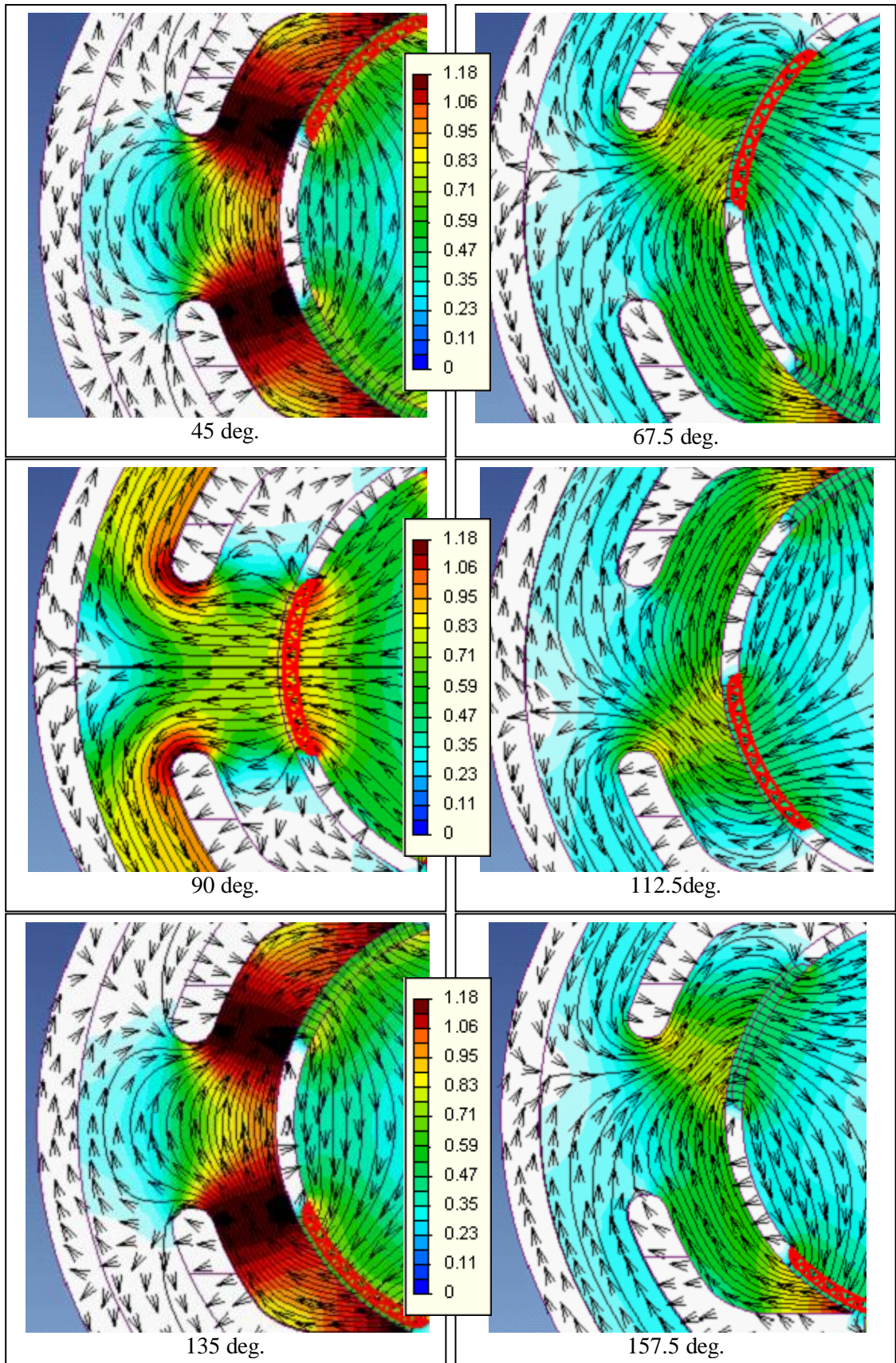


Fig. 6.2 Open circuit flux plots

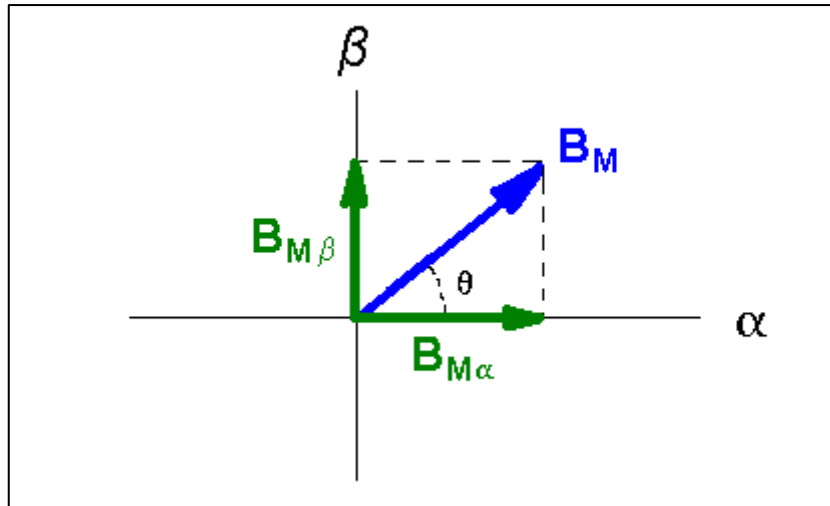


Fig. 6.3 Open circuit flux density phasor diagram in the stationary reference frame

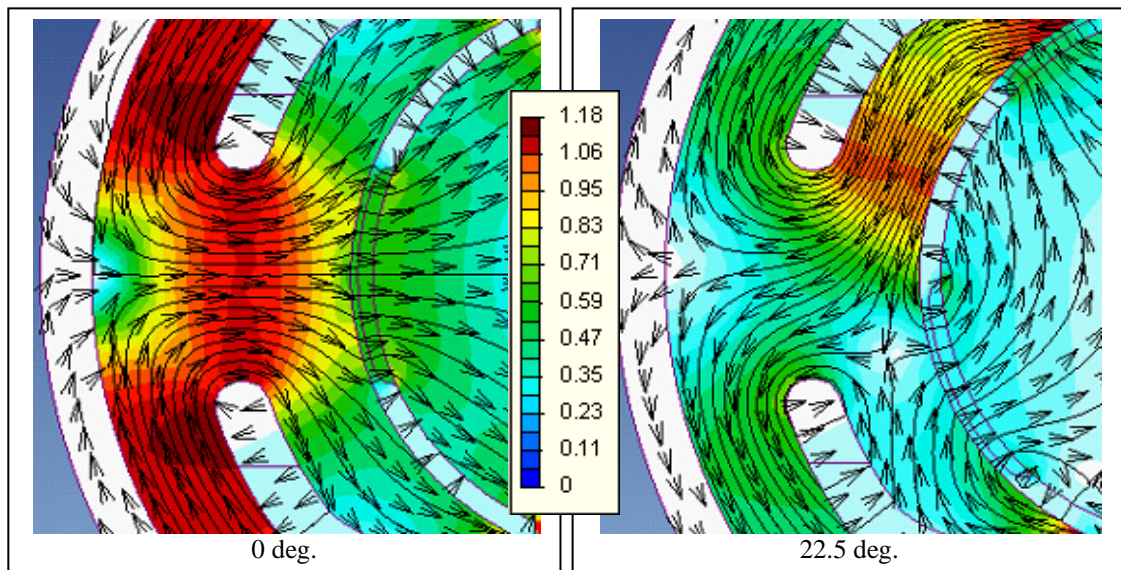
The total radial flux density component $B_{M\alpha}$ can be calculated from

$$B_{M\alpha} = B_M \cos \theta \tag{6.1}$$

Where θ is the electrical angular position. The tangential flux density component $B_{M\beta}$ can be calculated by

$$B_{M\beta} = B_M \sin \theta \tag{6.2}$$

Fig. 6.4 shows the flux plots in the stator iron while the motor is excited which shows the rotation of B_M is unaffected. .



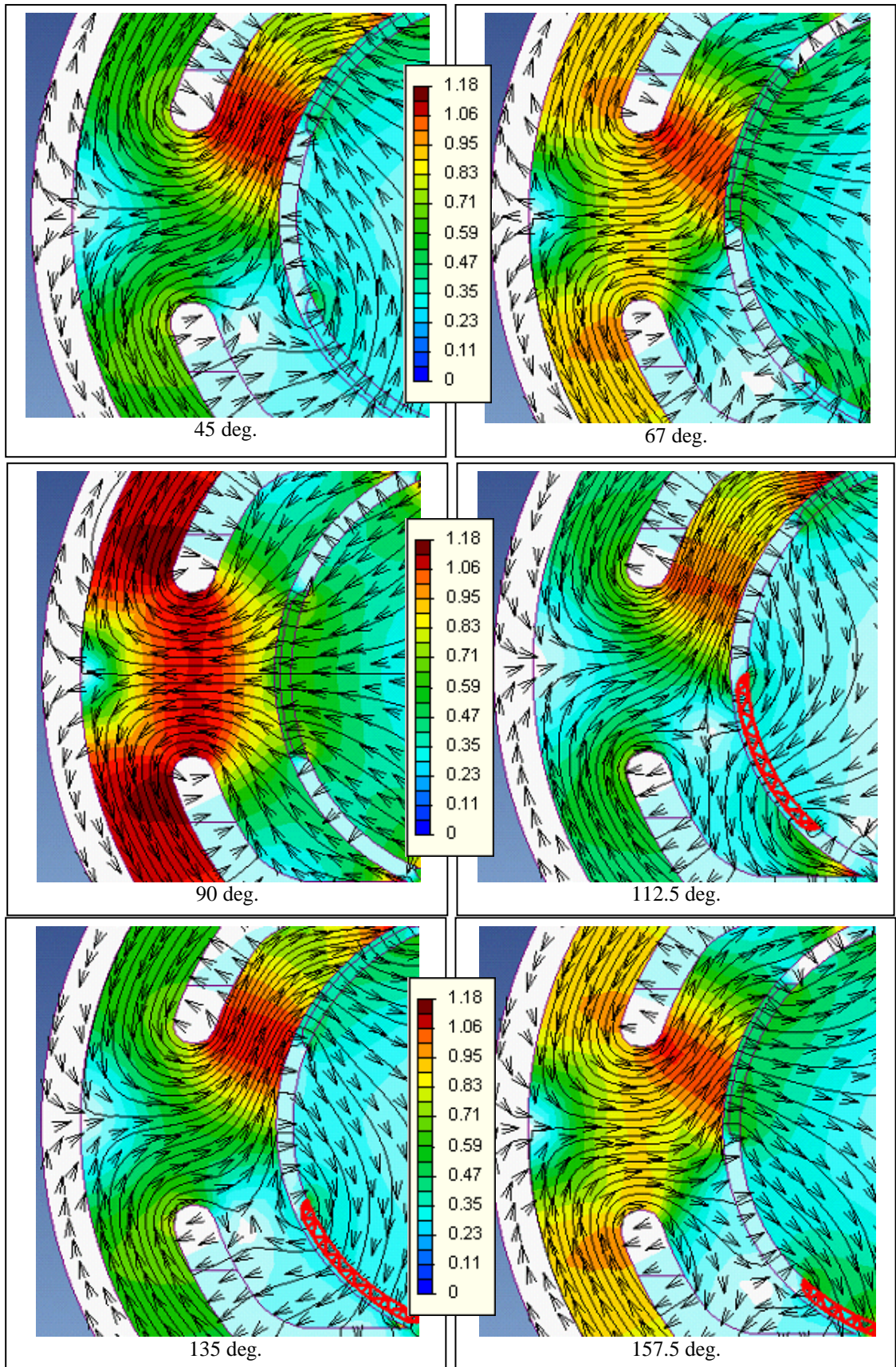


Fig. 6.4 Flux density plots with excitation

The flux density space vector phasor diagram with the excitation current is shown in Fig. 6.5. The total radial flux density component $B_{M\alpha}$ will be influenced by the flux density contributed from the winding current B_{exc} as shown in equation 6.3.

$$B_{M\alpha} = B_M \cos \theta + B_{exc} \quad 6.3$$

The tangential component of flux density $B_{M\beta}$ is not influenced by the excitation current because this component of the excitation flux is negligible. Therefore, the tangential resultant flux component will be represented by equation 6.2. The fundamental component of the waveforms of $B_{M\beta}$ and $B_{M\alpha}$ with and without excitation with respect to electrical degrees are shown in Fig. 6.6. Comparing the waveforms with the commutation signal it can be seen that $B_{M\beta}$ can be used to generate the rotor position signal for the following two reasons

1. The peak value of $B_{M\beta}$ is constant unlike $B_{M\alpha}$ which can be influenced by the excitation flux .
2. Since $B_{M\beta}$ is 180° electrical degrees out of phase with $B_{M\alpha}$, the fundamental component of $B_{M\beta}$ will be in phase with the excitation signal. Therefore monitoring the polarity and zero crossings of $B_{M\beta}$ will be enough to produce the excitation signal even at zero speed.

The next section demonstrates the way in which $B_{M\beta}$ is sensed in the proposed encoderless control method.

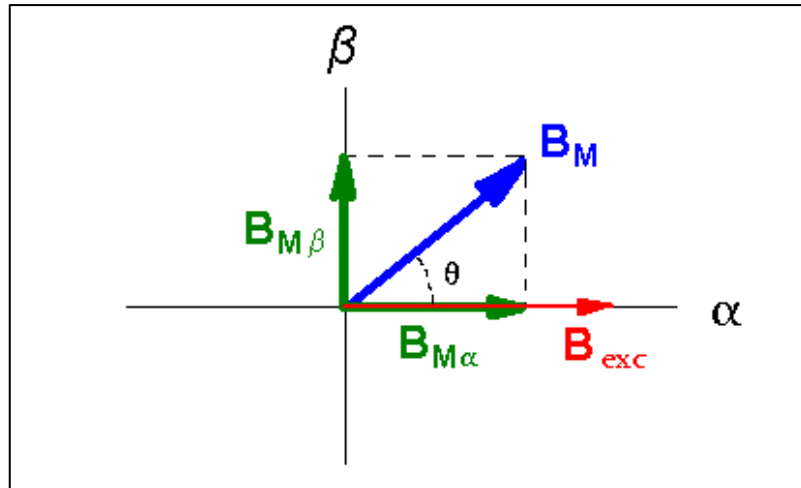


Fig. 6.5 Flux density phasor diagram of the tangential and radial components with excitation flux

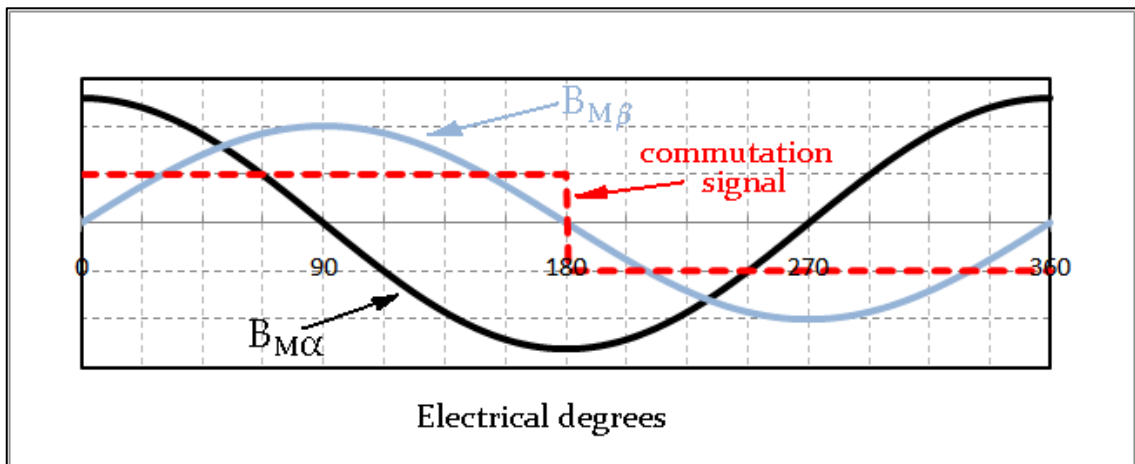


Fig. 6.6 Comparing the fundamental component of $B_{M\beta}$ and $B_{M\alpha}$ waveforms with commutation signal

6.4 Sensing the tangential component of the rotor PM flux

In this section a method for sensing the magnitude of the tangential component of flux $B_{M\beta}$ is presented. The method is based on using a search coil placed at a precise location in the yoke of the large stator pole, with its core perpendicular to the axis of the stator pole as shown in Fig. 6.7. Using a search coil for the purpose of sensing the magnitude and, more importantly, the direction of the flux for PM motors is new. Traditionally search coils are used to sense open circuit back EMF or to detect rotor saliency by injecting a high frequency signal.

By inserting coil windows into this section of the stator (i.e. inserting two areas of high reluctance), will inevitably modify the pattern of the flux in this location, compared with the flux plots in Fig. 6.2 and Fig. 6.4. The desired effect is still the same, but $B_{M\beta}$ may contain harmonic components.

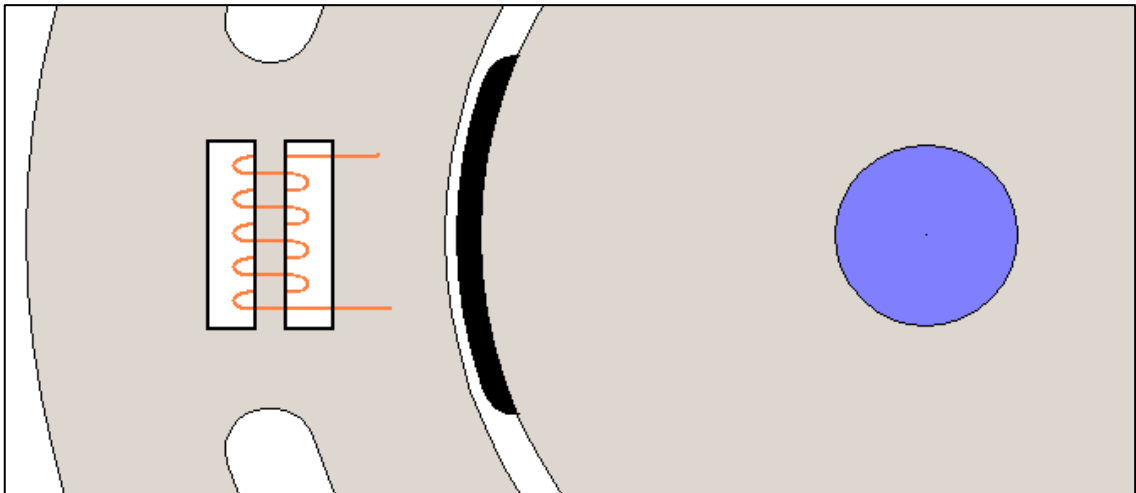


Fig. 6.7 Showing the location of the search coil for the proposed encoderless control method

Fig. 6.8 shows the BH curve of the stator iron. The aim is to operate the core of the search coil close to the nonlinear region, so that the tangential component of the flux density $B_{M\beta}$ will cyclically drive the core of the search coil into and out of saturation with rotor position. This cycle will cause a change in the inductance of the search coil and by monitoring the inductance, the rotor position can be deduced.

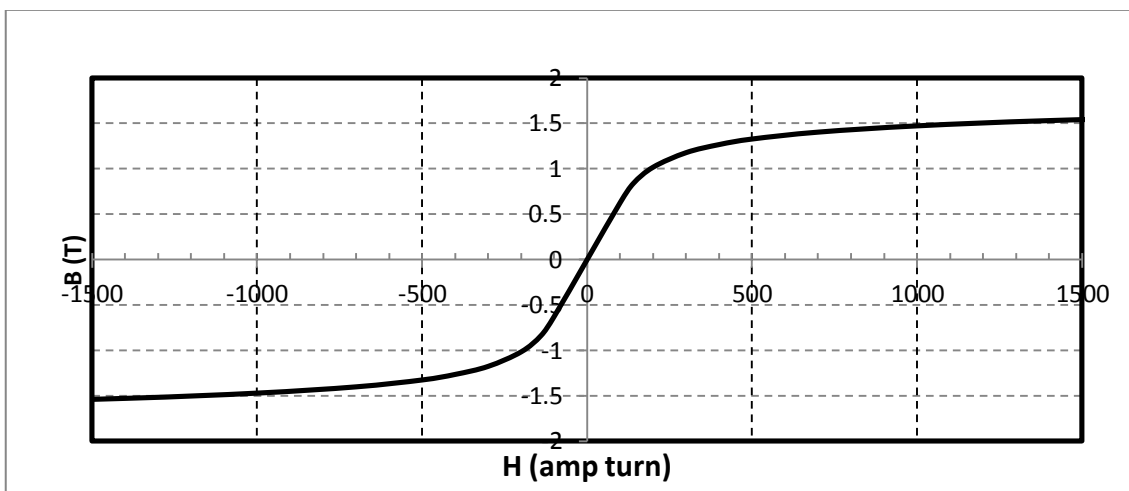


Fig. 6.8 B-H curve of a standard iron

This variation in inductance can be determined by injecting a high frequency current signal. The envelope of the HF current can be obtained which contains the rotor position information. In order to maximise the resolution of the rotor position measurement, the d/dt of the envelope has to be as high as possible. This can be achieved by ensuring that the peaks of the HF current vary within the range of high dL/dB . This region of flux density can be obtained from the B-H curve by plotting permeability vs flux density as shown in Fig. 6.9. It can be seen that when the core flux density is between 0.8T and 1.6T the change in the permeability of the core is a maximum. Therefore, operating in the knee area of the B-H curve will ensure maximum sensitivity of inductance to rotor position.

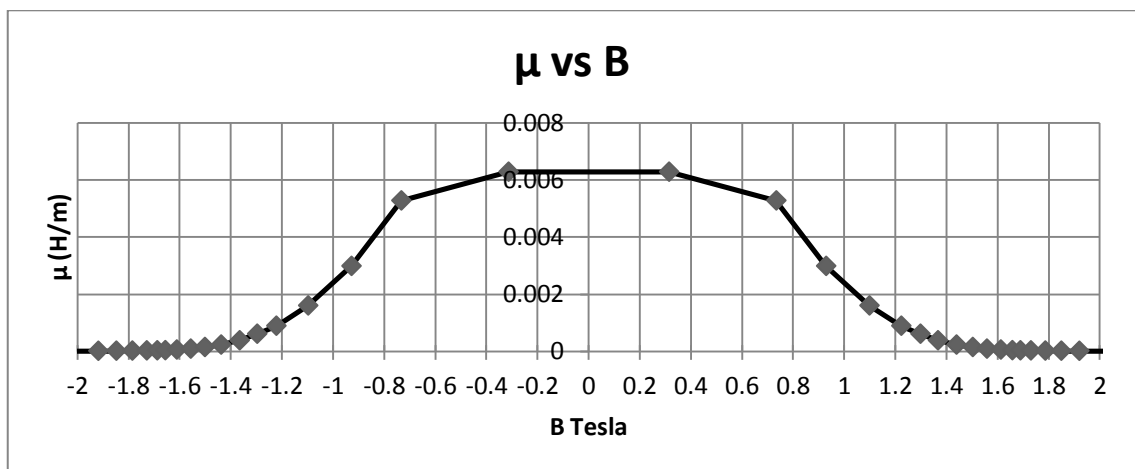


Fig. 6.9 The relationship between the flux density and permeability of the iron core

6.5 Search coil parameters

The radial distance of the search coil core from the airgap and the core volume will determine the peak value of $B_{M\beta}$. Therefore, care must be taken to choose appropriate values that will guarantee that the core will operate within the knee region of the B-H

curve. In order to ensure this, a DC current is set up in the search coil to offset the flux density of the core up a fixed level. Then the rotation of the rotor will cause $B_{M\beta}$ to oscillate about the dc flux level.

The first step is to find the combination of the DC current and $|B_{M\beta}|$ that can ensure the total operating flux density of the core to be within 0.8T and 1.6T. Fig. 6.10 shows how the core of the search coil is influenced by the tangential flux component from the magnet $B_{M\beta}$ and the flux produced by the DC current in the search coil B_{DC} .

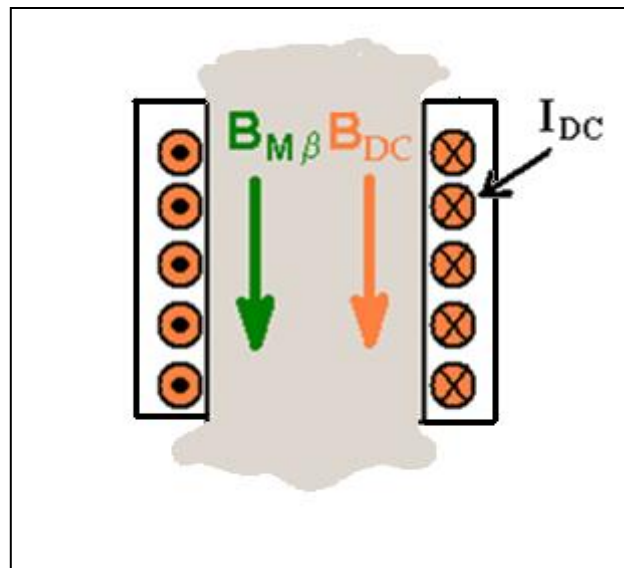


Fig. 6.10 Flux density components in the core of search coil

The total magnetic flux density in the search coil core B_T is the sum of the DC flux density B_{DC} and the tangential component of the permanent magnet flux density $B_{M\beta}$.

$$B_T = B_{DC} + B_{M\beta} \quad 6.4$$

When $B_{M\beta}$ is maximum B_T should be equal to 1.6T. And when $B_{M\beta}$ is minimum B_T should be equal to 0.8T. The magnitudes of the negative and positive peaks of $B_{M\beta}$ are the same. An appropriate $B_{M\beta}$ and B_{DC} need to be calculated that will guarantee operation around the knee region of the B-H curve.

The DC flux linkage is dependent on the current and the instantaneous permeability of the core which is a function of the total flux density in the core. B_{DC} can be found as follows:

$$B_{DC} = \frac{I N \mu(B_T)}{l} \quad 6.5$$

At maximum $B_{M\beta}$ $B_T = 1.6T$ then equation 6.4 will be

$$1.6 = \frac{I N \mu(B_T = 1.6)}{l} + |B_{M\beta(max)}| \quad 6.6$$

At minimum $B_{M\beta}$ $B_T = 0.8T$ then equation 6.5 will be

$$0.8 = \frac{I N \mu(B_T = 0.8)}{l} - |B_{M\beta(min)}| \quad 6.7$$

Using the graph in Fig. 6.9 the permeability at the two operating points can be obtained. When B_T equal to 1.6T μ equals 0.001 Hm^{-1} and when B_T equal to 0.8T μ equals 0.006 Hm^{-1} . The number of turns was chosen to be $N=20$ and core path length = 10 mm . Using $|B_{M\beta(min)}| = |B_{M\beta(max)}|$ equations 6.6 and 6.7 can be solved to obtain the magnitudes of the permanent magnet flux density and DC current I.

$$1.6 - \frac{I N 0.006}{l} = \frac{I N 0.001}{l} - 0.8 \quad 6.8$$

The solution to the equations is

$I = 0.17A$ and $|B_{M\beta}| = 0.76T$. The DC voltage required to achieve this current is $0.09V$ when the total resistance of the sensing coil is 0.6Ω .

The following step is to determine the distance and the volume of the core that will achieve $B_{M\beta} = \pm 0.76T$ in the core of the search coil with rotor position. The core dimension should be chosen to have small radial thickness for easy saturation. These dimensions were chosen to be 1mm width x 10mm length x 5mm depth. The distance from the centre of the search coil core to the air gap was obtained with aid of the FEM software which is found to be 16mm, this achieves $\pm 0.76T$ variation in the tangential permanent magnet flux. This configuration will ensure the operation of the core flux density within maximum variation of search coil inductance with rotor position. This variation of inductance can be captured by injecting a high frequency signal with a carefully selected voltage and frequency that keeps the operating points of the peaks of the high frequency current within the knee region of the B-H curve. Then by passing the HF current signal into a low pass filter, the instantaneous variation of the search coil inductance can be obtained which contains rotor position information. Appendix 9.4 contains the details of a similar signal processing for a HF injected signal to monitor rotor saliency for a special single phase switched reluctance motor with a high saliency ratio.

6.6 Analytical simulation results

The proposed new encoderless rotor position sensor has been implemented in Simulink. The nonlinear model of the search coil is shown in Fig. 6.11. It has two inputs: the voltage and the tangential component of the core flux density $B_{M\beta}$ from the rotor permanent magnets, which is a function of rotor position. The output is the current in which is governed by the inductance of the search coil.

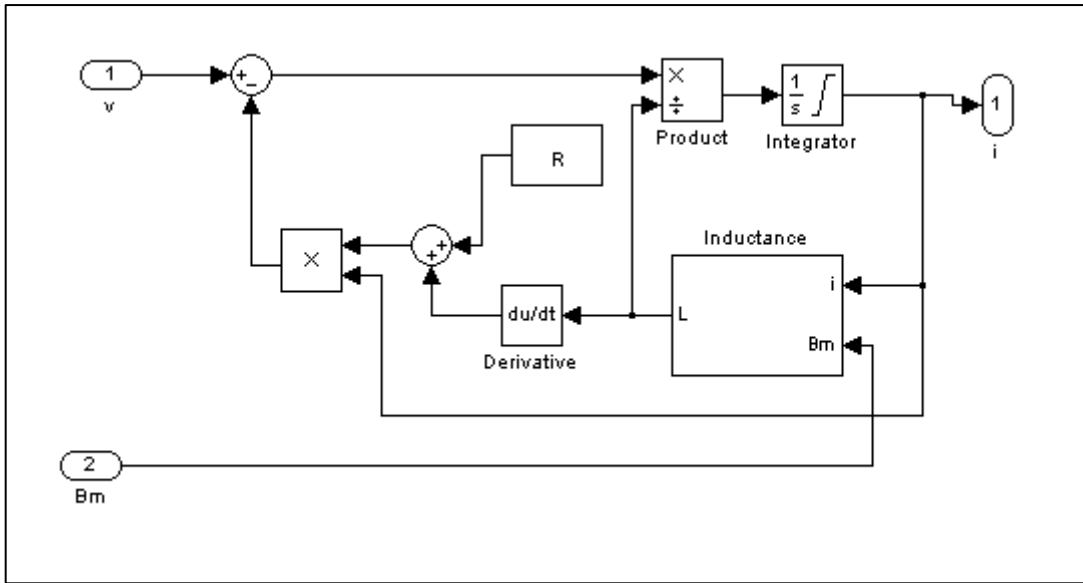


Fig. 6.11 Search coil Simulink model

The search coil model is based on the following equation

$$v = Ri + \frac{d(Li)}{dt} \quad 6.9$$

R is the total resistance of the circuit. Since the inductance and current are varying with time the equation will be

$$v = Ri + i \frac{dL}{dt} + L \frac{di}{dt} \quad 6.10$$

The shape of the HF current envelope is influenced by the variation in the inductance of the search coil. The permanent magnet flux $B_{M\beta}$ is responsible for varying the operating point in the BH curve of the sensor core. To simplify the analysis the variation in the magnitude of $B_{M\beta}$ due to sensor coil armature current is assumed to be unaffected. In this complex model the inductance is governed by the instantaneous permeability of the core which is a function of the total flux density B_T . The total core flux density is composed of the sum of magnet flux $B_{M\beta}$, the DC flux density and the flux density due to the HF current as shown below.

$$B_T = B_{HF} + B_{M\beta} + B_{DC} \quad 6.11$$

B_{HF} is the flux density in the search coil core due to the HF injected current which is found from equation 6.12

$$B_{HF} = \frac{i(t) N \mu(B_T)}{l} \quad 6.12$$

In order to calculate the inductance of the search coil a look up table of core flux density vs permeability is needed which was obtained from the B-H curve of the iron found in the FEM software library. The Simulink block that calculates the inductance is shown in Fig. 6.12. The inductance is calculated as follows:

$$L = \frac{\mu(B_T) N^2 A}{l} \quad 6.13$$

Where

L: Inductance

μ : core permeability

N: number of turns of search coil

A: cross sectional area of core.

l : length of core

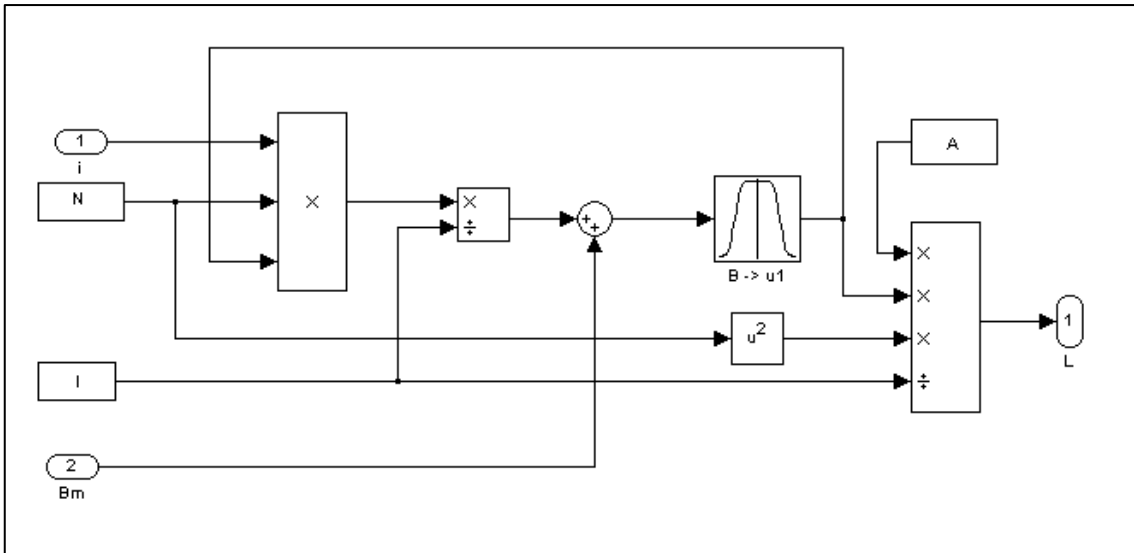


Fig. 6.12 Simulink model of inductance

The model for the complete search coil with a high frequency input sine wave current signal, influenced by the position dependent permanent magnet flux density is shown in Fig. 6.13.

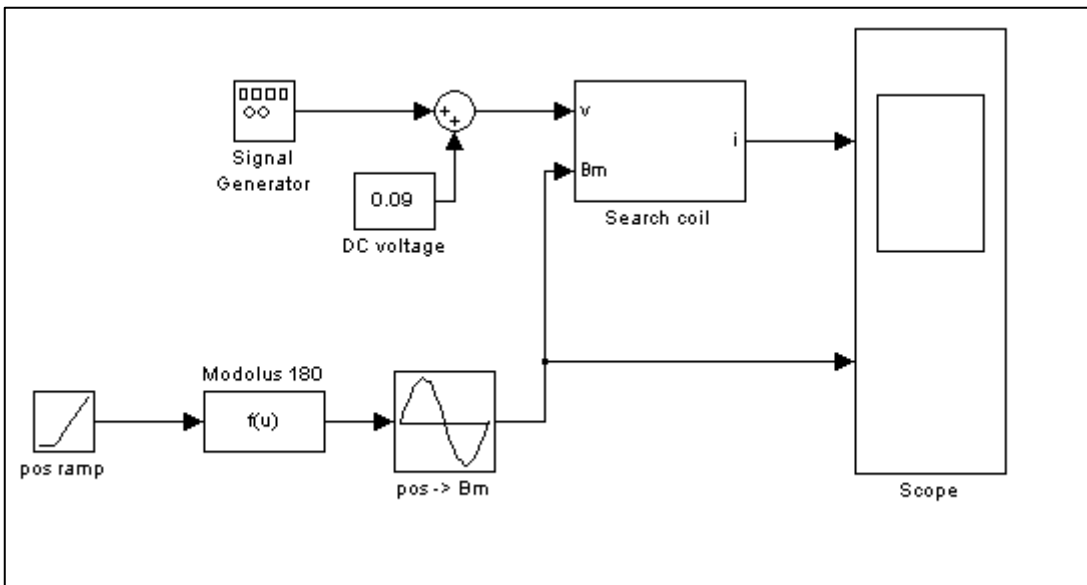


Fig. 6.13 Inputs and output of the Simulink search coil model

The table of position vs $B_{M\beta}$ is obtained from the FEM 2d static solver which varies by $\pm 0.8T$ with rotor position. The ramp represents the change in position with rotor speed

of 300 rpm. The HF signal was chosen to be a sine wave with amplitude $\pm 0.5V$ and frequency of 3000 Hz with a DC offset of 0.09V. This choice of voltage and frequency will guarantee that the peaks of the HF current operate in the knee area of the BH curve. Fig. 6.14 shows the resulting current in the search coil while the tangential component of the magnet flux density varies with rotor position running at 150 rpm.

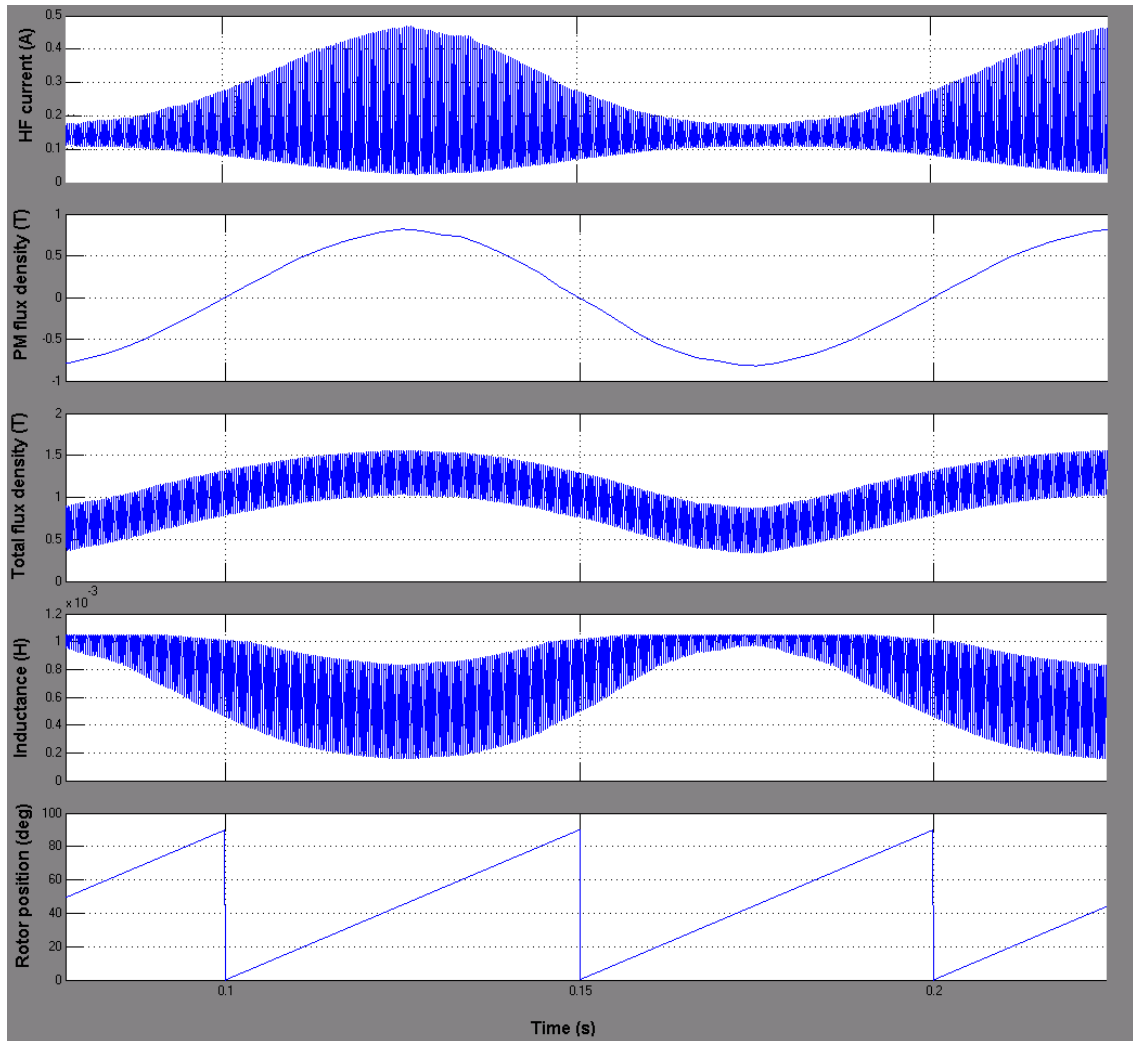


Fig. 6.14 Waveforms results with rotor rotation for position sensing

It can be seen that the HF current with the DC offset is amplitude modulated with rotor position. The envelope of the resultant flux density B_T in the search coil core represents the operating points at the peaks of the HF current. It can be seen that the chosen parameters for the search coil dimensions and input signal has ensured the envelope to

vary between $0.8T$ and $1.6T$ which agrees with the analytical calculations presented earlier. Further signal processing of the envelope of the modulated HF current yields accurate position information. Fig. 6.15 shows the block diagram of the signal processing steps.

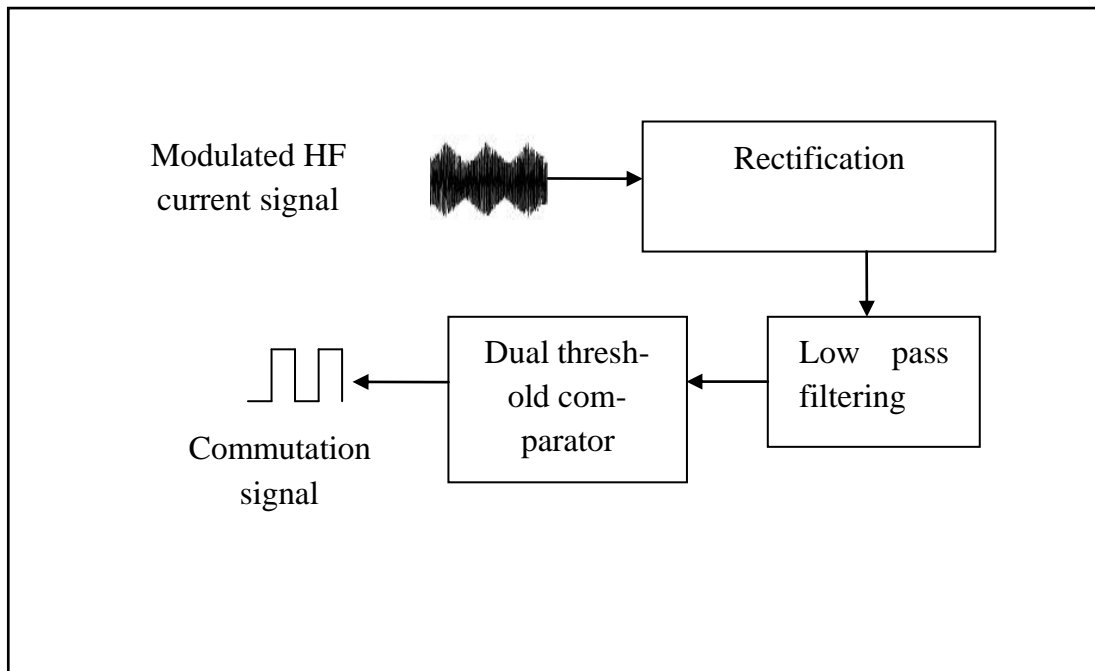


Fig. 6.15 Processing the HF modulated current signal.

The first step is that the modulated current signal is rectified then passed through a low pass filter to extract the envelope which contains the rotor position information. Finally the commutation signal for the power switching transistors is derived from this envelope using a comparator with a fixed threshold, to drive the single phase BLDC motor.

If phase advance control is to be implemented the fixed reference comparator can be replaced with a dual threshold Schmitt comparator shown in figure Fig. 6.16. The values of the threshold V_1 and V_2 can be found by using suitable values for R_1 and R_2 . This advancing method is suitable only for fixed phase advance applications. For dynamic advance angle control the calculation of V_1 and V_2 becomes more complicated.

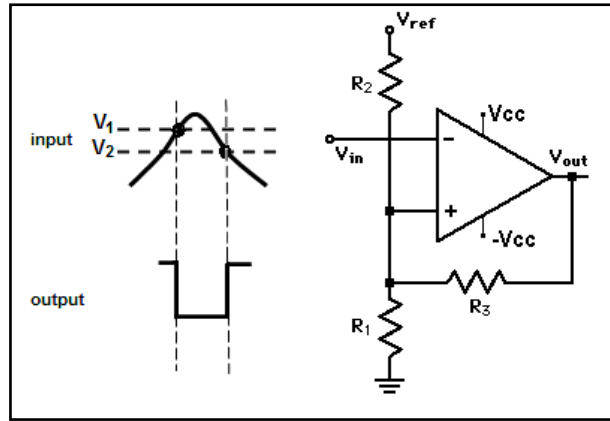


Fig. 6.16 Dual threshold comparator

$$V_1 = \frac{R_1 || R_2 || R_3}{R_2} V_{ref} + \frac{R_1 || R_2 || R_3}{R_3} V_{cc} \quad 6.14$$

$$V_2 = \frac{R_1 || R_2 || R_3}{R_2} V_{ref} - \frac{R_1 || R_2 || R_3}{R_3} V_{cc} \quad 6.15$$

6.7 FEM validation

To validate the numerical results produced by the Simulink model a dynamic FEM simulation was carried out. The FEM model was created with the search coil arrangement using the end 5mm of the stator stack laminations. Therefore, the complete stator stack comprises of three sets of laminations. The first set contains two slots (or windows) of total stack depth of 5mm, through which the sensing coil is wound. The second set contains a larger slot that represents a pocket to create a space for the inner end winding of the search coil with a stack depth of 2 mm. The third stator lamination set has no modification and it has a total depth that represents the remaining stack length of the motor.

The flux linkage of the search coils due to the rotation of the rotor has been plotted by 2D and 3D static solvers, see

Fig. 6.17. Since the search coil spans only the end 5mm of the motor stack, a 3D model was necessary to verify the waveform of the flux density in the sensor core. This will ensure that the flux density waveform produced from the 2D solver is accurate enough to perform a 2D dynamic simulation (which is time consuming in 3D). It can be seen there is good agreement between the two profiles.

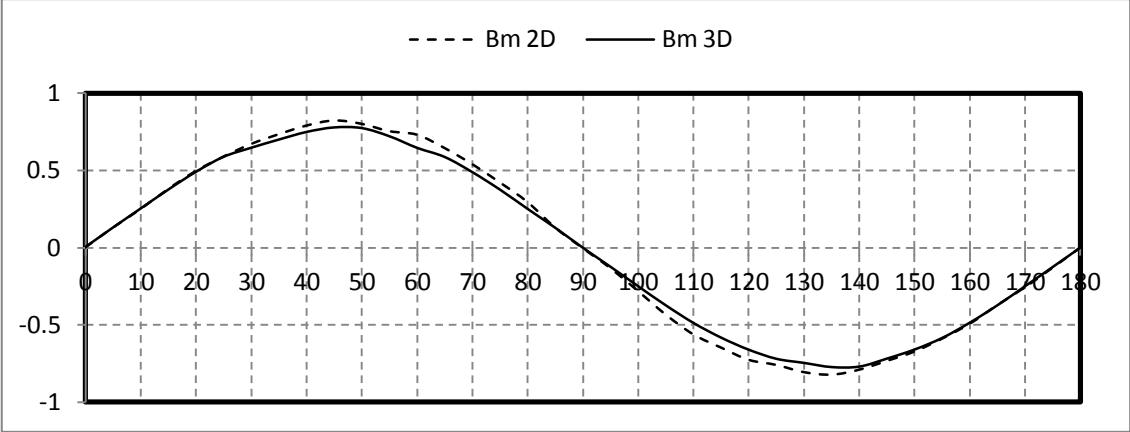


Fig. 6.17 2D and 3D FEM results of $B_{M\beta}$

A 2D dynamic solver was used with a simple H bridge circuit supplied with 5V. The search coil was injected with 3 kHz sine wave of $\pm 5v$ and with a DC offset of 0.09V. The resulting HF current in the search coil is shown in Fig. 6.18. It can be seen that the result is close to the result produced by the Simulink model shown in Fig. 6.14.

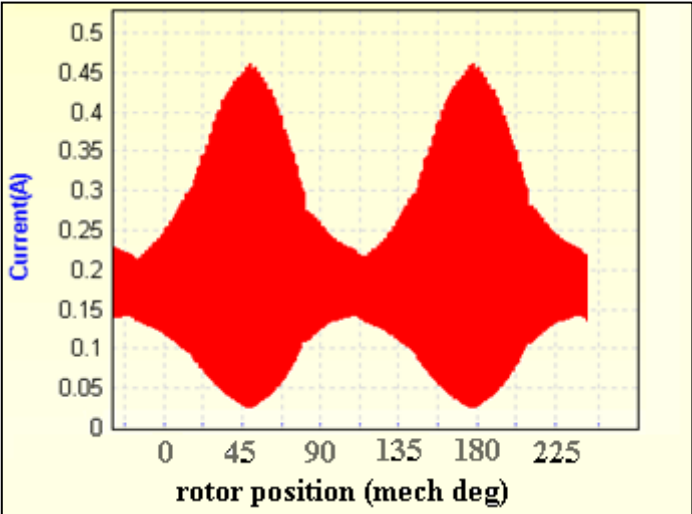


Fig. 6.18 HF modulated current signal from FEM dynamic solver

6.8 Discussions and Conclusions

The encoderless method presented in this chapter is capable of detecting the rotor position of any permanent magnet BLDC motor even at zero speed. The search coil placed in the stator iron is not used for the purpose of detecting the rotor saliency or the rotational back EMF as it is the tradition. The coil is placed in a position to detect the tangential component of the permanent magnet flux which varies with rotor position. This flux links with the search coil without the influence from the excitation flux therefore sensing the tangential component of the flux in the core of the search coil will enable rotor position to be detected. An analysis on how to obtain the highest rotor position resolution was presented, which is based on choosing an appropriate search coil position, dimensions and search coil signal parameters that give the steepest change in the envelop of the modulated HF current signal. The new proposed encoderless method has been verified by two Simulation softwares. A non-linear model represented by Simulink blocks was created to predict the search coil behaviour that is influenced by the permanent magnet tangential flux component. These results were further verified by using an FEM model that was configured with the same parameters as the Simulink model (i.e. HF signal, DC offset, resistance...etc). The resulting modulated HF current signal agrees very well with the results produced by the Simulink model. The signal processing of the HF current signal is simple. It composes of a diode, LPF and a comparator.

The main advantages of the new method are

1. Higher reliability due to elimination of the integrated circuit sensor that has limited electrical, mechanical and thermal constraints.

2. The method is able to detect the rotor position at zero speed even for a surface mounted magnet motor with inherently no saliency.
3. The main flux due to the excitation current has no influence on the sensor signal.

7. New Phase Advance Control for Single Phase PM Brushless DC Motors

7.1 Introduction

The commutation of BLDC motors needs to be synchronised with the rotor position or the motional back EMF. Due to the inductance of the winding the rate at which current changes is governed by the L/R time constant. At low speeds, when the period of conduction is several times the L/R time constant, the delay in current rise or fall is negligible. But at high speeds the electrical time constant L/R cannot be ignored because it represents a large percentage of the commutation cycle. For motors with 180° conduction period the current will be out of phase with the back EMF and a negative torque will be generated where the polarity of the back EMF and current are opposite. Consequently a considerable reduction in the average output torque will be the result.

Fig. 7.1 illustrates the relative positions of the current and back EMF waveforms in relation to the commutation signal for low and high speeds [86].

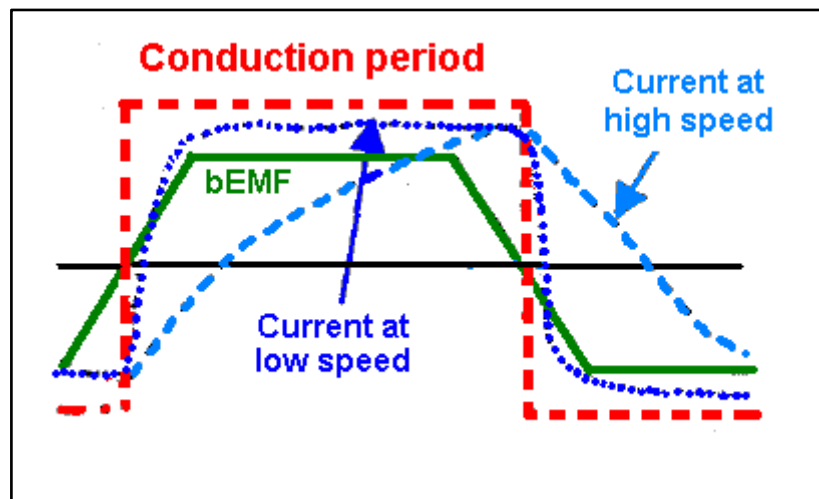


Fig. 7.1 Relationship between current and back EMF at low and high speeds

7.2 Advancing the commutation signal

To solve the current lag problem, advancing the commutation signal is employed. There are two ways to advance the current commutation signal. First by mechanically positioning the rotor sensor in a predefined advanced position that achieves the desired advance commutation angle. This way of advancing is suitable for fixed speed applications where the advance angle is optimum for that speed. The second way of achieving phase advance is by implementing a variable phase advance angle. This can be achieved by positioning the sensor in a fixed advanced position then by delaying the sensor signal by a certain amount the desired advance angle can be obtained. The delay will be inversely proportional to the required advance angle. This way of phase advance is suitable for variable speed applications where there is an optimum advanced angle for every speed.

7.3 Phase angle between back EMF and current

Based on the phase angle between the back EMF and current waveforms the phase advance control, for a 180° conduction mode BLDC motor, can be categorized into three categories:

- 1) No phase advance with current lags the back EMF waveform.
- 2) Phase advance with current in phase with the back EMF waveform.
- 3) Phase advance with the current leading back EMF waveform (field weakening)

There are two types of EMF in the phase of BLDC motor. One is the motional EMF due to the rotor permanent magnet which is commonly referred to as the back EMF. Another is due to the changing current which is referred to as the transformer EMF and it is equal to $d(Li)/dt$. In the following section the three phase advance conditions will

be explained with reference to back EMF and transformer EMF for a trapezoidal back EMF single phase brushless DC motor.

7.3.1 No phase advance mode

In this mode of operation the commutation point of the phase winding current is at the zero crossings of the back EMF waveform. At high speed the L/R time constant will cause the current not to change in polarity at the switching points which will result in a period where the back EMF is in the opposite polarity to the current and a negative torque will be produced. Fig. 7.2 shows the back EMF, applied commutation voltage, transformer EMF and current waveforms. The first half of the commutation cycle can be divided into 4 regions. In region **a** to **b** the back EMF is increasing until it reaches the top level. Since the applied voltage is constant and higher than the back EMF the resulting transformer EMF will be positive and decreasing. Knowing that the transformer EMF is proportional with $d(Li)/dt$ the resulting current in this period will be increasing nonlinearly from a negative value. From **b** to **c** the back EMF is constant and lower than the applied voltage. This will result in a positive constant transformer EMF which causes the current to increase linearly until it reaches 0A. Because the current polarity is opposite to the back EMF polarity from **a** to **c** the torque during this period will be negative. From **c** to **d** the current will continue to increase at the same rate, since there is no change in any of the voltage waveforms, but the produced torque is positive. From **d** to **e** the back EMF decreases linearly while the applied voltage is higher in value and constant. As a result the transformer EMF will increase linearly. This will cause the current to increase in a nonlinear way until it reaches its maximum value.

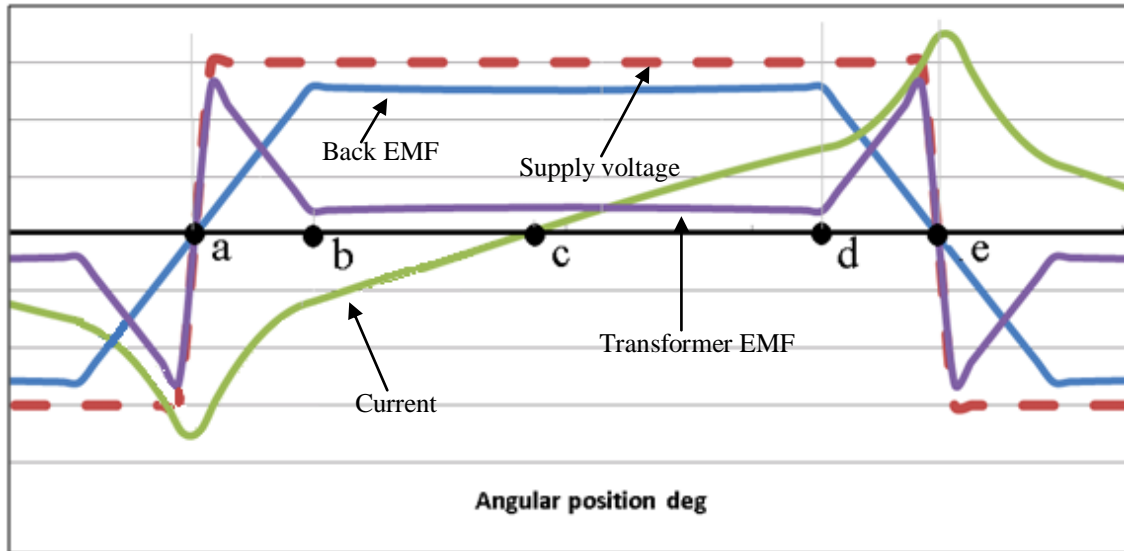


Fig. 7.2 No phase advance condition for 1Ph BLDC motor

The current phase lag can be reduced through phase advancing the commutation signal by an angle that will allow a polarity match between the back EMF and current.

7.3.2 Phase advance to match current polarity with back EMF

In this kind of phase advance the commutation signal is advanced by an amount that will ensure the polarity match between the back EMF and current waveforms as shown in Fig. 7.3. The first cycle of the phase commutation can be divided into four regions. In region **a** to **b** the applied commutation voltage is opposite to the back EMF. This will result in a high level of decaying transformer EMF which forces the current to rise from a negative value to zero at a high rate. In this region the resulting torque will be positive due to the polarity match between the current and the back EMF. From **b** to **c** the current increases from 0A to a peak value. From **c** to **d** the transformer EMF has a negative value that increases up to zero. As a result the current will decrease until the transformer EMF reaches 0v. From **d** to **e** the transformer EMF has an increasing positive value that will cause the current to increase nonlinearly until the end of the commutation cycle at point **e**.

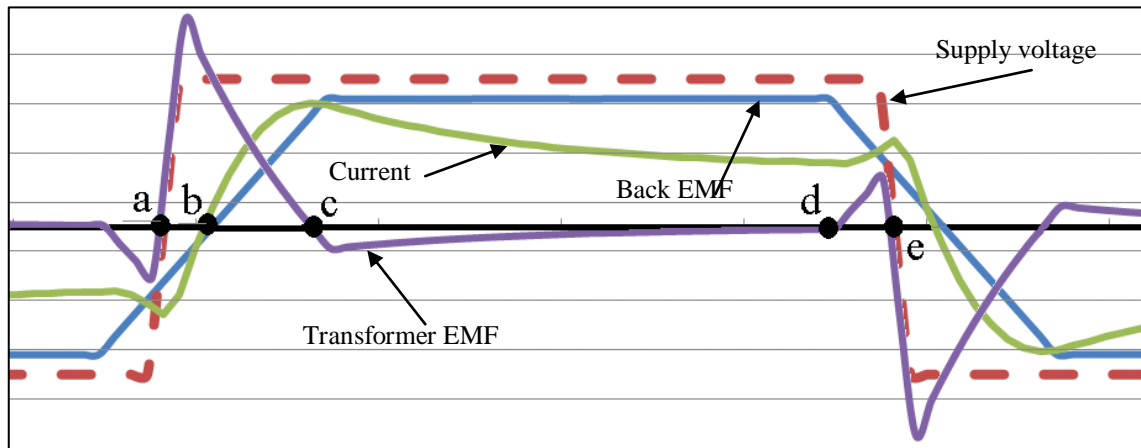


Fig. 7.3 Phase advance with current matching back EMF polarity

7.3.3 Phase advance with current leading back EMF waveform

Principally the maximum speed for a limited supply voltage is when the back EMF equals the supply voltage (ignoring losses) [87]. The only way to have more speed from a fixed supply voltage is by reducing the value of motor constant K_e . In a separately excited brushed DC motor, the motor constant is proportional to the field current and reducing the field current will reduce the K_e of the motor, which is inversely proportional to the speed. This behaviour is called field weakening or flux weakening. Field weakening can be achieved in trapezoidal and sinusoidal back EMF permanent magnet brushless motors. In sinusoidal brushless dc motors a vector control drive is implemented and the field weakening mode can be realized by decreasing the d-axis current. But for a trapezoidal BLDC motor vector control of the d-axis current is difficult [88-90].

In BLDC motors the field source is the rotor magnet which produces a constant magnetic field source. In order to reduce the airgap field K_e has to be reduced. K_e is proportional to rotor radius, stack depth, number of turns, and the operating airgap flux density of the motor. One way to achieve the field weakening effect for a BLDC motor

is by reducing the average air gap flux density which can be achieved by phase advancing the commutation signal.

In this mode the excitation signal is advanced so that the current is in opposite polarity to the back EMF before the rotor reaches the alignment position. The negative current will produce an opposing flux that will cause the effective rotor flux to be weakened. Fig. 7.4 shows the waveforms resulting from field weakening a single phase BLDC motor. The commutation cycle can be divided into 3 regions. In region **a** to **b** the current rises quickly until it reaches 0A. The torque produced will be positive. From **b** to **c** the current is increasing in opposite polarity to the back EMF, which will result in a negative torque being produced before the zero crossing of the back EMF (or alignment position). This negative torque will cause a reduction in the operating point of the airgap flux density. The current then rises up to a maximum value which coincides with the transformer EMF becoming zero. From **c** to **d** the transformer EMF is constant and negative which causes the current to decrease until the next commutation point.

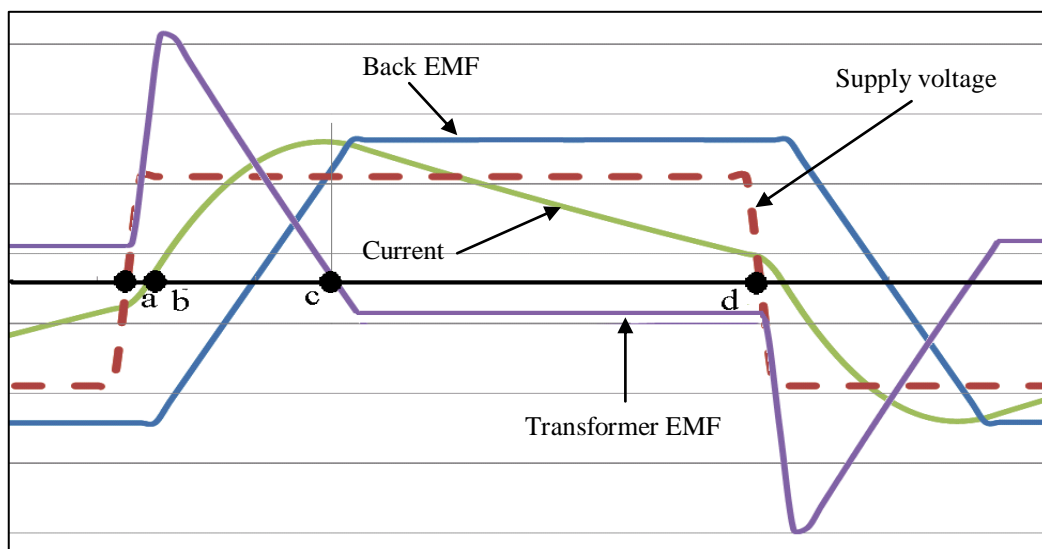


Fig. 7.4 Field weakening waveforms for single phase BLDC motor

Excessive field weakening is disadvantageous to the performance because of the negative torque and excessive current. The minimum advance angle that results in the desired

speed and torque is a reasonable choice. Theoretically the maximum speed occurs at a phase advance angle of 90° . But in practice the speed limit is governed by the reactance of the motor windings [91].

7.4 Phase advance for multi-phase and single-phase BLDC motors

Phase advance control is applied to single phase BLDC and multiphase BLDC motors to optimize their performance. Usually multi-phase BLDC motors employ phase advance commutation for two reasons. 1) to extend the speed range by achieving field weakening. 2) To enhance torque/amp performance. For single phase BLDC motors 180° conduction is used and the phase advance control tends to be used to reduce the current phase lag and not to field weaken, in order to achieve maximum torque/ampere and minimum copper loss.

7.5 Previous work on phase advance control for single phase BLDC motors

Chao [92] was the first to consider applying an automatic phase advance control to a single phase BLDC motor. A phase lead filter was used to adjust the phase of the hall sensor automatically, see Fig. 7.5. The mathematical model that describes the filter is shown in equations 7.1 to 7.3.

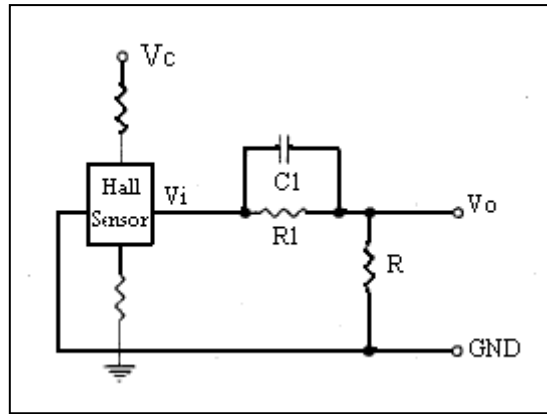


Fig. 7.5 automatic phase advance control by Chao [92]

$$\frac{V_o}{V_i} = \alpha \frac{\tau^s + 1}{\alpha\tau^s + 1} \quad (7.1)$$

$$\tau = R1 C1 \quad (7.2)$$

$$\alpha = \frac{R}{R1 + R} \quad (7.3)$$

In 2000 Zuh et al [86] proposes two methods to improve the performance of a single phase BLDC motor. One using the phase advance method and another by controlling the conduction period of the phase windings. The aim was to eliminate the polarity mismatch between the back EMF and phase current. It concluded that by implementing suitable voltage pulse width conduction the efficiency of the drive will be improved. The width of the pulse is proportional to the speed and inductance of the winding. The problem with this method is that by reducing the width of the current conduction period the available power from the supply is reduced.

In 2007 Lijian et al [93] calculated the optimum advance angle by using a developed linear steady state model instead of a dynamic model. The advantage of the linear model over the dynamic model is the reduction of computational time without sacrificing ac-

curacy. It had two optimization objective; 1) a high output power, 2) a low current ripple. The drawback of this method is that a look up table must be used in the algorithm which means a new lookup table is needed if the algorithm is to be applied to another motor with different parameters.

In 2007 Jian [94] proposed a low cost hardware circuit to advance the commutation signal. The phase advance was achieved by delaying the hall sensor signal which is mechanically advanced. The delay is based on an RC circuit, and was inversely proportional with the speed. The drawback of this method is that delay circuit parameters depends on the motor and that restricts the applicability of this method to another motor with different characteristics. Fig. 7.6 shows the hardware delay circuit that was used.

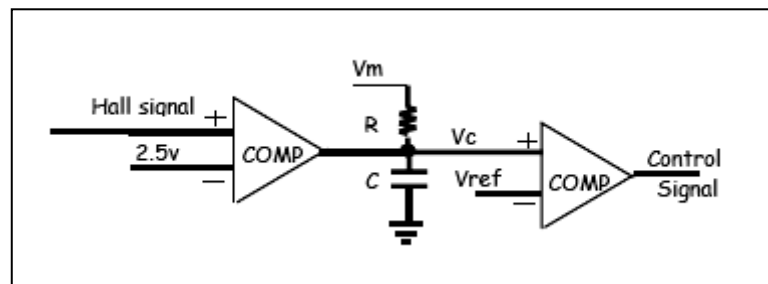


Fig. 7.6 Hardware delay circuit [94]

The delay time was calculated as follows.

$$V_c = V_m(1 - e^{-t/\tau}) \quad (7.4)$$

$$\tau = R C \quad (7.5)$$

$$V_c = V_{ref} \quad (7.6)$$

$$Delay\ time = \tau \ln\left(\frac{V_m}{V_m - V_{ref}}\right) \quad (7.7)$$

In 2009 Chun-Lung[95] proposed a new phase delay circuit that takes into account the harmonic components in the output of the hall sensor, which influences the phase advance of the signal. It states that the harmonic component exists in a sinusoidal output hall sensor and the output is not a pure sine wave. Ignoring the harmonics leads to inaccurate position information. However, this is not a problem for square wave excitation, because the excitation is achieved by a proximity sensor that produces a square commutation signal to drive the power switches.

7.6 A review on phase advance control techniques for multi phase BLDC motors

The first investigation on the suitability of a permanent magnet synchronous motor for field weakening was performed in mid 1980s by Sneyrs [96] and Jahns [97]. Then an attempt to optimize the field weakening performance of an inset permanent magnet rotor was performed by Sabastian and Slemon [98]. The first serious attempt to find the motor parameters that affects the field weakening was made by Schiferl and Lipo [99]. However, they failed to fully normalize the motor parameters to unity rated speed, which lead them to three independent motor parameters instead of two. In 1994 Soong and Miller [100] determined the effect of varying the motor parameters on the field weakening performance but with full normalization. They also introduced a new technique to graphically visualize the effect that the parameter change has on the field weakening performance which they referred to as an IPM (Interior Permanent magnet) parameter plane.

In 1995 Safi [87] was first to phase advance a trapezoidal BLDC to achieve field weakening. In 1995 C. Chan [101] was the first to explain the field weakening behaviour in

relation to the transformer EMF and back EMF and their relation with the supply voltage. In 1998 Jinyun [102] proposed a method based on the transformer EMF to achieve field weakening control, which is simpler than the control method applied to sinusoidal PM motors, because the latter requires coordinate transformation between abc phase variables and d-q variables. Although Fourier series can be implemented to represent the trapezoidal wave by sinewaves, but it is computationally expensive. In 1998 C. Chan [91] was the first to investigate the effect of phase advancement to improve the efficiency for 7 phase BLDC motor. The purpose of the paper was to present an efficiency optimization control system for this motor. The idea was to adaptively control the advance commutation angle to reduce the copper losses in the constant power region. But this paper adopted a linear relationship between the optimum advance angle and speed, which is not the case in practice. J.S. Lawler [103] has identified the limitations on the phase advance control for a BLDC motor. He concluded that there is a minimum value of phase inductance so that the current level does not exceed the rated current of the drive when operating in the constant power region. In another work he proposed an inverter topology, called dual mode inverter [104], which aimed at widening the range of motor inductance to extend the constant power region. In 2007 N. Binh [88] has stated that the relation between the optimum phase advance angle and speed is complicated and can not be approximated by a linear relation as proposed by Chan [101] in 1995. N. Binh [88] also stated that the phase resistance is not always negligible, and based on that fact, an analytical equation to calculate the phase advance angle taking the phase resistance into consideration was developed. In 2010 Safi [87] produced a mathematical expression for the phase advance angle with respect to rms current. A look up table is used to decide on the optimum advance angle for each speed.

The look up table restricts the flexibility of this method when applied to other BLDC motors with different characteristics.

7.7 The new phase advance control method

The way in which phase advance control is applied to a single phase BLDC motor, from the literature review, can be categorised as follows:

- a. Hardware advance circuit based on RC lead filter. The drawback of this method is that the advance angle is not accurately derived, and it is dependant on the motor parameters. Therefore, it is difficult to find suitable values of R and C that will produce an accurate phase delay for a wide range of speed.
- b. Conduction window width control which has the disadvantage of limiting the usage of the available supply voltage.
- c. Look-up table which is implemented by the use a digital signal processor. The drawback of this method is that the look-up table is not portable to other machines with different parameters.

A method that is independent of the motor characteristics was needed. This chapter presents such a new method for phase advance control. The method employs a digital controller that uses a PI controller to control the phase advance angle dynamically. The block diagram for this method is shown in Fig. 7.7.

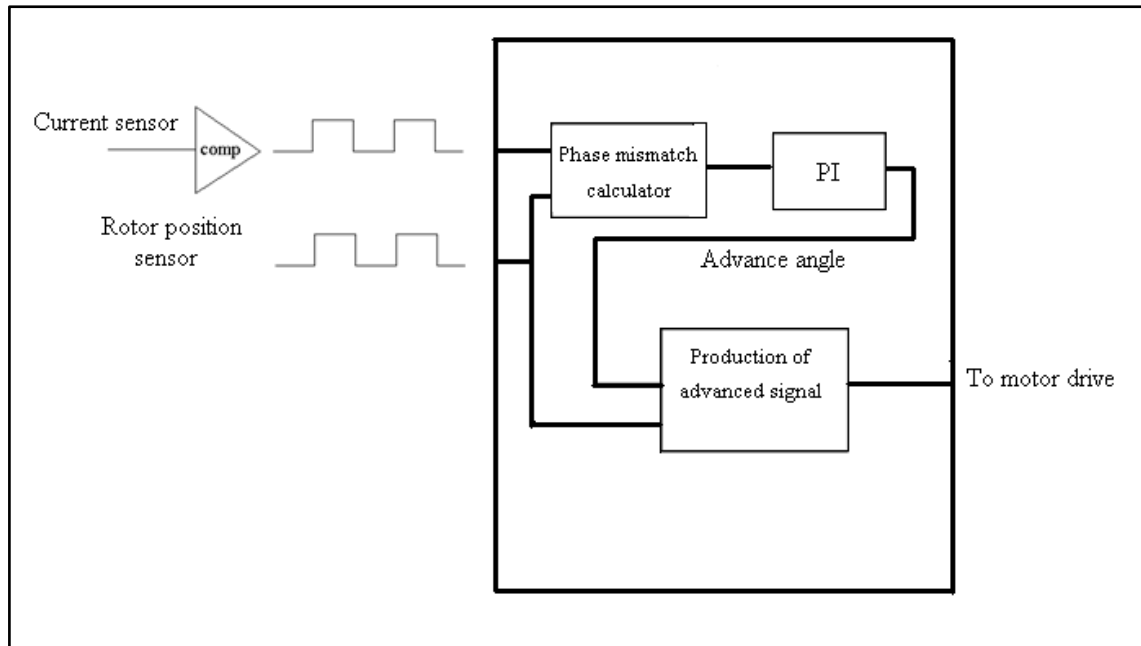


Fig. 7.7 Proposed PI phase advance control

The controller requires two inputs which are the back EMF polarity and current polarity signals. The back EMF polarity signal can be obtained from a position sensor that is positioned at zero advance angle. The current polarity signal is obtained by passing the current sensor signal into a comparator with zero reference voltage. The first stage of the controller calculates the phase mismatch between the back EMF polarity signal and current polarity signal. The phase error is fed into a PI compensator that is connected to a block that produces the appropriate advance commutation signal that achieves minimum phase mismatch error. The production of the advanced commutation signal is with reference to the non-advanced commutation signal, i.e. the back EMF polarity signal. In the following sections a detailed description of each process is presented.

7.8 Phase error calculation algorithm

The function of the phase error calculator is to detect the phase mismatch between the back EMF and current. It has two inputs and one output connected to the input of the PI compensator. One of the input signals is a square wave that represents the polarity of

the back EMF. The other input signal is the current polarity signal. The phase error calculator produces a positive error if the back EMF polarity is leading the current polarity signal and produces a negative error if the current polarity leads the back EMF polarity signal. Fig. 7.8 shows the two cases of phase mismatch.

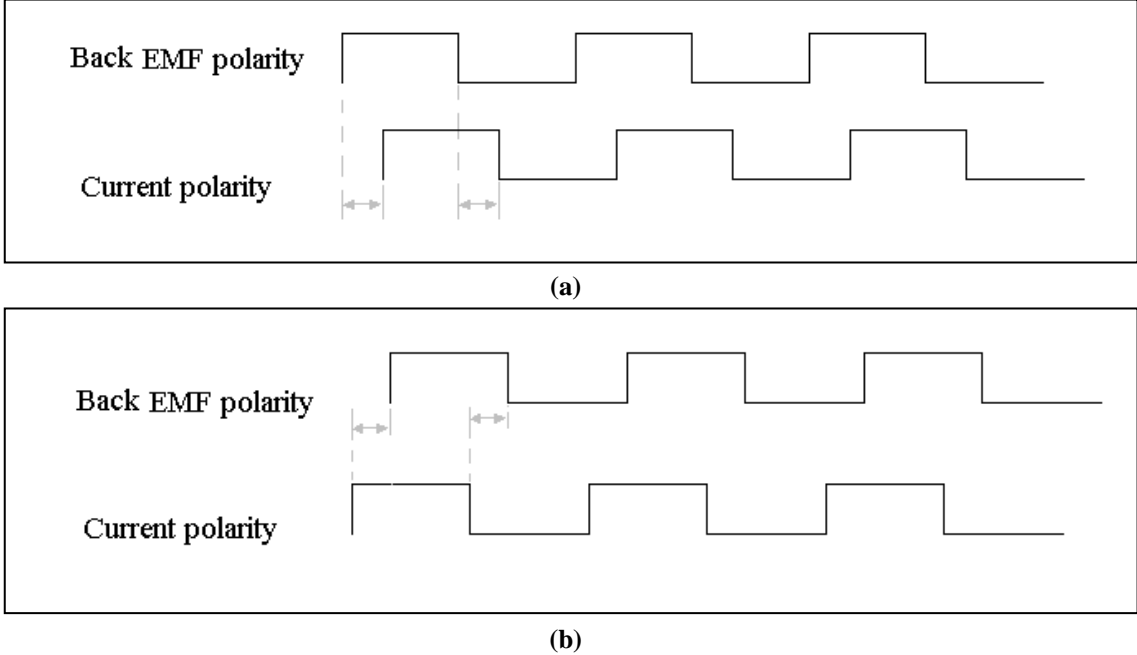


Fig. 7.8 (a) Back EMF leading the current (b) Current leading the back EMF

7.8.1 PI controller

A PI compensator with tuned P I values is used to produce the advanced angle that minimizes the phase error mismatch between the back EMF polarity signal and current polarity signal. The output signal of the compensator represents the advanced angle required which is sent to the advanced commutation signal production block.

7.8.2 Advanced commutation signal production

This part of the phase advance control is responsible for producing the advanced commutation signal. It has two inputs; 1) a reference commutation signal with zero advanced angle and 2) the required advance angle from the PI compensator. Phase advancing the commutation signal is achieved by delaying a signal by θ_{delay} which is calculated from 7.8:

$$\theta_{delay} = 360^\circ - \theta_{desired} \quad (7.8)$$

$\theta_{desired}$ is sent from the PI compensator. Once the desired delay angle is determined the following step calculates the time delay that is needed to achieve this delay angle.

$$\tau = \frac{\theta_{delay}}{360^\circ} \times T \quad (7.9)$$

Where τ is the delay needed in the signal and T is the period of the commutation signal. The last stage is to delay the reference signal by τ seconds.

The new phase advance control method was simulated in Simulink. The method was first implemented on a Simulink motor model then the feasibility of this method was experimentally validated by using the dSpace system to control the commutation angle for an existing single phase BLDC motor.

7.9 Simulink model of a single phase BLDC motor

The mathematical model for the single phase BLDC motor can be described as follows

The voltage equation:

$$v = Ri + \frac{d(Li)}{dt} + \frac{d\lambda_m}{dt} \quad (7.10)$$

The torque equation:

$$T_e = k_t \times i \quad (7.11)$$

Mechanical equations:

$$T_e + T_c = J \frac{d\omega_r}{dt} + B\omega_r + T_L \quad (7.12)$$

$$\omega_r = \frac{d\theta_r}{dt} \quad (7.13)$$

Where

v : supply voltage

R : winding resistance

i : current

L : winding inductance

λ_m : total flux linkage from magnets

T_e : developed electrical torque

k_t : torque constant

J : inertia of rotor

ω_r : rotor angular speed

B : damping ratio (or coefficient of friction)

T_L : load torque

T_c : cogging torque

θ_r : rotor position

The equations 7.10 to 7.13 are well known ordinary equations for single phase BLDC motor. $\frac{d(Li)}{dt}$ is the transformer EMF and $\frac{d\lambda_m}{dt}$ is the motional back EMF.

Fig. 7.9 shows the motor that was used to implement the new phase advance control method. The rated output torque is 0.2Nm. This is an existing single phase BLDC motor prototype.

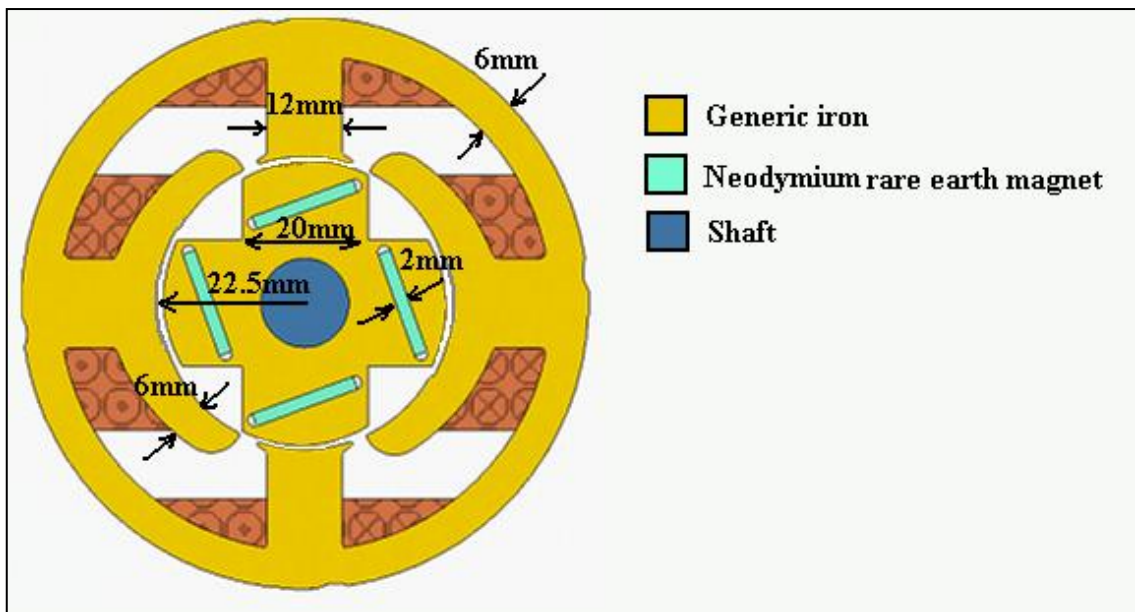


Fig. 7.9 Prototype of single phase BLDC motor

Since the rotor is of salient rotor the inductance of the winding will vary with rotor position and hence equation 7.10 will be

$$v = Ri + i \frac{dL}{dt} + L \frac{di}{dt} + \frac{d\lambda_m}{dt} \quad (7.14)$$

$$\frac{d\lambda_m}{dt} = \frac{d\lambda_m}{d\theta_r} \times \frac{d\theta_r}{dt} \quad (7.15)$$

$$\frac{d\theta_r}{dt} = \omega_r \quad (7.16)$$

$$\frac{d\lambda_m}{d\theta_r} = k_e \quad (7.17)$$

$$\therefore \frac{d\lambda_m}{dt} = k_e \omega_r \quad (7.18)$$

Solving for $\frac{di}{dt}$ will give:

$$i = \int \frac{v - iR - i \frac{dL}{dt} - k_e \omega_r}{L} dt \quad (7.19)$$

Equation 7.19 can be represented in Simulink blocks as shown in Fig. 7.10 .

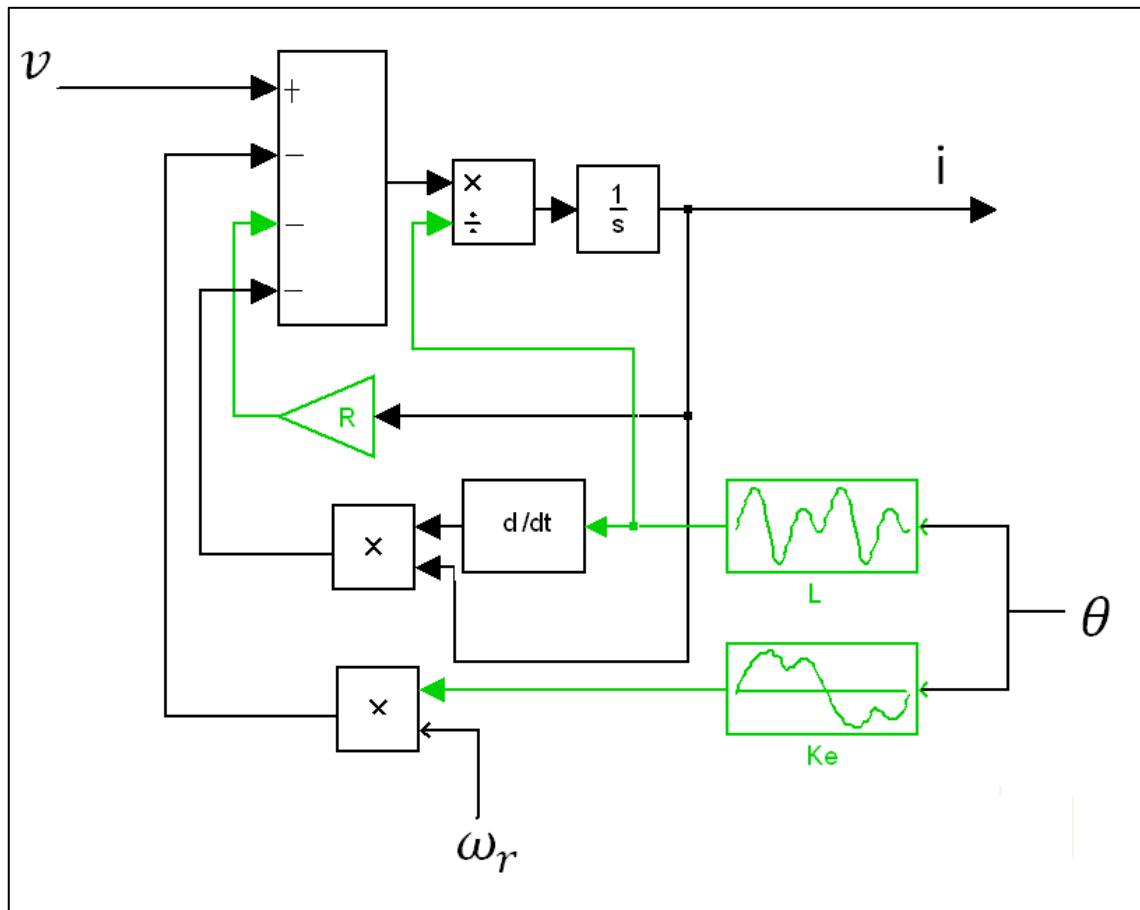


Fig. 7.10 Simulink model of the voltage equation for the prototype motor

Solving for $\frac{d\omega_r}{dt}$ from equation 7.12 will give

$$\omega_r = \int \frac{T_e - B\omega_r - T_L + T_c}{J} dt \quad (7.20)$$

θ_r is obtained from 7.16 as

$$\theta_r = \int \omega_r dt \quad (7.21)$$

Using equations 7.11, 7.20 and 7.21 the Simulink model for the mechanical part of the motor model can be represented as shown in Fig. 7.11.

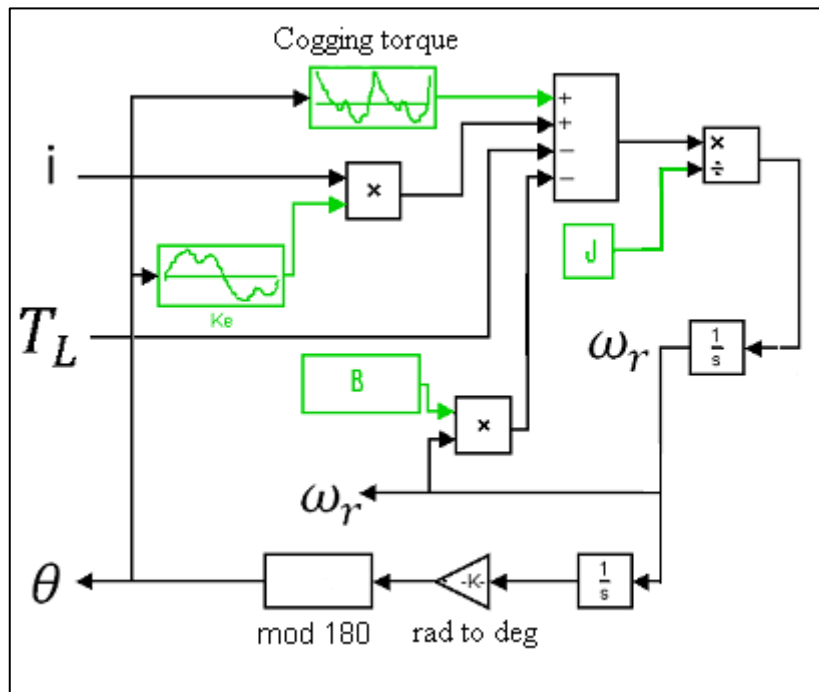


Fig. 7.11 Simulink model of the mechanical equation for the prototype motor

For the BLDC motor $k_e = k_t$, therefore equation 7.11 will become:

$$T_e = k_e \times i \quad (7.22)$$

The tables of k_e , cogging torque and L are obtained from the 2D FEM software with respect to mechanical rotor position. The commutation of the motor in Simulink is achieved as shown in Fig. 7.12. The model represents a zero advanced commutated mo-

tor. The position sensor block produces the appropriate commutation signal based on the angular position of the rotor. The rotor position sensor is modelled as shown in Fig. 7.13.

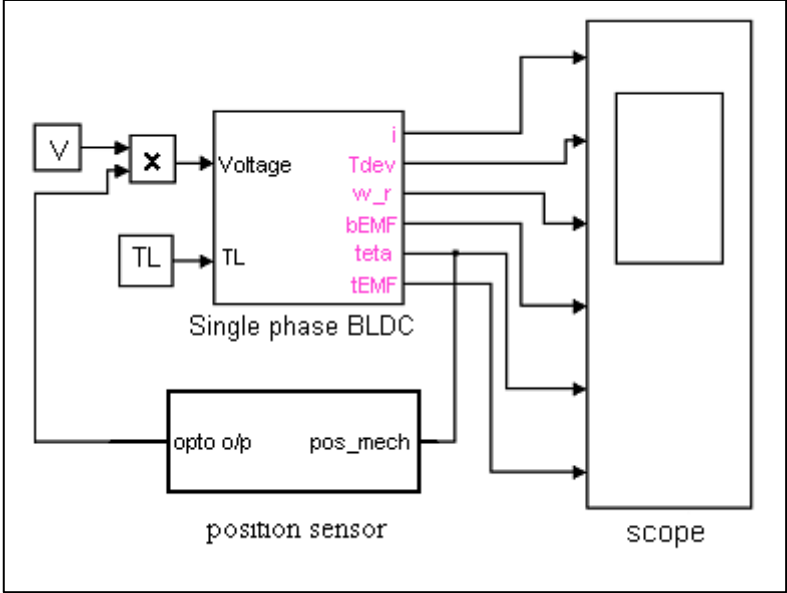


Fig. 7.12 Commutation of single phase BLDC in Simulink

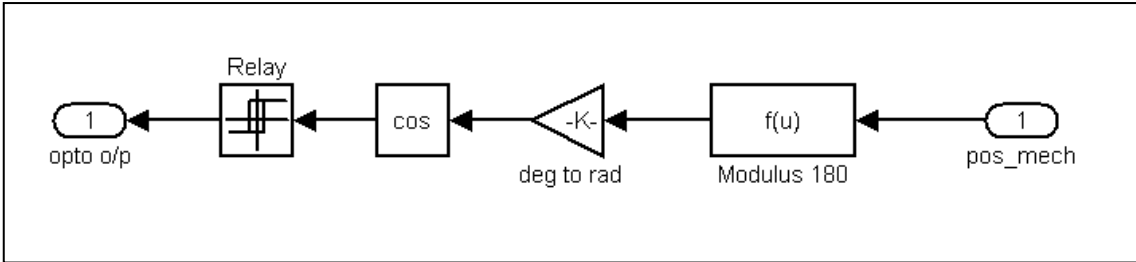


Fig. 7.13 Position sensor model in Simulink

Fig. 7.14 shows the torque speed characteristics at 50v with no phase advance applied. The efficiency-speed and efficiency-torque curves are shown in figures Fig. 7.15 and Fig. 7.16 respectively. It can be seen that the efficiency level at the rated torque is only 40%. The following section shows how the new phase advance control method is implemented in the Simulink model to enhance the efficiency.

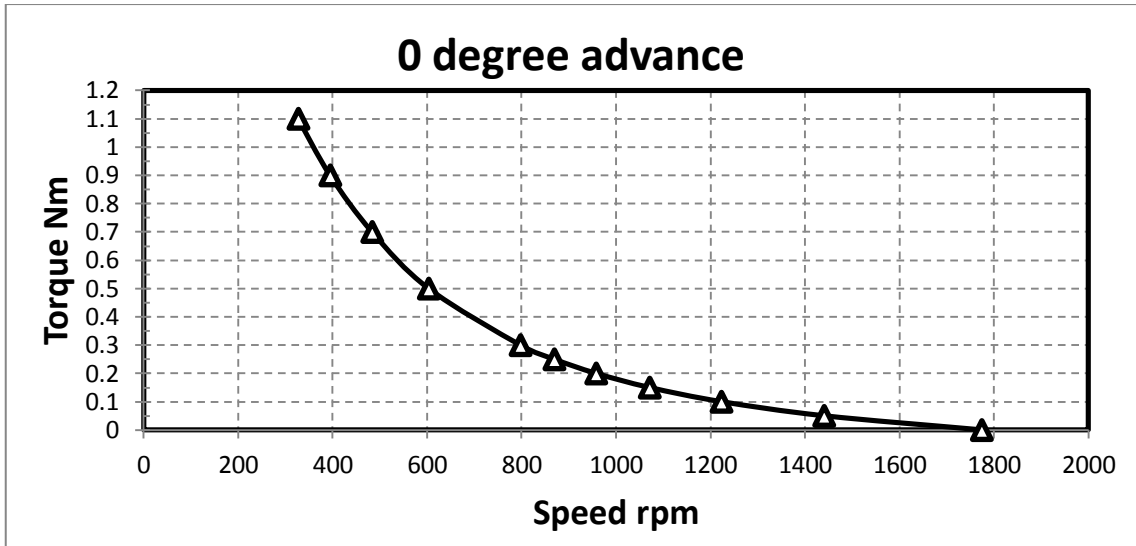


Fig. 7.14 Torque speed curve with no phase advance

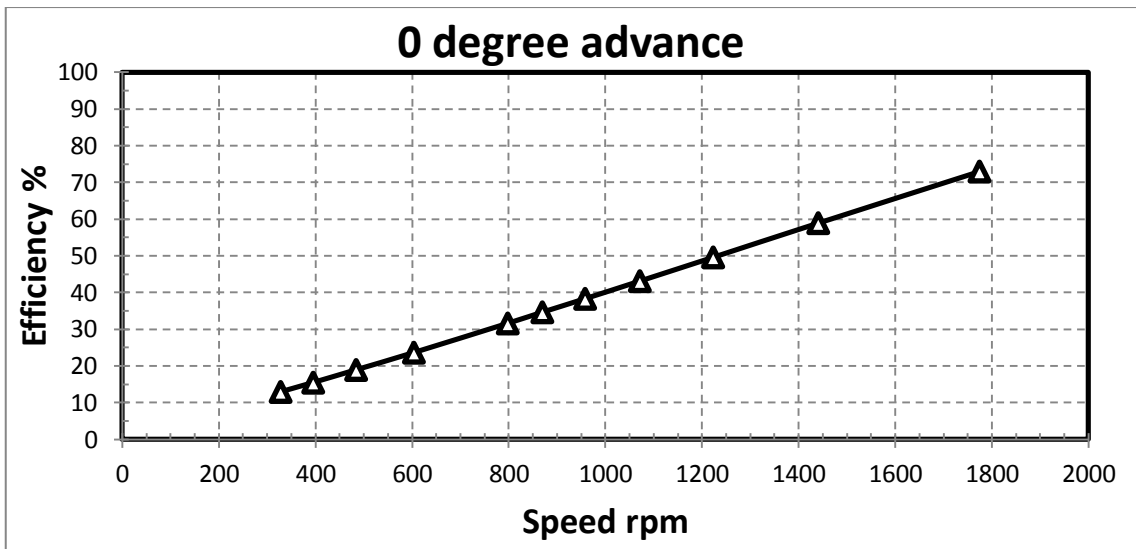


Fig. 7.15 Relationship between speed and efficiency

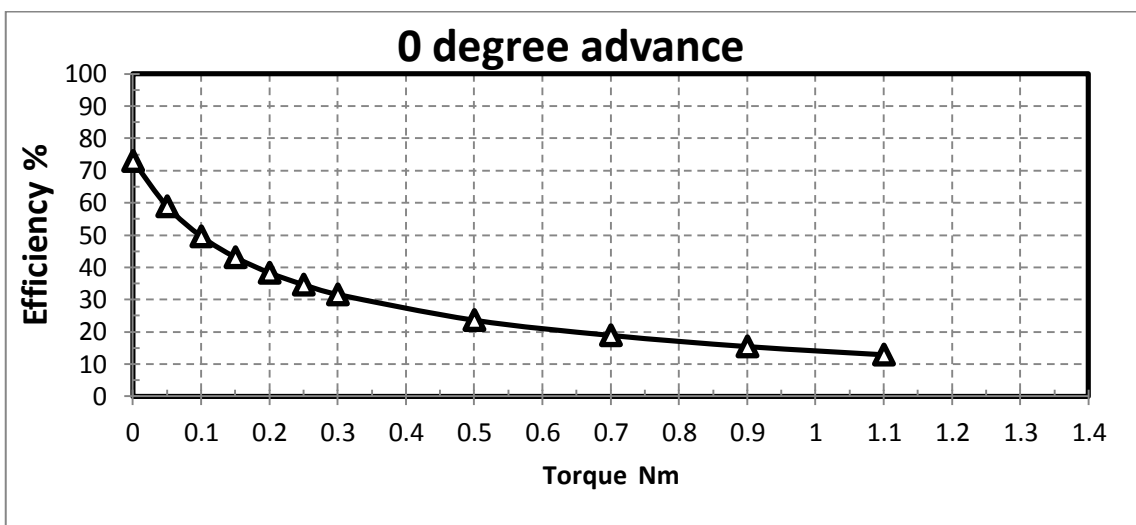


Fig. 7.16 Relationship between torque and efficiency

7.10 Simulink model of the new phase advance control

The new phase advance control is implemented in Simulink as shown in Fig. 7.17.

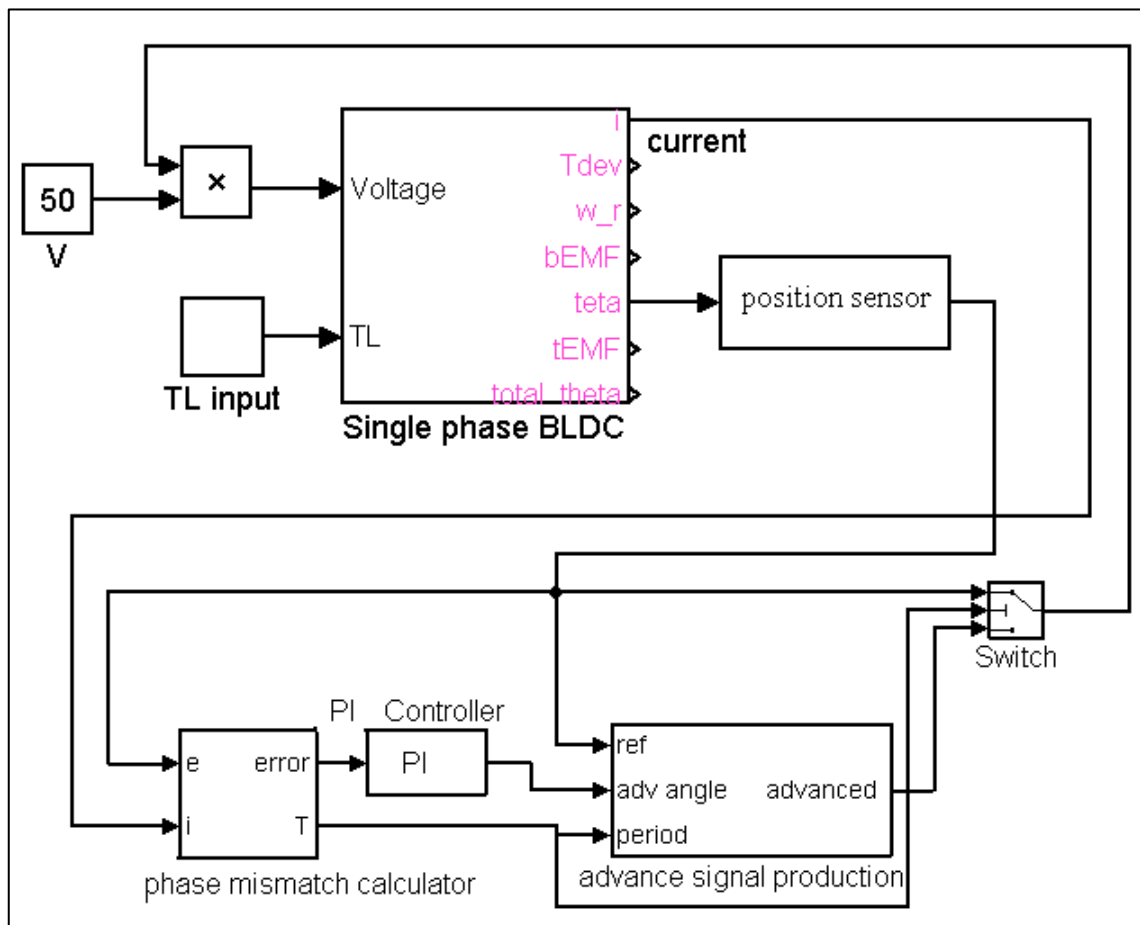


Fig. 7.17 Proposed phase advance control

The first stage of the algorithm is represented by the block *phase mismatch calculator*. The magnitude and polarity of the phase error are calculated in parallel inside the block as shown in Fig. 7.18.

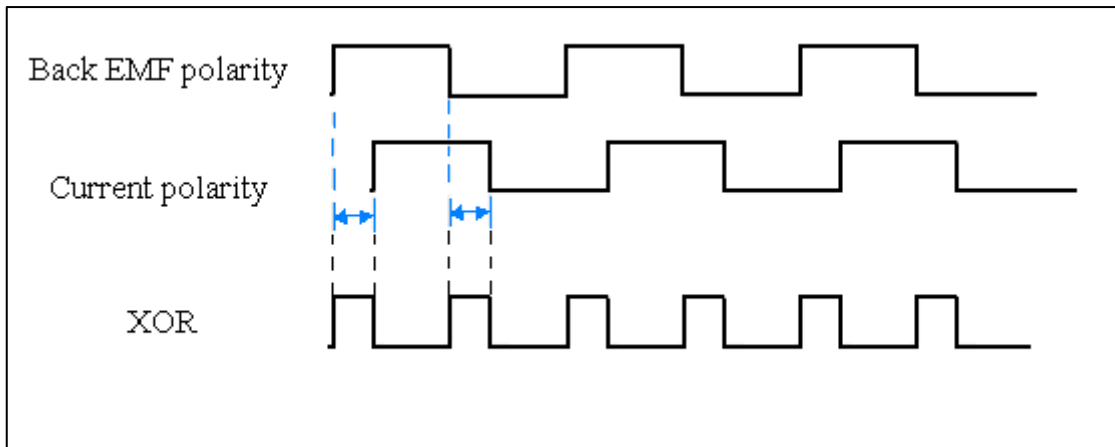


Fig. 7.19 Using XOR gate to determine the magnitude of the delay between the back EMF and current polarity signals

Measuring the pulse width using the Simulink block is achieved by storing the time at every rising edge from the output of the XOR gate and then calculating the duration of the pulse at every falling edge as shown in Fig. 7.20.

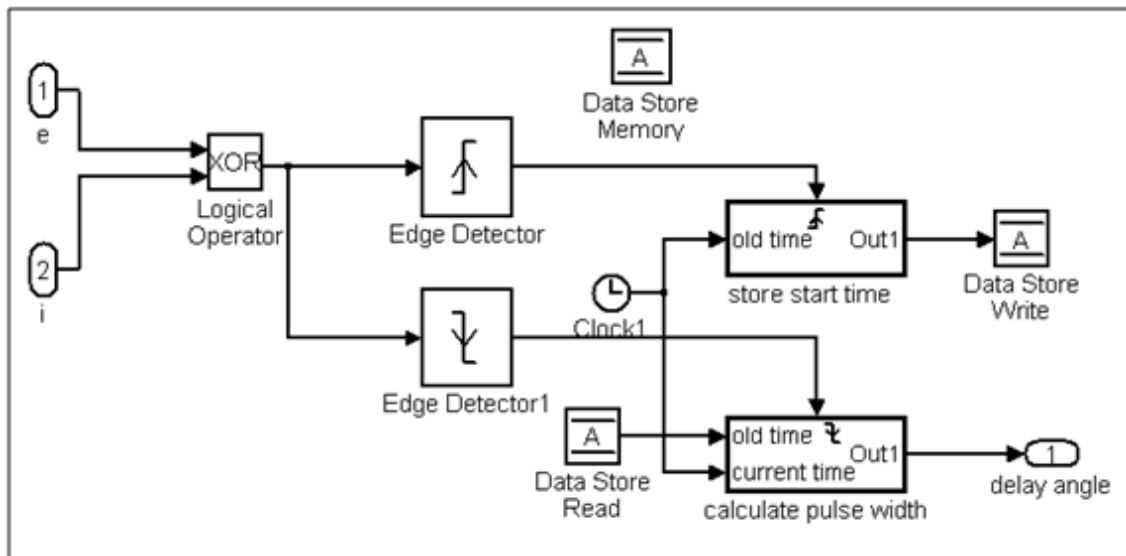


Fig. 7.20 Measuring the delay in seconds between the back EMF and current polarity signals

In parallel with calculating the magnitude of the delay the polarity of the error is calculated. Basically the polarity of the error is determined at every rising edge of the current and back EMF signal. The error should be positive when the back EMF leads the current signal and negative otherwise. At the rising edge of the current signal the back

EMF polarity signal will be read. If the back EMF signal is a logic high, that means the current lags the back EMF and the error will be set to positive. If the back EMF polarity signal is a logic low that means the current is leading the back EMF and the error is set to negative. The same test is implemented at every rising edge of the back EMF polarity just for confirmation although the test at either rising edge will be sufficient to determine the polarity of the error. Fig. 7.21 shows the error polarity determination block.

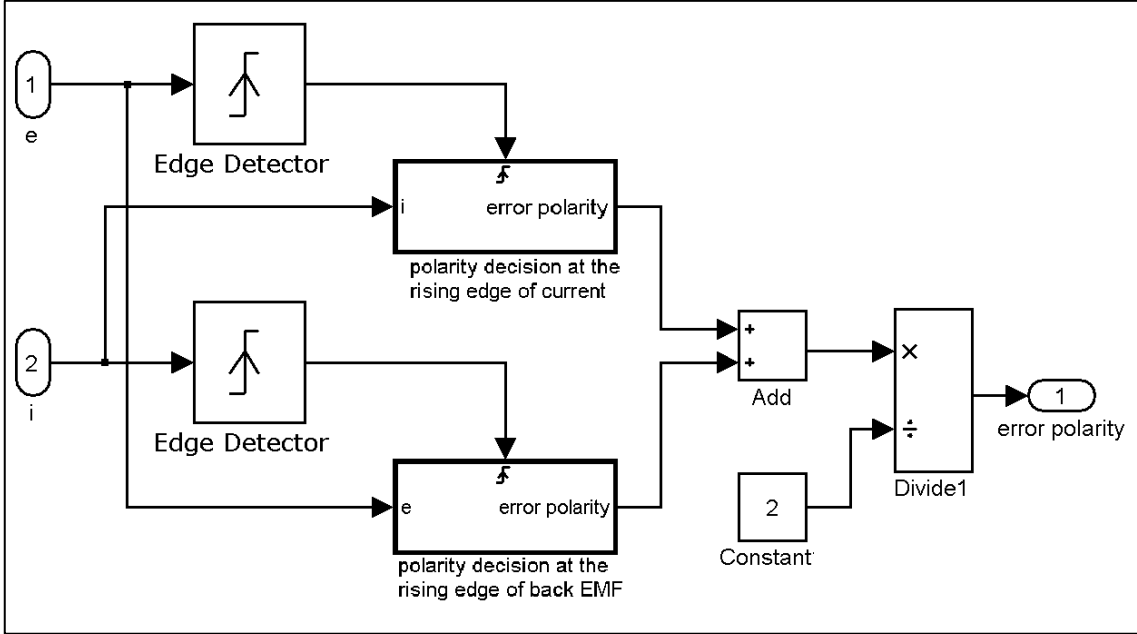


Fig. 7.21 Error polarity determination blocks

7.10.2 Phase mismatch by Simulink embedded function

The phase mismatch process can also be implemented by using the Matlab Embedded function in Simulink. The flowchart of the embedded code that determines the magnitude and polarity of the phase mismatch error are shown in Fig. 7.22 Fig. 7.23 respectively. The full code is available in appendix 9.5 and 9.6.

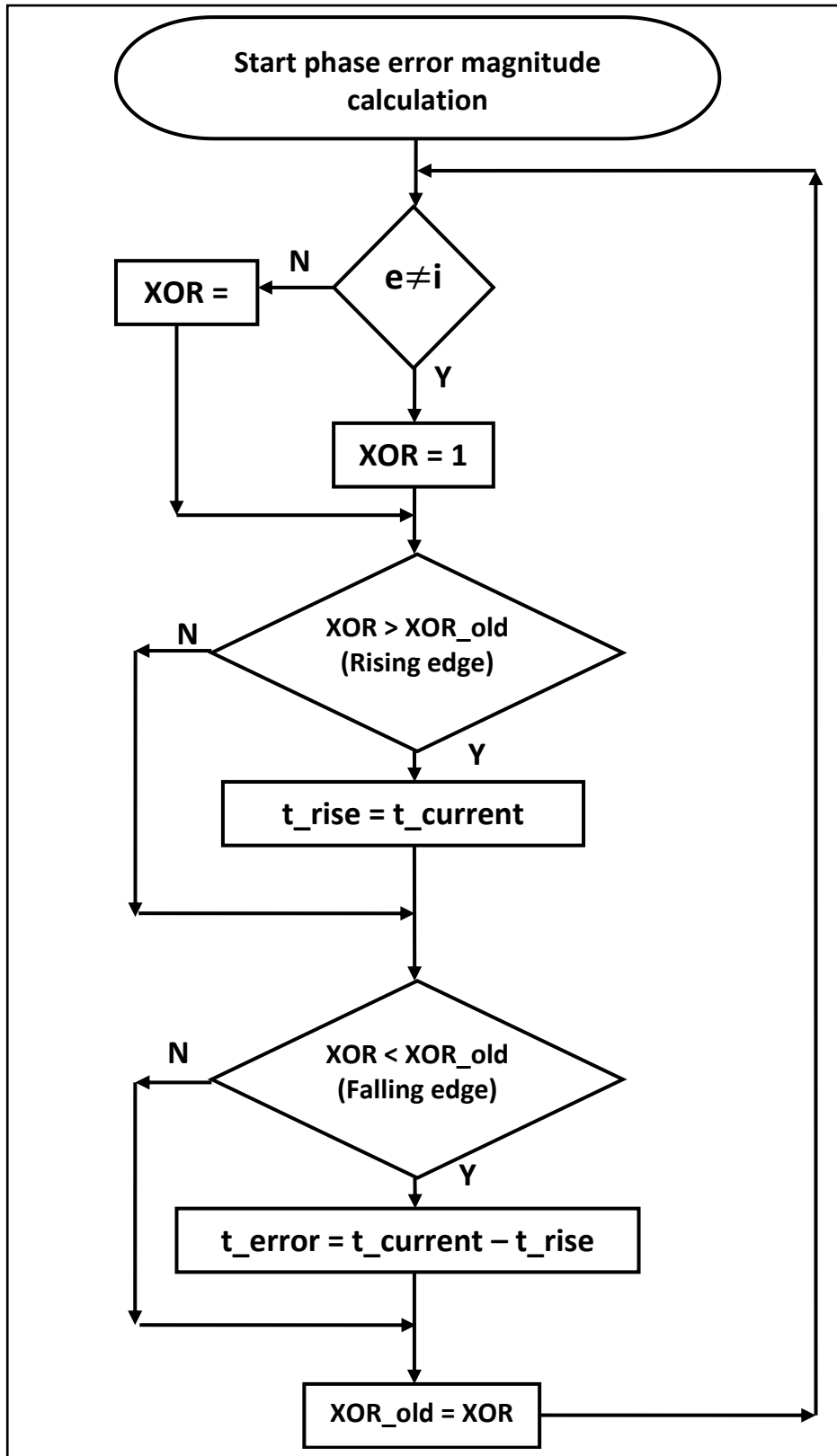


Fig. 7.22 Flowchart of calculating the delay between the back EMF and current

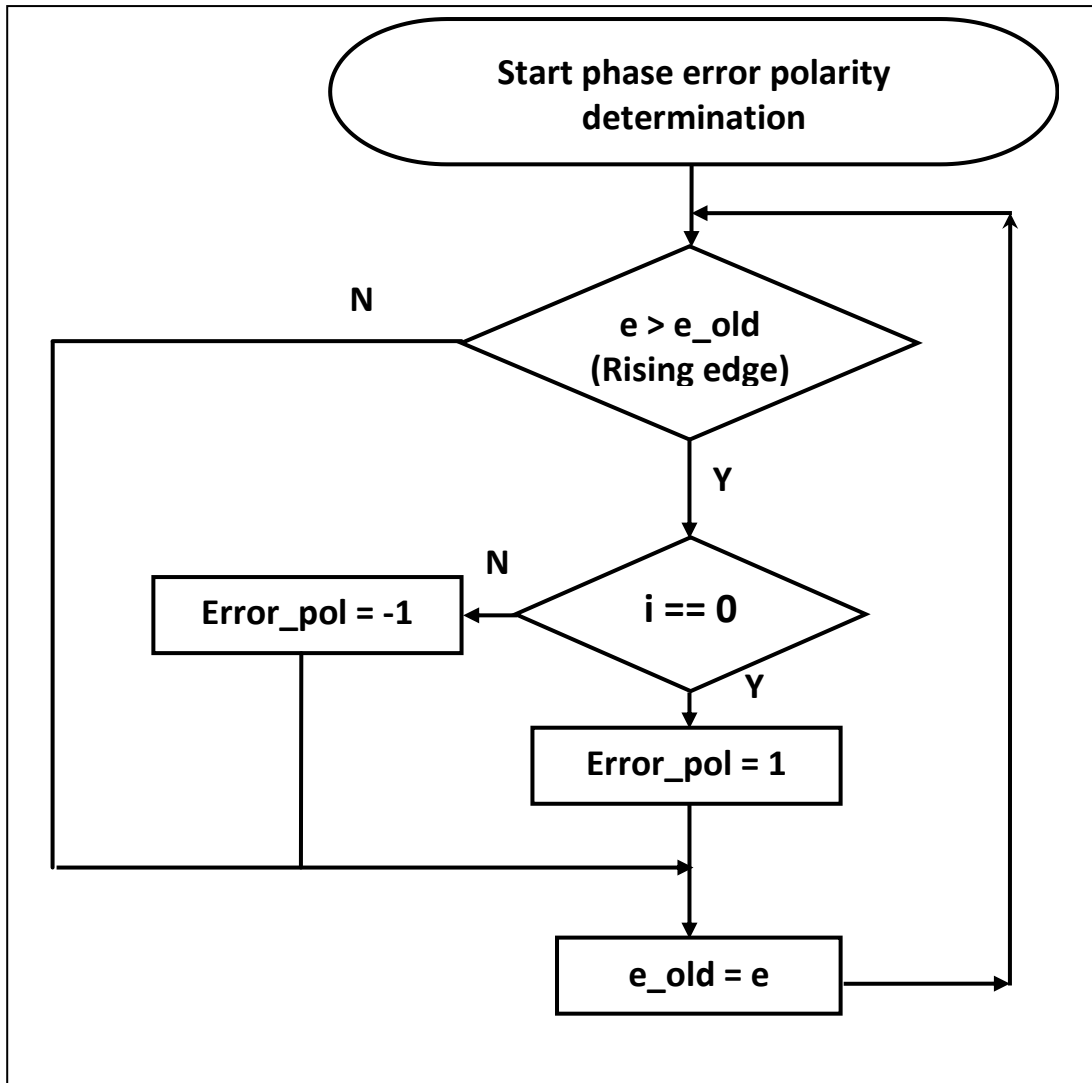


Fig. 7.23 Flowchart of error polarity determination

7.10.3 Advanced commutation signal production

This is the stage where the advanced commutation signal is produced. In this process the block from the Simulink block library *Variable Time Delay* is used. The block has a data input, a time delay input, and a data output. The block's output at the current time step equals the value of its data input at a previous time equal to the current simulation time minus a delay time specified by the block's time delay input [105]. So the output from this block is the delayed version of the reference signal that is delayed by an amount equal to the required delay angle from the PI compensator. The block uses

equation 7.9 to calculate the delay necessary in seconds that correspond to the required advance angle sent from the PI compensator. See Fig. 7.24.

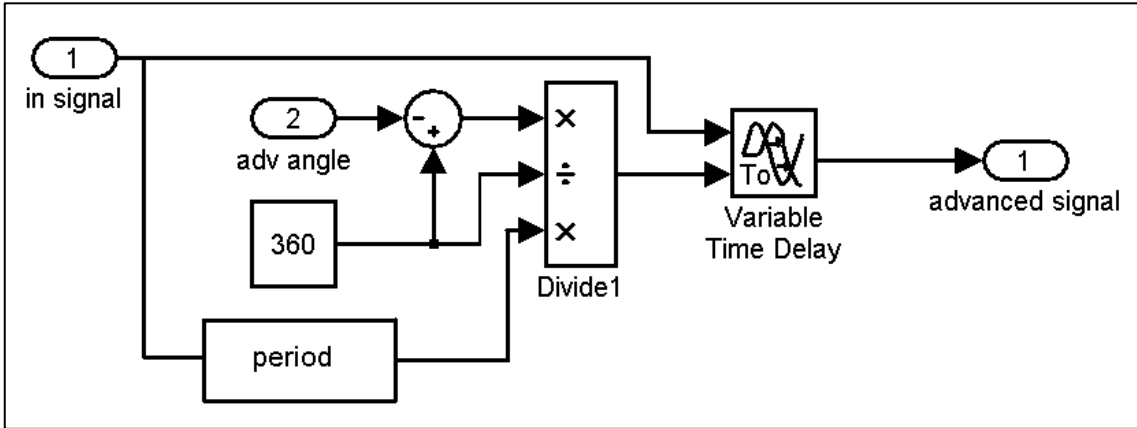


Fig. 7.24 Advanced commutation signal production

7.11 Simulink results of the proposed phase advance control

Fig. 7.25 and Fig. 7.26 show the motor waveforms with and without the proposed phase advance control respectively. The results are obtained with the supply voltage set to 50v and load torque 0.2Nm. It can be seen that with no phase advance the current lags the back EMF and the mismatched polarity between them has created a negative torque. When the proposed phase advance control method is implemented the back EMF polarity matches with the current polarity and no negative torque is produced. Therefore implementing the proposed method has improved the performance and efficiency of the motor which is apparent at a higher speed and a lower level of current for the same supply voltage and load torque.

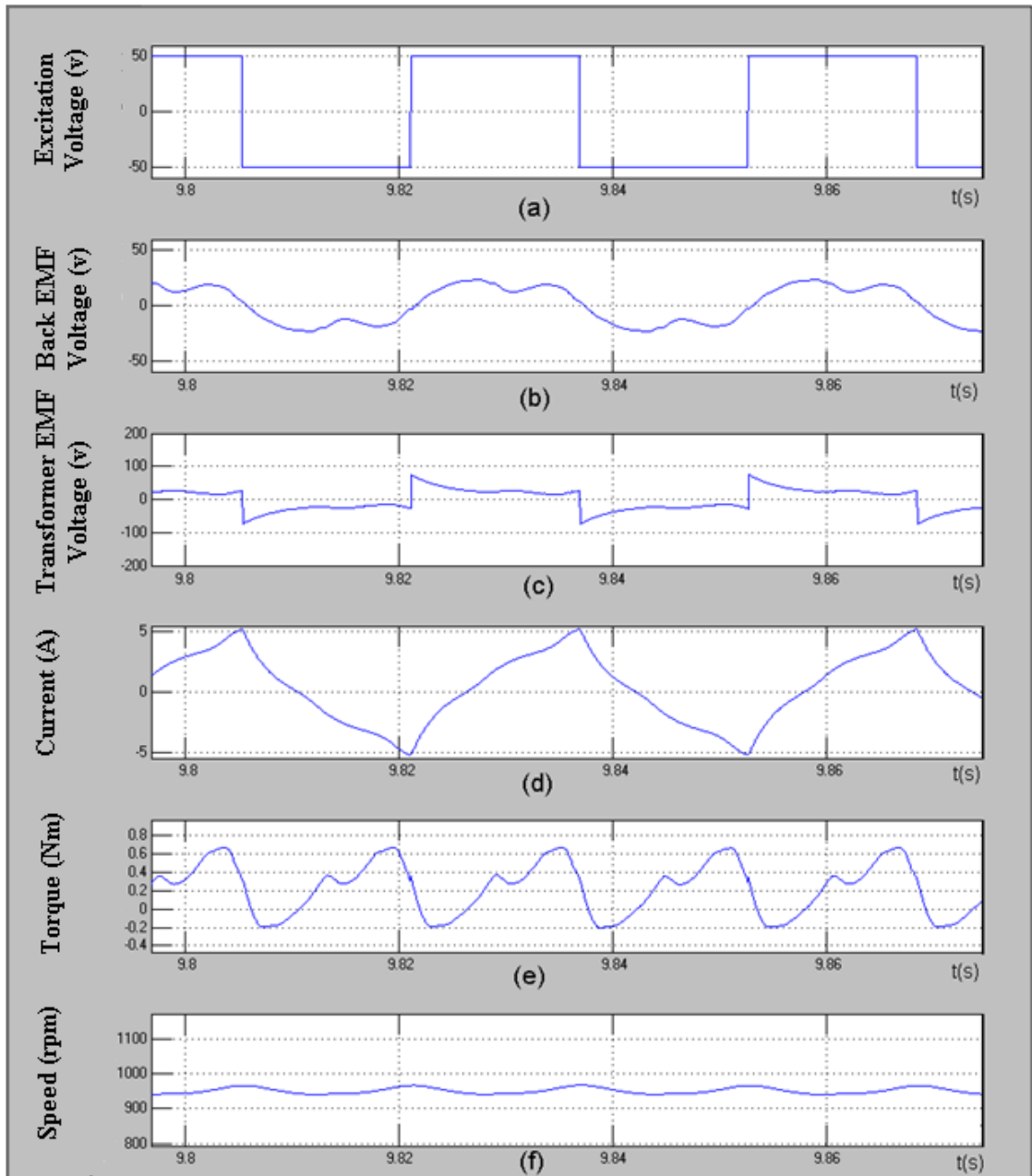


Fig. 7.25 Simulation results of a 0° advanced commutation

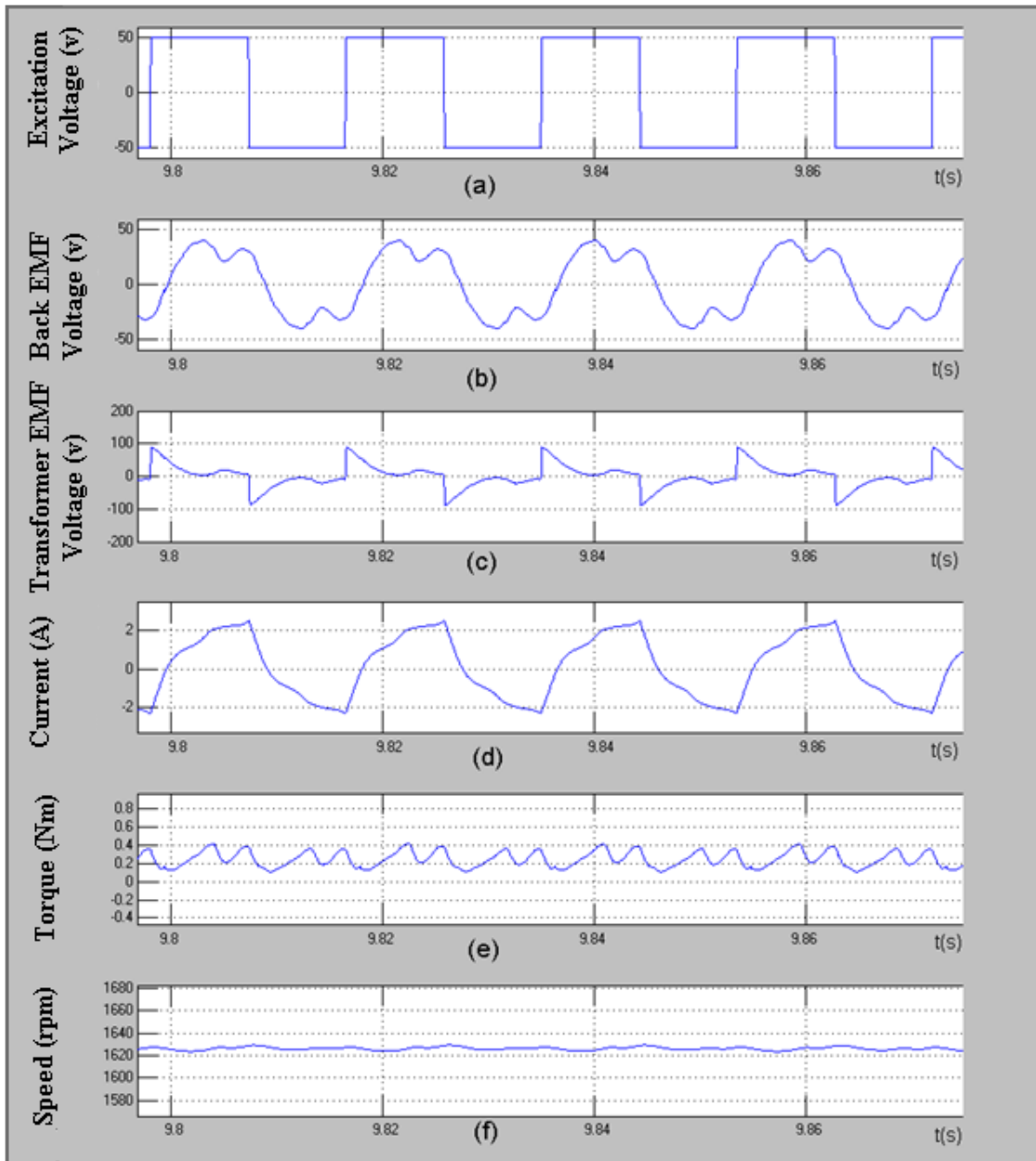


Fig. 7.26 Simulation results with the new phase advanced commutation

Fig. 7.27 Fig. 7.28 compares the torque speed curves for the same motor with and without the proposed phase advanced control. It is clear that employing the proposed phase advance control has shown an improvement in the torque speed characteristics and efficiency of the motor.

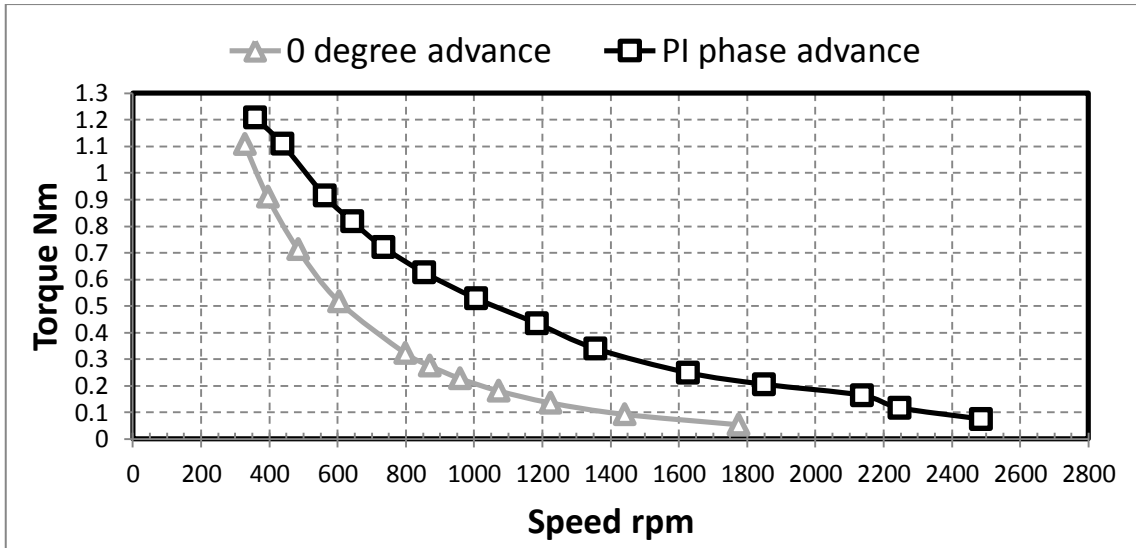


Fig. 7.27 Torque-speed curve with and without proposed phase advance control

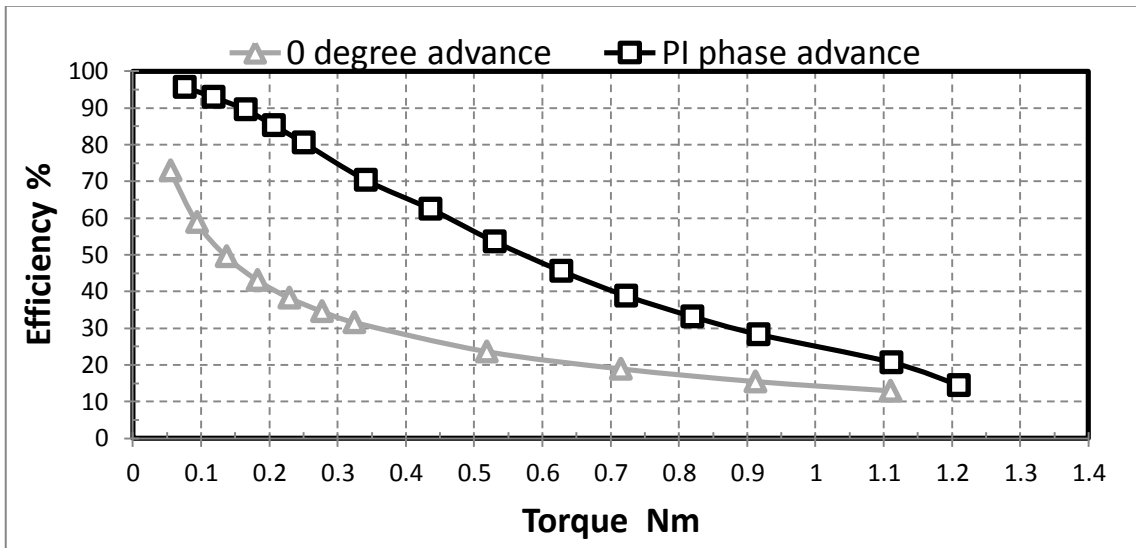


Fig. 7.28 Efficiency-torque results with and without phase advance control

7.12 Practical implementation

The feasibility of the new phase advanced method has been validated experimentally. dSpace was used to implement the proposed algorithm. dSpace has the advantage of transforming the Simulink blocks into a code that is programmed into a built in powerful digital signal processor DSP. A simplified circuit diagram for the whole system is shown in Fig. 7.29.

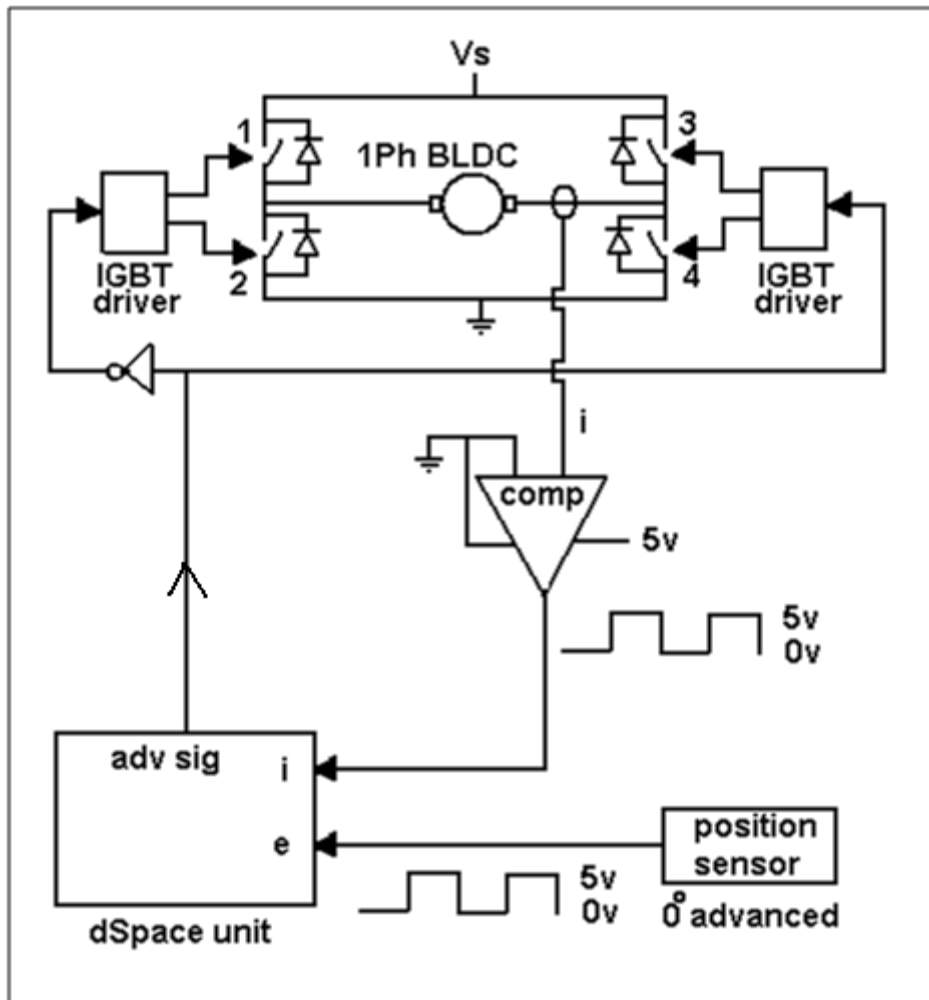


Fig. 7.29 Interfacing the motor with dSpace

The Simulink model presented in Fig. 7.17 has to be updated. The single phase motor block is replaced with a dSpace interface blocks as shown in Fig. 7.30.

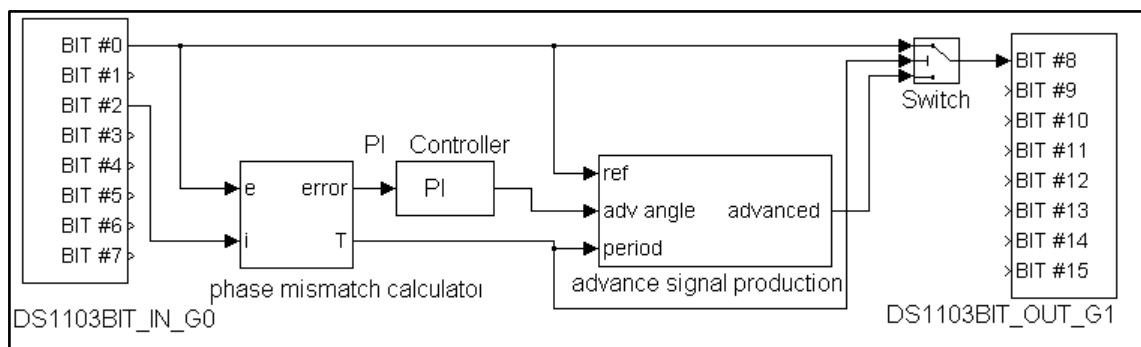


Fig. 7.30 Updated Simulink block for dSpace interface

The output from the position sensor is connected to the dSpace pin number 0 and the current polarity signal is connected to pin 2. Pin number 8 is the output from dSpace which produces the advanced commutation signal and it is connected to input of the H-bridge drive.

Fig. 7.31 shows the back EMF polarity, current polarity and current waveforms of the motor with supply voltage of 50v and average load torque of 0.2Nm. The current probe is set to 2A/10mv. The result agrees with the results produced by the Simulink model, see Fig. 7.25. Fig. 7.32 shows the motor waveforms with the proposed phase advance control implemented. The result agrees with the simulation results produced by Simulink, see Fig. 7.26. The experimental set up is shown in Fig. 7.33 and Fig. 7.34. More photos are available in appendix 9.7.

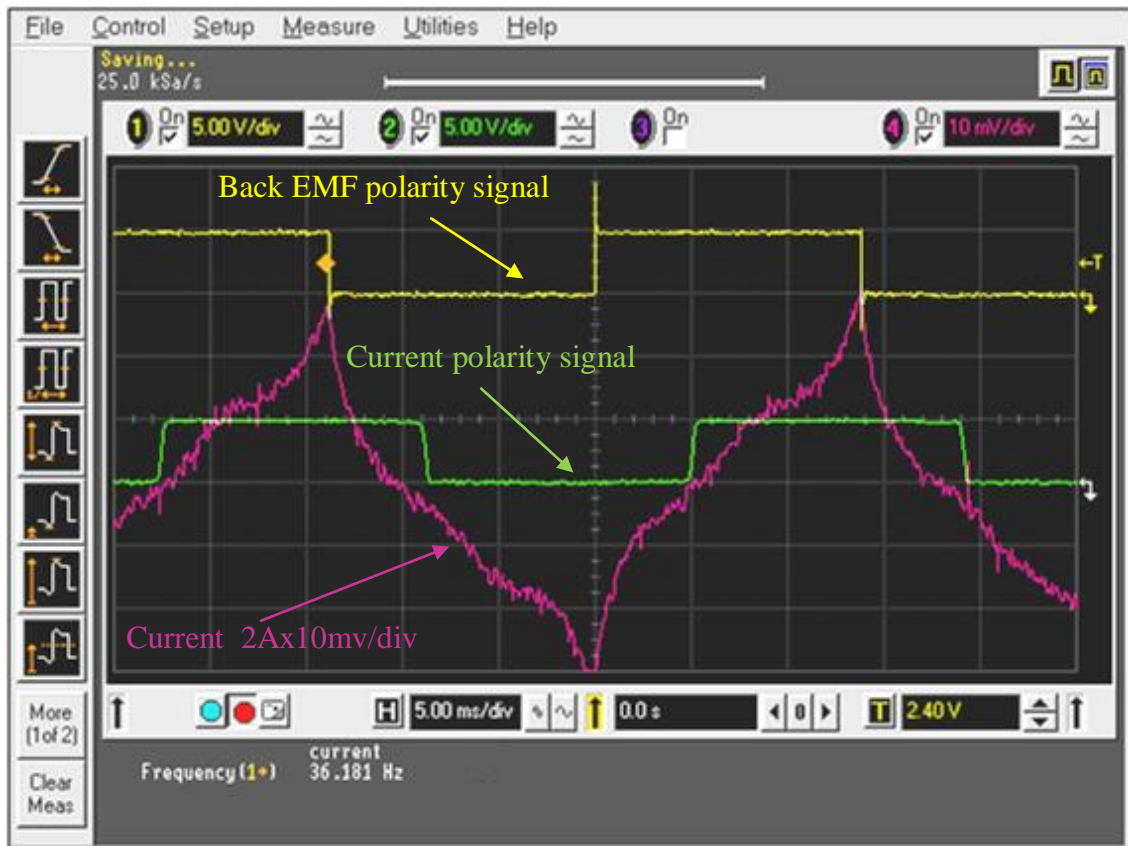


Fig. 7.31 Experimental waveform results with no phase advance $V=50\text{v}$ $T_L=0.2\text{Nm}$

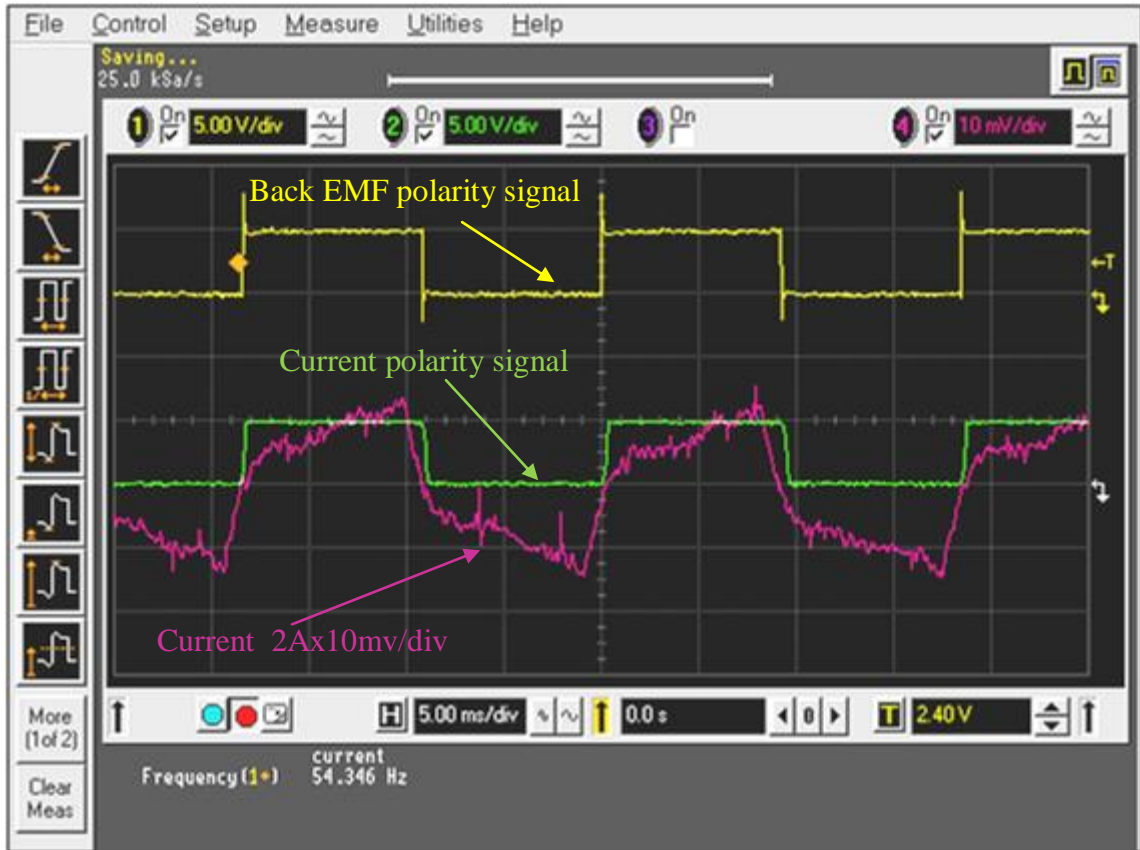


Fig. 7.32 Experimental waveform results with proposed phase advance $V=50v$ $TL=0.2Nm$

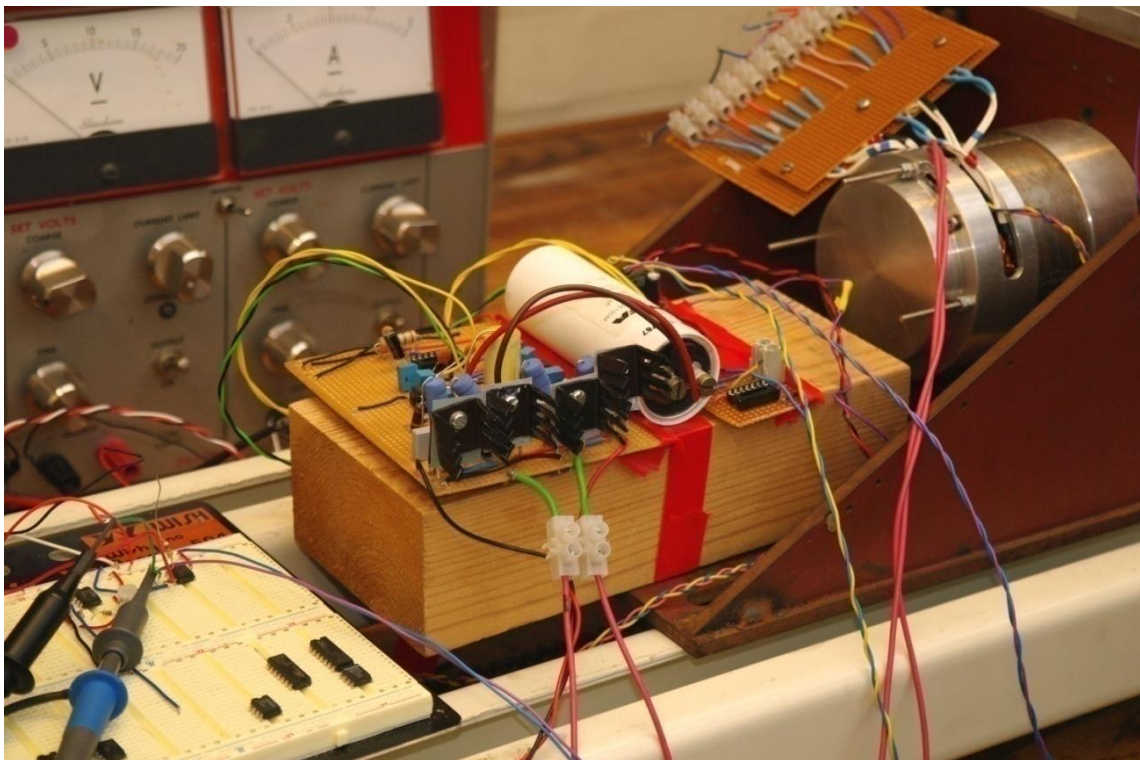


Fig. 7.33 Experimental motor and drive



Fig. 7.34 Practical implementation of proposed phase advance with dSpace

7.13 Discussions and conclusions

In this chapter a new phase advanced control method is presented to solve the problem of current polarity mismatch between the back EMF and current signal. The polarity mismatch reduces the performance and efficiency of the motor. Employing the proposed phase advanced control has improved the efficiency and torque/amperes of the motor and this has been verified by simulation and experiment. The main advantage of this method is in its non-complexity and its independency of motor parameters. The improvement in the efficiency is due to the reduction in the rms current for the same load conditions. The advance commutation angle was generated by delaying a reference signal by an amount that is proportional with speed. Due to the absence of error signal at zero speed the new method will not be able to produce the advanced commutation signal. To solve this problem the proposed phase advance method is designed to buffer the reference input signal at very low speeds. The phase advance control is not needed at very low speed because the current phase lag is negligible. Therefore the phase advance

angle control is programmed to start to function when the speed exceeds a preset threshold value. This adds more stability to the algorithm since generating an advanced commutation signal at zero speed is not possible

8. Conclusions

The original aim of this research work was to investigate into ways of improving various aspects of single phase PM BLDC motors. The research started with identifying the areas and characteristics of the motor, drive, and control system, which were deemed poor or deficient for this type of motor. Particular consideration has been given to the following three areas:

1. Open circuit torque
2. Encoderless control
3. Phase advance control

In the next section the conclusions derived from the work conducted in each area are presented.

8.1 Open circuit torque improvement

Since the open circuit torque of a single phase BLDC motor is due to the slot openings and the uneven airgap topology, the improvement of the open circuit torque was conducted in two stages. In the first stage, a study on the effect on an asymmetrical stator and rotor pole topology was conducted to reduce the open circuit torque due to the slot openings. It was found that employing a stator asymmetry of 1:3 and rotor magnet arc length that coincided with the shorter stator pole arcs, the slot cogging torque was reduced while maintaining the trapezoidal shape of the back EMF. This was confirmed analytically and numerically.

The second stage of the open circuit torque improvement was to improve the starting torque capability at any rotor position, and with reduced torque ripple. For this a study of the effects of notches in the stator iron was performed. The characteristics of the

notches, the depths and widths, have been investigated and their effect on the open circuit torque was understood. The study presents a valuable contribution to the knowledge about the influence of an asymmetrical distribution of notches on the open circuit torque. From these investigations the following was concluded:

1. Every single notch in the stator iron has an independent contribution to the open circuit torque.
2. Distributing different notches of variable depths and widths will enable the improvement of the open circuit torque characteristics (efficient starting torque with low ripple in the unaligned rotor/stator regions).

8.2 Encoderless control method

A new encoderless control method has been created. The method has the following advantages:

1. Can detect the rotor position for any surface or interior permanent magnet motor even at zero speed.
2. Not dependent on rotor saliency.
3. Increased reliability due to the absence of a semiconductor sensor.
4. No influence from the main excitation flux.

The new encoderless method has been verified analytically with Simulink and numerically with a 2D FE model.

8.3 Phase advance control

It was demonstrated that a relatively simple and hence low cost motor hardware system could be controlled via the proposed phase advance control method to provide maximisation of performance, efficiency and flexibility of application. The outcome of this re-

search work was a new phase advance control system for a single phase BLDC motor that has the following advantages:

1. The control algorithm is independent of the motor parameters and hence the control does not require a look up table of speed versus advance angle, as is the case with some currently used methods.
2. The PI controller that tracks the maximum torque/ampere advance angle is straightforward.
3. The existing position sensing algorithm can be used without the need to introduce additional position sensors.

8.4 Key contributions

Finally, it is worthy to mention that the most important contributions in this research work are:

1. Presented an analysis on the effect of asymmetrical topology for single phase BLDC motor on the open circuit torque and back EMF shape.
2. A new way of open circuit torque improvement by an asymmetrical distribution of notches to enhance the starting torque and reduce the torque ripple due to the slot openings.
3. New encoderless control method for single phase BLDC motor.
4. New phase advance control method for single phase PM BLDC motor that is independent on motor parameters.
5. Literature review on three areas of research that contain a compilation of useful knowledge and materials for others working in the same area. The three areas are:
 - a. Cogging torque reduction methods.
 - b. Phase advance control methods for permanent magnet BLDC motor.

- c. Encoderless control methods for permanent magnet BLDC motors.
- d.

8.5 List of Publications

- S. Ahmed and P. W. Lefley, "A new simplified sensorless control method for a single phase SR motor using HF signal injection," in *Universities Power Engineering Conference, 2007. UPEC 2007. 42nd International, 2007*, pp. 1075-1078.
- S. Ahmed and P. Lefley, "Development of a Single Phase PM BLDC Motor from a Novel Generic Model", in *11th. Spanish-Portuguese Conference on Electrical Engineering 2009*.
- S. Ahmed and P. Lefley, "Study of the impact of asymmetrical stator pole arc on the cogging torque for single phase Permanent Magnet BLDC Motor," in *Electric Power and Energy Conversion Systems, 2009. EPECS '09. International Conference on*, 2009, pp. 1-4.
- P. Lefley, L. Petkovska, S. Ahmed, and G. Cvetkovski, "Finite element analysis of a novel single phase permanent magnet brushless DC motor," in *Power Electronics and Motion Control Conference (EPE/PEMC), 2010 14th International*, pp. T4-96-T4-101.

9. Appendix

9.1 MEPS

The EU MEPS (European Minimum Energy Performance Standard) scheme sets mandatory minimum efficiency levels for electric motors introduced into the European market. The scheme covers 2, 4 and 6 pole single speed, three-phase induction motors from 0.75kW to 375 kW, rated up to 1000 Volts and will come into effect in three stages from June 2011 onwards.

16 June 2011 - Minimum efficiency requirement at IE2 for all motors covered 0.75 – 375kW

1 January 2015 - Minimum efficiency requirement at IE3 for 7.5 – 375kW motors alone, or IE2 level if fitted with a variable speed drive (inverter)

1 January 2017 - Minimum efficiency requirement at IE3 for 0.75 – 375kW motors alone, or IE2 level if fitted with a variable speed drive (inverter)

Replacing the voluntary CEMEP scheme, the mandatory EU MEPS scheme defines the following efficiency classes according to the new IEC 60034-30 standard.

What efficiency level and class will be used?

In order to inform buyers transparently on the motor quality a number of standards are in use. For the purpose of energy efficiency different classification schemes have been used so far:

CEMEP-EU 1999	Eff1 / Eff2 / Eff3 (based on IEC 60034-2:1996)
USA	EPAAct / NEMA Premium (based on IEEE 112B)
Australia	Minimum Efficiency/High Efficiency (based on IEC 60034-2:1996 or IEEE 112B)
China	Grade 1, 2 and 3 (based on GB/T 1032 which is similar to IEC 60034-2:1996)

In 2007 a project for a new harmonized global standard for energy classes for electric motors has been initiated by IEC. The IEC 60034-30 (Ed.1.0): 2008-10 has been published in October 2008. The new classification scheme will harmonize the regional and national standards that have been used so far. Three commercial levels of energy efficiency are defined in IEC 60034-30:

Premium Efficiency	IE3	NEMA Premium
High Efficiency	IE2	EPAAct, Eff1
Standard efficiency	IE1	Eff2

The standard also reserves IE4 (Super Premium Efficiency), a future level above IE3. These products are not yet commercially available and might need to go beyond AC induction motor technology to reach the necessary values. There are also lower efficient motors still in use now (i.e. Eff3) but they will not be used anymore in the new classification. The efficiency limits of the existing CEMEP-EU classes Eff1 and Eff2 have to be recalibrated according to the new testing standard IEC 60034-2-1 that includes a more accurate account of additional stray load losses in order to qualify for the IE2 and IE3 class respectively. The efficiency class and motor efficiency, tested according to IEC 60034-2-1 at nominal load, using a low uncertainty test method will be printed as shown in the following example on the rating plate and stated in the written product documentation and catalogue:

IE3 94.5%

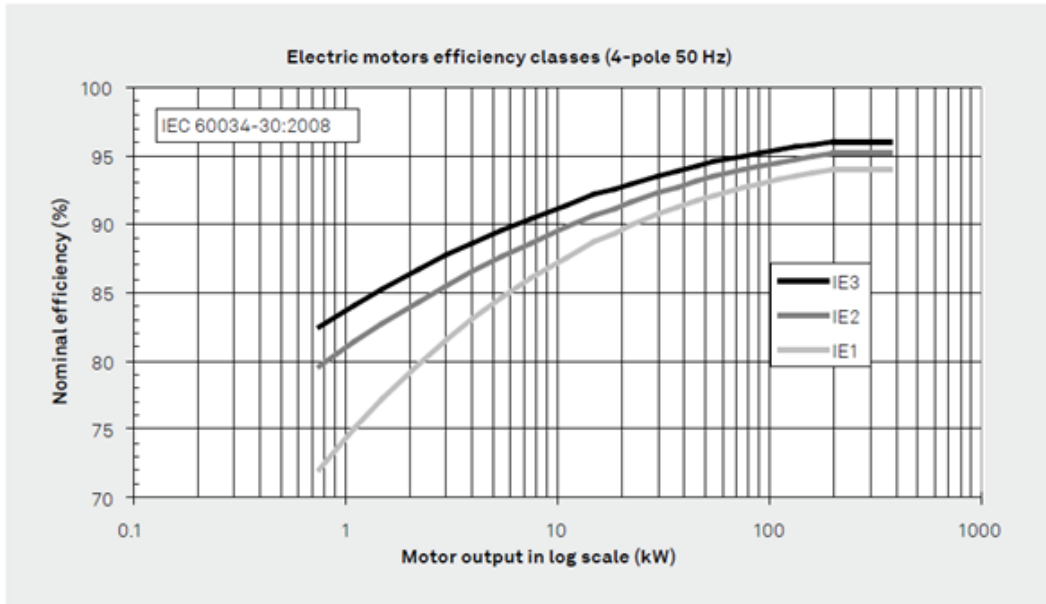


Figure 1: Efficiency classes for 50 Hz 4-pole motors (IEC 60034-30:2008)

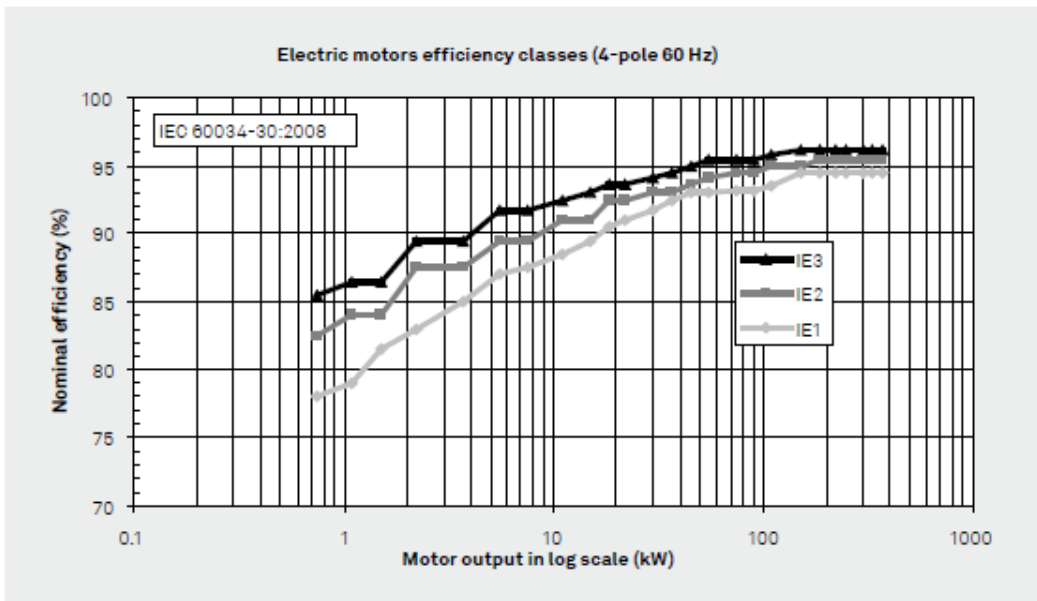


Figure 2: Efficiency classes for 60 Hz 4-pole motors (IEC 60034-30:2008)

9.2 Minimum Surface Area of a cylinder

$$\text{Let } V = \text{volume in m}^3 \quad (9.1)$$

$A = \text{surface area in m}^2$

$R = \text{the radius in m}$

$L = \text{the length in m}$

For a given cylinder the volume is

$$V = \pi r^2 L \quad (9.2)$$

$$A = 2\pi r^2 + 2\pi rL \quad (9.3)$$

From (1) (3)

$$L = \frac{V}{\pi r^2} \quad (9.4)$$

put in 3.75

$$A = 2\pi r^2 + \frac{2V}{r} \quad (9.5)$$

Minimum A is when $\frac{dA}{dr} = 0$

$$\frac{dA}{dr} = 4\pi r - 2V r^{-2} \quad (9.6)$$

Solving (5) will give us

$$r^3 = \frac{V}{2\pi} \quad (9.7)$$

Sub for V from (1) will give us

$$r = L/2 \quad (9.8)$$

9.3 The Matlab code for the sizing of 1 kW single phase BLDC motor.

```



```

```

r_3 = r_2*1e-3 + x_c;

%approximation for core path length (r3 instead r4)
lc = 2*(r_1+(r_3+(x_p/2)-r_2*1e-3)) + (2*pi*(r_3+(x_p/2)))/4);

%calculate the number of turns
N = 45*Ke*(2*mag_wid+2*g+lc/Mu_r)/(40*2*mag_wid*Br*r_2*len*1e-
6);

%calculate the required winding area
Aw = pi*(r_w^2)*2*N*3;

% the following is to find r_4 which is the radius of the inner
back iron

%calculate r_4 the inner radius of the back iron by solving
the
%equation see documents for details
equation_constants = [(pi) (-4*x_p) (4*x_p*r_3 - pi*(r_3^2) -
Aw)];
m = roots(equation_constants);
r_4 = m(1,1);

%only the +ve root will be considered which is m(1,1)

r_5 = r_4 + x_p/2; %external motor radius

l_wind = (pi*N*r_w^2)/(4*(r_4-r_3)); % height of copper over the
stator poles

overall_length= len*1e-3 + l_wind*2;

volume = pi*(r_5^2)* overall_length;

lc = 2*(r_1+(r_4+(x_p/2)-r_2*1e-3)) + (2*pi*(r_4+(x_p/2)))/4);

B_core = (N*IRated*Mu_o+
2*mag_wid*Br)/(2*mag_wid+2*g+(lc/Mu_r));
%winding_width=r_4-r_3

if(B_core <= B_sat)
    %to plot
    z(r_2,len)= B_core ;
    x(r_2,len)=r_2;
    y(r_2,len)= len;
    n(r_2,len)= N;

    r_2;
    len;
    N;

    if((N <= N_limit) && (r_5*2/overall_length <= 1) &&
(r_5*2/overall_length >= 0.8) && (B_core >= B_max))

        B_max = B_core;
        optimum_r_2= r_2*1e-3;
        optimum_lamination_length=len*1e-3;
        optimum_turns = N;
        optimum_overall_radius= r_5;
        optimum_overall_length = overall_length;

```

```

        pole_width = x_p;
        internal_back_iron_readius = r_4;
        optimum_volume = volume;
    end
end
end
end

surf(x,y,z)
xlabel('inner stator radius')
ylabel('Stack length')
zlabel('B')

fprintf('optimum inner stator radius  %6.4f m\n', optimum_r_2);
fprintf('optimum Stack length          %6.4f m\n', optimum_lamination_length);
fprintf('optimum turns                  %6.0f turns\n', optimum_turns);
fprintf('optimum overall radius          %6.4f m\n', optimum_overall_radius);
fprintf('optimum overall length           %6.4f m\n', optimum_overall_length);
fprintf('optimum volume                    %8.6f m3\n', optimum_volume);
fprintf('flux density B at full load %6.4f m\n\n\n', B_max);
pole_width
internal_back_iron_readius

%do the same calculations for more acceptal results within +5% of
%the minimum volume
acceptable_B = B_max - B_max*0.001 ;% 10% more
accept_count=1;

fprintf('the following are the results for upto +10 percent of the sat
flux\n\n\n');
for r_2=r_2_low_limit:1:r_2_limit % r_2 is the radius of the inner
stator
    arc in mm
    for len=len_low_limit:1:len_limit % len is the length of motor
        lamination in mm

        %calculate the number of turns
        % N= Ke/(((B*40/45)*r_2*len*1e-6));

        %Calculate r1
        r_1 = (r_2*1e-3) - g - mag_wid;
        %calculate the stator pole width
        x_p = sqrt(2*(r_2*1e-3)^2*(1-cos(40*pi/180)));
        %calculate the long arc width
        x_c = x_p/2;
        %calculate the radius of the outer stator arc
        r_3 = r_2*1e-3 + x_c;

        %approximation for core path length (r3 instead r4)
        lc = 2*(r_1+(r_3+(x_p/2)-r_2*1e-3)) + (2*pi*(r_3+(x_p/2)))/4;

        %calculate the number of turns
        N = 45*Ke*(2*mag_wid+2*g+lc/Mu_r)/(40*2*mag_wid*Br*r_2*len*1e-
6);

```

```

%calculate the required winding area
Aw = pi*(r_w^2)*2*N*3;

% the following is to find r_4 which is the radius of the inner
back iron

%calculate r_4 the inner radius of the back iron by solving
the
%equation see documents for details
equation_constants = [(pi) (-4*x_p) (4*x_p*r_3 - pi*(r_3^2) -
Aw)];
m = roots(equation_constants);
r_4 = m(1,1);

%only the +ve root will be considered which is m(1,1)

r_5 = r_4 + x_p/2; %external motor radius

l_wind = (pi*N*r_w^2)/(4*(r_4-r_3));% height of copper over the
stator poles

overall_length= len*1e-3 + l_wind*2;

volume = pi*(r_5^2)* overall_length;

lc = 2*(r_1+(r_4+(x_p/2)-r_2*1e-3)) + (2*pi*(r_4+(x_p/2))/4);

B_core = (N*IRated*Mu_o+
2*mag_wid*Br)/(2*mag_wid+2*g+(lc/Mu_r));

if((N <= N_limit) && (r_5^2/overall_length <= 1) &&
(r_5^2/overall_length >= 0.8) && (B_core <= B_sat) &&
(B_core >= acceptable_B) )

    fprintf('Result No %6.0f\n', accept_count);
    fprintf('acceptable volume %6.6f m3\n', volume);
    fprintf('acceptable r_2 %6.4f m\n', r_2*1e-3);
    fprintf('acceptable stack length %6.4f m\n', len*1e-3);
    fprintf('acceptable turns %6.0f turns\n', N);
    fprintf('acceptable overall radius %6.4f m\n', r_5);
    fprintf('acceptable overall length %6.4f m\n', overall_length);
    fprintf('acceptable B at fuul load %6.4f m\n\n', B_core);
    accept_count= accept_count+1;

end

end

end

```

9.4 Encoderless Method for a Novel Brushless SR Motor

The motor is a special 4 pole design, single phase SRM that has a single switching transistor and one optical sensor which would normally generate the commutation signal. The cross sectional view of the motor is shown in Fig. 9.1. The rotation of the rotor is achieved by a combination of reluctance torque and electromagnetic alignment torque. The reluctance torque component is due to the variable air gap.

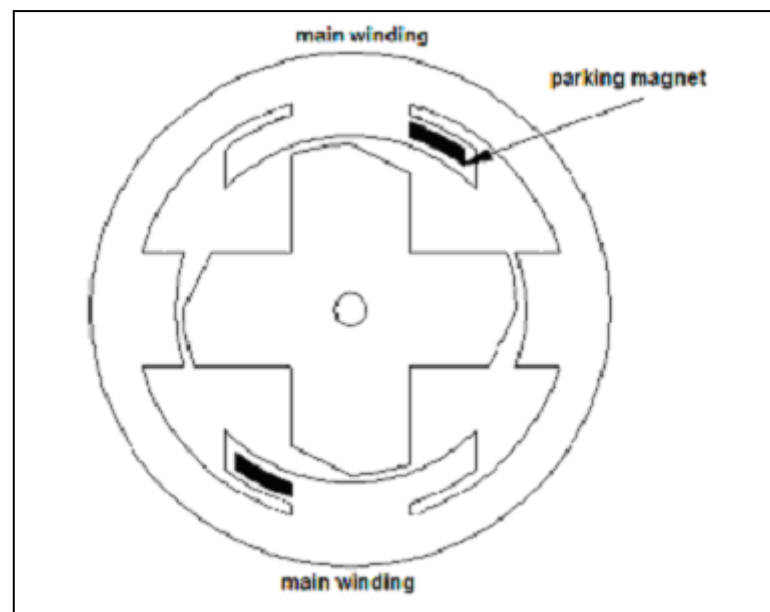


Fig. 9.1 Cross-sectional view of the SRM

Since the inductance of the rotor winding is a function of rotor position, and the rate of change of current depends on the winding inductance, then rotor position can be deduced from winding current and its rate of change. Practically the inductance variation of the winding can be monitored by injecting a high frequency current signal in to the motor winding, and while the rotor is rotating the change in the inductance of the windings causes the injected current to be amplitude modulated, the envelope of the modulated high frequency signal represents the instantaneous variation in the inductance which is related to the rotor position.

Injecting a low level high frequency current in an excited motor winding is not an easy task, the high frequency signal can be distorted by the main excitation current and this will complicate the signal processing operation. To further simplify the processing of the HF injected signal a separate search coils which are isolated from the main winding coils are added in the motor, the coils have few turns.

A number of practical experiments were carried out to monitor the saliency effect on the injected signal with different wiring configuration of sensing coils and for a range of frequencies of injected signal, the experiments and their results are presented in the next section.

9.4.1 Search coils wiring configurations

Two sensing coils of 20 turns each were added to the stator poles of the SR motor positioned as shown in Fig. 9.2. These two opposite sensing coils can be wired up in two different configurations, a four pole configuration or a two pole configuration. Four pole wiring means the two sensing coils are wired in such a way to produce a four pole stator flux when the same current is flowing through them, and this can be achieved by connecting the two coils in series with the 'start' end of one of them connected to the 'start' end of the other one as shown in Fig. 9.3. On the other hand two pole wiring is achieved by connecting the two coils in series with the 'start' of one of them is connected to the 'end' of the other. By connecting the coils in this way a two pole stator flux can be produced when the same current is flowing in them and hence the name two-pole wiring. Fig. 9.4 shows how the sensing coils can be wired in a two pole configuration.

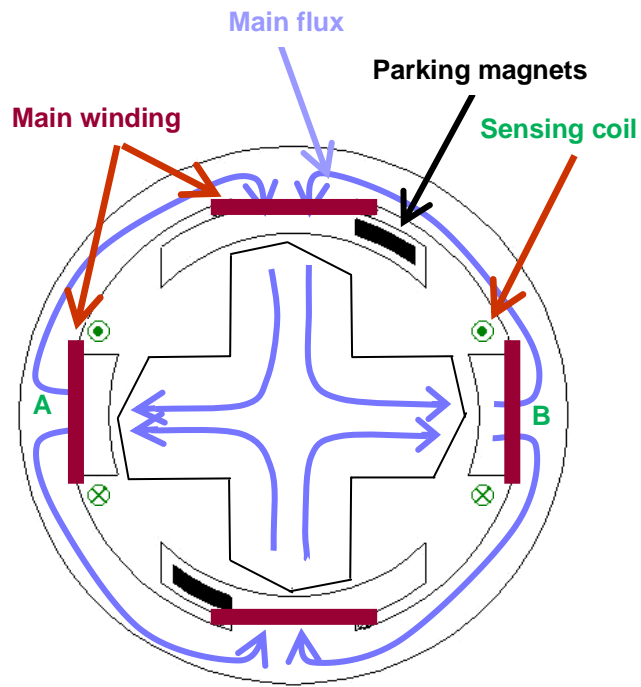


Fig. 9.2 Cross-sectional view of the SRM with sensing coils

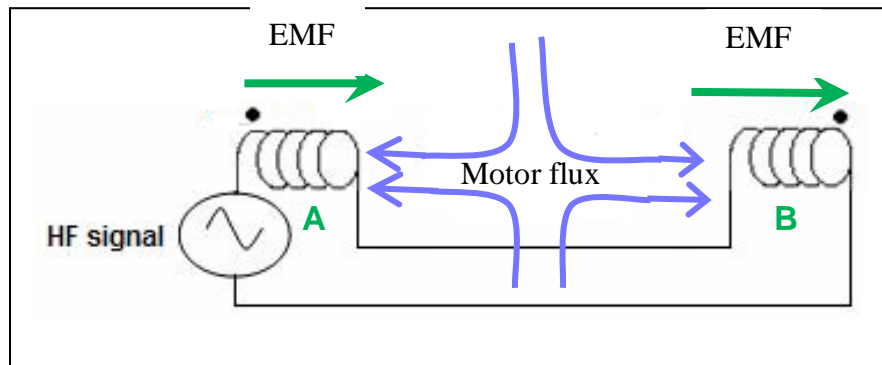


Fig. 9.3 Four pole wiring

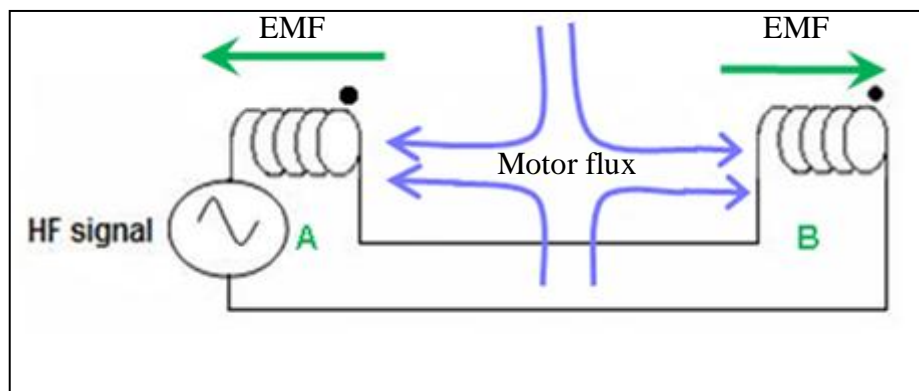


Fig. 9.4 Two pole wiring

When the search coils were wired up in a four pole configuration a 4 kHz sine wave signal was injected into them, and the current signal in the sensing coils were monitored while the rotor was rotating, since the two sensing coils are positioned at the main flux path of the motor's excitation coils, the changing main flux will induce a voltage across the two sensing coils which will contribute to the distortion of the rotor position information contained in the high frequency injected current. Fig. 9.5 shows the high frequency injected current in the sensing coils compared with the commutation signal from the position encoder. It shows how the excitation flux affects the high frequency current in the search coils.

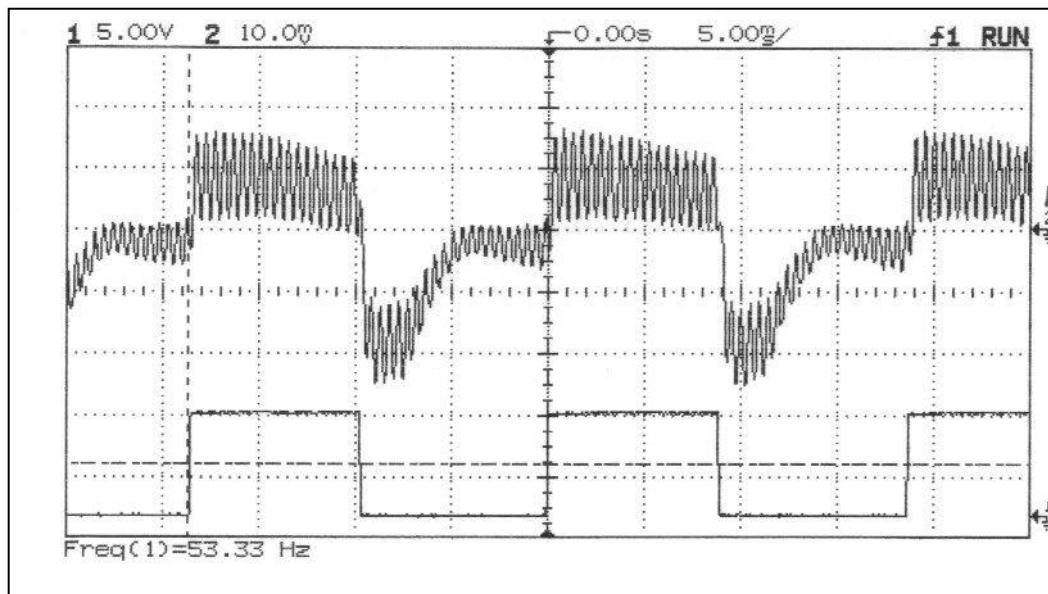


Fig. 9.5 Injected current for 4 pole wiring configuration

The high frequency current in the sensing coils were monitored again but this time the search coils were connected in a two pole wiring configuration as shown in Fig. 9.4. The induced voltage due to the main flux across each of the sensing coils was equal and opposite and the resultant induced voltage across the sensing coils circuit was zero. A

common mode rejection was achieved and the changing flux from the main winding had no effect on the injected signal and that improved the signal to noise ratio significantly. Fig. 9.6 shows the current in the sensing coils compared with the commutation signal with the two pole wiring. It is clear that the rotor position information contained in the high frequency injected signal is preserved. By further signal processing of the modulated HF current rotor position information can be obtained.

It should be noted that a carefully balanced construction of the sensing coils is required in order to maximise the signal to noise ratio by common mode rejection.

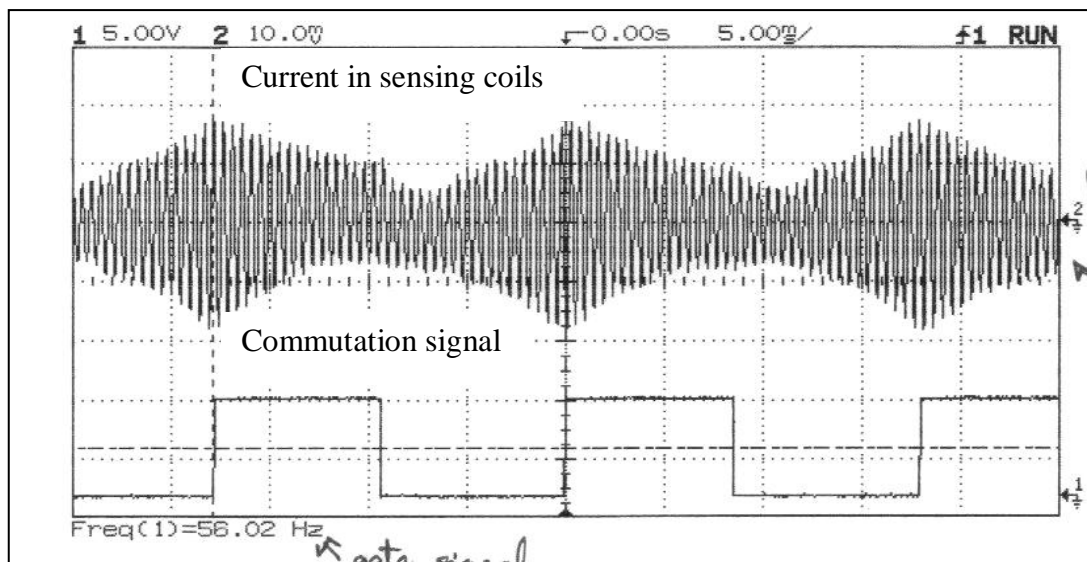


Fig. 9.6 Injected current for 2 pole wiring configuration

9.4.2 Running the motor without position Encoder

The search coil inductance varies with rotor position, maximum inductance is when the rotor is aligned with the sensing coils and minimum inductance is when the rotor is unaligned with the sensing coils. Since the inductance is inversely proportional to the rate of change of current, a change in the inductance of the sensing coils will cause a change in the amplitude of the HF injected current. This variation in inductance will be coincident with the change in inductance of the main windings, and so rotor position informa-

tion can be derived with respect to driving the main motor winding. In the experimental motor a high frequency signal of 12 kHz was injected into the pair of sensing coils, which sets up a low level high frequency flux within the motor with a 2 pole wired search coils. Fig. 9.7 (a) shows how the HF injected current in the sensing coils is amplitude modulated whilst the motor is running using a position sensor, which generates the commutation signal shown in Fig. 9.7(b).

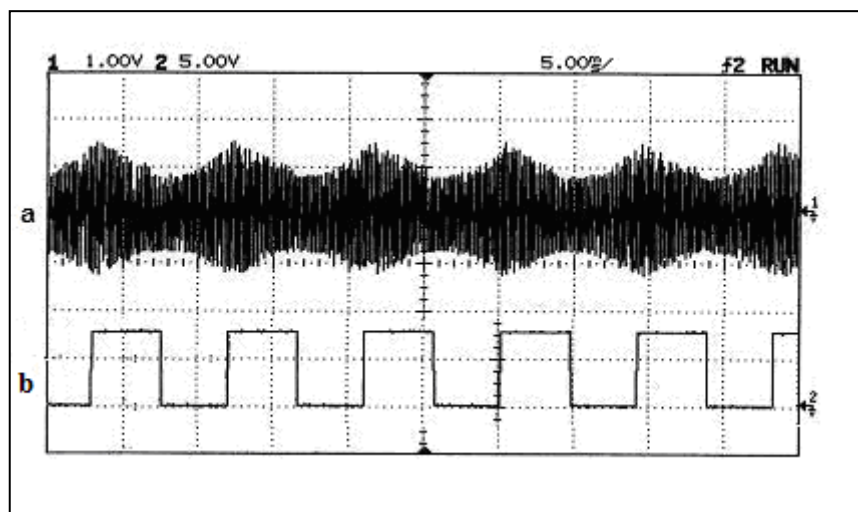


Fig. 9.7 a) current in sensing coil, b) main winding commutation signal

9.4.3 The signal processing

Further signal processing of the envelope yields accurate position information (10% max error). Fig. 9.8 shows the block diagram of the signal processing steps.

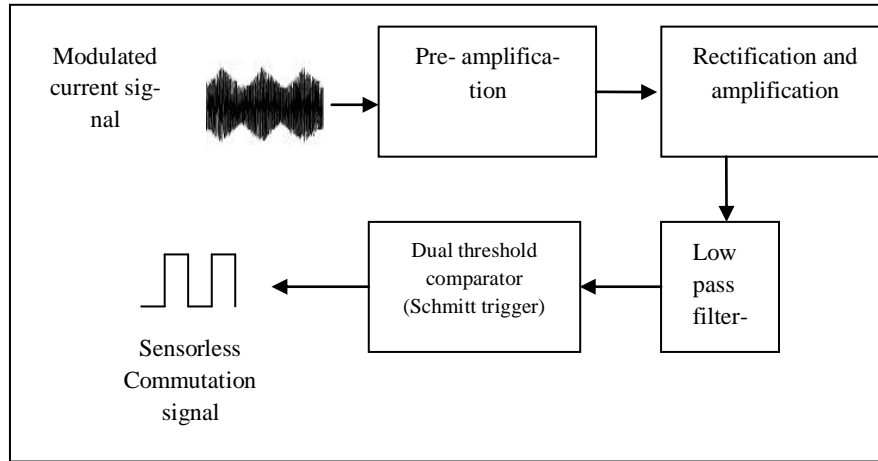


Fig. 9.8 Block diagram of processing the sensing coil signal.

Firstly the modulated current signal is amplified and then rectified and further amplified. Then the signal is passed through a 6 KHz RC low pass filter to extract the envelope which contains the rotor position information. Finally the commutation signal for the power switching transistor is derived from this envelope using a dual threshold Schmitt comparator. The Schmitt trigger comparator has dual threshold detection set at V_1 and V_2 . The input to the Schmitt trigger is the envelope generated from the low pass filter. It can be seen from equations 9.9 and 9.10 that by choosing suitable values for V_1 and V_2 , a square wave signal which has a fixed phase in relation with the input signal is generated. This waveform can be used to commutate the current in the single phase excitation winding. V_1 and V_2 can be found from the following equations:

$$V_1 = \frac{R_1 || R_2 || R_3}{R_2} V_{ref} + \frac{R_1 || R_2 || R_3}{R_3} V_{cc} \quad (9.9)$$

$$V_2 = \frac{R_1 || R_2 || R_3}{R_2} V_{ref} - \frac{R_1 || R_2 || R_3}{R_3} V_{cc} \quad (9.10)$$

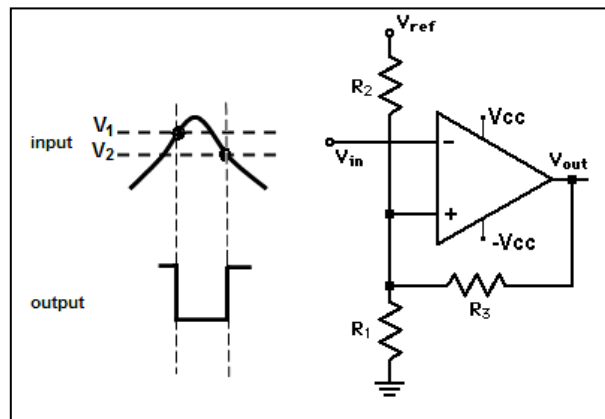


Fig. 9.9 Dual threshold comparator

9.4.4 Signal processing circuit tests

A number of tests were undertaken to compare the commutation signal (from the optical position sensor) with the commutation signal from the comparator in order to determine the accuracy of phasing and signal duty.

At first the motor was operated using the optical sensor signal. A 12 kHz sine-wave current of approximately a few hundred milliamps was injected into the sensing coils. The waveforms at each processing stage are shown in Fig. 9.10. Waveform a shows the modulated current signal after amplification, waveform b is the HF signal after rectification. After passing this signal into a low pass filter waveform c is obtained. A dual threshold comparator compares this envelope within a signal voltage band, to produce the sensorless commutation signal shown in waveform d. This waveform compares very favourably with the original commutation signal produced by the optical position sensor shown in waveform e.

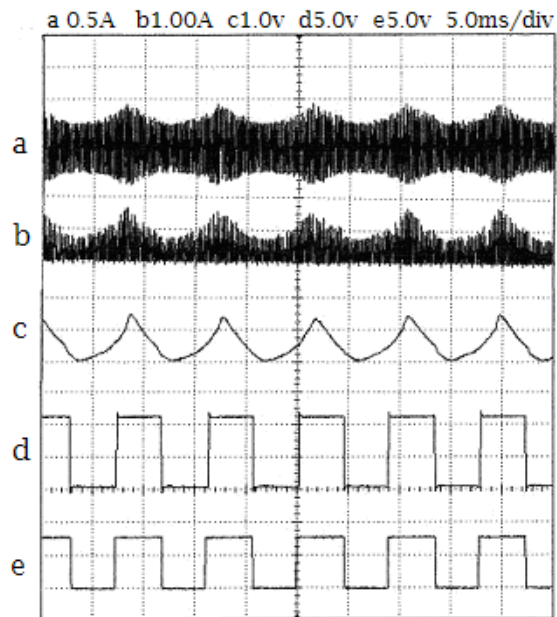


Fig. 9.10 Sensorless signal waveforms

9.4.5 Effect of Loading

In order to see the effect of load on the encoderless signal the envelope was observed at two different loads whilst the motor was running at fixed speed. Fig. 9.11 a and c show the waveforms of the envelope and encoderless commutation signal respectively at no load. When the motor was loaded with 100% of its maximum load the resultant envelope and sensorless signal are shown in Fig. 9.11b and Fig. 9.11d respectively. Comparing the two envelopes it is obvious how the shape of the envelope is affected due to saturation effects of the core and the change in the envelope shape is more noticeable at transition edges of the sensorless commutation signal. This change in the envelope shape has caused an error of about 10% in the timing of the generated sensorless signal as shown in Fig. 9.11c.

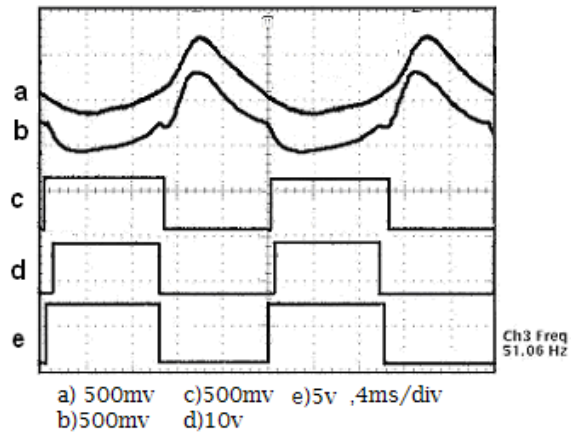


Fig. 9.11 a) Inductance variation envelope at no load, b) Inductance variation envelope at full load, c) No load sensorless signal, d) Sensorless signal at full load, e) Optical sensor signal

This experiment has presented an improved sensorless control method for a single phase SR motor and the results are published in the *42nd International University's Power Engineering* conference Brighton 4th -6th Sept 2007, see appendix A for full paper.

The method takes advantage of the salient poles and observes the variations in inductance of the sensing coils, which are isolated from the main windings. The sensing coils are wired to reject the influence of the main winding flux by common mode rejection. This significantly improves the signal to noise ratio of the injected signal and simplifies the processing of the signal in order to obtain rotor position information. The practical implementation of this method was verified experimentally and the results showed that the output signal from the rotor position observer is always within 10% of the timing of the encoder signal over the full speed range and up to the maximum load.

9.5 Matlab code of phase mismatch magnitude calculator

```
function Te = fcn(e,i,t_cur)
.
persistent s_old ;
persistent t_old ;
persistent Te_old ;

%initilization
if isempty(s_old)
    s_old = 0;
    t_old = 0;
    Te_old = 0;
end

s=0;
if e ~= i
    s = 1;
elseif e==i
    s=0;
end

if s_old < s %rising edge detected
    t_old = t_cur;
    Te = Te_old;
elseif s_old > s %falling edge detected
    Te = t_cur - t_old;
    Te_old = t_cur - t_old ;
else
    Te = Te_old;
end

s_old = s;
```

9.6 Matlab code of phase mismatch error polarity determination code

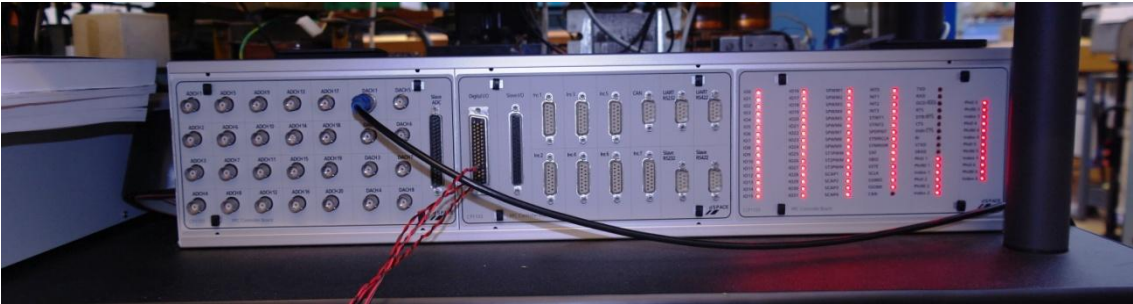
```
function errorP = fcn(e,i)

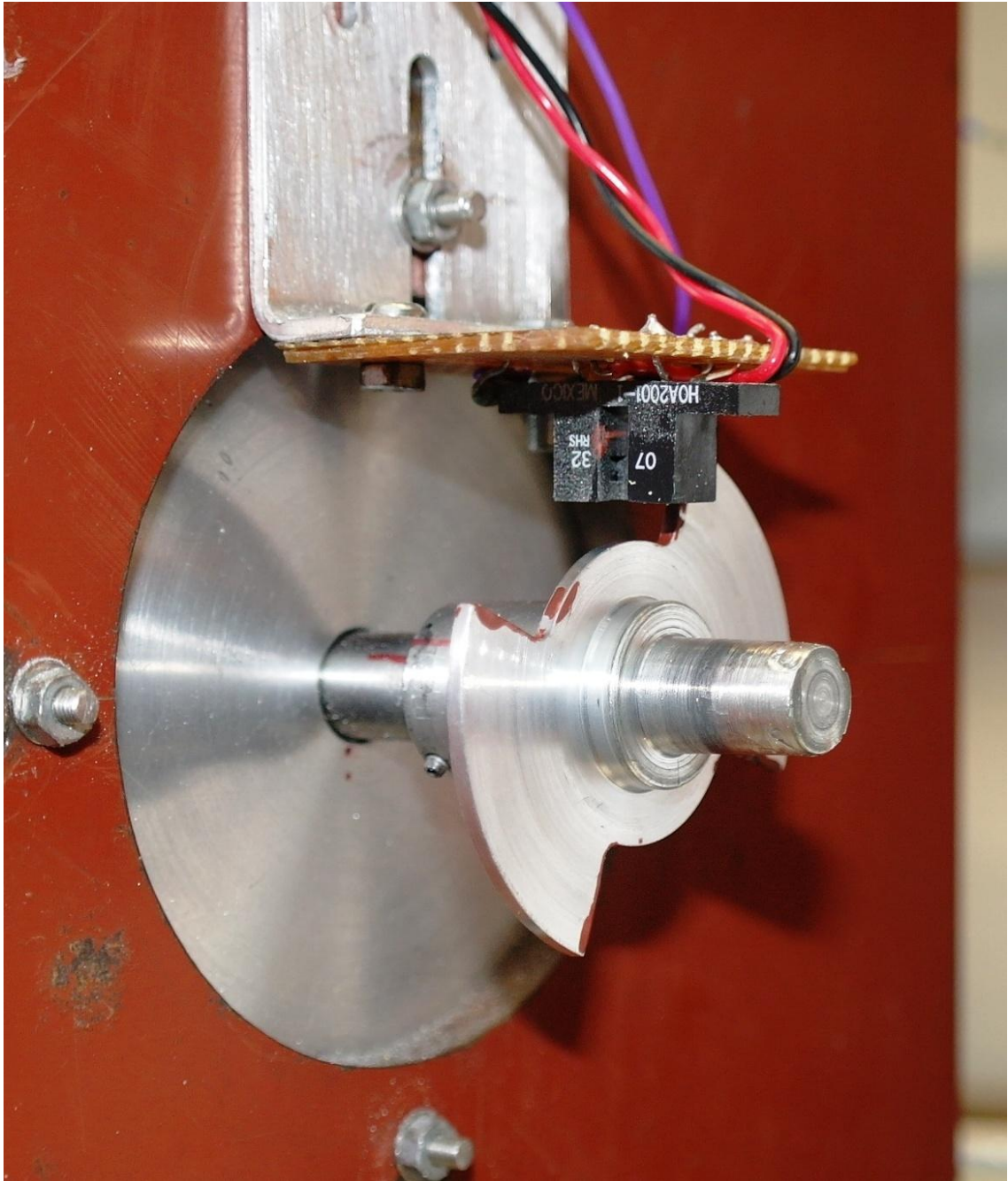
persistent e_old ;
persistent i_old ;
persistent errorP_old ;

%initilization
if isempty(e_old)
    e_old = 0;
    i_old = 0;
    errorP_old = 0;
end

if e_old < e && i == 0 %rising edge detected
    errorP = 1;
    errorP_old= errorP;
elseif e_old < e && i == 1
    errorP = -1;
    errorP_old= errorP;
else
    errorP = errorP_old;
end
e_old = e;
```

9.7 Experimental set up photos for phase advance control testing





9.8 Torque transducer datasheet

Rotary Shaft

TORQUE SENSOR

with Brushless Data Transmission System

TLT
Series



- Torque Ranges: 0-0.2Nm to 0-200Nm
- 0.25% Accuracy
- $\pm 5\text{Vdc}$ Output
- Suitable for continuously rotating applications
- Inductive non-contact data transmission system gives operating speeds up to 8000rpm
- 3 YEAR WARRANTY

Options Available

Special couplings can be manufactured to order
 $\pm 10\text{Vdc}$ Output

Supplied With Any Instrumentation and Calibrated as
a Complete System with Traceable Certificate

DESCRIPTION

The TLT series of torque transducers provides low-cost option for high-speed, high accuracy "in-line" torque measurement by utilising strain gauged shaft and 'non-contact' inductive technology.

The signal from the strain gauge bridge is converted into a modulated frequency that is proportional to the measured torque. This signal is transferred from a rotating coil to a static coil for processing by the on-board amplifier. Excitation voltage is also transferred using this system.

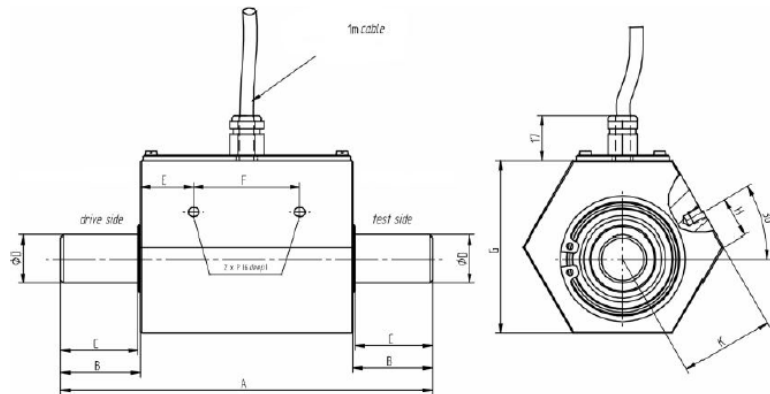
A $\pm 5\text{Vdc}$ output is provided as standard with $\pm 10\text{Vdc}$ as an option.

The TLS/TLSM series can be additionally be accompanied by any of our range of instrumentation to offer a complete system, supplied and calibrated from a single supplier.

SPECIFICATION

CHARACTERISTICS	TLT	UNITS
Maximum Torque Ranges:	0-0.2, 0-0.5, 0-1, 0-2, 0-5, 0-10, 0-15, 0-20, 0-50, 0-100, 0-200	Nm
Rated Output (FSO):	±5 (±10 optional)	Vdc
Excitation Voltage:	12-28	Vdc
Supply Current:	<90	mA
Safe Overload:	150	% FSO
Accuracy Class:	<0.25	±% FSO
Repeatability:	<0.05	±% FSO
Operating Temperature Range:	0 to +60	°C
Zero Temperature Shift:	<0.04	±%FSO/°C
Span Temperature Shift:	<0.02	±%FSO/°C
Environmental Protection:	IP50	

Capacity (Nm)	Max Speed (rpm)	Torsional Stiffness (Nm/rad)	Mass Moment of Inertia - Drive Side (kg/m ²)	Mass Moment of Inertia - Test Side (kg/m ²)	Max Axial Thrust (N)
0,2	8000	1,8*10 ^{^1}	1,6*10 ^{^-6}	1,0*10 ^{^-6}	20
0,5	8000	1,1*10 ^{^2}	1,6*10 ^{^-6}	1,0*10 ^{^-6}	30
1	8000	3,6*10 ^{^2}	1,6*10 ^{^-6}	1,1*10 ^{^-6}	40
2	8000	3,5*10 ^{^2}	1,6*10 ^{^-6}	1,1*10 ^{^-6}	40
5	8000	8,9*10 ^{^2}	1,7*10 ^{^-6}	1,1*10 ^{^-6}	50
10	8000	8,9*10 ^{^2}	1,7*10 ^{^-6}	1,1*10 ^{^-6}	50
15	8000	8,9*10 ^{^2}	1,7*10 ^{^-6}	1,1*10 ^{^-6}	50
20	6000	8,4*10 ^{^3}	4,2*10 ^{^-5}	2,1*10 ^{^-5}	1600
50	6000	8,4*10 ^{^3}	4,2*10 ^{^-5}	2,1*10 ^{^-5}	1600
100	6000	2,0*10 ^{^4}	4,7*10 ^{^-5}	2,7*10 ^{^-5}	3000
200	6000	2,0*10 ^{^4}	4,7*10 ^{^-5}	2,7*10 ^{^-5}	3000



Capacity (Nm)	A	B	C	D	E	F	G	H	K	P
0-0.2 to 0-2	100	17,5	17	8	15	35	46	8	26	M4
0-5 to 0-15	100	17,5	17	10	15	35	46	8	26	M4
0-20, 0-50	140	30	29	18	20	40	65	15	34,8	M5
0-100, 0-200	160	40	39	22	20	40	65	15	34,8	M5

10. References

- [1] P. P. Acarnley and J. F. Watson, "Review of Position-Sensorless Operation of Brushless Permanent-Magnet Machines," *IEEE Transactions on Industrial Electronics*, vol. 53, 2006.
- [2] J. R. Hendershot and T. Miller, *Design of Brushless Permanent-Magnet Motors*: Oxford University Press, 1994.
- [3] T. J. E. Miller, "Brushless Permanent-Magnet and Reluctance Motor Drives," ed: oxford, 1989, p. 207.
- [4] C. F. a. H. Caricchi F, "Low-Cost Compact Permanent Machine for Adjustable-Speed Pump Application," *IEEE Transactions on*

Industry Applications, IEEE Transactions on, vol. 34, pp. 109-116, 1998.

- [5] H. W. Gao and K. Marushima, "Development of Low-Cost and High-Power Brushless DC Motors," presented at the Proceedings of the 2nd CICEM, 1995.
- [6] S. K.Pal and N. M.Cochrane, "Brushless DC Motor With Low Cost High Energy Permanent Magnets and Integrated Drive for Novel High Speed Electric Atomisers," presented at the Proceedings of the Intelligent Motion Conference, 1996.
- [7] V. Ostovic, "Performance Comparison of U-Core and Round Stator Single Phase Permanent Magnet motors for Pump Applications," *IEEE Transactions on*

Industry Applications, IEEE Transactions on, 1999.

- [8] A. Kusko and S. M. Peeran, "Brushless DC Motors Using Unsymmetrical Field Magnetization," *IEEE Transactions on Industry Applications*, vol. IA-23, 1987.
- [9] G. Zhenhong, C. Liuchen, and X. Yaosuo, "Cogging torque of permanent magnet electric machiens: An overview," in *Electrical and Computer Engineering, 2009. CCECE '09. Canadian Conference on*, 2009, pp. 1172-1177.
- [10] D. C. Hanselman, "Effect of skew, pole count and slot count on brushless motor radial force, cogging torque and back EMF," *Electric Power Applications, IEE Proceedings -*, vol. 144, pp. 325-330, 1997.
- [11] B. Ackermann, J. H. H. Janssen, R. Sottek, and R. I. van Steen, "New technique for reducing cogging torque in a class of brushless," *Electric Power Applications, IEE Proceedings B*, vol. 139, pp. 315-320, 1992.
- [12] H. Sang-Moon, E. Jae-Boo, H. Geun-Bae, J. Weui-Bong, and J. Yoong-Ho, "Cogging torque and acoustic noise reduction in permanent magnet motors by teeth pairing," *Magnetics, IEEE Transactions on*, vol. 36, pp. 3144-3146, 2000.
- [13] K. Gyu-Hong, S. Young-Dae, K. Gyu-Tak, and H. Jin, "A Novel Cogging Torque Reduction Method for Interior-Type Permanent-Magnet Motor," *Industry Applications, IEEE Transactions on*, vol. 45, pp. 161-167, 2009.
- [14] C. Breton, J. Bartolome, J. A. Benito, G. Tassinario, I. Flotats, C. W. Lu, and B. J. Chalmers, "Influence of machine symmetry on reduction of cogging torque in permanent-magnet brushless motors," *Magnetics, IEEE Transactions on*, vol. 36, pp. 3819-3823, 2000.
- [15] M. Rizwan and M. A. N. Doss, "Reduction of cogging torque in PMBLDC motor with reduced stator tooth width and bifurcated surface area using Finite

- Element analysis," in *Electrical Energy Systems (ICEES), 2011 1st International Conference on*, pp. 128-132.
- [16] C. Studer, A. Keyhani, T. Sebastian, and S. K. Murthy, "Study of cogging torque in permanent magnet machines," in *Industry Applications Conference, 1997. Thirty-Second IAS Annual Meeting, IAS '97., Conference Record of the 1997 IEEE*, 1997, pp. 42-49 vol.1.
- [17] K. Hong-Seok and K. Kwang-Joon, "Characterization of noise and vibration sources in interior permanent-magnet brushless DC motors," *Magnetics, IEEE Transactions on*, vol. 40, pp. 3482-3489, 2004.
- [18] L. Touzhu and G. Slemon, "Reduction of cogging torque in permanent magnet motors," *Magnetics, IEEE Transactions on*, vol. 24, pp. 2901-2903, 1988.
- [19] L. Chang, A. R. Eastham, and G. E. Dawson, "Permanent magnet synchronous motor: finite element torque calculations," in *Industry Applications Society Annual Meeting, 1989., Conference Record of the 1989 IEEE*, 1989, pp. 69-73 vol.1.
- [20] J. Mizia, K. Adamiak, A. R. Eastham, and G. E. Dawson, "Finite element force calculation: comparison of methods for electric machines," *Magnetics, IEEE Transactions on*, vol. 24, pp. 447-450, 1988.
- [21] Y. Kawaguchi, T. Sato, I. Miki, and M. Nakamura, "A reduction method of cogging torque for IPMSM," in *Electrical Machines and Systems, 2005. ICEMS 2005. Proceedings of the Eighth International Conference on*, 2005, pp. 248-250 Vol. 1.
- [22] K. Dong-Hun, P. Il-Han, L. Joon-Ho, and K. Chang-Eob, "Optimal shape design of iron core to reduce cogging torque of IPM motor," *Magnetics, IEEE Transactions on*, vol. 39, pp. 1456-1459, 2003.
- [23] Z. Q. Zhu, S. Ruangsinchaiwanich, N. Schofield, and D. Howe, "Reduction of cogging torque in interior-magnet brushless machines," *Magnetics, IEEE Transactions on*, vol. 39, pp. 3238-3240, 2003.
- [24] G. Zhenhong and C. Liuchen, "Calculation and study on cogging torque of small wind turbine PMSG," in *Electrical and Computer Engineering, 2008. CCECE 2008. Canadian Conference on*, 2008, pp. 000589-000594.
- [25] J. Coulomb, "A methodology for the determination of global electromechanical quantities from a finite element analysis and its application to the evaluation of magnetic forces, torques and stiffness," *Magnetics, IEEE Transactions on*, vol. 19, pp. 2514-2519, 1983.
- [26] J.-Y. Choi and S.-M. Jang, "Experimental verification and analytical approach to cogging torque calculation and reduction of permanent magnet generators with multipole rotor for wind power applications," *Journal of Applied Physics*, vol. 103, pp. 07F106-07F106-3, 2008.
- [27] T. Tudorache, L. Melcescu, and M. Popescu, "Methods for cogging torque reduction of directly driven PM wind generators," in *Optimization of Electrical and Electronic Equipment (OPTIM), 2010 12th International Conference on*, pp. 1161-1166.
- [28] C. Jang-Sung, J. Hyun-Kyo, and Y. Joong-Suk, "Shape optimization of closed slot type permanent magnet motors for cogging torque reduction using evolution strategy," *Magnetics, IEEE Transactions on*, vol. 33, pp. 1912-1915, 1997.
- [29] R. Lateb, N. Takorabet, and F. Meibody-Tabar, "Effect of magnet segmentation on the cogging torque in surface-mounted permanent-magnet motors," *Magnetics, IEEE Transactions on*, vol. 42, pp. 442-445, 2006.

- [30] H. Sang-Moon, E. Jae-Boo, J. Yoong-Ho, L. Deug-Woo, and K. Beom-Soo, "Various design techniques to reduce cogging torque by controlling energy variation in permanent magnet motors," *Magnetics, IEEE Transactions on*, vol. 37, pp. 2806-2809, 2001.
- [31] Z. Fengge, T. Ningze, and W. Fengxiang, "Study on cogging torque reduction methods of PM stepping motor," in *Power System Technology, 2004. PowerCon 2004. 2004 International Conference on*, 2004, pp. 796-800 Vol.1.
- [32] !!! INVALID CITATION !!!
- [33] C. Bianchini, F. Immovilli, A. Bellini, and M. Davoli, "Cogging torque reduction methods for internal permanent magnet motors: Review and comparison," in *Electrical Machines (ICEM), 2010 XIX International Conference on*, 2010, pp. 1-6.
- [34] N. Bianchi and S. Bolognani, "Design techniques for reducing the cogging torque in surface-mounted PM motors," *Industry Applications, IEEE Transactions on*, vol. 38, pp. 1259-1265, 2002.
- [35] T. Ishikawa and G. R. Slemon, "A method of reducing ripple torque in permanent magnet motors without skewing," *Magnetics, IEEE Transactions on*, vol. 29, pp. 2028-2031, 1993.
- [36] T. M. Jahns and W. L. Soong, "Pulsating torque minimization techniques for permanent magnet AC motor drives-a review," *Industrial Electronics, IEEE Transactions on*, vol. 43, pp. 321-330, 1996.
- [37] W. Lijian, J. Wanbing, N. Jian, and Y. Jianping, "A cogging torque reduction method for surface mounted permanent magnet motor," in *Electrical Machines and Systems, 2007. ICEMS. International Conference on*, 2007, pp. 769-773.
- [38] Y. Lu and Y. Li, "Tooth-slot cogging torque and noise analysis of permanent magnet motors," in *Electrical Machines and Systems, 2001. ICEMS 2001. Proceedings of the Fifth International Conference on*, 2001, pp. 860-862 vol.2.
- [39] G. Sooriyakumarv, R. Perryman, and S. J. Dodds, "Improved Cogging Calculation Methods for Surface Mounted Permanent Magnet Synchronous Motors," in *Universities Power Engineering Conference, 2006. UPEC '06. Proceedings of the 41st International*, 2006, pp. 753-757.
- [40] K. Gyu-Hong and H. Jin, "Analytical prediction and reduction of the cogging torque in interior permanent magnet motor," in *Electric Machines and Drives, 2005 IEEE International Conference on*, 2005, pp. 1620-1624.
- [41] E. R. Braga Filho, A. M. N. Lima, and T. S. Araujo, "Reducing cogging torque in interior permanent magnet machines without skewing," *Magnetics, IEEE Transactions on*, vol. 34, pp. 3652-3655, 1998.
- [42] L. Sun, Q. Feng, and J. Shang, "Drive of Single-Phase Brushless DC Motors Based on Torque Analysis," *Magnetics, IEEE Transactions on*, vol. 43, pp. 46-50, 2007.
- [43] D. Hanselman, *Brushless Permanent Magnet Motor Design: The Writers' Collective*, 2003.
- [44] H. Der-Ray, Y. Tai-Fa, W. Shyh-Jier, Z. Chi-mou, L. Yin Kwang, S. Kai-Wen, and C. I. G. Hsu, "Cogging torque reduction of a single-phase brushless DC motor," *Magnetics, IEEE Transactions on*, vol. 34, pp. 2075-2077, 1998.
- [45] L. Iepure, L. Tutelea, and I. Boldea, "FEM analysis and control of a tapered airgap single phase PMSM," in *Optimization of Electrical and Electronic Equipment, 2008. OPTIM 2008. 11th International Conference on*, 2008, pp. 241-248.

- [46] S. Bentouati, Z. Q. Zhu, and D. Howe, "Influence of design parameters on the starting torque of a single-phase PM brushless DC motor," *Magnetics, IEEE Transactions on*, vol. 36, pp. 3533-3536, 2000.
- [47] K. Byung-Il, Y. Byoung-Yull, P. Seung-Chan, and J. Young-Sun, "Novel topology of unequal air gap in a single-phase brushless DC motor," *Magnetics, IEEE Transactions on*, vol. 37, pp. 3723-3726, 2001.
- [48] S. Bentouati, Z. Q. Zhu, and D. Howe, "Permanent magnet brushless DC motors for consumer products," in *Electrical Machines and Drives, 1999. Ninth International Conference on (Conf. Publ. No. 468)*, 1999, pp. 118-122.
- [49] A. Hamler and B. Hribernik, "Impact of shape of stator pole of one phase brushless motor on cogging torque," *Magnetics, IEEE Transactions on*, vol. 32, pp. 1545-1548, 1996.
- [50] P. Lefley, "Flux Impulse Motor," 2007 Patent No. US 7,276,830 B2.
- [51] Z. Q. Zhu, Y. Chen, Y. Li, D. Howe, and J. H. Gliemann, "Dynamic Modelling of a High-Speed Single-Phase PM Brushless DC Drive," in *Power Electronics, Machines and Drives, 2006. The 3rd IET International Conference on*, 2006, pp. 484-488.
- [52] W. Weizi, W. Zhigan, J. Wanbing, and Y. Jianping, "Starting methods for hall-less single phase BLDC motor," in *Industrial Electronics Society, 2005. IECON 2005. 31st Annual Conference of IEEE*, 2005, p. 5 pp.
- [53] C. Yu, Z. Q. Zhu, and D. Howe, "Three-Dimensional Lumped-Parameter Magnetic Circuit Analysis of Single-Phase Flux-Switching Permanent-Magnet Motor," *Industry Applications, IEEE Transactions on*, vol. 44, pp. 1701-1710, 2008.
- [54] S. Ahmed and P. Lefley, "Study of the impact of asymmetrical stator pole arc on the cogging torque for single phase Permanent Magnet BLDC Motor," in *International Conference on Electric Power and Energy Conversion Systems, 2009. EPECS '09.*, Sharjah, UAE, 2009, pp. 1-4.
- [55] J. R. Frus and B. C. Kuo, "Closed-loop control of step motors using waveform detection," in *Int. Conf. Stepping Motors and Systems*, 1976 pp. 77 -84
- [56] A. S. Budden, D. Holliday, and P. H. Mellor, "Zero Speed Sensorless Position Detection For Permanent Magnet Synchronous Machines," presented at the IEEE Power Electronics Specialist Conference (PESC), 2005.
- [57] P. P. Acarnley and J. F. Watson, "Review of Position-Sensorless Operation of Brushless Permanent-Magnet Machines," *IEEE Transactions on Industrial Electronics*, vol. 53, 2006.
- [58] K. Iizuka, H. Uzuhashi, M. Kano, T. Endo, and K. Mohri, "Microcomputer control for sensorless brushless motor " *IEEE Transactions Industrial Applications*, vol. IA, pp. 595-601, May/June 1985 1985.
- [59] J. X. Shen and K. J. Tseng, "Analyses and Compensation of Rotor Position Detection Error in Sensorless PM Brushless DC Motor Drives," *IEEE TRANSACTIONS ON ENERGY CONVERSION*, vol. 18, March 2003 2003.
- [60] J. C. Moreira, "Indirect sensing for rotor flux position of permanent magnet AC motors operating over a wide speed range," *IEEE Trans. Ind. Appl.*, vol. 32, pp. 1394-1401, Nov/Dec 1996 1996.
- [61] J. Shao, "Direct Back EMF Detection Method for Sensorless Brushless DC," MSc Virginia Polytechnic Institute and the State University, Blacksburg, Virginia, 2003.

- [62] T. M. Jahns, R. C. Becerra, and M. Ehsani, "Integrated current regulation for a brushless ECM drive," *Power Electronics, IEEE Transactions on*, vol. 6, pp. 118-126, 1991.
- [63] R. C. Becerra, T. M. Jahns, and M. Ehsani, "Four-quadrant sensorless brushless ECM drive," in *Applied Power Electronics Conference and Exposition, 1991. APEC '91. Conference Proceedings, 1991., Sixth Annual*, 1991, pp. 202-209.
- [64] J. P. Johnson, M. Ehsani, and Y. Guzelgunler, "Review of Sensorless Methods for Brushless DC," in *34th IAS Annula Meeting*, 1999.
- [65] S. Ogasawara and H. Akagi, "An Approach to Position Sensorless Drive for Brushless DC Motors," *IEEE Transactions on Industry Applications*, vol. 27, pp. 928-933, 1991.
- [66] T. J. E. Miller, *Electronic Control of Switched Reluctance Machine* Newnes Power Engineering Series, 2001.
- [67] S. Bolognani, S. Bolognani, L. Tubiana, and M. Zigliotto, "EKF-based sensorless IPM synchronous motor drive for flux-weakening applications," *Industry Applications, IEEE Transactions on*, vol. 39, pp. 768-775, 2003.
- [68] R. Dhaouadi, N. Mohan, and L. Norum, "Design and implementation of an extended Kalman filter for the state estimation of a permanent magnet synchronous motor," *IEEE Transactions on Power Electronics* 1991.
- [69] A. S. Budden, D. Holliday, and P. H. Mellor, "Zero Speed Sensorless Position Detection For Permanent Magnet Synchronous Machines " in *Proceedings of the IEEE Power Electronics Specialist Conference (PESC) 2005*, pp. 2436-2441.
- [70] C. Elmas and H. Parra, "Position Sensorless Operation of a Switched Reluctance Drive Based on Observer," in *European Power Electronics Conference*, 1993.
- [71] Z. Chen, Z. Chen, M. Tomita, S. Doki, and S. A. O. S. Okuma, "New adaptive sliding observers for position- and velocity-sensorless controls of brushless DC motors," *Industrial Electronics, IEEE Transactions on*, vol. 47, pp. 582-591, 2000.
- [72] I. Husain, S. Sodhi, and M. Ehsani, "A Sliding Mode Observer Based Controller for Switched Reluctance Motor Drives," in *IEEE Industry Appliaction Society Annual Meeting*, 1994.
- [73] M. Tursini, M. Tursini, R. Petrella, and F. Parasiliti, "Adaptive sliding-mode observer for speed-sensorless control of induction motors," *Industry Applications, IEEE Transactions on*, vol. 36, pp. 1380-1387, 2000.
- [74] N. Matsui, "Sensorless salient-pole PM synchronous motor drive in all speed ranges," *IEEE Trans. Ind. Electronics*, 1996.
- [75] J.-I. Ha, K. Ide, T. Sawa, and S.-K.Sul, "Sensorless rotor position estimation of an interior permanent magnet motor from initial states," *IEEE Trans. Ind. Appl*, 2003.
- [76] G. H. Jang, J. H. Park, and J. H. Chang, "Position detection and start-up algorithm of a rotor in a BLDC motor utilizing inductance variation," 2002.
- [77] S. Ostlund and M. Brokemper, "Sensorless rotor position detection from zero to rated speed for an integrated PM synchronous motor drive," *IEEE Trans. Ind. Appl*, 1996.
- [78] M. Tursini, R. Petrella, and F. Parasiliti, "Initial rotor position estimation method for PM motors," *Industry Applications, IEEE Transactions on*, vol. 39, pp. 1630-1640, 2003.

- [79] P. P. Acarnley, R. J. Hill, and C. W. Hooper, "Detection of Rotor Position in Stepping and Switched Motors by Monitoring of Current Waveforms," *IEEE Transactions on Industrial Electronics*, 1985.
- [80] P. J. Lawrenson, J. M. Stephenson, P. T. Blenkinshop, J. Corda, and N. N. Fulton, "variable speed switched reluctance motrs," *IEE Electric Power Application*, 1980.
- [81] S. K. Panda and g. A. J. Amaratunga, "Analysis of the waveform detection techniques for indirect rotor sensing of switched reluctance motor drives," *IEEE Trans. In Energy Conversions*, 1991.
- [82] N. H. Mvungi and J. M. Stephenson, "Accurate Sensorless Rotor Position Detection in an SR Motor," *IEEE Transactions on Industry Applications*, 1991.
- [83] M. S. Arefeen, M. Ehsani, and T. A. Lipo, "Elimination of discrete position sensor for synchronous reluctance motor," in *Power Electronics Specialists Conference, 1993. PESC '93 Record., 24th Annual IEEE*, 1993, pp. 440-445.
- [84] M. Ehsani, I. Husain, S. Mahajan, and K. R. Ramani, "New modulation encoding techniques for indirect rotor position sensing in switched reluctance motors," *Industry Applications, IEEE Transactions on*, vol. 30, pp. 85-91, 1994.
- [85] H. S. Patel and R. G. Hoft, "Generalized Techniques for Harmonic Elimination and Voltage Control in Thyristor Inverters, Part I," *IEEE Transactions Industrial Applications*, 1973.
- [86] Z. Q. Zhu, S. Bentouati, and D. Howe, "Control of single-phase permanent magnet brushless DC drives for high-speed applications," in *Power Electronics and Variable Speed Drives, 2000. Eighth International Conference on (IEE Conf. Publ. No. 475)*, 2000, pp. 327-332.
- [87] S. K. Safi, P. P. Acarnley, and A. G. Jack, "Analysis and simulation of the high-speed torque performance of brushless DC motor drives," *Electric Power Applications, IEE Proceedings -*, vol. 142, pp. 191-200, 1995.
- [88] N. Binh Minh and M. C. Ta, "Phase Advance Approach to Expand the Speed Range of Brushless DC Motor," in *Power Electronics and Drive Systems, 2007. PEDS '07. 7th International Conference on*, 2007, pp. 1255-1262.
- [89] K. Han, L. Jinglin, and C. Guangzhao, "Study on Field-Weakening Theory of Brushless DC Motor Based on Phase Advance Method," in *Measuring Technology and Mechatronics Automation (ICMTMA), 2010 International Conference on*, 2010

pp. 583-586.

- [90] S. Shinn-Ming and W. Kun-Lin, "A voltage-controlled Brushless DC motor drive over extended speed range," in *Industrial Technology, 2008. ICIT 2008. IEEE International Conference on*, 2008, pp. 1-5.
- [91] C. C. Chan, W. Xia, J. Z. Jiang, K. T. Chan, and M. L. Zhu, "Permanent magnet brushless drives," *Industry Applications Magazine, IEEE*, vol. 4, pp. 16-22, 1998.
- [92] C. M. Chao, C. P. Liao, D. R. Huang, and T. F. Ying, "A new automatic phase adjustment of optical drive signal," *Magnetics, IEEE Transactions on*, vol. 34, pp. 417-419, 1998.
- [93] W. Lijian, J. Wanbing, L. Yi, and Y. Jianping, "Steady performance analysis on single-phase brushless DC motor," in *Electrical Machines and Systems, 2007. ICEMS. International Conference on*, 2007, pp. 774-779.
- [94] N. Jian, W. Lijian, Z. Bo, J. Wanbing, and Y. Jianping, "A novel adaptive commutation angle method for single phase BLDC motor," in *Electrical*

- Machines and Systems, 2007. ICEMS. International Conference on, 2007, pp. 446-449.*
- [95] C. Chun-Lung, C. Yie-Tone, S. Yu-Hsiang, and L. Ruey-Hsun, "An Accurate Automatic Phase Advance Adjustment of Brushless DC Motor," *Magnetics, IEEE Transactions on*, vol. 45, pp. 120-126, 2009.
 - [96] B. Sneyers, D. W. Novotny, and T. A. Lipo, "Field Weakening in Buried Permanent Magnet AC Motor Drives," *Industry Applications, IEEE Transactions on*, vol. IA-21, pp. 398-407, 1985.
 - [97] T. M. Jahns, "Flux-Weakening Regime Operation of an Interior Permanent-Magnet Synchronous Motor Drive," *Industry Applications, IEEE Transactions on*, vol. IA-23, pp. 681-689, 1987.
 - [98] T. Sebastianigordon and G. R. Slemon, "Operating Limits of Inverter-Driven Permanent Magnet Motor Drives," *Industry Applications, IEEE Transactions on*, vol. IA-23, pp. 327-333, 1987.
 - [99] R. F. Schiferl and T. A. Lipo, "Power capability of salient pole permanent magnet synchronous motors in variable speed drive applications," *Industry Applications, IEEE Transactions on*, vol. 26, pp. 115-123, 1990.
 - [100] W. L. Soong and T. J. E. Miller, "Field-weakening performance of brushless synchronous AC motor drives," *Electric Power Applications, IEE Proceedings -*, vol. 141, pp. 331-340, 1994.
 - [101] C. C. Chan, J. Z. Jiang, W. Xia, and K. T. Chau, "Novel wide range speed control of permanent magnet brushless motor drives," in *Power Electronics and Drive Systems, 1995., Proceedings of 1995 International Conference on*, 1995, pp. 780-785 vol.2.
 - [102] G. Jinyun, C. C. Chan, K. T. Chau, and J. Z. Jiang, "Advanced conduction angle control of permanent magnet brushless motor drives," in *Power Electronic Drives and Energy Systems for Industrial Growth, 1998. Proceedings. 1998 International Conference on*, 1998, pp. 552-557 Vol. 2.
 - [103] J. S. Lawler, J. M. Bailey, J. W. McKeever, and J. Pinto, "Limitations of the conventional phase advance method for constant power operation of the brushless DC motor," in *SoutheastCon, 2002. Proceedings IEEE, 2002*, pp. 174-180.
 - [104] J. S. Lawler, J. M. Bailey, J. W. McKeever, and P. Joao, "Extending the constant power speed range of the brushless DC motor through dual-mode inverter control," *Power Electronics, IEEE Transactions on*, vol. 19, pp. 783-793, 2004.
 - [105] "Matlab Help Document."